CHEMIA

STUDIA
UNIVERSITATIS BABEŞ-BOLYAI

CHEMIA

3/2015

S T U D I A

UNIVERSITATIS BABEŞ–BOLYAI

CHEMIA

3

**DEDICATED TO PROF. DR. I. C. POPESCU
ON THE OCCASION OF HIS 70TH ANNIVERSARY**

CUPRINS – CONTENT – SOMMAIRE – INHALT

Professor Ionel Catalin Popescu on his 70th Anniversary

Professor Ionel Catalin Popescu was born on the 15th of July 1945. After graduating from Babeş-Bolyai University Cluj-Napoca (UBB) as a chemist in 1968, he became a research assistant at "Petru Poni" Macromolecular Chemistry Research Institute Iasi, until 1969. Back to the Faculty of Chemistry of Cluj-Napoca, he received his PhD diploma in 1976, working under the supervision of the distinguished Professor Candin Liteanu in the field of electroanalytical chemistry.

As Teaching Assistant (1972), Assistant Professor (1976), Associate Professor (1985) and Professor (1995) at the Faculty of Chemistry and Chemical Engineering Cluj-Napoca, his work continuously contributed to the development and growth of the Departments of Analytical and Physical Chemistry. His courses in the field of applied electrochemistry were highly appreciated by the undergraduate and graduate students. Between 1979 and 1985 he worked as an Associate Professor at the National Institute of Industrial Chemistry, Setif, Algeria. In 1994, Prof. Popescu contributed to the foundation of the master program in Applied Electrochemistry at Babes-Bolyai University, coordinating it until 2008.

The research interests of Professor Popescu span the fields of electroanalytical chemistry, sensors / biosensors, modified electrodes, and electrocatalysis. Among his major contributions, one can count the obtaining and characterization of various non-conventional electrode materials exhibiting electrocatalytic activity and/or selective recognition properties for sensors or biosensors construction, self-assembled electrochemical nanostructures on

gold, electropolymerization on carbonaceous materials and adsorption on conventional electrode materials. In addition to over 150 scientific papers, and 8 patents Professor Popescu also co-authored 8 books and managed numerous grants and research projects. He counts more than 170 participations to scientific conferences with lectures, posters and oral communications. The research grants he coordinated, substantially contributed to the development of electrochemical and electroanalytical research at the Babeş-Bolyai University.

Professor Popescu was a very active member of the international electrochemical community. He has served two terms as national secretary of the International Society of Electrochemistry and he is member of the Romanian Society of Chemistry and of the Romanian Society of Electrochemistry (elected President).

He has served as the head of Physical Chemistry Department (2004-2008), of Chemistry Department (2008-2012), and of the Center of Electrochemistry and Non-conventional materials (excellence diploma of Babes-Bolyai University, 2010). He was member of UBB Senate (2004-2012) and of the Faculty Council during several years.

For his outstanding achievements, he was rewarded with UBB prizes, such as Prize for the best scientific book - 2005 („Amperometric Biosensors. Theory and applications"), Professor of the year – 2011, Prize of representativity -2009, 2010, Prize of scientific excellence - 2008, and the Prize for didactic excellence - 2006, 2007.

This issue of Studia Universitas Babeş-Bolyai, Seria Chemia is dedicated to Professor Popescu in recognition of his exceptional achievements within the Romanian academic community. The intention of the editors was to bring together contributions from the large international circle of his coworkers, scientists that have close professional contact with him and those working intensively in the field of Electrochemistry.

Now, at his 70th anniversary, we–the colleagues of the Electrochemistry group, as well as all the colleagues and researchers of the Faculty of Chemistry and Chemical Engineering of the Babeş-Bolyai University, along with the Editorial Board and all the contributors - wish Professor Ionel Catalin Popescu health and all the best in the many years to come!

Liana Muresan
Petru Ilea
Graziella Turdean

Cluj-Napoca, July 2015

Dedicated to prof. dr. I. C. Popescu
on the occasion of his 70th anniversary

DNA-ELECTROCHEMICAL BIOSENSORS:
A MINI-REVIEW

VICTOR CONSTANTIN DICULESCU, ANA MARIA OLIVEIRA-BRETT[a*]

ABSTRACT. DNA-electrochemical biosensors allow rapid detection of hazard compounds interaction with dsDNA with great sensitivity. The application of the DNA-electrochemical biosensor for the detection of DNA oxidative damage by hazard compounds and pharmaceutical drugs, namely by hydroxyl free radicals, *in situ* generated at the boron doped diamond electrode surface, the hepato-toxins microcystine-LR and nodularine, the temozolomide, the nucleoside analogue gemcitabine, the anticancer disubstituted triazole-linked acridine compounds, and the anticancer antibody rituximab, showing current directions and strategies, will be revisited.

Keywords: DNA, oxidative damage, electrochemistry, biosensor, cancer.

INTRODUCTION

DNA is a major target for interaction with many hazard compounds. These interactions induce changes to dsDNA structure and base sequence, damaging the genetic information code, and are the main cause of health anomalies including cancer [1-3]. Hence, the development of technologies and methodologies to detect dsDNA-hazard compound interactions is very important.

The electrochemical transducers for the characterization of dsDNA-hazard compound interaction received a particular interest due to their rapid detection and great sensitivity, representing an attractive solution in many different fields of application such as the investigation and the

---

[a] *Chemistry Department, University of Coimbra, 3004-535, Coimbra, Portugal.*
[*] *Corresponding author: brett@ci.uc.pt*

evaluation of dsDNA-hazard compound interaction mechanisms, detection of DNA base damage in clinical diagnosis, or detection of specific DNA sequences in human, viral, and bacterial nucleic acids [4-9].

Among the electrochemical transducers, carbon and especially glassy carbon electrodes (GCE) exhibit several unique properties. The extensive potential window in the positive direction allows sensitive electrochemical detection of dsDNA conformational changes and oxidative damage caused to DNA, by monitoring the appearance of the oxidation peaks of the DNA components such as, nucleotides, nucleosides, purine and pyrimidine bases, and guanine (Gua) oxidation product 8-oxoguanine (8-oxoGua), and adenine (Ade) oxidation product 2,8-dyhydroxyadenine (2,8-oxoAde), biomarkers of DNA base oxidative damage [5, 7, 9].

The DNA-electrochemical biosensors design is essential to understand the DNA electrochemical properties and the performance of the DNA-electrochemical biosensor is related to the DNA immobilization procedure. Therefore, a full understanding of the surface morphology of the DNA-electrochemical biosensor is necessary to guarantee the correct interpretation of the experimental results.

This review presents the electrochemical behaviour of DNA, its adsorption morphology, and applications of the DNA-electrochemical biosensor, prepared by three different procedures on glassy carbon surfaces, for the detection of DNA damage by reactive oxygen species, toxins, anticancer drugs and antibodies.

ELECTROCHEMISTRY OF DNA

The electrochemical properties of all DNA bases, nucleosides and nucleotides were studied at a glassy carbon electrode [10].

Differential pulse (DP) voltammograms (**Figure 1**) recorded at the GCE in solutions of DNA bases guanine (Gua), adenine (Ade), thymine (Thy) and cytosine (Cyt) have shown that all DNA bases undergo electrochemical oxidation at different potentials.

The oxidation of purine bases Gua and Ade occurs at more negative values than the oxidation of pyrimidines bases Thy and Cyt. Gua being the easiest oxidised base. At the same time, DP voltammograms in nucleoside solutions, of the sugar purine bases, deoxyguanosine (dGuo) and deoxyadenosine (dAdo) (**Figure 1**), have shown that their oxidation occurs at ~ 200 mV more positive potential than the corresponding purine base oxidation.
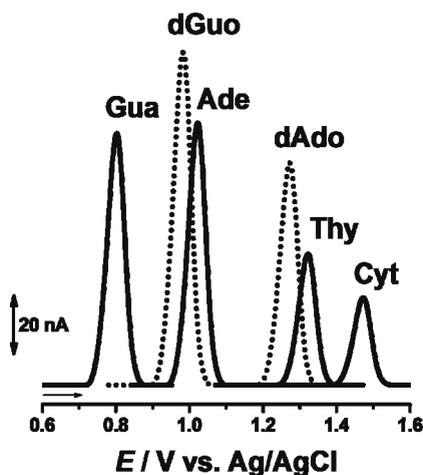
Figure 1. DP voltammograms base-line corrected at the GCE in solutions of: 10 μM guanine (Gua), guanosine (dGuo), adenine (Ade), adenosine (dAdo), and 50 μM thymine (Thy) and cytosine (Cyt) in pH = 4.5 0.1 M acetate buffer.

The electrochemical oxidation of DNA at the GCE shows two anodic peaks corresponding to the oxidation of Gua and Ade residues (**Figure 2**). The DP voltammogram of single stranded DNA (ssDNA) shows higher currents for both bases oxidation when compared to the voltammogram in the solution of double stranded DNA (dsDNA).
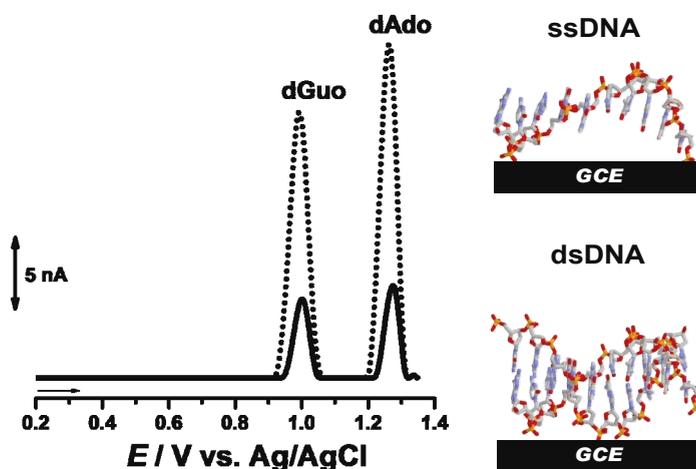
Figure 2. DP voltammograms base-line corrected at the GCE in solutions of 60 μg mL^{-1} (•••) ssDNA and (—) dsDNA in pH = 4.5 0.1 M acetate buffer.

The electrochemical behaviour obtained for dsDNA and ssDNA illustrates the greater difficulty for the transfer of electrons from the inside of the rigid DNA double-strand helix to the electrode surface, than from the flexible DNA single strand where the bases are in close proximity to the electrode surface. Thus, DP voltammetry allows the detection and characterisation of DNA structure in different samples.

DNA-ELECTROCHEMICAL BIOSENSORS PREPARATION

The immobilization of the dsDNA probe on the electrode surface is done in the pH range 4.5 - 5.5 due to the better adsorption of dsDNA at this pH on the GCE surface, consequently leading to an enhanced electrochemical response (**Figure 3**).

A
x, y: 1000 nm; z: 0.5 nm

B
x, y: 1000 nm; z: 3 nm

C
x, y: 1000 nm; z: 131 nm

D
x, y: 1000 nm; z: 25 nm
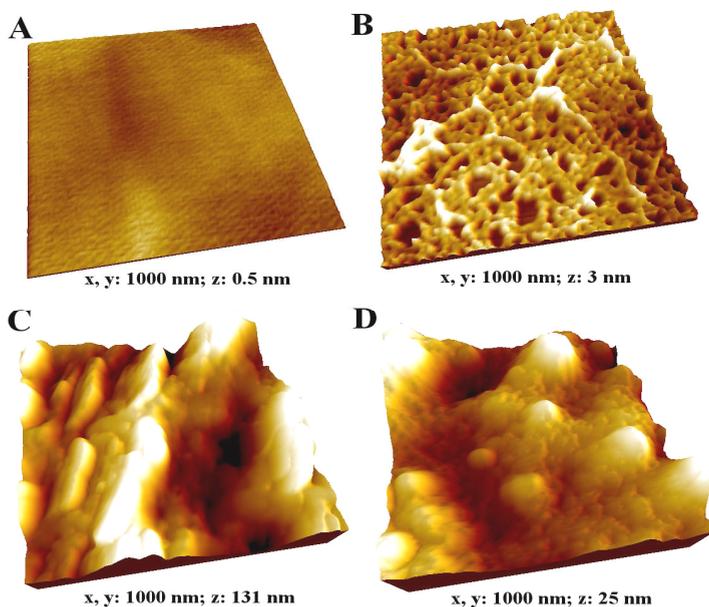
Figure 3. MAC Mode AFM three-dimensional images in air of:
A) clean HOPG electrode;
B) thin-layer dsDNA-electrochemical biosensor surface, prepared onto HOPG by 3 min free adsorption from 60 µg mL^{-1} dsDNA in pH 4.5 0.1 M acetate buffer;
C) multi-layer dsDNA-electrochemical biosensor, prepared onto HOPG by evaporation of 3 consecutive drops each containing 5 µL of 50 µg mL^{-1} dsDNA in pH 4.5 0.1 M acetate buffer;
D) thick-layer dsDNA-electrochemical biosensor, prepared onto HOPG by evaporation from 37.5 mg mL^{-1} dsDNA in pH 4.5 0.1 M acetate buffer.
From reference [5] with permission.

Three different procedures have been followed in the DNA-electrochemical biosensor construction:

1. A thin-layer dsDNA-electrochemical biosensor: prepared by immersing the GCE surface in a 60 µg mL^{-1} dsDNA solution during 3 min (**Figure 3B**).

2. A multi-layer dsDNA-electrochemical biosensor: prepared by successively covering the GCE surface with three drops, of 5 µL each of 50 µg mL^{-1} dsDNA solution. After placing each drop on the electrode surface the biosensor is dried under a constant flux of N$_2$ (**Figure 3C**).

3. A thick-layer dsDNA-electrochemical biosensor: prepared by covering the GCE surface with 10 µL of 35 mg mL^{-1} dsDNA solution and allowing it to dry overnight in a normal atmosphere (**Figure 3D**).

ADSORPTION OF DNA

The development of DNA-electrochemical biosensors is associated with an adsorption processes of dsDNA on charged electrode surfaces [5, 7, 9].

The immobilization of dsDNA, to form the DNA-electrochemical biosensor, and the morphological characterization of the modified electrode surface is essential for the correct evaluation of all factors that may influence the electrochemical response.

The surface characteristics of dsDNA-electrochemical biosensors on highly oriented graphite (HOPG) visualized by *ex situ* MAC mode AFM showed different patterns of adsorption dependent on polynucleotide primary and secondary structures, concentration and potential applied during immobilization procedure (**Figure 3**).

The complete coverage of the electrode surface is crucial for the robustness of the dsDNA film and reduction of non-specific adsorption.

The AFM studies enabled the correct evaluation of factors influencing the development of DNA-electrochemical biosensors for detection of DNA-hazard compound interactions.

APPLICATIONS OF THE DNA-ELECTROCHEMICAL BIOSENSOR

Free radical damage

Reactive oxygen species (ROS) such as superoxide (O$_2^{-}$•), peroxyl (ROO•), and hydroxyl (OH•) radicals are generated inside cells as products of metabolism, by leakage from mitochondrial respiration, and also under the influence of exogenous agents such as ionizing radiation, quinones, and peroxides.

13

Excess ROS are responsible for causing DNA oxidative modifications and mutations, which can initiate carcinogenesis and may play a role in the development of several age-correlated degenerative diseases [11].

The *in situ* interaction and oxidative damage caused by hydroxyl radicals to dsDNA was investigated using a thick multilayer DNA-electrochemical biosensor prepared onto the oxidized boron doped diamond electrode (BDDE) surface [11]. The BDDE allows the generation of OH• at approximately + 3.00 V (vs. Ag/AgCl in pH = 4.5 0.1 M acetate buffer) in agreement with the reaction

$$BDD + H_2O \rightarrow BDD(OH•) + H^+ + e^-$$

The DNA-electrochemical biosensor on the BDDE enabled preconcentration of the OH• electrogenerated at the BDDE surface. Controlling the applied potential, different concentrations of OH• were electrochemically generated *in situ* on the BDDE surface.
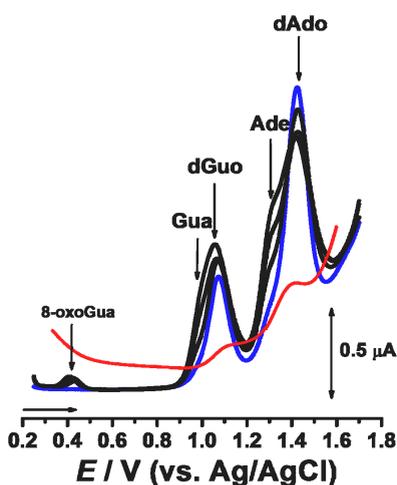
Figure 4. DP voltammograms in pH = 4.5 0.1 M acetate buffer with a thick multi-layer dsDNA-BDDE biosensor: (—) control and (—) first scan and (—) subsequent scans after applying + 3.0 V during 2 h to the BDDE surface causing electrogeneration of hydroxyl radicals. From reference [11] with permission.

After monitoring the modification of the oxidation peak currents of the purine deoxynucleoside residues (**Figure 4**), it was found that OH• oxidatively damaged the immobilized dsDNA on the BDDE surface, leading to modifications in the dsDNA structure, exposing more purinic residues to the electrode surface and facilitating their oxidation. The dsDNA structural

modifications were confirmed by electrophoresis and the voltammetric results demonstrated the occurrence of the 8-oxoGua oxidation peak, a biomarker of DNA oxidative damage.

The electrochemical transduction is dynamic in that the electrode is itself a tuneable charged reagent as well as a detector of all surface phenomena, which greatly enlarges the DNA-electrochemical biosensing capabilities.

Toxins

Microcystine-LR (MC-LR) and nodularine (NOD) (*Scheme 1*) are among the most commonly reported toxins produced by cyanobacteria [12-14]. Several previous studies have brought evidence for the possibility of direct induction of dsDNA damage *in vitro* and *in vivo* upon interaction with any of these toxins whereas other studies suggested that MC-LR and NOD genotoxicity and carcinogenicity arise mainly from the secondary effects of these toxins rather than direct toxin-DNA interaction.
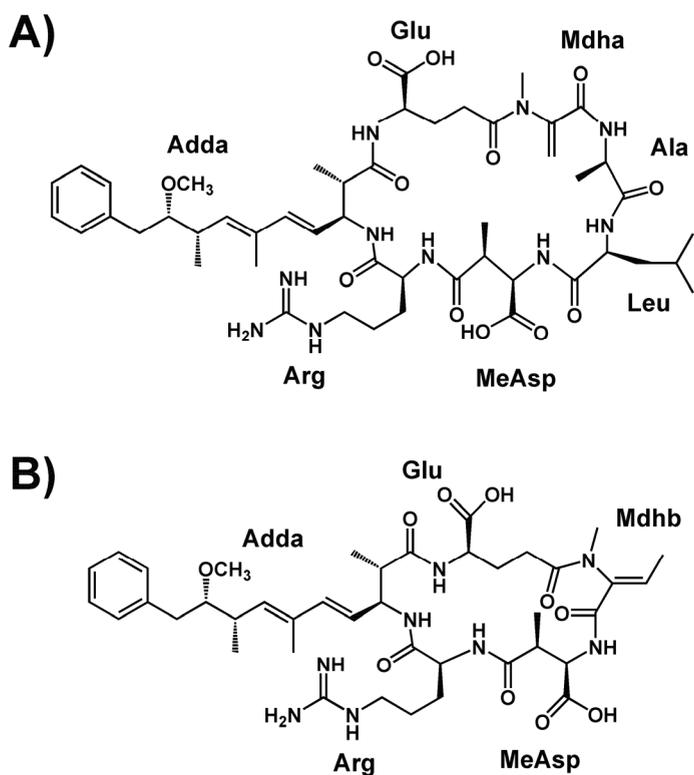
Scheme 1. Chemical structures of A) MC-LR and B) NOD.

The interaction between dsDNA and MC-LR or NOD was investigated using the DNA-electrochemical biosensors and in DNA incubated with MC-LR or NOD solutions [15]. The results have shown the decrease with time of the dsDNA oxidation peaks (**Figure 5A**).
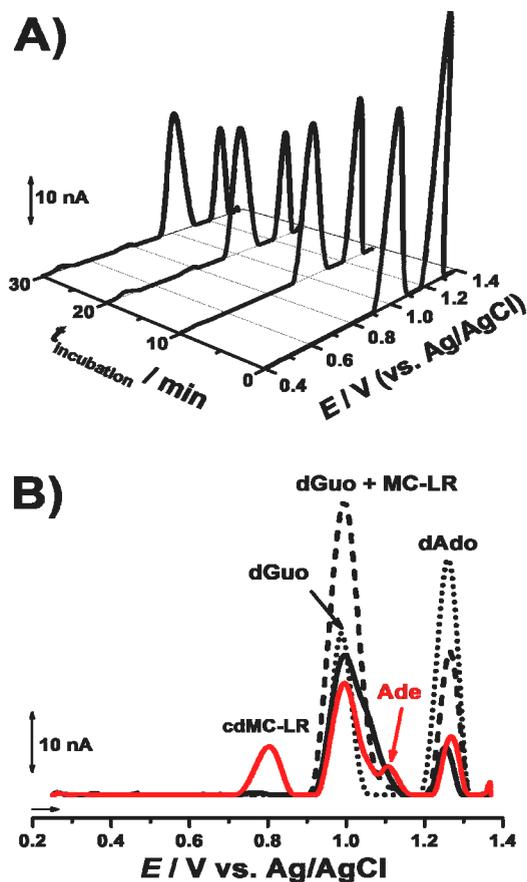
Figure 5. DP voltammograms with: **A)** the dsDNA-electrochemical biosensor in buffer pH = 4.5 incubated for different times in 30 μM MC-LR and **B)** GCE in 50 μg mL^{-1} dsDNA solution in pH = 4.5 0.1 M acetate buffer (•••) before and after incubation with 30 μM MC-LR during (---) 0, (—) 6 and (—) 24 h. From reference [15] with permission.

The analysis of dsDNA interaction with MC-LR or NOD in incubated solutions, where dsDNA strands are allowed to move freely and adopt the better conformation before and after the interaction, enabled the detection of free adenine residues (**Figure 5B**).

Experiments carried out with purine polyhomonucleotides of guanine, polyguanylic (poly[G]) acid, and adenine, polyadenylic (poly[A]) acid, demonstrated that the interaction between dsDNA and MC-LR or NOD, caused strand aggregation, and the interaction occurred preferentially at adenine residues. Free adenine molecules were liberated upon cleavage of the bond between phosphate-sugar backbone of dsDNA, leading to the formation of DNA abasic sites, a type of DNA damage which, if left unrepaired can lead to mutations during the replication process.

Anticancer Drugs

Temozolomide (TMZ) is an antineoplasic alkylating agent with activity against serious and aggressive types of brain tumours. It has been postulated that TMZ exerts its antitumor activity via its spontaneous degradation at physiological pH resulting first in 5-(3-methyltriazen-1-yl)imidazole-4-carboxamide (MTIC) and finally in 5-aminoimidazole-4-carbox-amide (AIC) and methyldiazonium ion [16]

TMZ → MTIC → AIC + methyldiazonium ion

The *in vitro* evaluation of the interaction of TMZ and its final metabolites, AIC and methyldiazonium ion, with dsDNA was studied using DP voltammetry at a GCE [17]. The DNA damage was electrochemically detected following the changes in the oxidation peaks of guanosine and adenosine residues. The results obtained revealed the decrease of the dsDNA oxidation peaks with incubation time, showing that TMZ and AIC/methyldiazonium ion interacted with dsDNA causing its condensation (**Figure 6**).

Furthermore, the experiments using the DNA-electrochemical biosensor for the *in situ* TMZ and AIC/methyldiazonium ion–dsDNA interaction confirmed the condensation of dsDNA caused by these species and showed evidence of a specific interaction between the guanosine residues and the TMZ metabolites, since the free guanine oxidation peak was detected. The oxidative damage caused to dsDNA bases by TMZ metabolites was also detected electrochemically by monitoring the appearance of the 8-oxoguanine/2,8-dyhydroxyadenine oxidation peaks (**Figure 6**). Agarose gel electrophoresis of AIC/methyldiazonium ion–dsDNA samples confirmed the occurrence of dsDNA condensation and the DNA oxidative damage observed in the electrochemical results. The importance of the DNA-electrochemical biosensor in the *in situ* evaluation of TMZ–dsDNA interactions was clearly demonstrated.

Nucleoside analogs (NA) of nucleobases are a pharmacological class of compounds with cytotoxic, immunosuppressive and antiviral properties.

The interaction of dsDNA with purines NA cladribine [18] and clofarabine [19] was investigated in incubated solutions and using the DNA-electrochemical biosensor. Both compounds interacted with dsDNA causing structural modifications in a time-dependent manner confirmed using the purine homo-polynucleotide single stranded sequences of guanosine and adenosine, poly[G] and poly[A]-electrochemical biosensors. No DNA oxidative damage was observed.
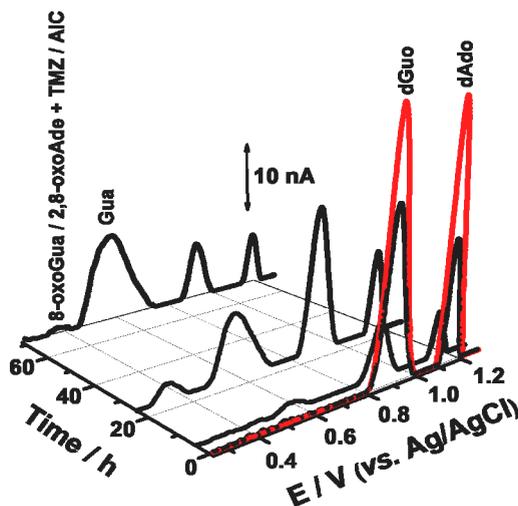
Figure 6. DP voltammograms baseline corrected in 0.1 M phosphate buffer pH = 7.0 using a multilayer dsDNA-electrochemical biosensor (—) control and after (—) 10 min, 4, 24 and 72 h in 250 µM TMZ solution. From reference [17] with permission.

The electrochemical behaviour of the cytosine NA and anti-cancer drug gemcitabine [20] was investigated at GCE, using cyclic voltammetry, differential pulse and square wave voltammetry in different pH supporting electrolytes and no electrochemical process was observed.

Gemcitabine (GEM), 2,2 difluorodeoxycitidine (*Scheme 2A*) is a pyrimidine NA of cytidine (*Scheme 2B*) and plays a major role in the treatment of several cancers.

The results obtained revealed that the interaction mechanism occurs in two sequential steps. The initial process is independent of the dsDNA sequence and leads to the condensation/aggregation of DNA strands. The formation of these rigid structures favours a second step during which the guanine hydrogen atoms participating in the C-G base pair and the fluorine atoms in the ribose moiety of GEM interacted provoking the release and/or exposure of guanine residues on the electrode surface.

A)

B)
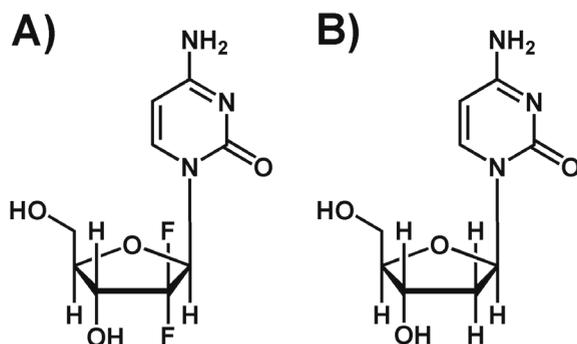
Scheme 2. Chemical structures of A) gemcitabine (GEM) and B) cytidine.

The evaluation of the interaction between GEM and DNA was studied in incubated solutions using a GCE and with the DNA-electrochemical biosensor [20] (**Figure 7**).
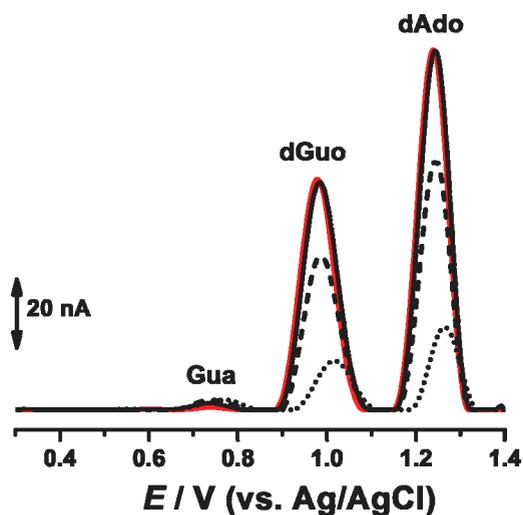
Figure 7. DP voltammograms baseline-corrected in pH = 4.5 0.1 M acetate buffer with dsDNA-electrochemical biosensor incubated with 10 µM GEM during (—) 0, (—) 15 min, (---) 2 h and (•••) 4 h. From reference [20] with permission

Redox mechanisms of two disubstituted triazole-linked acridine compounds (GL15 and GL7), previously reported as quadruplex DNA-binding molecules, and *in situ* electrochemical interaction with dsDNA using a DNA-electrochemical biosensor were investigated [21]. The redox properties of GL15 and GL7 involved a complex, pH-dependent, adsorption-controlled

irreversible process and were investigated using cyclic, differential pulse, and square wave voltammetry at a GCE. The interaction between dsDNA and GL15 or GL7 was investigated using the dsDNA-, poly[G]-, and poly[A]-electrochemical biosensors. It was demonstrated that the interaction is time-dependent, both GL15 and GL7 interacting with dsDNA, causing condensation of dsDNA morphological structure but not oxidative damage.

Anticancer Antibodies

Rituximab (RTX) is a chimeric human/mouse monoclonal antibody (mAb), which belongs to a class of anticancer drugs that targets specifically the CD20 antigen, a receptor expressed on the majority of malignant B-cells (more than 80%) and on normal differentiated B-lymphocytes (pre-B and mature B-lymphocytes) [22].

This antibody was the first Food and Drug Administration (FDA) approved genetically engineered mAb for use in indolent B-cell non-Hodgkin's lymphomas (B-NHLs), a type of lymphoma that affects B-lymphocytes. Currently, RTX is indicated in both indolent and aggressive B-NHLs, B-cell chronic lymphocytic leukemia (B-CLL) and some autoimmune diseases, administered as monotherapy or in combination with chemotherapy and immunotherapy [23]. Recently, it was demonstrated a relation between RTX and type 1 diabetes showing that patients treatment with a four-dose of this mAb, partially preserved beta-cell function over a period of one year and reduced the intake of insulin.

The interaction between RTX and dsDNA has great importance to predict its action mechanism as a genotoxic anticancer drug and to understand its biological activity and toxicity *in vivo*. The dsDNA-RTX interaction was investigated by DP voltammetry in incubated samples and using a multilayer DNA-electrochemical biosensor and gel electrophoresis, at pH 7.0 [23].

The DP voltammetric study showed a strong condensation of the dsDNA helical structure promoted by the dsDNA-RTX interaction, as well as the dAdo oxidation peak disappeared, the dGuo oxidation peak current decreased, and free Gua and Ade were released from DNA, but no DNA base oxidative damage was detected (**Figure 8**). This was confirmed by electrophoresis.

The sensitivity of the multilayer DNA-electrochemical biosensors offered the possibility to follow the interaction of RTX with DNA under different conditions, and the results enabled a better understanding of the dsDNA-RTX interaction molecular mechanism, with electroanalytical applications in clinical diagnostics.
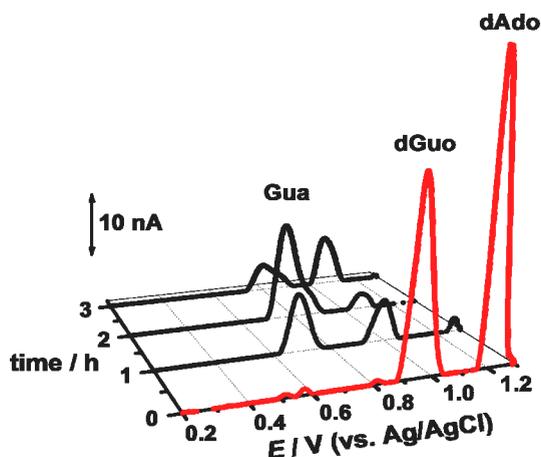
Figure 8. 3D plot of baseline subtracted DP voltammograms of multilayer (━) dsDNA-electrochemical biosensor control and (━) after incubation in 2.5 mg mL^{-1} RTX in phosphate buffer pH = 7.0 during 0, 1, 2 and 3 h. From reference [23] with permission.

CONCLUSIONS

The development of the DNA-electrochemical biosensor opened wide perspectives using a particularly sensitive and selective method for the detection of specific interactions. The possibility of predicting the damage that chemical compounds may cause to DNA arises from the preconcentration of either the starting materials or the redox reaction products on the DNA-electrochemical biosensor surface, thus allowing the electrochemical probing of the presence of short-lived intermediates and of their damage to DNA.

The use of DNA-electrochemical biosensors for the understanding of DNA interactions with molecules or ions exploits the use of voltammetric techniques for *in situ* generation of reactive intermediates and is a complementary tool for the study of biomolecular interaction mechanisms. The interpretation of the electrochemical data can contribute to the elucidation of the mechanism by which DNA is oxidatively damaged by such compounds, in an approach to the real action scenario that occurs in the living cell.

ACKNOWLEDGMENTS

REFERENCES

1. M.S. Cooke, M.D. Evans, M. Dizdamglu, J. Lunec, *Faseb Journal*, **2003**, *17*, 1195.
2. M.D. Evans, M. Dizdaroglu, M.S. Cooke, *Mutation Research*, **2004**, *567*, 61.
3. S.I. GrivennikovI, F.R. Greten, M. Karin, *Cell*, **2010**, *140*, 883.
4. M. Fojta, "Electrochemistry of Nucleic Acids and Proteins-Towards Electrochemical Sensors for Genomics and Proteomics", Elsevier, Amsterdam, **2005**, chapter 12.
5. V.C. Diculescu, A.M. Oliveira Brett, "Biosensors and Cancer", CRC Press, London, **2012**, chapter 10.
6. E. Palecek, *Electroanalysis*, **2009**, *21*, 239.
7. A.M. Oliveira Brett, V.C. Diculescu, A.M. Chiorcea-Paquim, S.H.P. Serrano, "Electrochemical Sensor Analysis", Elsevier, Netherlands, **2007**, chapter 20.
8. S. Rauf, J.J. Gooding, K. Akhtar, M.A. Ghauri, M. Rahman, M.A. Anwar, A.M. Khalid, *Journal of Pharmaceutical and Biomedical Analysis*, **2005**, *37*, 205.
9. V.C. Diculescu, A.M. Chiorcea-Paquim, A.M. Oliveira Brett, *Sensors*, **2005**, *5*, 377.
10. A.M. Oliveira Brett, J.A.P. Piedade, L.A. Silva, V.C. Diculescu, *Analytical Biochemistry*, **2004**, *332*, 321.
11. S.C.B. Oliveira, A.M. Oliveira-Brett, *Langmuir*, **2012**, *28(10)*, 4896.
12. P.V.F. Santos, I.C. Lopes, V.C. Diculescu, M.C.U. de Araújo, A.M. Oliveira-Brett, *Electroanalysis*, **2011**, *23*(10), 2310.
13. I.C. Lopes, P.V.F. Santos, V.C. Diculescu, F.M.P. Peixoto, M.C.U. Araújo, A.A. Tanaka, A.M. Oliveira-Brett, *Analyst*, **2012**, *137*(8), 1904.
14. I.C., Lopes, P.V.F. Santos, V.C. Diculescu, M.C.U. Araújo, A.M. Oliveira-Brett, *Analytical Letters*, **2012**, *45*(4), 408.
15. P.V.F. Santos, I.C. Lopes, V.C. Diculescu, A.M. Oliveira-Brett, *Electroanalysis*, **2012**, *24*, 547.
16. M. Ghalkhani, I.P.G. Fernandes, S.C.B. Oliveira, S. Shahrokhian, A.M. Oliveira Brett, *Electroanalysis*, **2010**, *22*, 2633.
17. I.C. Lopes, S.C.B. Oliveira, A.M. Oliveira Brett, *Analytical Bioanalytical Chemistry*, **2013**, *405*, 3783.
18. A.D.R. Pontinha, H.E. Satana, V.C. Diculescu, A.M. Oliveira-Brett, *Electroanalysis*, **2011**, *23*, 2651.
19. H. Eda Satana, A.D.R. Pontinha, V.C. Diculescu, A.M. Oliveira-Brett, *Bioelectrochemistry*, **2012**, *87*, 3.
20. R.M. Buoro, I.C. Lopes, V.C. Diculescu, S.H.P. Serrano, L. Lemos, A.M. Oliveira-Brett, *Bioelectrochemistry*, **2014**, *99*, 40.
21. A.D.R. Pontinha, S. Sparapani, S. Neidle, A.M. Oliveira-Brett, *Bioelectrochemistry*, **2013**, *89*, 50.
22. S.C.B. Oliveira, I.B. Santarino, A.M. Oliveira-Brett, Electroanalysis, **2013**, *25*, 1029.
23. I.B. Santarino, S.C.B. Oliveira, A.M. Oliveira Brett, *Electroanalysis*, **2014**, *26*, 1304.

Dedicated to prof. dr. I. C. Popescu
on the occasion of his 70th anniversary

REPLACEMENT OF THE GLASS ELECTRODE BY GRAPHITE AT ACID-BASE POTENTIOMETRIC TITRATIONS

GYÖRGY INZELT[a*], KATALIN BORSOS

ABSTRACT. Examples are shown that the paraffin-impregnated graphite (PIGE) electrode can be used as a replacement of the fragile and expensive glass electrodes in acid-base potentiometric titration. Based on the preliminary investigations this, simple, robust and cheap electrode can be an alternative of the electrodes used in the practice at present. The open-circuit potential of the paraffin-impregnated graphite in aqueous solutions of different pHs is not sensitive to the presence of oxygen. Because of the large difference between the open-circuit potential and the pH-dependent formal potential determined by using the mid-peak potential obtained by cyclic voltammetry, it can be stated that the pH dependence is due to a surface ionic exchange process with the participation of the oxidized surface groups of carbon.

Keywords: potentiometric titration, acid-base titration, paraffin-impregnated graphite electrode

INTRODUCTION

Glass electrodes have been used for more than a century for the measurement of pH and also in the case of acid-base titration. The story has started when Max Cremer (1865 - 1935) recognized that the potential of a glass membrane responded to the acidity of the solution [1]. Albeit hydrogen electrode and several other electrodes applied in a carefully designed cell supply exact data concerning the mean activity of hydrogen ions, glass electrode is overwhelmingly used in practice and almost exclusively at acid-base titrations. The theoretical understanding of the functioning of the glass electrode by

ª *Eötvös Loránd University, Institute of Chemistry, Pázmány Péter sétány 1a, H-1117 Budapest, Hungary*
* *Corresponding author: inzeltgy@chem.elte.hu*

now is well-established [2-6]. However, there are several shortcomings of the glass electrodes. A calibration is needed, they are fragile and expensive. Several electrodes have been tested, among others quinhydrone [3], metal-metal oxide electrodes [7, 8], graphite [9-12], and polymers [13, 14], which are sensitive and show an appropriate selectivity to the hydrogen ion concentration, and a fast response to the change of pH, as well as can be used more conveniently.

In fact, the working principle of a glass electrode essentially differs from the other electrodes listed above. Glass is a solid electrolyte which is applied as a membrane between two electrolyte solutions. One of the electrolytes has a constant composition, it is the so-called internal reference solution inside the usually bulb-shaped thin glass. An internal reference electrode is immersed into this electrolyte solution. In the other side of the glass there is another solution, the hydrogen ion activity of which is to be determined, and another reference electrode is immersed into this solution. The potential difference between the two terminal reference electrodes is measured. Albeit it is a classical arrangement for measuring the membrane potential, in fact, the potential difference between the glass and the contacting outer electrolyte is caused by an interfacial ionic exchange process [2-5]. Because the standard (or formal) potential is unknown, the glass electrode should be calibrated.

There are electrodes, e.g., the quinhydrone electrode, where the formal potential ($E_c^{\ominus}{}'$) is known with a relatively high accuracy. In these cases a redox reaction occurs where the electron transfer steps coupled with protonation:

$$\text{Ox} + n\,\text{e}^- + m\,\text{H}^+ \underset{\longleftarrow}{\overrightarrow{}} \text{H}_m\,\text{Red}^{(m-n)+} \qquad\qquad E_c^{\ominus}{}' \quad (1)$$

$$\text{H}_m\,\text{Red}^{(m-n)+} \underset{\longleftarrow}{\overrightarrow{}} \text{H}_{m-1}\,\text{Red}^{(m-n-1)+} + \text{H}^+ \qquad\qquad K_{a1} \quad (2)$$

$$\text{H}_{m-1}\,\text{Red}^{(m-n-1)+} \underset{\longleftarrow}{\overrightarrow{}} \text{H}_{m-2}\,\text{Red}^{(m-n-2)+} + \text{H}^+ \qquad\qquad K_{a2} \quad (3)$$
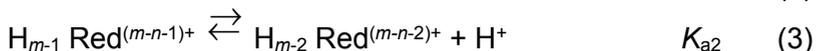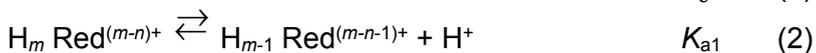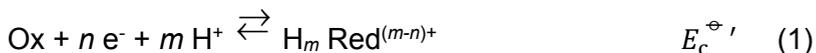
where: K_{a1} and K_{a2} are the dissociation constants of the hydroquinone.

For $m = n = 2$, e.g., for the quinhydrone electrode the following Nernst equation can be written

$$E = E_c^{\ominus}{}' + \frac{RT}{nF}\ln\left(\frac{a_{\text{ox}}}{a_{\text{red}}}\,\frac{1+K_{a1}a_{\text{H}^+}+a_{\text{H}^+}^2}{K_{a1}K_{a2}}\right) \qquad\qquad (4)$$

In this paper we deal with the application and the working principle of the paraffin-impregnated graphite electrode (PIGE) for acid-base potentiometric titration.

RESULTS AND DISCUSSION

Electrodes based on graphite are considered as a quinhydrone-type electrode [9-12]. Usually these electrodes are activated, i.e., treated with a strong oxidant, *e.g.*, with permanganate dissolved in sulfuric acid in order to increase the potential jump at the end-point of the acid-base potentiometric titration. However, the idea that a quinone-hydroquinone redox couple is formed on the graphite surface as a consequence of the oxidation of graphite is not entirely true. There are oxo- and probably hydroxide groups on the graphite surface without any additional oxidation, most likely due to the reaction between the oxygen from air and the carbon atoms on the surface. The activation certainly generates more oxo-groups, even the hydroxide groups that were present also being oxidized to oxo-groups. After activation the potentiometric curves starts at about 1 V when acid is titrated by a base. Without activation the starting potential under similar conditions is between ca. 0.2 and 0.8 V [10]. However, the difference in the end-potential, i.e., in basic solution is much smaller. Albeit we still have reasonable titration curves. Of course, the potential jump is smaller. Figures 1 and 2 show examples for acid-base titration, when the performance of PIGE is compared with that of a glass electrode in the course of the titration of a strong acid by a strong base (Fig. 1), and that of a weak base by a strong acid (Fig. 2).
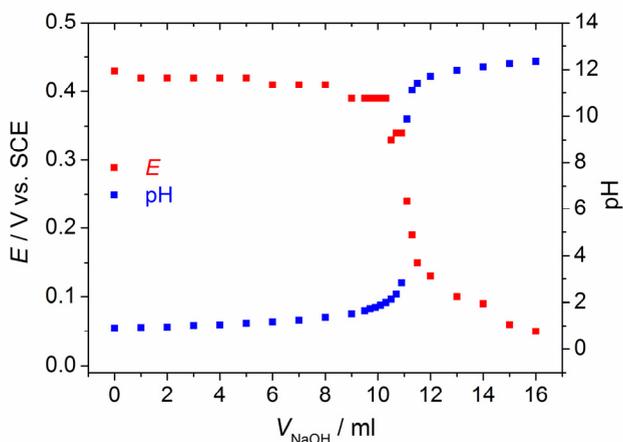
Figure 1. Potentiometric titration curves obtained for the titration of 100 cm^3 of 0.1 mol dm^{-3} HClO$_4$ with 1 mol dm^{-3} NaOH at a PIGE (*E* vs. *V* curve) and at a glass electrode (pH vs. *V* curve), respectively.
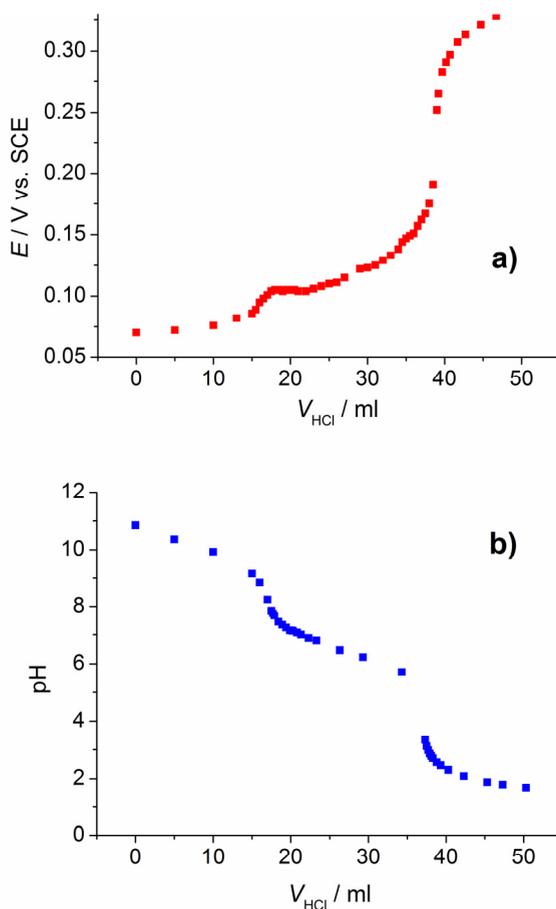
Figure 2. Potentiometric titration curves obtained for the titration of 2.5 mmol Na₂CO₃ dissolved in 100 cm³ water by 0.1 mol dm⁻³ HCl at a PIGE (a) and a glass electrode (b), respectively.

If there is a redox couple on the surface, the formal potential of it can be determined by the help of cyclic voltammetry. The cyclic voltammetric curves obtained for a PIGE in acidic and basic media, respectively, are shown in Figures 3 and 4. It is evident from the cyclic voltammetric curves that i) there are two – more or less well-defined – pairs of peaks, ii) these peaks shift with the pH with ca. 60-65 mV/pH, iii) the formal potentials of these redox couples are ca. 0.3 V and 0 V. Therefore, if the starting potential in the case of the voltammetric curves is higher than ca. 0.6 V, there is only the oxidized form of the redox couple exists.
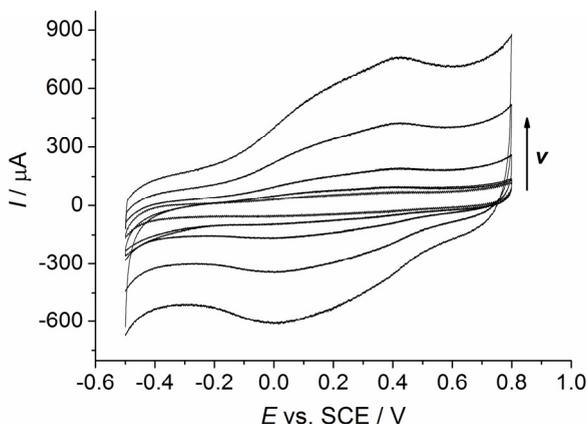
Figure 3. Cyclic voltammograms of a PIGE electrode in contact with 0.5 mol dm^{-3} H$_2$SO$_4$ solution. Scan rates are 5, 10, 20, 50, and 100 mV/s, respectively.
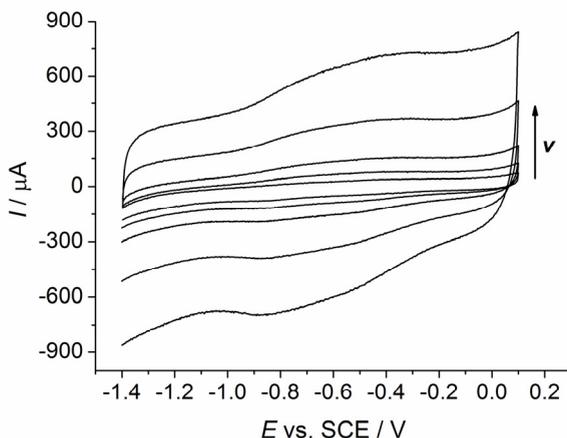
Figure 4. Cyclic voltammograms of a PIGE electrode in contact with 0.1 mol dm^{-3} NaOH solution. Scan rates are 5, 10, 20, 50, and 100 mV/s, respectively.

It follows that the simple quinone-hydroquinone concept is not adequate in the case of the so-called activated graphite electrode, and even below ca. 0.6 V the open-circuit potential in acid solution is far from the formal potential, i.e., the ox/red ratio is far from 1. Albeit in this case beside the "fully oxidized" reduced form(s) may also exist, and those may be protonated, partially

protonated or unprotonated depending on the pH of the solution. One can estimate the ratio of the oxidized and reduced forms from the formal potentials determined by the cyclic voltammetric experiments. On the other hand, at high positive potentials two possibilities can be considered. There is only the protonation of the fully oxidized groups occurs and/or further oxidation of the surface carbon atoms takes place resulting in the formation of –COOH groups. In fact, several other groups beside quinone, hydroquinone, carboxyl are assumed on the carbon surface, such as hydroxyl, keto, ether, anhydride, phenolic, lactone, epoxy bridges etc. [15]. The situation is even more complicated taking into account the different planes and sites of the graphite (edge plane, basal plane, defect sites etc.). Nevertheless, if we consider only quinone (oxo groups) or carboxyl groups as a result of the further oxidation, the potential of the electrode is determined by an ionic exchange process on the surface similarly to the glass electrode, and nothing to do with the quinone-hydroquinone redox couple. It follows that during the titration the graphite remains in its unreduced form or only slightly reduced, and we are far from the 1:1 ox/red ratio. We may assume that the open-circuit potential, $E_{\mathrm{ocp}}^{\ominus}{}'$ is determined by the proton transfer at the electrode surface; i.e., the potential is related to the ratio of the activities of the protonated and unprotonated forms, which eventually leads to an equation similar to that of the glass electrode:

$$E = E_{\mathrm{ocp}}^{\ominus}{}' + \frac{RT}{nF}\ln\left(\frac{a_{\mathrm{C}}a_{\mathrm{H^+}}}{a_{\mathrm{CH}}}\right) \qquad (5)$$

Assuming a constant $a_{\mathrm{C}}/a_{\mathrm{CH}}$ ratio

$$E = E_{\mathrm{ocp}}^{\ominus}{}' + \frac{RT}{nF}\ln a_{\mathrm{H^+}} \qquad (6)$$

If $n=1$ we arrive at the equation used in the case of the glass electrode

$$E = E_{\mathrm{ocp}}^{\ominus}{}' - 0.059\ln\mathrm{pH} \qquad (7)$$

Of course, the pH dependence can also be observed when the graphite is (partially) reduced, in this case the following equation is operative

$$E = E_{\mathrm{c}}^{\ominus}{}' + \frac{RT}{F}\ln\left(\frac{a_{\mathrm{ox}}a_{\mathrm{H^+}}}{a_{\mathrm{red}}}\right) \qquad (8)$$

Nevertheless, the ox/red ratio is rather uncertain after an electrochemical reduction because "due the reaction with oxygen" the ox/red ratio, and consequently the open-circuit potential increases.

CONCLUSIONS

Graphite electrode especially the paraffin impregnated graphite (PIGE) rod can be used as a replacement of the fragile and expensive glass electrodes in acid-base potentiometric titration. Based on the preliminary investigations this, simple, robust and cheap electrode can be an alternative of the electrodes used in the practice at present. The open-circuit potential of the paraffin impregnated graphite in aqueous solutions of different pHs is not sensitive to the presence of oxygen. Because of the large difference between the $E_{\mathrm{ocp}}^{\ominus}{}'$ and the pH-dependent formal potential ($E_{\mathrm{c}}^{\ominus}{}'$) determined by using the mid-peak potential obtained by cyclic voltammetry, it can be concluded that the pH dependence is due to a surface ionic exchange process. It follows that the concept that has been generally accepted in the previous literature is not correct. Of course, it would be better to establish the potential at $E_{\mathrm{c}}^{\ominus}{}'$, i.e., at the ratio $a_{\mathrm{ox}}/a_{\mathrm{red}} = 1$, however, at open-circuit conditions a positive drift of the potential occurs, probably due to the effect of oxygen.

EXPERIMENTAL SECTION

Spectral grade graphite rods with 5 mm diameter and 6 cm long were used. In order to decrease the background current and the contamination during successive experiments these graphite rods were impregnated by paraffin. For the preparation of PIGE, solid paraffin with low melting point was melted in a closed vessel in a water bath. The graphite rods were immersed into the paraffin and the vessel was evacuated. The impregnation was finished when no more gas bubbles evolved which took ca. 2 hours. Then ambient pressure was established, and the rods were removed before the paraffin solidified again [16]. The PIGE rods were placed onto filter paper, and allowed to cool down and dry. The lower end of the rods was carefully polished. In order to renew the surface the electrode was polished after each experiments. Analytical grade chemicals such as $HClO_4$, HCl, H_2SO_4, (Sigma Aldrich), Na_2CO_3, Na_2SO_4, $NaOH$ (Molar Chemicals), KH_2PO_4, Na_2HPO_4, (Reanal) were used as received. Doubly distilled water was used (Millipore water). All solutions were purged with oxygen-free argon (purity: 5.0, Linde Gas Hungary Co. Cltd.), and an inert gas blanket was maintained during the cyclic voltammetric experiments. In the case of potentiometric titration with the PIGE indicator electrode argon bubbling or magnetic stirring was also used. However, when the parent (unreduced) compound was applied, there was no difference in the presence of oxygen or when the oxygen was removed. A sodium chloride saturated calomel electrode

(SCE) was used as the reference electrode which was carefully separated from the main compartment by using a double frit. A platinum wire served as the counter electrode. An Elektroflex 453 potentiostat and a Universal Frequency Counter PM6685 (Fluke) connected with an IBM personal computer were used for the control of the measurements and for the acquisition of the data. The variation of pH of the solution during the potentiometric titration was detected by a calibrated glass electrode (OP-0719P Radelkis, Budapest) by using a pH meter (Cole-Parmer, Chemcadet, Model 05986-62, U.S.A.).

ACKNOWLEDGMENTS

REFERENCES

1. M. Cremer, *Zeitschrift für Biologie*, **1906**, *47*, 562.
2. H. Bach, F. Baucke, D. Krause (eds.), "Electrochemistry of glasses and glass melts, including glass electrodes", Springer, Berlin, **2001**.
3. H. Kahlert, "Potentiometry" in "Electroanalytical Methods: Guide to Experiments and Applications", F. Scholz (ed.), Springer, Berlin, 2nd edition, **2010**, chapter II.9.
4. F.G.K. Baucke, *Journal of Solid State Electrochemistry,* **2011**, *15*, 23.
5. L. Kékedy, "Műszeres analitikai kémia" Erdélyi Múzeum-Egyesület*,* Kolozsvár-Cluj*,* **1995**, chapters 12 and 13.
6. R.G. Bates, "Determination of pH - Theory and Practise", Wiley, New York, **1973**, pp. 280-294.
7. Y. Wen, X. Wang, *Journal of Electroanalytical Chemistry,* **2014**, *45*, 714.
8. A. Fog, R.P. Buck, *Sensors and Actuators,* **1984**, *5,* 137.
9. J. Bercik, *Chemické Zwesti*, **1970**, *14*, 372.
10. E. Pungor, É. Szepesváry, *Periodica Polytechnica,* **1972***, 16*, 326.
11. P. Riyazuddin, D. Devika, *Journal of Chemical Education*, **1997**, *74*, 1198.
12. F. Regisser, M-A. Lavoie, G.Y. Champagne, D. Bélanger, *Journal of Electroanalytical Chemistry,* **1996**, *415*, 47.
13. J. Bobacka, A. Ivaska, A. Lewenstam, *Chemical Reviews,* **2008**, *108*, 329.
14. O. Korostynska, K. Arshak, E. Gill, A. Arshak, *Sensors,* **2007**, *7*, 3027.
15. H. He, J. Klinowski, M. Forster, A. Lerf, *Chemical Physics Letters,* **1998**, *287*, 53.
16. D.A. Fiedler, F. Scholz, "Electrochemical studies of solid compounds and materials" in "Electroanalytical Methods: Guide to Experiments and Applications"; F. Scholz (ed.), Springer, Berlin, 2nd edition, **2010**, chapter II.8.

*Dedicated to prof. dr. I. C. Popescu
on the occasion of his 70th anniversary*

GRAPHENE AND CARBON NANOTUBE NANOMATERIALS IN LAYER-BY-LAYER STRUCTURED ELECTROCHEMICAL ENZYMATIC BIOSENSORS: A REVIEW

MADALINA M. BARSAN, CHRISTOPHER M.A. BRETT[a*]

ABSTRACT. This review highlights the recent developments made, during the past five years, from 2010 onwards, in biosensors that bring together the advantages of the layer-by-layer (LbL) methodology and the use of graphene and carbon nanotubes as carbon nanomaterials. LbL methodology in biosensor assembly has been widely used to incorporate suitable materials with controlled molecular architecture, enabling the build-up of stable and complex architectures. At the same time, the incorporation of nano-sized materials into a sensing device has been exploited in order to improve the electronic communication between the enzyme and the electrode substrate. The advantages of incorporating carbon nanomaterials (CN) into LbL multilayers for the development of biosensors with improved analytical performance are described. The key steps for the incorporation of CN in self assembled architectures are the choice of the type of CN functionalization and pairing with an adequate oppositely-charged polyelectrolyte. The preparation of the LbL assembly will be described in detail. Electrochemical and surface characterization will underline the importance of incorporating CN and identify their nanostructures and build-up in the LbL assembly. Finally, applications of CN-LbL biosensors will exemplify their utility as analytical tools for the detection of key analytes, such as glucose, ethanol, cholesterol and neurotoxins.

Keywords: carbon nanomaterials, graphene, carbon nanotubes, layer by layer, self-assembly, enzyme biosensors.

---

[a] *Department of Chemistry, Faculty of Sciences and Technology, University of Coimbra, 3004-535 Coimbra, Portugal*
[*] *Corresponding author: cbrett@ci.uc.pt*

1. INTRODUCTION

Electrochemical enzyme biosensors can have a wide range of applications in the clinical and diagnostic field, environmental, agricultural and food industry. The key to produce effective biosensors is to immobilize the enzyme in such a way as to maintain their bio-functionality, at the same time providing accessibility toward the target analyte and an intimate contact with the electrode substrate. The assembly of suitable materials with controlled molecular architecture in multicomponent thin films can be carried out by techniques such as physical immobilization, through weak bonds such as Van der Waal's forces, by electrostatic and/or hydrophobic interactions. Such configurations offer both a good preservation of enzyme activity [1] and the possibility of direct electron transfer between enzyme and electrode [2]. Since enzymes are natural polyelectrolytes, their alternate deposition together with tailored oppositely charged species in layer-by-layer structures onto solid substrates, has been widely used to develop LbL biosensors [3, 4]. The deposition of more bilayers implies immobilization of more enzyme through the LBL procedure, but a thicker multilayer film may also lead to an increase in the electron transfer resistance and a decrease in enzyme substrate diffusion [5]. In order to improve electronic communication between the enzyme and the electrode substrate, the incorporation of nano-sized materials into a sensing device has been extensively investigated. Among nano-sized materials, carbon-based ones are those most employed for the construction of new and improved biosensor architectures, due, particularly, to their good biocompatibility and relatively low cost. Both graphene (G) and carbon nanotubes (CNT) exhibit excellent thermal conductivity, mechanical properties and extraordinary electronic transport properties [6]. The large surface area and excellent electrical conductivity allow them to act as an ''electron wire'' between the redox centres of an enzyme or protein and an electrode surface, leading to their wide use as electrocatalysts in a large variety of biosensor constructions [7-9]. The functionalization of carbon nanomaterials is a critical step, prior to their use, being required for their solubilisation by dispersion, purification and further processing and applications [10]. In the case of graphene, functionalization is required for its application in sensors, since pristine graphene is a zero band gap, inert material [11, 12]. For their use in layer-by-layer assemblies based on electrostatic interactions, CN can be functionalized so as to possess either positively- or negatively-charged surfaces [8, 13].

The present review highlights the important developments during the last 5 years in biosensors that make use of the advantages of both carbon nanomaterials and LbL methodology. Different strategies for preparing the

self-assembled multilayered structures are discussed, based mainly on electrostatic attraction, but also on other interactions such as hydrogen bonding, π-π interaction, sequential covalent reactions. It will stress the functionalization of the carbon nanomaterials and the species used to enable their incorporation in LbL structures, such as metal nanoparticles, polyelectrolytes, and polymers, including dendrimers. The chemical structure of the most used charged polymers is given in Fig. 1.

Electrochemical and surface characterization of the LbL structures will be discussed, focusing on the monitoring of the multilayer deposition and on the electronic conductivity of the final assembly.
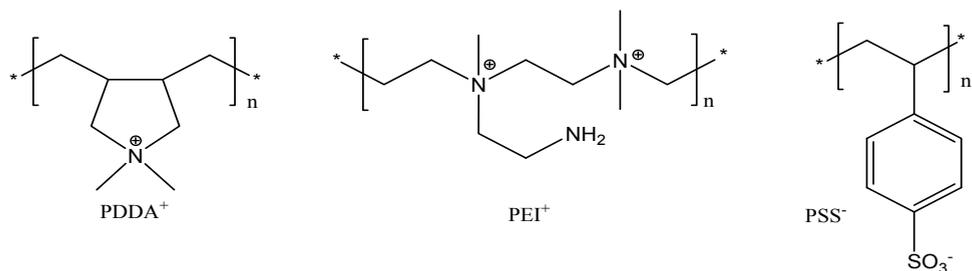
Figure 1. Chemical structures of commonly used charged polymers in LbL: poly(dimethyldiallyammonium chloride) (PDDA+), polyethylimine (PEI+) and polystyrene sulfonate(PSS-).

Finally, examples of biosensor application will be given, with a focus on the analytical performance of the biodevice.

2. PREPARATION

Biosensors prepared by using LbL assembly have been mainly based on electrostatic, and some on either covalent or non-covalent π-π stacking interaction or biospecific interaction. A typical LbL assembly, containing graphene or CNT is exemplified in Fig. 2.

2.1. Graphene in LbL

In order to enable the assembly of negatively-charged graphene (G) in LbL structures, several positively-charged species were used, such as the polymers poly(dimethyldiallyammonium chloride) (PDDA+) [14-16] or polyethyleneimine (PEI+) [17], amino-terminated ionic liquid [18], amino functionalized CNT [15, 16, 19], and redox compounds such as methylene green (MG) [16] and alcian blue pyridine (AB) [20]. In [21], pyrene-functionalized glucose oxidase (GOx) was assembled with graphite through π-π stacking interactions. In [22, 23], graphene was dispersed into positively-charged

chitosan together with the enzyme, and assembled in LbL by using poly(styrene sulfonate) (PSS[-]). Some non-enzymatic LbL structures containing graphene were developed as substrates for enzyme immobilization, based on electrostatic interaction between bovine serum albumin (BSA[+]) functionalized G and AuNP[-] [24], negatively-charged G and chitosan [25], one based on the π-π interaction between MB and G [26], and another based on both covalent and hydrophobic interactions between G and Prussian blue (PB) through octadecylamine linkers [27].

Multilayer films composed of Prussian blue nanoparticles (PB), graphene and GOx have been assembled on a glassy carbon electrode (GCE). Prior to LbL formation, an adsorbed positively-charged monolayer of PDDA[+] was first allowed to form, followed by multilayer film growth by sequential dipping of the modified electrodes into the graphene solution, into the as-prepared positively charged PDDA-PB[+], the negatively-charged GOx solution, PDDA-PB[+], then repeating these steps to form GCE/{G[-]/PDDA-PB[+]/GOx[-]/PDDA-PB[+]}$_3$ [14].

(a)

(b)
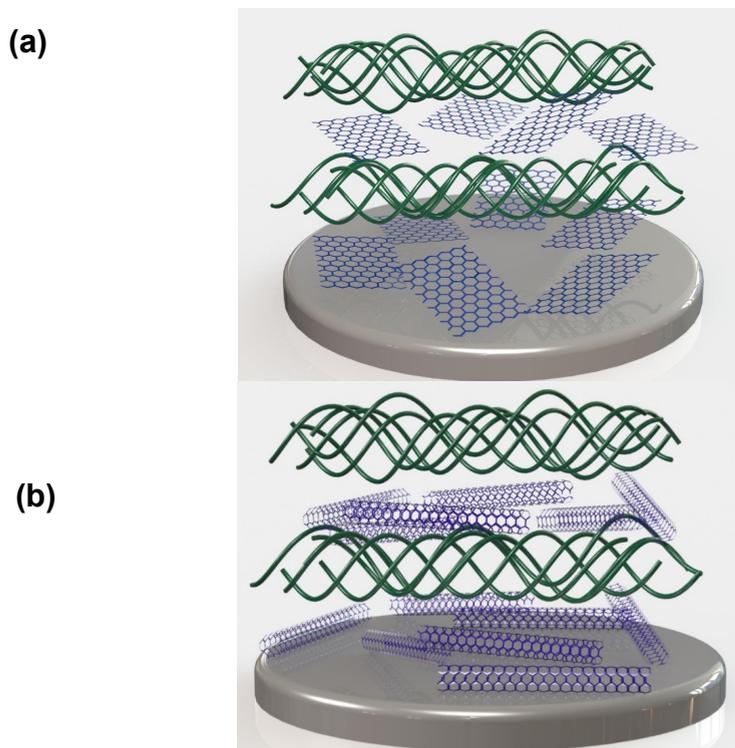
Figure 2. Schematic representation of carbon nanomaterials assembled in LbL multilayer structures of (a) graphene and (b) CNT.

A graphite electrode (GE) modified with PDDA$^+$ and polystyrenesulphonate (PSS$^-$) was used as substrate for the deposition of G-COO$^-$ and CNT-NH$_3^+$ to obtain GE/PDDA$^+$/PSS$^-${CNT-NH$_3^+$/G-COO$^-$}$_5$, on top of which alcohol dehydrogenase (AlcDH) was immobilized by drop casting. G-COO$^-$ was obtained by treating G with concentrated HNO$_3$, and CNT-NH$_3^+$ was obtained by first treating CNT with H$_2$SO$_4$:HNO$_3$ (3:1 v/v) followed by thionyl chloride and then ethylene diamine [15].

The positively-charged species, methylene green (MG$^+$) and methylimidazolium-functionalized CNT, were assembled with negatively-charged graphene *via* electrostatic and/or π-π interactions to form multilayered structures of G$^-$/MG$^+$ and G$^-$/CNT$^+$. The substrate was first modified with PDDA$^+$ and then with G$^-$ and MG$^+$ or CNT$^+$ to obtain the final modified electrode assemblies, designated as GCE/PDDA$^+$/{G$^-$/MG$^+$}$_5$ and GCE/PDDA$^+$/{G$^-$/CNT$^+$}$_5$. The enzymes AlcDH and glucose dehydrogenase (GDH) were immobilized on top by cross-linking with glutaraldehyde [16].

Modification with PEI$^+$ and poly(acrylic acid)$^-$-G (PAA$^-$-G) multilayer films on GCE was performed by alternately immersing the electrode in PEI$^+$ solution and in PAA$^-$-G solution. The GCE/{PEI$^+$/PAA$^-$-G}$_n$ was used as substrate for the deposition of the enzyme, in a similar manner, using negatively charged GOx$^-$ or glucoamylase (GA$^-$) enzyme solutions and PEI$^+$ to obtain the biosensors GCE/{PEI$^+$/PAA$^-$-G}$_3$/{PEI$^+$/GOx$^-$}$_5$ and GCE/{PEI$^+$/PAA$^-$-G}$_3$/{PEI$^+$/GOx$^-$}$_5$/{PEI$^+$/GA$^-$}$_4$ [17].

Amine-terminated ionic liquid (G-IL-NH$_3^+$), and sulfonic acid functionalized graphene (G-SO$_3^-$) were self-assembled by covalent bonding. GOx adhered to G-IL-NH$_3^+$, after immersing the electrode in GOx in solution, the biosensor being finally coated with Nafion to obtain GCE/{G-IL-NH$_3^+$/G-SO$_3^-$}/G-IL-NH$_3^+$/GOx$^-$/Nafion [18].

Positively-charged CNT-NH$_3^+$ and negatively charged G/TiO$_2$–Pd$^-$ hybrid were assembled on a GCE. Negatively-charged GOx$^-$ was then adsorbed on CNT-NH$_3^+$ and was finally covered with Nafion to obtain GCE/{CNT-NH$_3^+$/G-TiO$_2$-Pd$^-$}$_9$/CNT-NH$_3^+$/GOx$^-$/Nafion [19].

For the deposition of LbL layers of positively- and negatively-functionalized G, first a negatively-charged layer was formed on GCE by electrochemical potential cycling modification with sulfanilic acid (ABS$^-$). Graphene composites functionalized with copper phthalocyanine-3,4,4,4-tetrasulfonic acid tetrasodium salt (G-TSCuPc$^-$) or its alcian blue pyridine variant (G-AB$^+$) were assembled via alternate electrostatic adsorption onto the GCE/ABS$^-$ surface to form GCE/ABS$^-$/{G-AB$^+$/G-TSCuPc$^-$}$_3$/G-AB$^+$. GOx solution in Nafion was afterwards dropped onto the LbL modified electrode to obtain the biosensor [20].

In another procedure, GOx was first modified with pyrene functionalities in order to be self-assembled onto graphene basal plane *via* π-π stacking interactions to obtain GCE/{G/GOx-pyrene}$_3$ [21].

In [22, 23], carbon nanomaterials (CN), nitrogen doped graphene (NG) and HNO$_3$ and KOH functionalized G and CNT were dispersed together with the enzyme GOx in the positively-charged polymer chitosan. LbL assembly was carried out together with the negatively charged PSS$^-$, to finally obtain {chit$^+$(CN+GOx)/PSS$^-$}$_n$ structures on gold electrodes. When the CN was NG the best biosensor contained 2 bilayers whereas when the CN was HNO$_3$ or KOH functionalized G (and CNT), the optimum biosensor was based on 4 bilayers.

Four types of LbL modified electrodes were reported for use as supports for posterior enzyme immobilization [24-27]. Negatively-charged AuNP$^-$ have been assembled in multilayers with BSA functionalized G (BSA-G$^+$) on fluorine doped tin oxide (FTO) electrodes previously modified with PEI$^+$. To improve the conductivity of the modified electrode, thermal annealing was introduced in order to decompose BSA on the surface of the graphene nanosheets [24]. Multilayer films of positively-charged chitosan and negatively-charged G were assembled on GCE to obtain GCE{chit$^+$/G$^-$}$_5$ [25]. The electroactive dye methylene blue (MB) was adsorbed onto G through π-π stacking and hydrophobic interactions and assembled on GCE to form GCE/{G/MB}$_n$ [26]. Finally, films of graphene oxide (GO)-Prussian blue (PB) hybrids were deposited on graphite screen-printed electrodes (GrSPE) using octadecylamine (ODA), acting as a bifunctional linker between GrSPE and the GO and as an anchoring layer for the immobilization of the PB through hydrophobic interactions. Before immobilizing PB, GO was chemically reduced in NaBH$_4$ solution [27].

2.2. CNT in LbL

For the assembly of negatively-charged CNT into multilayer films, different cationic polymers were used: PEI$^+$ [28], poly[(vinylpyridine) Os(bipyridyl)$_2$Cl] (PVI-Os$^+$) [29, 30], poly(amido amine) (PAMAM$^+$) [31, 32], poly(allylamine hydrochloride) (PAH) [33], and thionine$^+$ [34]. Positively-charged CNT were also used in LbL assemblies and were obtained by functionalization with PDDA$^+$ [35] or PEI$^+$ [36, 37], and enabled direct adsorption of negatively-charged enzymes. In [38], negatively-charged CNT were co-immobilized with PtNP.

In [28], CNT$^-$ were immobilized together with GOx$^-$ alternately with PEI$^+$, to obtain GCE/CNT$^-$/{PEI$^+$/GOx$^-$}$_3$/PEI$^+$ [28].

Cationic PVI-Os$^+$ was also used to enable the incorporation of GOx and CNT in multilayer structures deposited on screen printed carbon electrodes (SPCE). First, the polymer was electrodeposited to obtain a positively-charged substrate, GCE/PVI-Os$^+_{el}$, followed by alternate deposition of GOx-CNT conjugate and cationic PVI-Os from their respective solutions. As last step, PVI-Os

was again electrodeposited on top to stabilize the multilayer structures and the final biosensor was SPCE/PVI-Os$^+_{el}$/{GOx-CNT$^-$/PVI-Os$^+$}$_4$/PVI-Os$^+_{el}$ [29]. A similar approach was used by the same authors, but instead of CNT-GOx conjugates, using CNT and GOx separately, in order to obtain SPCE/{PVI-Os$^+_{el}$/CNT$^-$/PVI-Os$_{el}$/ GOx$^-$}$_5$/PVI-Os$_{el}$ [30].

PAMAM dendrimer-encapsulated platinum nanoparticles (PtNP-PAMAM$^+$) were used to immobilize negatively-charged GOx$^-$. PtNP-PAMAM$^+$ were linked to CNT, previously dropped on the ITO, with 1-ethyl-3-[3 -(dimethylamino)propyl] carbodiimide (EDC), to obtain GCE/CNT$^-$/PtNP-PAMAM$^+$ which served as anchor for the negatively-charged GOx, and the steps repeated to form ITO/CNT$^-$/{PtNP-PAMAM$^+$/GOx$^-$}$_3$ [31].

A bienzyme biosensor prepared for the detection of cholesterol was based on CNT mixed with gold nanoparticles (AuNP) wrapped with cationic poly(allylamine hydrochloride) (PAH). An Au electrode was first immersed in mercaptopropansulfonate (MPS) to form Au-MPS$^-$, followed by deposition of the polycation PAH$^+$ and then the polyanion PSS$^-$. Au/MPS$^-$/PAH$^+$/PSS$^-$ was then modified by LbL assembly of {PAH-CNT-AuNP$^+$/HRP$^-$}$_n$ and {PAH-CNT-AuNP$^+$/ChOx$^-$}$_n$ were deposited on top to obtain Au/MPS$^-$/PAH$^+$/PSS$^-$/{PAH-CNT-AuNP$^+$/HRP$^-$}$_m$/{PAH-CNT-AuNP$^+$/ChOx$^-$}$_n$ [33].

Multilayer films of PDDA$^+$ wrapped CNT and two negatively-charged enzymes acyl-CoA synthetase (ACoAS) and acyl-CoA oxidase (ACoAOx) were assembled to obtain SPCE/{PDDA-CNT/ACoAOx}$_2$, or SPCE/{PDDA-CNT/ACoAOx/PDDA-CNT/ACoAS}$_2$ [35].

Carboxylated-CNT were covalently bound to an Au electrode modified with either 11-amino-n-undecanethiol (AUT) or thionine via the Au-S bond to provide amino groups. Multilayer films of PAA$^+$ and poly(vinyl sulfonate) (PVS$^-$), {PAA$^+$/PVS$^-$}$_3$/{PDDA$^+$/GOx$^-$}$_8$ were formed on Au/thionine$^+$ /CNT$^-$ or Au/AUT/CNT [34].

Carboxylated CNT were assembled together with PAMAM-NH$_3^+$-Au and the enzyme acetylcholine esterase (AChE$^-$) to obtain GCE/CNT$^-$/PAMAM-NH$_3^+$-Au/AChE$^-$[32]. In [37], carboxylated CNT were functionalized with either PEI$^+$, DNA$^-$, or AChE$^-$, the latter being achieved with the aid of EDC/NHS, and self-assembled on GCE to obtain GCE/CNT-PEI$^+$/CNT-DNA$^-$/{CNT-PEI$^+$/CNT-AChE$^-$}$_3$ [36]. In a similar way, GCE/{CNT-PEI$^+$/CNT-DNA$^-$}$_2$ served as support for the deposition of organophosphate hydrolase (OPH$^+$) together with AChE$^-$ to obtain GC$_2$/OPH$^+$/AChE$^-$ [37].

A glucose biosensor was developed based on as-prepared PtNP-CNT$^-$ composite and sugar-lectin biospecific interactions between concanavalin A (Con A) and GOx to obtain GCE/chit$^+$/PtNP-CNT$^-$/{Con A/GOx}$_3$[38].

3. ELECTROCHEMICAL AND SURFACE CHARACTERIZATION OF THE LBL MODIFIED ELECTRODES

3.1. Characterization by cyclic voltammetry

Cyclic voltammetry (CV) has often been employed to follow the deposition process of the multilayer composite films containing graphene and/or CNT. Unless the multilayers contained an electroactive component, $[Fe(CN)_6]^{4-/3-}$ was used as a redox probe to investigate the electrochemical properties of the modified electrodes.

3.1.1. Graphene modified electrodes

A Prussian blue (PB) containing multilayer deposited on GCE, GCE/{G/PDDA$^+$-PB/GOx$^-$/PDDA$^+$-PB}$_3$, exhibited a pair of redox peaks at 0.2 V *vs*. SCE in PBS pH 7.4, which corresponds to the redox conversion between PB and its reduced form, Prussian white (PW). The electrochemical properties of PB were not changed in the multilayer films and the redox peak currents increased with increasing number of bilayers [14]. Similarly, CVs confirmed the effective formation of the PB layer within the multilayer structure, based on octadecylamine (ODA) assembly to form SPE/ODA-G/ODA/PB, seen by the appearance of a well-defined pair of peaks with mid-point potential E_m = 0.19 V *vs*. Ag/AgCl, attributed to PB. The high peak-to-peak separation (100 mV) was due to mixed charge transfer and mass transport-limited process, attributed to the surface confined PB redox process and the physical transport of K$^+$ ions [27].

CVs of GCE/PDDA$^+$/{G$^-$/MG$^+$}$_n$ showed two pairs of peaks with E_m values of -0.13 V and -0.25 V *vs*. Ag/AgCl, the redox process being diffusion-controlled. When MG was adsorbed on GCE/PDDA$^+$/{G$^-$/CNT$^+$}$_5$, the redox peaks were located at -0.08 and -0.17 V *vs.* Ag/AgCl, and the process was surface-confined. The difference is explained considering the pH-dependent redox process of MG since, when MG is in multilayer structures, the diffusion of H$^+$ within the multilayers controls the redox process whilst when MG is adsorbed on the outer surface, H$^+$ in the buffer solution can easily participate in the redox process of MG and, so that the redox is surface-controlled. The high stability of the modified electrode was demonstrated by continuously cycling the electrode, the peak currents remaining constant after 50 cycles [16]. In [26], another phenazine monomer, methylene blue (MB), was used together with graphene in multilayer structures. In this case the electrode GCE/{G/MB}$_n$ displayed a pair of redox peaks with E_m = -0.25 V *vs*. SCE, corresponding to MB redox activity, which increased with the number of layers, reflecting the loading of MB and G in each layer onto GCE [26].

When G was acidically functionalized, well-defined peaks with E_m = 0.09 V *vs.* SCE observed for the Gr/PDDA$^+$/PSS$^-$/{CNT-NH$_3^+$/G-COO$^-$}$_5$, were attributed to the redox process of oxygen-containing groups, which increased linearly with the number of bilayers. The CV profile remained unaltered on continuous potential cycling, indicating the robustness of the multilayer film [15].

The deposition of {chit$^+$(CN+GOx)/PSS$^-$}$_n$ structures was monitored through the variation in the capacitance values calculated from the CVs. In [22], the deposition of first layer of chit$^+$(NG+GOx) led to a substantial increase in the capacitance value, decreasing when the second chit layer was adsorbed. In [23], the chitosan concentration was decreased to 0.5% compared to the 1% used in [22], due to the resistive nature of chitosan, but when the chitosan membrane contained HNO$_3$ or KOH functionalized CNT, the capacitance increased gradually up to the fourth chit layer. Highest capacitance values were recorded for electrode assemblies containing HNO$_3$_CNT and KOH_G, confirmed by electrochemical impedance spectroscopy measurements. CVs recorded without CN in the chitosan layer, revealed a continuous decrease in the capacitive currents upon chitosan deposition, underlying their importance.

The electrochemical properties of the multilayer film GCE/{PEI$^+$ /PAA$^-$}$_3$, with and without G, were assessed by using [Fe(CN)$_6$]$^{4-/3-}$ as electrochemical probe. Without graphene, the peak currents of the redox probe were smaller at the modified electrodes, and peak separation increased, indicating that the probe was hindered from permeating through the multilayer film and undergoing electron transfer at the electrode substrate. For the GCE/{PEI$^+$/PSS-G$^-$}$_3$ modified electrode, the CV response was nearly the same as that of the bare GC electrode, indicating that graphene can promote electron transfer through the multilayer film [17].

In a similar way, graphene promoted electron transfer through the multilayer film at GCE/ABS$^-$/{G-AB$^+$/G-TSCuPc$^-$}$_3$/G-AB$^+$, when graphene was functionalized prior to LbL assembly with either AB$^+$ or TSCuPc$^-$. The peak-to-peak separation of [Fe(CN)$_6$]$^{4-/3-}$ increased almost by a factor of 3 when GCE was modified with ABS$^-$, attributed to the presence of negatively-charged sulfonate groups on the surface, while upon inclusion of G as G-AB$^+$ and G-TsCuPC$^-$ in the multilayer, the reversibility was significantly reduced, and peak currents were enhanced [20]. Modification with {BSA-G$^+$/AuNP$^-$} led to an increase in the electroactive area, as measured using [Fe(CN)$_6$]$^{4-/3-}$. Moreover, annealed modified electrodes showed a higher electroactive area than non-annealed electrodes, due to an increase in film porosity; however, for annealing temperatures higher than 340ºC, the peak currents decreased, probably due to the partial decomposition of graphene [24]. Using chitosan matrices, an increase in the electroactive area, from 0.08 for GCE to 0.12 cm^2 GCE/{chit$^+$/G$^-$}$_5$, using [Fe(CN)$_6$]$^{4-/3-}$, was observed, indicating high conductivity of the multilayer films [25].

Successful attachment of pyrene-functionalized GOx was demonstrated by CV, the monolayer modified electrode presenting a redox peak at -50 mV *vs*. Ag/AgCl, related to GOx redox activity. $[Fe(CN)_6]^{4-}/^{3-}$ redox peaks were significantly decreased in height after immobilization of graphene together with pyrene functionalized GOx due to the hindered access of the redox probe [21].

3.1.2. CNT modified electrodes

The deposition of PVI-Os$^+$ polymer in a multilayer structure with GOx-CNT$^-$ was monitored by CV in phosphate buffer saline, pH 7.0. A pair of well-defined peaks with E_m = 0.23 V *vs*. Ag/AgCl was observed after the assembly of the first bilayer, ascribed to the PVI-Os groups' activity, which increased with the number of bilayers, suggesting an increase in the amount of electroactive PVI-Os immobilized on the electrode surface. Above 5 bilayers, the conductivity of the multilayer decreased, due to incorporated GOx hindering electron transfer through the film. The robustness of the SPCE/PVI-Os$^+_{el}$/{GOx-CNT$^-$/PVI-Os$^+$}$_4$/PVI-Os$_{el}^+$ modified electrode was confirmed by the stable CV profile upon potential cycling [29].

Similarly, the Os redox peaks which were observed for the first GOx/SWCNT/PVI-Os layer assembled, increased with the number of GOx/SWCNT/PVI-Os layers, suggesting an increase in Os complex content. However, the peak to peak separation increased due to the slower charge transfer displayed by PVI-Os. The electrochemical process was diffusion-controlled at both SPCE/PVI-Os$^+_{el}$/{GOx-CNT$^-$/PVI-Os$^+$}$_4$/PVI-Os$_{el}^+$ and SPCE/{PVI-Os$^+_{el}$/CNT$^-$/PVI-Os$_{el}$/ GOx$^-$}$_5$/PVI-Os$_{el}$, being related to electron transfer in the redox polymer [30].

CNT$^-$ deposition on GCE$^+$ led to an increase in the peak currents of $[Fe(CN)_6]^{4-/3-}$ and a decrease in the peak potential separation (ΔE_p). Moreover, due to the deposited positively-charged PEI$^+$, the peak currents increased more at GCE/CNT$^-$/PEI$^+$, due to more $[Fe(CN)_6]^{4-/3-}$ being adsorbed onto the positively charged PEI$^+$. Deposition of GOx led to a decrease in peak currents and an increase in ΔE_p as expected, indicative of the fact that GOx was immobilized successfully in the GCE/CNT$^-$/{PEI$^+$/GOx$^-$}$_3$ multilayer film [28].

CVs of the GCE/chit$^+$/PtNP-CNT$^-$/{Con A/GOx}$_3$ electrode, where Con A is concanavalin A, exhibited a pair of well-defined and stable redox peaks with E_m −0.42 V vs. SCE, with ΔE_p = 60 mV, attributed to the quasi-reversible redox reaction of GOx. The value of ΔE_p increased with increase in the number of layers, due to slower electron transfer kinetics. The electrochemical process was surface-confined up to 120 mV s^{-1}, above which it was diffusion-controlled [38]. In another PtNP containing multilayer deposited on ITO,

ITO/CNT$^-$/{PtNP-PAMAM$^+$/GOx$^-$}$_n$, the oxidation peak at -0.2 V vs. Ag/AgCl was ascribed to Pt redox activity and increased gradually with the number of deposited layers, up to 3 bilayers, after which the current tended to decrease gradually. The electrochemical oxidation of glucose was a diffusion-controlled process at the surface of the modified electrode [31].

The electrochemical performance of Au/thionine$^+$/CNT$^-$/{PAA$^+$/PVS$^-$}$_3$ was improved by replacing 11-amino-n-undecanethiol (AUT) with thionine to perpendicularly immobilize CNT on the Au surface, demonstrated by the increase in peak current of [Fe(CN)$_6$]$^{4-/3-}$. Au/AUT gave zero response and the calculated electroactive surface areas of Au/thionine$^+$, Au/AUT$^+$/CNT$^-$ and Au/thionine$^+$/CNT$^-$ were, respectively, 1.1, 1.0 and 1.2 that of the unmodified Au electrode, indicating that the insulating AUT layer completely blocked electron transfer, while thionine can increase the electron exchange between the Au electrode and the redox probe [34].

The peak current of the redox probe increased and ΔE_p decreased in the order GCE, GCE/{CNT-PEI$^+$/CNT-DNA$^-$}$_2$ and GCE/{CNT-PEI$^+$/CNT-DNA$^-$}$_2$/OPH$^+$/AChE$^-$. The electroactive area followed the same tendency, increasing from 0.06 cm^2, for the GCE, to 0.08 cm^2 and 0.12 cm^2. The electrochemical process was found to be diffusion-controlled. The six layered enzyme/polymer nanocomposite was found to have the highest surface area [37].

3.2. Surface characterization by AFM, SEM and TEM

3.2.1. Atomic force microscopy (AFM)

3.2.1.1. Graphene

AFM images of graphene-containing LbL-modified electrodes enabled the thickness of graphene oxide and of reduced graphene to be estimated in some cases. Usually, the deposition of LbL was monitored via the change in the surface roughness.

In [17], the thickness of graphene oxide was estimated to be 0.9 nm from AFM images, being larger for PAA-graphene in {PEI$^+$/PAA$^-$-G}, of 1.8 nm. Since the thickness of graphene is assumed to be less than that of graphene oxide, the thicker PAA-G indicates that PAA-pyrene is attached to graphene sheets, to obtain PAA$^-$-G. Similarly, in [18], the thickness of graphene oxide was about 0.95 nm, and the larger thickness of 1.36 and 1.59 nm for G-SO$_3^-$ and G-IL-NH$_3$ was verification of the successful functionalization of G. The typical crumpled thin flake shape of GO is maintained after its functionalization [18]. AFM images show that BSA-G nanosheets were rougher and thicker than pristine GO indicating successful reduction and modification by BSA [24]. In [21], the graphene sheets in

{G/GOx-pyrene} were found to be mostly single-layered with an average size of about 300 nm.

AFM images of {G/PDDA⁺-PB} multilayer films revealed a flat and homogeneous surface, in which the presence of both PB particles and graphene sheets are clear [14].

3.2.1.2. CNT

CNT networks can be more easily seen by AFM imaging, than those of graphene. It was observed that CNT form a monolayer of densely-packed bundles on Au/11-amino-n-undecanethiol (AUT) and Au/thionine, being perpendicularly fixed on both substrates. The similar densities observed confirmed that thionine can substitute AUT in the CNT assembly and the low average lateral dimensions of CNT of about 70 nm, indicate insignificant aggregation during CNT surface condensation [34]. In the CNT-PEI⁺/CNT-DNA⁻/{CNT-PEI⁺/CNT-AChE⁻} layers, bio-functionalized CNT, CNT-DNA⁻ and CNT-AChE⁻, form an interlocked network structure, the surface roughness increasing with the number of deposited layers, due to increased film thickness [36].

3.2.2. Scanning and transmission electron microscopy (SEM and TEM)

3.2.2.1. Graphene

SEM imaging revealed the shape of wrinkled graphene sheets, typical of exfoliated sheets of graphene, which is usually maintained even after its functionalization, as exemplified in Fig. 3a.

SEM images of both {G⁻/CNT⁺}$_n$ and {G⁻/MG⁺}$_n$, with methylene green, reveal an increase in surface coverage with the number of bilayers. In the case of {G⁻/CNT⁺}$_n$ the typical crumpled graphene structures were interconnected with the nanowire structures of CNT and form a network with large surface area. The same graphene structures were observed for {G⁻/MG⁺}$_n$ which were well interconnected to each other at the edges forming a well-structured conducting graphene/MG network [16]. The graphene crumpled sheet structures are visible in the SEM images of GCE/{chit⁺/G⁻}$_n$, and ITO/ (chit(G+GOx) [23] with a denser and more uniform surface with deposition of more bilayers [25].

The morphologies of G-SO$_3$⁻ and G-IL-NH$_3$⁺ used in {G-IL-NH$_3$⁺/G-SO$_3$⁻} multilayers are different. The G-SO$_3$⁻ is not greatly changed compared to G, while the G-IL-NH$_3$⁺ has a different aspect to that of G, appearing to be covered by a thin layer of IL. The first monolayer did not cover the ITO surface completely with G, but with an increasing number of bilayers, the graphene gradually

builds up and is densely assembled up to the 5th bilayer [18]. Similar structures of wrinkled graphene sheets were observed for both G-AB+ and G-TSCuPc-, which retained the initial shape of G. The EDS spectra of the composites confirmed the presence of AB, by Cu and Cl signals and the Cu, O and S signals proved the presence of TSCuPc, after 3 layers the substrate being densely covered by graphene [20].

In the case of G-TiO$_2$-Pd- used in the {CNT-NH$_3$+/G-TiO$_2$-Pd-}$_9$ multilayer film, SEM images of graphene without any particle loading revealed thicker platelets with multiple layers of graphene sheets, indicating that the exfoliated parts restacked together due to capillary and van der Waals forces. After reacting with TiCl$_3$, the multi-layered graphene sheets are entirely covered by TiO$_2$, which form distinct irregular spherical and rod-like morphologies, while the wrinkle structure of graphene is maintained. Elemental analyses further attest the presence of Ti on graphene surfaces. TEM images of G-TiO$_2$-Pd- show uniformly distributed small PdNP on top of G-TiO$_2$ with no agglomeration and with an average nanorod diameter of 7–10 nm and length 40–60 nm. The average size of the deposited PdNPs is 5.5±0.3 nm [19].

SEM images of graphene/AuNP hybrid multilayer films, FTO/PEI/ {BSA-G+/AuNP-}, showed that AuNPs were uniformly distributed on the surface of the graphene nanosheets. Side-view SEM images illustrated that the AuNPs were LbL-stacked, the film thickness increasing linearly with the number of bilayers [24].

Finally, SEM images obtained during the LbL modification of graphite substrate showed that the cavities observed at the bare graphite electrode, decreased upon modification with the first CNT-NH$_3$+/G-COO− bilayer, more G and CNT being adsorbed in the following bilayers [15].

3.2.2.2. CNT

SEM images of CNT within the LBL multilayers usually reveal their typical nanotube, three-dimensional structures (see Fig. 3b). As in the case of graphene, typically more than 2-3 bilayers are needed to completely cover the substrate surface.

An increase in CNT surface thickness demonstrates the effectiveness of the LbL process, when bio-functionalized CNTs, CNT-DNA- and CNT-AChE-, are randomly dispersed in the thin films of CNT-PEI+/CNT-DNA-/{CNT-PEI+/ CNT-AChE-}$_3$ [36].
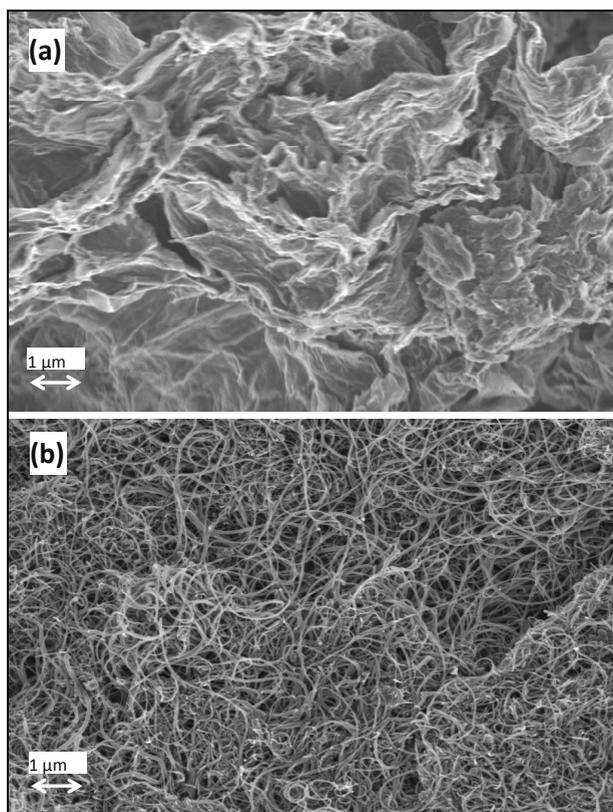
Figure 3. Typical SEM images of a) G and b) CNT on indium tin oxide substrates

CNT were efficiently covered by the PEI$^+$ polymeric net in GCE/CNT$^-$/PEI$^+$ and were homogenously distributed on the GCE surface. GOx molecules adsorbed on the surface of GCE/CNT$^-$/PEI$^+$ tended to aggregate into island-like structures. In GCE/CNT$^-$/{PEI$^+$/GOx$^-$}$_3$/PEI$^+$, CNT are hardly visualized, being totally wrapped by both protein and PEI polymer [28]. In the case of SPCE/{PVI-Os$^+_{el}$/CNT$^-$/PVI-Os$_{el}$/GOx$^-$}$_5$/PVI-Os$_{el}$ SEM images show that the substrate is almost completely covered with a homogeneous, porous, three-dimensional CNT-polymer nanocomposite [30].

Typical SEM images of CNT dispersed in chitosan clearly reveal the CNT tubular structure with a more curved and less aligned arrangement, with no sign of residual metal particles. The images showed nanotubes with diameters between 20 and 44 nm, which correspond with the initial values after fabrication (30±10 nm), which indicates that their functionalization does not modify their initial structure [23].

TEM images at LbL modified electrodes containing PtNP and CNT show that PtNP are highly dispersed and distributed either on the sidewall, in chit$^+$/PtNP-CNT$^-$ [38], or on the surface of CNT, in CNT$^-$/Pt-PAMAM$^+$ [31], in the latter case the dendrimer acting as a stabilizer, by impeding the regrouping of nanoparticles. Also, when AuNP were used together with CNT, they were uniformly dispersed without aggregation on the CNT surface, which were randomly oriented and distributed in the PAH-CNT-AuNP layer without aggregation. Up to 4 layers, the surface was not fully covered, while eight layers ensured a high surface coverage [33]. SEM images confirmed the presence of some free AuNP and intra-PAMAM dendrimer AuNP nanostructures, with 13 nm diameter, with the size of the AuNPs inside being of 8 nm [32].

4. APPLICATIONS

The majority of the biosensors developed in the past 5 years based on LbL methodology have been glucose biosensors utilizing GOx, some others containing the enzymes AlcDH, ChOx, acyl-CoA oxidase/ synthetase. Three biosensors were based on enzyme inhibition and two were developed to be used in biofuel cells.

Table 1 summarises the biosensors that have been developed and their principal analytical characteristics.

Table 1. Biosensors based on carbon nanomaterials, graphene and CNT, and LbL methodology from 2010-2015

Analyte	Electrode architecture	Technique	Linear range / mM	LOD / µM	Sensitivity / µA mM^{-1} cm^{-2}	Ref.
Glucose	GCE/{G/PDDA$^+$-PB/GOx$^-$/PDDA$^+$-PB}$_3$	Amp. +0.2 V[(b)]	0.1-6.5	6	1.6*	[14]
	GCE/{PEI$^+$/PAA$^-$-G}$_3$/{PEI$^+$/GOx$^-$}$_5$	Amp. +0.9 V	0.2-10	168	0.261	[17]
	GCE/{G/GOx-pyrene}$_3$	Amp. +0.28 V[(a)]	0.2-30	154	2.0	[21]
	GCE/{G-IL-NH$_3$$^+$/G-SO$_3$$^-$}$_5$/G-IL-NH$_3$$^+$/GOx$^-$/Nafion	Amp. -0.2 V	0.01-0.5	3.3	1	[18]
	GCE/ABS$^-$/{G-AB$^+$/G-TSCuPc$^-$}$_3$/G-AB$^+$/Nafion/GOx	CV-0.45 V[(b)]	0.1-8.0	50	17.5	[20]
	AuQC/{chit$^+$(HNO$_3$_G+GOx)/PSS$^-$}$_4$	Amp -0.3 V[(a)]	0.2-1.6	64	6.0	[23]
	AuQC/{chit$^+$(KOH_G+GOx)/PSS$^-$}$_4$		0.2-1.6	12	18.6	
	AuQC/{chit$^+$(NG+GOx)/PSS$^-$}$_2$	Amp. -0.2 V[(a)]	0.2-1.6	18.6	10.5	[22]

Analyte	Electrode architecture	Technique	Linear range / mM	LOD / μM	Sensitivity / μA mM^{-1} cm^{-2}	Ref.
	GCE/{CNT-NH$_3$$^+$/G-TiO$_2$-PdNP}$_9$/CNT-NH$_3$$^+$/GOx$^-$/Nafion	Amp. -0.05 V[b]	0.001-1.5	0.6	0.18	[19]
	AuQC/{chit$^+$(HNO$_3$_CNT+GOx)/PSS$^-$}$_4$	Amp. -0.3 V[a]	0.2-1.6	18	18.6	[23]
	AuQC/{chit$^+$(KOH_CNT+GOx)/PSS$^-$}$_4$		0.2-1.6	50	13.7	
	GCE/CNT$^-$/{PEI$^+$/GOx$^-$}$_3$/PEI$^+$	CV -0.5 V[b]	0.3	-	106.6	[28]
	SPCE/PVI-Os$^+$$_{el}$/{GOx-CNT$^-$/PVI-Os$^+$}$_4$/PVI-Os$_{el}$$^+$	Amp. +0.3 V[a]	0.2-7.5	0.07	32	[29]
	SPCE/{PVI-Os$^+$$_{el}$/CNT$^-$/PVI-Os$_{el}$/ GOx$^-$}$_5$/PVI-Os$_{el}$	Amp. +0.3 V[a]	0.2-6.0	100	16.4	[30]
	GCE/chit$^+$/PtNP-CNT$^-$/{Con A/GOx}$_3$	Amp. +0.3 V[b]	0.001-2.0	0.4	41.9	[38]
	Au/thionine$^+$/CNT$^-$/{PAA$^+$/PVS$^-$}$_3$/{PDDA$^+$/GOx$^-$}$_8$	Amp. +0.6 V[a]	0.05-6.3	11	19	[34]
Maltose	GCE/{PEI$^+$/PAA$^-$-G}$_3$/{PEI$^+$/GOx$^-$}$_5$/{PEI/GA}$_4$	Amp. +0.9 V	10-100	1370	0.00715	[17]
Ethanol	Gr/PDDA$^+$/PSS$^-$/{CNT-NH$_3$$^+$/G-COO$^-$}$_5$/AlcDH.	Amp. +0.1 V[b]	0.025-0.2	25	82.5	[15]
	GCE/PDDA$^+$/{G$^-$/MG$^+$}$_5$/AlcDH	Amp. +0.1 V[a]	0.5-11.0	-	0.025	[16]
Cholesterol	Au/MPS$^-$/PAH$^+$/PSS$^-$/{PAH-CNT-AuNP/HRP}$_m$/{PAH-CNT-AuNP/ChOx}$_n$	Amp. -0.15 V[b]	0.18-11	20	0.12	[33]
Palmitoyl-CoA Oleic acid	SPCE/{PDDA-CNT/ACoAOx}$_2$ SPCE/{PDDA-CNT/ACoAOx/PDA-CNT/ACoAS}$_2$	LSV +0.5 V[c]	up to 1.2 up to 0.9	- -	8.9 12.3	[35]

* Area not specified; [a] *vs*. Ag/AgCl, [b] *vs*. SCE; [c] Ag
G - graphite, **PDDA** - poly(dimethyldiallyammonium chloride), **PB** - Prussian blue nanoparticles; **GOx** – glucose oxidase; **PEI** - polyethyleneimine, **PAA** -polyallylamine, **IL**-ionic liquid, **ABS**$^-$ - sulfanilic acid, **AB** - alcian blue pyridine variant, **TSCuPc** - copper phthalocyanine-tetrasulfonic acid tetrasodium salt, **PSS** -poly(sodium-p-styrene-sulfonate), **chit** – chitosan, **NG**- nitrogen doped graphene, **PdNP** – Pd nanoparticles, **SPCE** - screen printed carbon electrode, **PVI-Os**-(poly[(vinylpyridine) Os(bipyridyl)$_2$Cl, **PVI-Os**$_{el}$ – PVI-Os electrodeposited, **PtNP**- Pt nanoparticles, **Con A**- concanavalin A, **PVS** - poly(vinyl sulfate), **GA-** glucoamylase, **AlcDH** –alcohol dehydrogenase, **MG** – methylene green, **MPS**- 3-mercapto-1-propanesulfonate, **PAH** - poly(allylamine hydrochloride), **AuNP**- Au nanoparticles, **HRP** – horseradish peroxidase, **ChOx** – cholesterol oxidase, **ACoAOx** -acyl-CoA oxidase, **ACoAS** acyl-CoA synthetase.

4.1. Glucose biosensors

Glucose oxidase (GOx) has several favourable attributes that contribute to its common usage such as high turnover rate, excellent selectivity, good thermal and pH stability, and low cost and robustness [39-41]. Hence, GOx based biosensors are continuously developed, serving usually as a strategy to evaluate new electrode biosensor platforms. Glucose biosensors have been developed based on the LbL methodology and will be briefly described in this section.

The glucose biosensors developed were based on H_2O_2 detection [14, 17-19, 34], or direct electronic communication between the enzyme and the electrode [20, 22, 23, 28, 38], only few utilizing a redox mediator [21, 29, 30].

In [14], the use of PB, which has been demonstrated to have intrinsic peroxidase activity, allowed glucose monitoring through detection of H_2O_2 at +0.20 V *vs*. SCE. Also on the basis of the high electrocatalytic activity of GCE/{PEI$^+$/PAA$^-$-G}$_6$ toward H_2O_2, glucose and maltose enzyme-based biosensors were fabricated, incorporating GOx together with glucoamylase (GA) [17]. Similarly, GCE/{G-IL-NH$_3^+$/G-SO$_3^-$}[18], GCE/{CNT-NH$_3^+$/G-TiO$_2$-PdNP$^-$}$_n$ [19] and Au/thionine$^+$/CNT$^-$/{PAA$^+$/PVS$^-$}$_3$, [34] showed a similar electrocatalytic effect towards H_2O_2, the measurement of glucose being based on H_2O_2 detection.

Graphene used in GCE/ABS$^-$/{G-AB$^+$/G-TSCuPc$^-$}$_3$/G-AB$^+$/Nafion/GOx enabled direct electron transfer between the redox centres of GOx molecules and the electrode substrate, the glucose being detected by monitoring the GOx peaks in CV. The mechanism was based on the gradual decrease of the reduction peaks, due to O_2 consumption upon addition of glucose [20].

Biosensors based on carbon nanomaterials (CN) in the configuration {chit$^+$(CN+GOx)/PSS$^-$}$_n$, n = 2, where CN = nitrogen-doped graphene (NG) and n = 4 when CN = HNO$_3$ or KOH functionalized G and CNT, showed good electronic communication between GOx and the electrode substrate *via* G or CNT. The mechanism was based on direct cofactor regeneration at the electrode at -0.3 and -0.2 V *vs.* Ag/AgCl. The biosensor architectures with best sensitivities and stability were based on four bilayers, the sensitivity being greatly influenced by the capacitance of the modified electrodes [22, 23].

In the case of the GCE/CNT$^-$/{PEI$^+$/GOx$^-$}$_3$/PEI$^+$ biosensor, it was demonstrated that CNT play a critical role in the direct electron transfer of GOx, their presence leading to a significant increase of the GOx redox peaks. The CV peak currents also increased linearly with the number of bilayers up to the third, no increase being observed on depositing more bilayers. The midpoint potential of GOx was -0.45 V, very close to the standard FAD/FADH$_2$ potential of −0.46 V *vs.* SCE at pH 7.0, 25 ∘C [42], indicating that most GOx molecules retain their native structure after immobilization. Moreover, the peak-to-peak separation was only 40 mV, indicating fast electron transfer [28].

Similar to the biosensor developed in [28], the GCE/chit+/PtNP-CNT-/{Con A/GOx}$_3$ biosensor was based on direct electron transfer, the CV displaying a pair of peaks around -0.45 V, again close to the standard FAD/FADH$_2$ potential. PtNP play a dual role, as immobilization matrices for the enzyme and as electrocatalytic material for glucose oxidation, at +0.3 V vs. SCE [38].

In [21], the LbL assembly was based on π-π interaction between pyrene-functionalized GOx and graphene; therefore, the enzymatic activity of GOx-pyrene was first assessed, results indicating retention of 76% of its biocatalytic activity. Ferrocene was used to mediate electrical communication between the enzyme and the electrode.

SPCE/PVI-Os+$_{el}$/{GOx-CNT-/PVI-Os+}$_n$ and SPCE/{PVI-Os+$_{el}$/CNT-/PVI-Os$_{el}$/GOx-}$_n$/PVI-Os$_{el}$ biosensors were based on oxidation of the mediator at +0.3 V vs. Ag/AgCl [29, 30]. The currents increased linearly up to 4 and 5 bilayers respectively, further bilayers tending to gradually decrease the catalytic current, due to hindered glucose transport through the multilayers.

Negligible or no interferences were observed from ascorbic acid (AA), uric acid (UA) and dopamine (DA) [14, 18-23, 34] nor acetaminophen [29, 34], H$_2$O$_2$ and L-cysteine [20], or citric and oxalic acid [22, 23]. UA and AA greatly influenced biosensor response in [29], their pre-oxidation being required before the use of the biosensor for glucose detection in complex matrices. In [30], the authors decreased the interferences by using a Nafion membrane as an outer negative layer,

Biosensors retained 83% [18], 86% [19] and 90% [34] of their initial activities after two weeks of storage at 4 ºC. Biosensor response decreased by only 7% [20], 10 % [29, 30] and 18% [21] after one month of storage at 4 ºC. The current recorded at GCE/CNT-/{PEI+/GOx-}$_3$/PEI+ decreased by 5% after storage at 4 ºC for 20 days[28] and the biosensor current response in CV decreased by 5.6% in 10 days, and by 13% after 1 month of storage [38]. In most of these reports, the storage medium (air or buffer solution) is not specified, only the temperature.

After 10 days of continuous use, sensitivities decreased by 10 % for HNO$_3$_CNT and KOH_G biosensors, and 5 % for KOH_CNT and HNO$_3$_G biosensors, respectively. After 20 days the sensitivities maintained 70 %, for HNO$_3$_CNT and KOH_G biosensors, and 60% of their initial values for KOH_CNT and HNO$_3$_G biosensors. The biosensor based on NG maintained 95 % of its initial sensitivity after two weeks of continuous use [22, 23].

4.2. Biosensors for ethanol, cholesterol and fatty acids

Two biosensors for the determination of ethanol were developed, both based on alcohol dehydrogenase (AlcDH), one containing both CNT and G, Gr/PDDA+/PSS-/{CNT-NH$_3$+/G-COO-}$_5$/AlcDH [15] and one comprising the redox mediator methylene green (MG) and G, GCE/PDDA+/{G-/MG+}$_5$/AlcDH [16].

The oxidation of NADH was first tested at Gr/PDDA$^+$/PSS$^-$/{CNT-NH$_3^+$/G-COO$^-$}$_5$ at +0.07 V *vs*. SCE, no significant interferences being observed from UA, DA, acetaminophen and H$_2$O$_2$. The biosensor operated at +0.10 V *vs*. SCE and the mechanism was based on the oxidation of the cofactor. After 5 days, the biosensor retained 92% of the initial response [15].

The assembled GCE/PDDA$^+$/{G$^-$/MG$^+$}$_5$ possessed electrocatalytic activity toward the oxidation of NADH, which occurred at -0.10 V *vs*. Ag/AgCl. The AlcDH biosensor operated at +0.10 V, the mechanism being based on cofactor regeneration [16].

A bi-enzymatic biosensor based on horseradish peroxidase (HRP) and cholesterol oxidase (ChOx) was developed for the detection of cholesterol. The mechanism of Au/MPS$^-$/PAH$^+$/PSS$^-$/{PAH-CNT-AuNP/HRP)$_m$ /{PAH-CNT-AuNP/ChOx}$_n$ was based on the amperometric detection of H$_2$O$_2$ at -0.15 V *vs*. SCE, a by-product of the enzymatic conversion of cholesterol in the presence of oxygen. The biosensor could detect cholesterol without HRP at -0.15 V, due to the catalytic properties of AuNP and CNT, but the presence of HRP significantly increased the sensitivity. No significant interferences were observed from urea, glycine, l-cysteine, glucose and AA. After 25 days of storage the biosensor maintained 90% of its initial response. The biosensor was successfully applied to the detection of cholesterol in human serum samples [33].

An acyl-CoA oxidase (ACoAOx) biosensor, SPCE/{PDDA-CNT/ACoAOx}$_2$, was developed for the detection of palmitoyl oil and a bi-enzymatic biosensor based on ACoAOx together with acyl-CoA synthetase (ACoAS), SPCE/{PDDA-CNT/ACoAOx/PDA-CNT/ACoAS}$_2$, for the determination of oleic acid. The detection of both oleic acid and palmitoyl-CoA was based on the oxidation of enzymatic generated H$_2$O$_2$ at +0.5 V *vs*. Ag. The bi-enzyme biosensor exhibited good electrocatalytic activity for oxidation of non-esterified fatty acids, the thin LbL polymer–enzyme layers allowing good reactant mass transport to accomplish the two-step enzyme reactions [35].

4.3. Biosensors based on inhibition

Three LbL biosensors based on acetylcholinesterase (AChE) inhibition were developed for the detection of pesticides and neurotoxins. The inhibition measurements for carbofuran were performed by differential pulse voltammetry at +0.63 V *vs*. SCE at GCE/CNT/PAMAM-NH$_3^+$-AuNP/AChE$^-$, and the sensor exhibited a detection limit of 4 nM, with a linear range 5-90 µM [32]. The inhibition by neurotoxins at GCE/CNT-PEI$^+$/CNT-DNA$^-$/{CNT-PEI$^+$/CNT-AChE$^-$}$_3$ was detected by fixed potential amperometry at +0.58 V *vs*. Ag/AgCl [36]. Organophosphorus and non-organophosphorus pesticides, namely paraoxon and carbaryl, were successfully detected by CV at +0.6 V *vs*. Ag/Agcl at a bi-enzymatic biosensor containing together with AChE the enzyme organophosphate

hydrolase (OPH), GCE/{CNT-PEI$^+$/CNT-DNA$^-$}$_2$/OPH$^+$/AChE$^-$. The detection limits were 0.5 and 1 µM for paraoxon and carbaryl respectively, the biosensors being successfully applied for detection of pesticides in apples [37].

4.4. Bioanodes for fuel cells

Three biosensors were developed for use as bioanodes in fuel cells, two based on GOx: ITO/CNT$^-$/{PtNP-PAMAM$^+$/GOx$^-$}$_3$ and ITO/CNT$^-$/{PDDA$^+$/GOx$^-$}$_3$ [31] and one on glucose dehydrogenase (GlcDh), GCE/PDDA$^+$/MG/{G$^-$/CNT$^+$}$_5$/ GlcDh [16]. In [31] the the ITO/CNT$^-$/{PtNP-PAMAM$^+$/GOx$^-$}$_3$ anode is coupled with a cathode consisting on electrodeposited Pt. Maximum power density and current density for ITO/CNT$^-$/{PDDA$^+$/GOx$^-$}$_3$ were 7 µW cm^{-2} and 75 µA cm^{-2}, respectively, while for (ITO/CNT$^-$/{PtNP-PAMAM$^+$/GOx$^-$}$_3$ the maximum power density was 17 µW cm^{-2} and current density was 90 µA cm^{-2}. Open circuit potentials were 0.52 V and 0.64 V, respectively. In [16], the anode GCE/PDDA$^+$/ MG/{G$^-$/CNT$^+$}$_5$/GlcDh was assembled with a laccase-based biocathode to form a glucose/O$_2$ biofuel cell, with an open circuit potential of 0.69 V and a maximum power density of 22.5 µW cm^{-2} at 0.48 V.

5. CONCLUSIONS

The use of LbL methodology incorporating graphene and carbon nanotubes in the modified electrode assemblies offers the possibility of developing a vast diversity of biosensor architectures, by exploiting different functionalizations of the carbon nanomaterials and choosing an appropriate polyelectrolyte for the build-up of the multilayers. The typical nanostructures of both graphene and CNT remain mostly unaltered after functionalization and self-assembly, their incorporation in the LbL structures leading to an overall increase in electronic conductivity and electroactive surface area of the modified electrodes which, as a result, improved the analytical performances of the LbL CN-based biosensors. During the time period reviewed, the majority of the LbL CN biosensors developed were based on glucose oxidase. Other biosensors were based on cholesterol oxidase, alcohol dehydrogenase, acyl-CoA oxidase/synthetase for the detection of ethanol, cholesterol and fatty acids, respectively. Biosensors based on the inhibition of acetylcholinesterase for the detection of neurotoxins and pesticides and three bioanodes were also reported using the enzymes glucose oxidase and glucose dehydrogenase.

Future research in this area should bring valuable contributions for the development of advanced LbL biosensors containing a variety of materials tailored in self-assembled thin multilayers, which can find applications in a variety of fields, such as clinical, food/environmental industry, and including the design of new bioanodes for fuel cells.

ACKNOWLEDGEMENTS

REFERENCES

1. L. Caseli, D.S. dos Santos Jr., R.F. Aroca, O.N. Oliveira Jr., *Material Science & Engineering C*, **2009**, *29*, 1687.
2. L. Caseli, D.S. dos Santos Jr., M. Foschini, D. Goncalves, O.N. Oliveira Jr., *Material Science and Engineering C*, **2007**, *27*, 1108.
3. R.M. Iost, F.N. Crespilho, *Biosensor & Bioelectronics*, **2012**, *31*, 1.
4. O.N. Oliveira, R.M. Iost, J.R. Siqueira Jr., F.N. Crespilho, L. Caseli, *ACS Applied Materials & Interfaces*, **2014**, *6*, 14745.
5. V. Flexer, E.S. Forzani, E.J. Calvo, *Analytical Chemistry*, **2006**, *78*, 399.
6. S.M. Zhu, J.J. Guo, J.P. Dong, Z.W. Cui, T. Lu, C.L. Zhu, D. Zhang, J. Ma, *Ultrasonics Sonochemistry*, **2013**, *20*, 872.
7. Y. Shao, J. Wang, H. Wu, J. Liu, I.A. Aksay, Y. Lin, *Electroanalysis*, **2010**, *22*, 1027.
8. S.K. Vashist, D. Zheng, K. Al-Rubeaan, J.H.T. Luong, F.-S. Sheu, *Biotechnology Advances*, **2011**, *29*, 169.
9. T. Kuila, S. Bose, P. Khanra, A.K. Mishra, N.H. Kim, J.H. Lee, *Biosensors & Bioelectronics*, **2011**, *26*, 4637.
10. D. Tasis, N. Tagmatarchis, A. Bianco, M. Prato, *Chemical Reviews*, **2006**, *106*, 1105.
11. T. Kuila, S. Bose, A.K. Mishra, P. Khanra, N.H. Kim, J.H. Lee, *Progress in Materials Science*, **2012**, *57*, 1061.
12. V. Georgakilas, M. Otyepka, A.B. Bourlinos, V. Chandra, N. Kim, K.C. Kemp, P. Hobza, R. Zboril, K.S. Kim, *Chemical Reviews*, **2012**, *112*, 6156.
13. Q. He, Y. Cui, S. Ai, Y. Tian, J. Li, *Current Opinion in Colloid and Interface Science*, **2009**, *14*, 115.
14. J. Yan, T. Zhong, W. Qi, H. Wang, *Journal of Inorganic* and *Organometallic Polymers and Materials*, **2015,** *25*, 275.
15. S. Prasannakumar, R. Manjunatha, C. Nethravathi, G.S. Suresh, M. Rajamathi, T.V. Venkatesha, *Journal of Solid State Electrochemistry*, **2012**, *16*, 3189.
16. X. Wang, J. Wang, H. Cheng, P. Yu, J. Ye, L. Mao, *Langmuir*, **2011**, *27*, 11180.
17. G. Zeng, Y. Xing, J. Gao, Z. Wang, X. Zhang, *Langmuir*, **2010**, *26*, 15022.
18. H. Gu, Y. Yu, X. Liu, B. Ni, T. Zhou, G. Shi, *Biosensors & Bioelectronics*, **2012**, *32*, 118.
19. Y. Yu, Y. Yang, H. Gu, D. Yu, G. Shi, *Analytical Methods*, **2013**, *5*, 7049.

20. Y.-Q. Zhang, Y.-J. Fan, L. Cheng, L.-L. Fan, Z.-Y. Wang, J.-P. Zhong, L.-N. Wu, X.-C. Shen, Z.-J. Shi, *Electrochimica Acta*, **2013**, *104*, 178.
21. J. Liu, N. Kong, A. Li, X. Luo, L. Cui, R. Wang, S. Feng, *Analyst*, **2013**, *138*, 2567.
22. M.M. Barsan, M. David, M. Florescu, L. Ţugulea, C.M.A. Brett, *Bioelectrochemistry*, **2014**, *99*, 46.
23. M. David, M.M. Barsan, M. Florescu, C.M.A. Brett, *Electroanalysis*, **2015,** in press.
24. Q. Xi, X. Chen, D.G. Evans, W. Yang, *Langmuir*, **2012**, *28*, 9885.
25. X. Weng, Q. Cao, L. Liang, J. Chen, C. You, Y. Ruan, H. Lin, L. Wu, *Talanta*, **2013**, *117*, 359.
26. D. Zhang, L. Fu, L. Liao, B. Dai, R. Zou, C. Zhang, *Electrochimica Acta*, **2012**, *75*, 71.
27. A. Michopoulos, A. Kouloumpis, D. Gournis, M.I. Prodromidis, *Electrochimica Acta*, **2014**, *146*, 477.
28. C. Deng, J. Chen, Zhou Nie, S. Si, *Biosensors & Bioelectronics*, **2010**, *26*, 213.
29. Q. Gao, Y. Guo, W. Zhang, H. Qi, C. Zhang, *Sensors & Actuators B*, **2011**, *153*, 219.
30. Q. Gao, Y. Guo, J. Liu, X. Yuan, H. Qi, C. Zhang, *Bioelectrochemistry*, **2011**, *81*, 109.
31. J. Zhang, Y. Zhu, C. Chen, X. Yang, C. Li, *Particuology*, **2012**, *10*, 450.
32. Y. Qu, Q. Sun, F. Xiao, G. Shi, L. Jin, *Bioelectrochemistry*, **2010,** *77*, 139.
33. X. Cai, X. Gao, L. Wang, Q. Wu, X. Lin, *Sensors & Actuators B*, **2013**, *181*, 575.
34. M. Ma, Z. Miao, D. Zhang, X. Du, Y. Zhang, C. Zhang, J. Lin, Q. Chen, *Biosensors & Bioelectronics*, **2015**, *64*, 477.
35. J. Kang, A.T. Hussain, M. Catt, M. Trenell, B. Haggett, E.H. Yu, *Sensors & Actuators B*, **2014**, *190*, 535.
36. Y. Zhang, M.A. Arugula, J.S. Kirsch, X. Yang, E. Olsen, A.L. Simonian, *Langmuir*, **2015**, *31*, 1462.
37. Y. Zhang, M.A. Arugula, M. Wales, J. Wild, A.L. Simonian, *Biosensors & Bioelectronics*, **2015**, *67*, 287.
38. W. Li, R. Yuan, Y. Chai, H. Zhong, Y. Wang, *Electrochimica Acta*, **2011**, *56*, 4203.
39. R. Wilson, A.P.F. Turner, *Biosensors & Bioelectronics*, **1992**, *7*, 165.
40. J. Wang, *Chemical Reviews*, **2008**, *108*, 814.
41. N.S. Oliver, C. Toumazou, A.E.G. Cass, D.G. Johnston, *Diabetic Medicine*, **2009**, *26*, 197.
42. S. Q. Liu, H.X. Ju, *Biosensors & Bioelectronics*, **2003**, *19*, 177.

Dedicated to prof. dr. I. C. Popescu
on the occasion of his 70th anniversary

ON THE ELECTROCATALYTIC PROPERTIES OF YCo$_{1-x}$Fe$_x$O$_3$ (*x* = 0, 0.5 and 1) PEROVSKITE SERIES

SLOBOTKA ALEKSOVSKA[a,b,c*], SANDRA DIMITROVSKA-LAZOVA[a], VALENTIN MIRČESKI[a,b]

ABSTRACT. The results on the investigation of the electrocatalytic activity of YCo$_{1-x}$Fe$_x$O$_3$ (*x* = 0, 0.5 and 1) perovskites towards several redox reactions, are presented. The perovskites were synthesized by solution combustion method using citric acid as a fuel. They are isomorphous with orthorhombic perovskite structure, within the space group *Pnma.* The electrocatalytic properties of these perovskites were studied by cyclic voltammetry using paraffin impregnated graphite electrode (PIGE) modified with microcrystals of the investigated perovskites. Such modified electrodes were used to study their catalytic properties towards: oxidation of OH$^-$ ions, oxidation of H$_2$O$_2$ in phosphate buffer and oxidation of CH$_3$OH in alkaline solution. It was found that, in general, the catalytic activity is strongly dependent on the cobalt content.

Keywords: perovskites, cyclic voltammetry, electrocatalytic properties

INTRODUCTION

Perovskites (ABO$_3$) are well-known class of ceramic materials with specific chemical and physical properties based on the huge flexibility in composition and structure but still keeping the basic perovskite-type structural pattern. The ideal perovskite-type structure is cubic (*Pm$\bar{3}$m*) consisting of BO$_6$ corner-sharing octahedra with A-cations in the cubooctahedral cavities [1]. The

[a] *University "Sts. Cyril & Methodius", Institute of Chemistry, Faculty of Natural Sciences and Mathematics, Arhimedova 5, 1000 Skopje, Republic of Macedonia*
[b] *Faculty of Medical Sciences, Goce Delcev University, Štip, Republic of Macedonia*
[c] *Research Center for Environment and Materials, Macedonian Academy of Sciences and Arts, Bul. "Krste Misirkov" 2, P.O. Box 428, 1000 Skopje, Republic of Macedonia*
* *Corresponding author: bote.aleksovska@gmail.com*

partial substitution in A or/and B positions in so-called complex perovskites, leads to different types of structural distortions such as tilting of the octahedra, displacement of the cations from the centers of coordination polyhedra, and Jahn-Teller distortion of the octahedra [1]. These compositional and structural variations are responsible for exhibition of important and unique properties determining their application.

The rare-earth perovskites containing Mn, Fe, Co, Ni in B-position, and particularly those with partial substitution in A or/and B position, are considered as catalysts in numerous catalytic processes [2], such as CO oxidation [2, 3], hydrocarbon oxidation [2], nitrogen oxides decomposition [2] etc. The electrical properties of simple and complex perovskites are also very important. According to the literature data perovskites show insulating, semiconducting and metal-conducting properties, depending on the constituents, structure and metal-to-insulator transitions with variation of the temperature [4, 5]. Some perovskites exhibits appropriate performances as cathode materials in solid-oxides fuel cells (SOFCs) [2, 6, 7], and some are used as electrochemical gas sensors [8].

In recent years the electrocatalytic properties of perovskite-type materials have been also extensively studied. Thus, some complex perovskites containing Ni in B-position were used in preparation of carbon paste electrodes as glucose sensors [9, 10], as well as, some other complex perovskites [11]. Manganese containing complex perovskites were also used for preparing carbon paste modified electrodes for amperometric determination of hydrogen peroxide [12]. Also, manganites partially substituted with Sr in A position show electrocatalytic activity towards hydrogen peroxide in alkaline solutions [13]. Xu et al. [14] have developed a nonenzymatic biosensor for hydrogen peroxide based on a glassy carbon electrode loaded with layered nano-structured perovskite-type oxide. Most recently [15] Liotta et al. fabricated and tested $La_xSr_{1-x}FeO_{3-d}$ and $La_xSr_{1-x}Co_yFe_{1-y}O_{3-d}$ modified carbon screen printed electrodes for H_2O_2 and glucose electrochemical sensors. The electrodes were electrochemically characterized in alkaline medium by cyclic voltammetry and chrono-amperometric methods. It was found that the key factor for sensing characteristics is the mixed valence states stabilized in the perovskite structure, in particular to the presence of Co^{3+}/Co^{2+} and Fe^{3+}/Fe^{2+} couples accountable for charge transfers.

Perovskites with partial substitution of Co^{3+} were subject of our previous investigations regarding the synthesis and electrical properties [16-19]. However, we were also interested in their electrocatalytic activities. Thus, we have reported [20] on the catalytic properties on $YCoO_3$ and $YCo_{0.5}Cr_{0.5}O_3$ towards oxidation of chloride anions and oxidation of methanol in alkaline solutions, studied by cyclic voltammetry. We have also started

the investigation of YCo$_{1-x}$Fe$_x$O$_3$ (x = 0, 0.33, 05. 0.67 and 1) perovskite series. The publication of the results on their crystal structure and crystallochemical characteristics is in progress [21], and the results on the influence of Y-ion substitution on structural and electrochemical properties of YCo$_{0.5}$Fe$_{0.5}$O$_3$ have been published most recently [22]. Continuing our work on this perovskite series, here we present the electrocatalytic properties of YCo$_{1-x}$Fe$_x$O$_3$ (x = 0, 0.5 and 1) perovskite series towards oxidation of OH$^-$ ions, oxidation of methanol in basic solutions and oxidation of H$_2$O$_2$, in phosphate buffer.

RESULTS AND DISCUSSION

The perovskite series YCo$_{1-x}$Fe$_x$O$_3$ (x = 0, 0.5 and 1) was synthesized by solution combustion method with citric acid as a fuel. The compounds were identified and characterized by powder XRD. They are isomorphous and crystallize in *Pnma* space group with Z = 4 (Fig. 1).
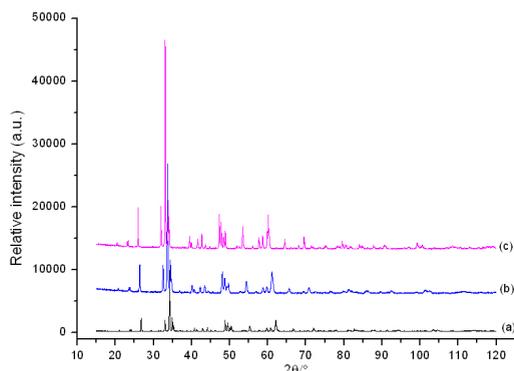
Fig.1. The powder XRD patterns of: (a) YCoO$_3$, (b) YCo$_{0.5}$Fe$_{0.5}$O$_3$ and (c) YFeO$_3$.

The lattice cell parameters calculated by Rietveld refinement are given in Table 1.

Table 1. The lattice cell parameters of YCo$_{1-x}$Fe$_x$O$_3$ (x = 0, 0.5 and 1)

	YCoO$_3$	YCo$_{0.5}$Fe$_{0.5}$O$_3$	YFeO$_3$
a/Å	5.42156(12)	5.5087(2)	5.59245(7)
b/Å	7.36536(16)	7.4807(3)	7.60387(10)
c/Å	5.13809(11)	5.2133(2)	5.28056(7)

The electrochemical behaviour of these perovskites was investigated by cyclic voltammetry by means of a specially designed paraffin impregnated graphite electrode (PIGE) [23]. The electrode was modified by deposition of the microcrystals of the investigated perovskites on its surface by abrasion.

Firstly, the electrochemical behaviour of such modified electrode was investigated in 0.1 M KOH solutions (Fig. 2).
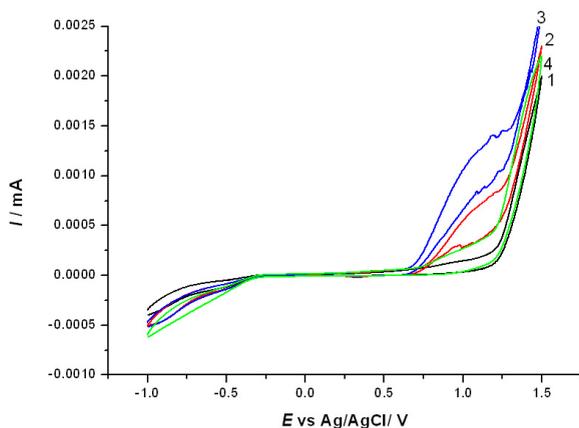
Fig. 2. The voltammograms of modified electrodes in contact with 0.1 M solution of KOH. 1- blanc electrode; 2 - $YFeO_3$; 3 - $YFe_{0.5}Co_{0.5}O_3$ and 4 - $YCoO_3$.

As can be seen from the figure, in the voltammograms of the studied perovskites in solutions of 0.1 M KOH, a significant enlargement of the anodic current commencing at potential of about 0.7 V can be noticed. The catalytic effect of the deposited perovskite microcrystals on the electrode is manifested as a shift of the anodic tail in the voltammograms towards less positive potentials. The most pronounced catalytic activity towards oxidation of OH^- ions exhibits $YFe_{0.5}Co_{0.5}O_3$. In the cathodic part of the cyclic voltammograms, within the potential region from – 0.3 to –1.0 V, a voltammetric pattern typical for two-step reduction process appears, the intensity of which increases in proportion to the catalytic effect of the studied perovskites.

The overall voltammetric response can be assigned as a catalytic oxygen evolution reaction (OER) (anodic part of the voltammograms), accompanied with a two-step reduction (cathodic part of the voltammograms) of electrochemically formed oxygen. However, the voltammograms consist of several peaks indicating a complex electrochemical process which takes place in several steps. One of the proposed mechanisms of oxygen evolution reaction on perovskite surface was proposed by Bockris and Otagawa [24]. It is based on interaction of the transition metal in the perovskite structure with the OH^- ions resulting with hydrogen peroxide formation, which is physisorbed on the perovskite surface.

The physisorbed H$_2$O$_2$ undergoes further catalytic decomposition with O$_2$ evolution. The overall process can be represented [24] with the electrode reactions (1-2), followed by the chemical reactions (3-4):

$$M^z + OH^- \longrightarrow M^z{-}OH + e^- \qquad (1)$$

$$M^z{-}OH + OH^- \longrightarrow M^z{\cdots}H_2O_2 + e^- \qquad (2)$$

$$(H_2O_2)_{phys} + OH^- \longrightarrow (HO_2^-) + H_2O \qquad (3)$$

$$(H_2O_2)_{phys} + (HO_2^-)_{phys} \longrightarrow H_2O + OH^- + O_2{\uparrow} \qquad (4)$$
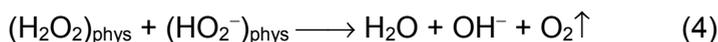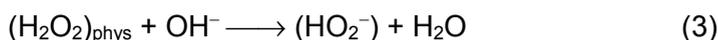
Interestingly, similar voltammetric pattern, considering both anodic and cathodic parts of the cyclic voltammograms, was observed with perovskites modified PIGE in contact with phosphate buffer (pH = 7.35) (Fig. 3.). Though the concentration of hydroxide ions is very low in the phosphate buffer, the catalytic effect of perovskites is clearly visible in the anodic part of the voltammograms. Accordingly, the onset of the anodic current is associated with potentials close to 1.0 V, being significantly more positive compared to voltammograms recorded in 0.1 M KOH (cf. Fig. 2.), reflecting both concentration and activation overpotential required for proceeding of the electrode reaction. In accordance with the results presented in Fig. 3, the most pronounced catalytic activity was observed for YCoO$_3$, implying similar mechanism of the catalytic activity. Though, one can speculate that in phosphate buffer solution the initiate reactant of the oxidation process is water itself producing in the first step OH$^-$ ions which further react according to reaction scheme (1-4).
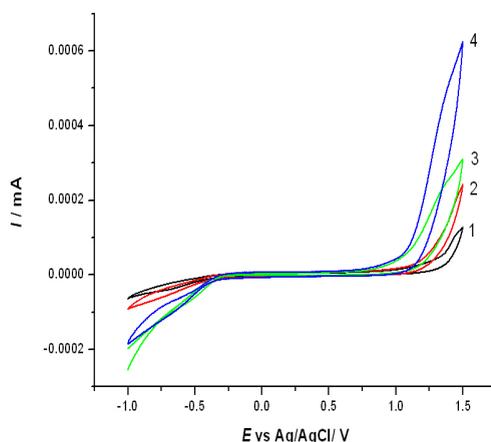
Fig. 3. The voltammograms of modified electrodes in contact with phosphate buffer solution. 1-blank electrode; 2-YFeO$_3$; 3-YCo$_{0.5}$Fe$_{0.5}$O$_3$ and 4-YCoO$_3$.

In aim to support the electrocatalytic mechanism proceeding via H_2O_2 formation, H_2O_2 was gradually added to the phosphate buffer solution over the concentration interval from 10^{-3} to 10^{-1} M. Cyclic voltammograms for each of the perovskite modified PIGE electrodes were recorded in the potential range from -1 V to 1.5 V (Fig. 4). The voltammograms recorded at low concentration of H_2O_2 almost overlap the volammogram of the blank electrode. But, obviously, by increasing the H_2O_2 concentration, the current increases and the oxidation e.g. the evolution of oxygen starts at less positive potentials for each of the perovskite modified PIGE electrode (Fig.4.). The onset of the anodic current recorded in H_2O_2 solutions is drastically shifted towards less positive potentials compared with potentials recorded in phosphate buffer (Fig. 3) and are very close to those recorded in 0.1 M KOH (Fig. 2). This could be considered as indirect support of the proposed mechanisms for oxidation of OH^- proceeding in steps (1-4).
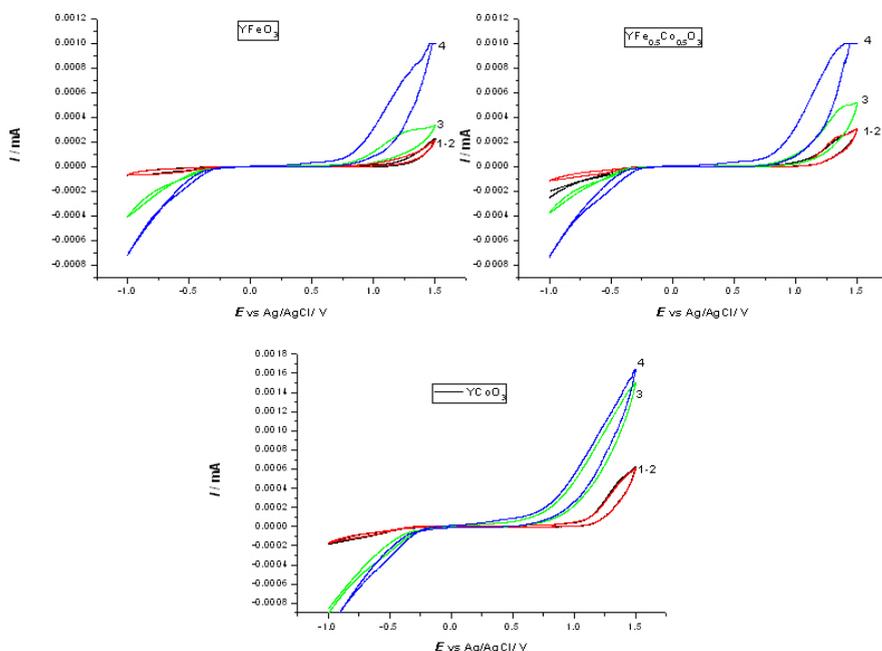
Fig. 4. The investigated compounds in: 1-phosphate buffer solution; 2-phosphate buffer + 10^{-3} M H_2O_2; 3-phosphate buffer + 10^{-2} M H_2O_2; 4-phosphate buffer + 10^{-1} M H_2O_2.

In the last part of our investigation, the electrocatalytic properties of the investigated perovskites were also analysed alkaline solution in the potential range of 0.0 to 0.8 V (Fig. 4.). The oxidation of methanol in alkaline solutions is

of special interest since it takes place in so-called direct methanol fuel cells. Therefore, as electrolyte in our investigation 1M CH$_3$OH in 1 M KOH solution was used. The recorded voltammograms of the blank (1) and of the YFeO$_3$ modified PIGE (2) are of the same shape indicating that YFeO$_3$ do not show any catalytic properties towards methanol oxidation. However, the voltamograms of PIGE modified with Co-containing perovskites clearly shows electrocatalytic effect. In these cases the onset anodic potential of the oxidation of methanol is shifted towards less positive potentials in comparison when it is performed with blank electrode and also the current is extensively increased. The best catalytic activity shows YCoO$_3$ indicating that the electrocatalyitic activity of YCo$_{1-x}$Fe$_x$O$_3$ (x = 0, 0.5 and 1) perovskites towards oxidation of methanol in alkaline solutions increases with increasing of the cobalt content in perovskite structure.
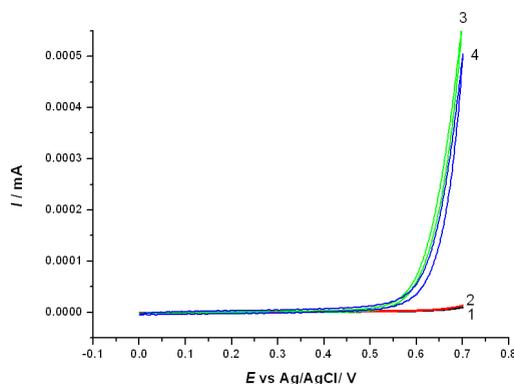
Fig. 4. The voltammograms of PIGE modified electrodes in contact with 1 M KOH + 1 M CH$_3$OH. 1-blank electrode; 2-YFeO$_3$; 3-YCo$_{0.5}$Fe$_{0.5}$O$_3$ and 4-YCoO$_3$.

CONCLUSIONS

YCo$_{1-x}$Fe$_x$O$_3$ (x = 0, 0.5 and 1) perovskites were synthesized by solution combustion method using citric acid as a fuel. The identification and characterization was performed by powder XRD. The compounds are isomorphous and crystallize in orthorhombic *Pnma* unit cell with Z = 4.

The electrocatalytic properties of the obtained perovskites were studied by cyclic voltammetry by means of perovskite modified PIGE electrode. It was found that these perovskites catalyze the oxidation of OH$^-$ ions. It was supposed that the oxygen evolution process proceeds through H$_2$O$_2$ formation. The indirect support for this assumption was obtained from the voltammograms recorded when perovskite modified PIGE was in contact with phosphate

buffer in which H_2O_2 was gradually added to the solution over the concentration interval from 10^{-3} to 10^{-1} M. The shift of the oxidation current towards less positive potentials with increasing of the H_2O_2 concentration confirms this assumption.

The perovskites modified PIGE electrodes were also investigated for their catalytic properties towards oxidation of methanol in alkaline solutions. A prominent electrocatalytic activity for this reaction was found for the Co-containng perovskites. The catalytic activity increases with increasing of the cobalt content.

EXPERIMENTAL SECTION

The perovskite series $YCo_{1-x}Fe_xO_3$ ($x = 1$, 0.5 and 1) was synthesized by solution combustion method using citric acid as a fuel. The quantity of the fuel was calculated using the oxidizer/fuel ratio which was set to 1. The citric acid was dissolved in small quantity of water and was slowly added to the solution containing the constituent metal nitrates. The pH of the reaction mixture was adjusted to 7 with addition of NH_4OH. The as-prepared solutions were heated on magnetic stirrer at temperature of 80 °C and after evaporation of the water almost to dryness the beakers were transferred on a hot plate preheated at ~350 °C. The vigorous reaction took place evolving large amount of gases and resulting in formation of black spongy-like powder precursors. The precursors were additionally heated 4 hours at 800 °C, yielding perovskites. However, since all synthesized complex perovskites using citric acid contained small amount of Y_2O_3, they were washed with diluted HCl ($c = 1$ M). After washing and filtration, the samples were dried and additionally heated for 6 h at 950 °C.

The identification of the obtained perovskites was performed by powder X-ray diffraction. The XRD patterns were recorded at room tem-perature on *Bruker D8 Advance* with CuKα radiation and SolX detector within the range 10–120 ° 2θ with step-scanning of 0.02°.

The electrocatalytic properties of $YCo_{1-x}Fe_xO_3$ perovskites were investigated by cyclic voltammetry on μAUTOLAB, model III instrument. The electrochemical cell consisted of three electrodes: PIGE as a working electrode, Ag/AgCl (sat. KCl) as reference electrode, and a platinum wire as auxiliary electrode. The microcrystals of the investigated perovskites were deposited on the surface of PIGE. The electrochemical activity was investigated at room temperature, in 0.1 M of KOH; 1M CH_3OH + 1 M KOH; phosphate buffer (pH = 7.35) and buffer in which H_2O_2 ($10^{-1} - 10^{-3}$ M) was added.

ACKNOWLEDGMENTS

REFERENCES

1. R.H. Mitchell, "Perovskites: Modern and Ancient", Almaz press – Thunder Bay, **2002**.
2. M.A. Peña, J.L.G. Fierro, *Chemical Reviews*, **2001**, *101,* 1981.
3. S. Yakovleva, L.A. Isupova, V.A. Rogov, V.A. Sadykov, *Kinetics and Catalysis,* **2008**, *49,* 261.
4. C.N.R. Rao, *Annual Review of Physical Chemistry*, **1989**, *40,* 291.
5. S. Bhalla, R. Guo, and R. Roy, *Material Research Innovations,* **2000**, *4,* 3.
6. T. Ishihara, "Perovskite Oxide for Solid Oxide Fuel Cells", Springer, Dordrecht, **2009**.
7. A. Orera, P.R. Slater, *Chemistry of Materials,* **2010**, *22,* 675.
8. A. Dutta, T. Ishihara, *Chemistry of Materials,* **2004**, *16,* 5198.
9. Y. Wang, X. Yanhong, L. Liqiang, D. Yaing, L. Xiaojuan, H. Anquan, *Sensors and Actuators B: Chemical,* **2010**, *151,* 65.
10. 11. D. Ye, Y. Xu, L. Luo, Y. Ding, Y. Wang, X. Liu, L. Xing, J. Pen, *Colloids and Surfaces B: Biointerfaces,* **2012**, *89,* 10.
11. Y. Wang, H. Zhong, X. Li, F. Jia, Y. Shi, W. Zhang, Z. Cheng, L. Zhang, J. Wang, *Biosensors and Bioelectronics*, **2013**, *48,* 56.
12. G.L. Luque, N.F. Ferreyra, A.G. Leyva, G.A. Rivas, *Sensors and Actuators B: Chemical,* **2009**, *142,* 331.
13. G. Wang, Y. Bao, Y. Tian, J. Xia, D. Cao, *Journal of Power Sources,* **2010**, *195,* 6463.
14. Y. Xu, Yanhong, X. Zhang, D. Chen, J. Hou, C. Li, X. Zhu, *Current Nanoscience,* **2013**, *9,* 737.
15. L.F. Liotta, F. Puleo, V. La Parola, S.G. Leonardi, N. Donato, D. Aloisio and G. Neri, *Electroanalysis,* **2015**, *27,* 684.
16. S. Dimitrovska-Lazova, D. Kovacheva, S. Aleksovska, M. Marinšek, P. Tzvetkov, *Bulgarian Chemical Communications*, **2012,** *44,* 235.
17. S. Dimitrovska-Lazova, D. Kovacheva, P. Tzvetkov, *Bulgarian Chemical Communications*, **2012**, *44,* 245.

18. M. Pecovska Gjorgjevich, S. Aleksovska, Marjan Marinšek and Sandra Dimitrovska-Lazova, *Journal of the American Ceramic Society*, **2014**, *97(12),* 3864.
19. M. Pecovska Gjorgjevich, S. Aleksovska, S. Dimitrovska-Lazova, *Physica Macedonica,* **2012**, *61*, 21.
20. S. Dimitrovska-Lazova, V. Mirčeski, D. Kovacheva, S. Aleksovska, *Journal of Solid State Electrochemistry*, **2012**, *16*, 219.
21. S. Dimitrovska-Lazova, S. Aleksovska and P. Tzvetkov, *Journal of Chemical Sciences,* (accepted for publication).
22. S. Dimitrovska-Lazova, S. Aleksovska and P. Tzvetkov, V. Mirčeski, D. Kovacheva, *Bulgarian Chemical Communications*, **2015**, *47(1),* 245.
23. F. Scholz, U. Schröder, R. Gulaboski, "Electrochemistry of immobilized particles and droplets", Springer, Berlin, **2005**.
24. J. O′M. Bockris, T. Otagawa, *Journal of Physical Chemistry*, **1983**, *87*, 2960.

Dedicated to prof. dr. I. C. Popescu
on the occasion of his 70th anniversary

EFFECT OF AMINES AS PROTON VECTORS ON CATALYTIC HYDROGEN EVOLUTION REACTION ON COPPER

ÁGNES JAKAB[a], NICOLAE VASZILCSIN[a*], FLORICA MANEA[a], MIRCEA DAN[a]

ABSTRACT. In this study, the catalytic effect of several organic amines on hydrogen evolution reaction (HER) was studied on copper. Kinetic parameters of electrode process were determined from Tafel polarization curves in order to obtain more information about the catalytic effect of the organic amines. The best electrocatalytic effect was reached in 0.5 M H_2SO_4 solution for N,N-dimethylaniline (DMA). A correlation between molecular parameters and electrocatalytic effect of amines have been performed. A larger dipole moment determined for N,N-dimethylanilinium (DMAH$^+$) showed that the orientation of these molecules are more favorable ordered on the electrode surface. Also, electrochemical impedance spectroscopy (EIS) technique was used to assess quantitatively the DMA effect over the electrochemical parameters for HER on copper. A significant enhancement of charge transfer rate was noticed with DMA concentration and temperature increasing. In addition, the adsorption behavior of DMA on copper surface followed the Langmuir adsorption isotherm. The low negative values of the standard Gibbs free energy of adsorption ΔG_{ads} at different temperature suggested a physical sorption. The value of the activation energy determined for 10^{-3} M DMA was 37% lower than that determined in its absence. A direct involving of DMA in HER mechanism on the copper as proton carrier from bulk to the solution/ metal interface was found.

Keywords: *proton carrier, electrocatalytic effect, hydrogen evolution reaction, Tafel plots, EIS*

---

[a] *Politehnica University of Timisoara, Faculty of Industrial Chemistry and Environmental Engineering, V. Pârvan. No. 6, 300223 Timisoara, Romania.*
[*] *Corresponding author: nicolae.vaszilcsin@upt.ro*

INTRODUCTION

It is well known that hydrogen can play an important role as energy carrier in the possible scenario for the future, with socio-economic benefits and positive environmental impact [1,2]. Hydrogen can be produced by a large number of processes, *i.e.*, thermochemical [3-5], electrochemical [4-9], photochemical [10-13], photocatalytic [14,15] and photo-electrochemical [16-18], having as a primary energy source a wide range of resources.

Among the above-mentioned processes, the electrochemical procedure based on the water electrolysis exhibits many advantages, such as: high purity, simple process, environmental friendliness and plenty of sources. However, the researchers are continuously motivated to find solutions for two major problems during electrolysis, related to the high energy consumption and the low gas evolution. To overcome these problems, most of research studies are focused on new electrode materials and strategies for improving the production process efficiency involving also, new electrolytic system [19].

Currently, cathodes based on platinum metals offer the best performance for catalytic enhancement of the hydrogen evolution reaction (HER). From an economic point of view, use of Pt-type catalysts present an obstacle to hydrogen energy economy, due to their high cost and low-abundance. For this reason, it is crucial to develop inexpensive advanced HER catalyst materials characterized by high activity and stability. Recent studies have been reported the high catalytic effect of molybdenum sulfide based catalysts for HER [20-26]. In few reports, researchers used carbon fibers as HER electrode materials modified with Pt nanoparticle/MoS_2 nanosheets characterized by low loading of Pt and thus, a higher electrocatalytic activity was obtained [27]. Metal alloys [28] and transition metal carbides (WC, Mo_2C, TaC, NbC) [29] have also used as potential electrocatalysts for HER. *In-situ* adding catalytic compounds into electrolyte to enhance gas evolution reaction was less approached, although it is promising due to the low cost and the simple operation. Kaninski et al. [30] added in electrolyte the mixture of Na-molybdate and tris(ethylenediamine) Co(III)chloride as ionic activator to catalyze HER. In this case, energy saving was about 10% in comparison with blank electrolyte solution.

Another very promising way to enhance HER on different metal electrodes is the addition of organic amines as proton vectors in electrolyte, which facilitate the transport of protons from bulk solution to the interface. In recent papers, the catalytic effect of various organic amines, *i.e.*, benzylamine, m-toluidine, aniline, 4-chloroaniline and methylamine towards HER was studied on different metal electrodes. The performed studies showed that the protonated form of amines act as proton carriers, accelerating the hydrogen evolution reaction [31-34].

The aim of this study was to investigate the catalytic effect of aniline (A), N,N-diethylaniline (DEA), N-ethyilaniline (EA), N-methylaniline (MA), N,N-dimethylaniline (DMA), o-toluidine (oTO), m-toluidine (mTO) and p-toluidine (pTO) over HER on copper electrode in 0.5 M H_2SO_4 at different temperatures using Tafel polarization curves and electrochemical impedance spectroscopy (EIS) technique. Experiments were carried out at higher current densities, similar with those applied in commercial water electrolysers, in contrast with results reported by Vaduva et al [33,34]. The adsorption features of amines on the cathode surface were studied based on Langmuir isotherm model.

RESULTS AND DISCUSSION

Based on previous studies regarding catalytic effect of amines on the hydrogen evolution reaction at copper [34], several organic amines with aromatic substituents have been investigated as catalysts in 0.5 M H_2SO_4 solution at copper electrode. Linear voltammetry curves were recorded from -0.5 to -1 V *vs.* Ag/AgCl on copper at 10 mVs^{-1}. Figure 1 presents the polarization curves for HER on copper in 0.5 M H_2SO_4 solution in the absence and the presence of various organic amines, *i.e.*, aniline (A), N,N-diethylaniline (DEA), N-ethylaniline (EA), N-methylaniline (MA), N,N-dimethylaniline (DMA), o-toluidine (oTO), m-toluidine (mTO) and p-toluidine (pTO).
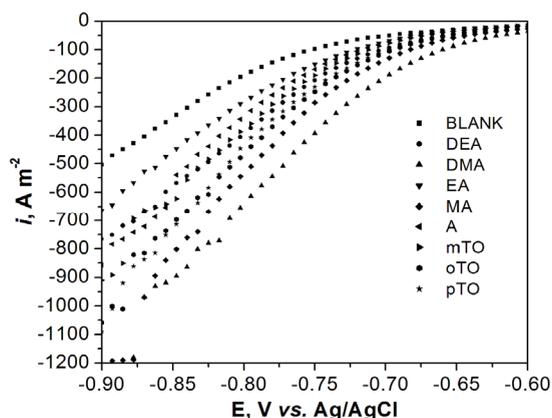
Figure 1. Linear voltammograms recorded on copper electrode in 0.5 M H_2SO_4 solution at 298 K; concentration of amines: 10^{-3} M, scan rate: 10 mVs^{-1}.

The above-presented linear polarization curves show that the current density increased in the presence of amines. The most significant electrocatalytic effect is observed in the presence of N,N-dimethylaniline (DMA) in relation to shifting the hydrogen evolution overpotential to less

negative potential value. Thus, in the presence of 10^{-3} M DMA in 0.5 M H_2SO_4 solution at 298 K, the current density of 500 $A \cdot m^{-2}$ is reached at -0.75 V *vs.* Ag/AgCl in comparison with -0.9 V *vs.* Ag/AgCl for blank solution. In order to obtain more information about the catalytic effect of organic amines, kinetic parameters, *e.g.*, Tafel slope (*b*), exchange current density (*i_o*) and cathodic transfer coefficient (*1-α*), were determined from Tafel polarization curves. Two important parameters i_o and *b* obtained by fitting the linear relationship between log(*i*) and *η*, are the criterions for the assessment of the catalytic activity of the catalysts. The higher exchange current and the smaller Tafel slope informed about the better catalytic performance of the catalyst. The obtained experimental results are gathered in Table 1, and it can be noticed that the best electrocatalytic effect was reached for DMA (i_o=0.181 $A \cdot m^{-2}$, *b*=-138 $mV \cdot dec^{-1}$) and DEA (i_o=0.180 $A \cdot m^{-2}$, *b*=-159 $mV \cdot dec^{-1}$).

Table 1. Kinetic parameters for HER in 0.5 M H_2SO_4 solution in the presence of different organic amines at 298 K and electronic characteristics of protonated amines.

Amine, 10^3 [M]	-*b* [$mV \cdot dec^{-1}$]	1-*α*	i_o [$A \cdot m^{-2}$]	Molecular coverage [$Å^2$] [35]	Dipole moment [D] [35]	LUMO [eV] [35]	HOMO [eV] [35]
DEAH+	159	0.37	0.180	71.5	3.25	-0.009	-0.483
DMAH+	138	0.43	0.181	58.5	5.30	-0.017	-0.489
EAH+	149	0.39	0.084	51.1	4.85	-0.020	-0.489
MAH+	143	0.41	0.117	45.0	6.32	-0.025	-0.493
AH+	149	0.39	0.095	39.4	7.46	-0.032	-0.500
mTOH+	138	0.43	0.054	44.4	8.32	-0.024	-0.483
oTOH+	136	0.43	0.068	40.2	6.92	-0.027	-0.485
pTOH+	142	0.41	0.090	40.5	8.85	-0.027	-0.488

It is well-known that the catalytic effect of the amines largely depends on their molecular characteristics [33]. The catalytic activity of the amine is due to a free electron pair present on the nitrogen atom and is dependent upon the availability of this electron pair for complexation [36]. Energy level of HOMO characterizes the ability of chemical entities to interact as electron donor, while energy level of LUMO is a descriptor of the electron acceptor properties [37]. Hence, DEAH+ and DMAH+ molecules with the lowest LUMO energy values (-0.009 eV, respectively -0.017 eV) are more able to accept electron than other molecules with higher LUMO energy values. This descriptor can be used to characterize adsorption properties of protonated amines. Despite the fact that DEAH+ is characterized by LUMO energy value lower than that of DMAH+, a modest catalytic effect was observed for DEA in comparison with DMA. This fact can be explained by the largest groups on the nitrogen atom that should increase steric hindrance and thus, for DEAH+ it is difficult to remove the proton that is masked by ethyl groups. As a consequence, methyl groups tend to

push electrons toward the nitrogen increasing the accessibility of the free electron pair, while ethyl groups tend to withdraw electrons, diminishing accessibility, thus reducing catalytic activity. Furthermore, the coverage area of DMAH+ (58.5 $Å^2$) is smaller than that of DEAH+ (71.5 $Å^2$), which allows the adsorption of a higher number of DMA molecules on the cathode surface. Under these conditions, a local concentration of hydronium ion at the electrode/solution interface is higher and as consequence, a higher exchange current density [32]. On the other hand, a larger dipole moment for DMAH+ (5.30 D) means that the orientation of these dipoles on the electrode surface are more ordered than of DEAH+ dipoles. This is another reason why a larger number of DMAH+ molecules will be able to adsorb on the electrode surface, favoring exchange current density increasing.

Based on above-presented results, DMA was selected for further experiments as catalyst for HER in 0.5 M H_2SO_4 solution. The critical operating parameters in the kinetics of HER are the temperature and the concentration of amine catalyst. Cathodic polarization experiments were performed at 298, 308, 318, 328 K, using different concentrations of DMA (10^{-6}, 10^{-5}, 10^{-4}, 10^{-3} M). Figure 2 shows as examples Tafel plots for the HER on copper electrode in absence and presence of DMA at different temperatures.
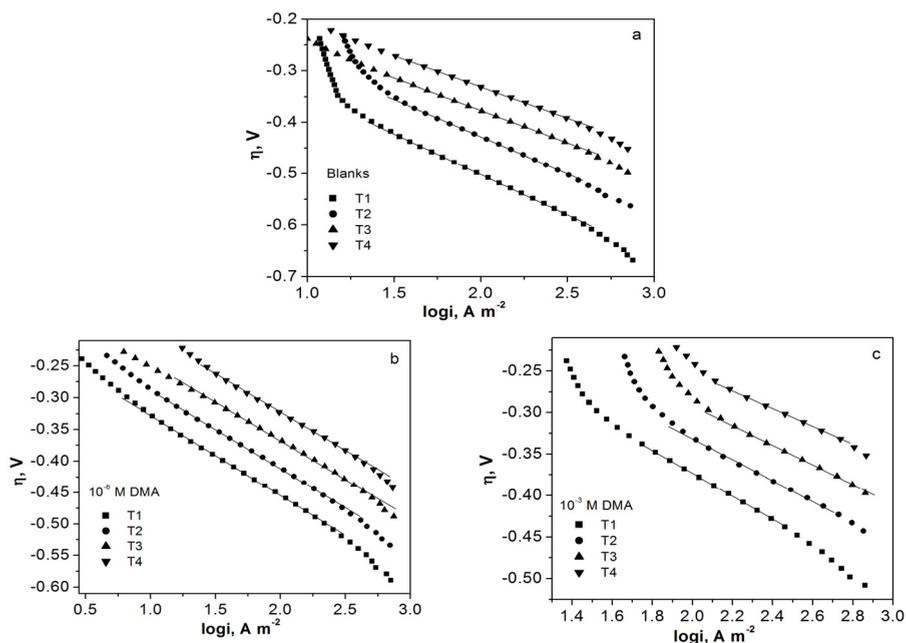
Figure 2. Tafel plots for HER on copper electrode in blank 0.5 M H_2SO_4 solution (a) and in the presence of different concentrations of DMA: 10^{-6} M (b), 10^{-3} M (c); at different temperatures: T_1 = 298 K; T_2 = 308 K; T_3 = 318 K; T_4 = 328 K.

Based on Tafel plots, the kinetic parameters for the HER at different temperatures and concentrations of DMA were determined and summarized in Table 2.

It can be noticed, that in the presence of different concentrations of DMA a larger electrocatalytic activity was obtained than in its absence, according to the comparison of the exchange current density i_o. For example, the addition of 10^{-3} M DMA leads to increasing the exchange current density of about 12 times as compared to the blank solution at 298 K. In addition, the Tafel slope obtained for all studied cases was about -120 mV·dec^{-1} approaching to the theoretical value of -118 mV·dec^{-1}, showing that the HER in the absence and presence of DMA proceeded based on a Volmer-Heyrovsky mechanism. According to Flecher [38], this fact indicate that the formation of (H·)$_{ads}$ is slow and the destruction of (H·)$_{ads}$ is fast.

Table 2. Kinetic parameters for HER on copper electrode in the absence and presence of DMA at different temperatures

C_{DMA} [M]	T [K]	$-b$ [mV dec^{-1}]	$1-\alpha$	i_o [A·m^{-2}]
0	298	132	0.45	0.015
	308	128	0.48	0.037
	318	126	0.50	0.103
	328	121	0.54	0.194
10^{-6}	298	126	0.47	0.024
	308	124	0.49	0.045
	318	122	0.52	0.094
	328	120	0.54	0.214
10^{-5}	298	126	0.47	0.039
	308	121	0.50	0.054
	318	115	0.55	0.102
	328	115	0.57	0.222
10^{-4}	298	135	0.44	0.109
	308	132	0.46	0.191
	318	119	0.53	0.220
	328	116	0.56	0.378
10^{-3}	298	138	0.43	0.181
	308	126	0.48	0.232
	318	118	0.53	0.347
	328	107	0.61	0.461

Also, the apparent activation energies for HER charge transfer process were calculated from the slope of the linear dependence $\lg i_o = f(T^{-1})$ according to Eq.(1) [33]:

$$E_a = -2.303 R \frac{\partial(\lg i_0)}{\partial(T^{-1})} \tag{1}$$

Figure 3 shows the Arrhenius plots in the absence and presence of DMA at different temperatures. The values of the activation energy obtained based on Figure 3 were 69.14 kJ·mol^{-1} in the absence of DMA, 58.83 kJ·mol^{-1} for 10^{-6} M DMA, 46.01 kJ·mol^{-1} for 10^{-5} M DMA, 30.89 kJ·mol^{-1} for 10^{-4} M DMA and respective, 25.6 kJ·mol^{-1} for 10^{-3} M DMA. It is obviously that the charge transfer rate is favored by increasing DMA concentration due to the activation energy decreased at higher DMA concentration. This aspect informed that even if DMA adsorption on the cathode surface is a prerequisite conditions to enhance HER, removing of adsorbed DMA from the cathode surface did not require an extra energy, which indicates a weak adsorption effect.
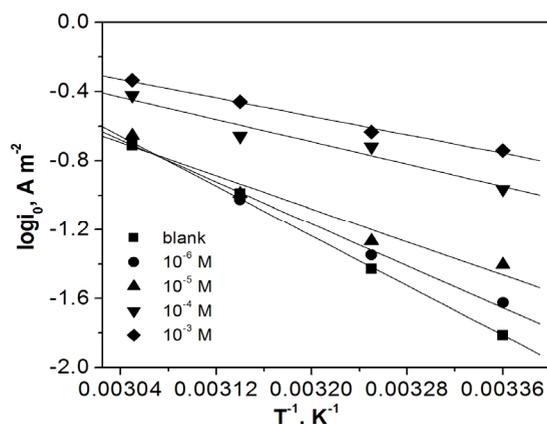
Figure 3. Arrhenius plots for HER in 0.5 M H$_2$SO$_4$ and in the presence of different concentrations of DMA.

DMA action on HER kinetics is rather complex, since the catalytic activity depends not only on concentration, temperature and molecular properties, but also on the surface coverage degree related to amine adsorption on the electrode-electrolyte interface [34]. Organic amines are very slightly soluble in water, protonation of these amine molecules potentially increase solubility and ion balance in water is given by Eq.(2):

$$C_6H_5\text{-}NH^+(CH_3)_2 + H_2O \rightleftharpoons C_6H_5\text{-}N(CH_3)_2 + H_3O^+ \qquad (2)$$
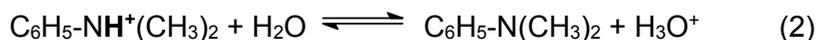
N,N-dimethylaniline is protonated in sulphuric acid forming aryl-ammonium ions [34], which are preferentially oriented with the ammonium group to the metal surface and the catalytic effect is due to their strong adsorption.

In order to assess quantitatively the electrochemical parameters for HER, electrochemical impedance spectroscopy (EIS) technique was used as a very useful tool. Based on polarization curve results, EIS spectra were recorded on copper electrode at the overpotential of -0.4 V *vs.* Ag/AgCl in 0.5 M

H_2SO_4 supporting electrolyte without and respective, with various concentrations of DMA and different temperatures ranged between 298 and 328 K. As example, in Figure 4 are shown EIS results expressed as Nyquist and Bode plots determined for the temperature of 308 K and various DMA concentrations.
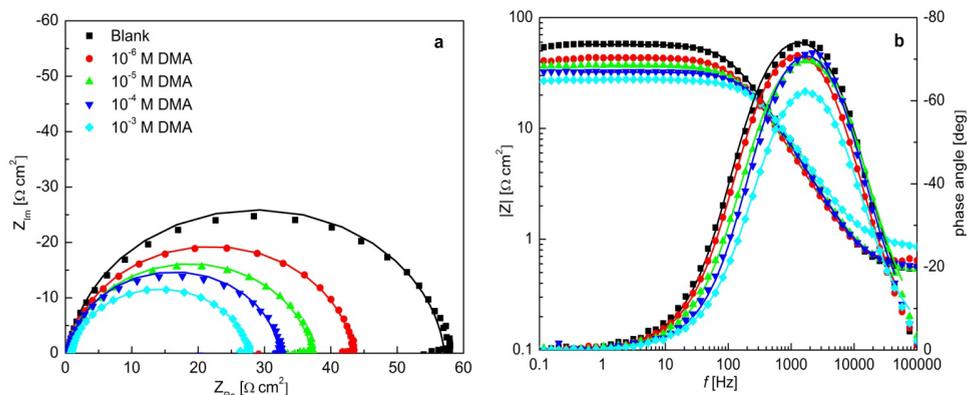
Figure 4. Experimental Nyquist (a) and Bode (b) plots at overpotential of -0.4 V and T = 308 K for HER on copper in 0.5 M H_2SO_4 with different concentrations of DMA. Symbols are experimental points and continuous line are simulated by the CNLS fitting according to the electrical equivalent circuit.

Nyquist spectra showed a slightly supressed semicircle that indicates about an electron transfer limiting process, which is assessed by charge transfer resistance (R_{ct}). It is obviously that increasing DMA concentration led to decreasing R_{ct} that can be easily evaluated as semicircle width. R_{ct} decreasing in the presence of DMA indicates the enhancement of the charge transfer process rate. From Bode spectrum, it can be noticed the existence of one time constant phase for both supporting electrolyte and DMA presence, which confirm that DMA presence did not change the HER mechanism. Also, the thermal effect is to accelerate the charge transfer process (see Table 3).

For a precise description of the HER process, the experimental impedance data were fitted to the electrical equivalent circuit (EEC) given in Figure 5, using a complex non-linear least squares (CNLS) procedure.
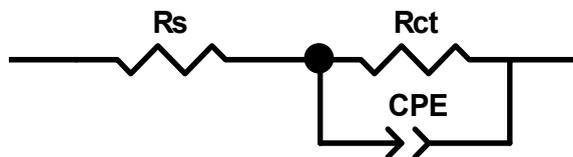
Figure 5. Equivalent electrical circuit for modelling the HER on copper electrode in acid medium.

The electrical equivalent circuit consists of a resistance R_s in series with a parallel connection of the charge transfer resistance R_{ct} and a constant phase element (CPE). The resistance R_s includes the uncompensated solution resistance. The ideal capacitor characterized by double layer capacity is usually replaced by a constant phase element (CPE) since it describes more accurately the behaviour of real electrochemical systems, the CPE impedance is described by the Eq.(3) [33]:

$$Z_{CPE} = 1/T(j\omega)^n \qquad (3)$$

where T is a parameter proportional with double layer capacity, n is an exponent ranged between 0 and 1, which describes *CPE* angle.

The results of the fitting are shown as continuous line in Figure 4 and the corresponding values of the circuit elements are given in Table 3.

Table 3. EEC parameter values for HER at overpotential of -0.4 V on copper in 0.5 M H_2SO_4 with different concentrations of DMA.

C [M]	T [K]	R_s [Ω cm^2]	$T \cdot 10^5$ [F cm^{-2} s^{n-1}]	n	R_{ct} [Ω cm^2]	$C_{dl} \cdot 10^5$ [F cm^2]	Chi^2
0	298	0.32	6.19	0.86	158	1.01	$2.0 \cdot 10^{-3}$
	308	0.53	3.70	0.91	56.6	1.27	$3.8 \cdot 10^{-3}$
	318	0.67	3.55	0.92	23.0	1.41	$1.0 \cdot 10^{-3}$
	328	0.99	3.84	0.92	12.8	1.60	$3.1 \cdot 10^{-4}$
10^{-6}	298	0.77	4.53	0.88	136	1.10	$2.5 \cdot 10^{-3}$
	308	0.59	4.21	0.92	42.8	1.67	$5.1 \cdot 10^{-4}$
	318	0.91	4.01	0.93	19.6	1.87	$9.1 \cdot 10^{-4}$
	328	0.91	4.38	0.92	8.57	1.83	$9.9 \cdot 10^{-4}$
10^{-5}	298	0.64	5.07	0.89	105	1.45	$2.6 \cdot 10^{-3}$
	308	0.52	4.56	0.92	36.6	1.83	$1.2 \cdot 10^{-3}$
	318	0.75	4.05	0.94	13.3	2.10	$4.4 \cdot 10^{-4}$
	328	0.46	3.91	0.95	6.08	2.21	$7.7 \cdot 10^{-4}$
10^{-4}	298	0.39	5.48	0.90	75.2	1.66	$3.2 \cdot 10^{-3}$
	308	0.57	3.69	0.95	31.6	2.15	$2.7 \cdot 10^{-3}$
	318	0.88	4.42	0.94	9.39	2.33	$8.8 \cdot 10^{-4}$
	328	0.74	3.93	0.96	4.91	2.61	$2.4 \cdot 10^{-3}$
0^{-3}	298	0.54	5.95	0.91	44.6	2.14	$2.9 \cdot 10^{-3}$
	308	0.88	4.46	0.94	26.8	2.34	$7.5 \cdot 10^{-4}$
	318	0.63	4.94	0.95	6.68	2.76	$2.2 \cdot 10^{-3}$
	328	0.67	4.25	0.97	3.45	3.09	$1.1 \cdot 10^{-3}$

Based on the results gathered in Table 3, it can be noticed the catalytic effect of DMA over hydrogen evolution process, which is confirmed by decreasing the value of charge transfer resistance with increasing the DMA concentration and the temperature. Also, increased values of double layer capacity indicated DMA adsorption on internal Helmholtz layer, which is favored by higher DMA concentration and temperature.

Therefore, the degree of surface coverage (θ) can be calculated from the charge transfer resistance as the following Eq.(4) [39]:

$$\theta = 1 - \frac{R_{ct}}{R_{ct}^*} \times 100 \qquad (4)$$

where R_{ct} is the charge transfer resistance for catalyzed solution and R_{ct}^* is the charge transfer resistance for blank solution. Basic information on the interaction between the surface of copper and amine can be determined from Langmuir adsorption isotherm.

The degree of surface coverage (θ) for different concentrations of the amine (C_{DMA}) has been evaluated. The data were tested graphically to determine a suitable adsorption isotherm. The straight line with linear correlation coefficient (R^2) is almost equal to 1.0, was obtained on plotting C_{DMA}/θ vs. C_{DMA} at all studied different temperatures as shown in Figure 6, suggesting that adsorption of the amine on the copper surface obeys the Langmuir adsorption isotherm. According to the Langmuir adsorption isotherm, the surface coverage is related to DMA concentration by Eq.(5) [40]:

$$\frac{C_{DMA}}{\theta} = \frac{1}{K_{ads}} + C_{DMA} \qquad (5)$$

where K_{ads} is the equilibrium constant.

The intercept allows the calculation of the equilibrium constant K_{ads} being related to the standard free energy adsorption (ΔG_{ads}) as shown in the following Eq.(6) [41]:

$$K_{ads} = \frac{1}{55.5} \exp\left(-\frac{\Delta G_{ads}^0}{RT} \right) \qquad (6)$$

where 55.5 is the concentration of water in solution expressed in mole.

The obtained linear regressions and correlation coefficients are given in Table 4.

Table 4. Thermodynamic parameters for the adsorption of DMA on copper in 0.5 M H_2SO_4 at different temperatures

T [K]	Linear regression	R^2	K_{ads} [M^{-1}]	$-\Delta G_{ads}$ [kJ·mol^{-1}]
298	y = 4.58 10^{-5}+1.09x	0.999	1.09	10.17
308	y = 9.80 10^{-5}+1.18x	0.999	1.18	10.71
318	y = 4.86 10^{-4}+1.34x	0.998	1.34	11.40
328	y = 3.08 10^{-4}+1.56x	0.999	1.56	12.17

The negative values of standard free energy obtained for different temperatures, indicate the spontaneous adsorption of DMA, due to the electrostatic interaction between the protonated molecules of amine and the charge metal surface (physical sorption).

In this case, the values of ΔG_{ads} less than -20 kJ·mol^{-1} are consistent with the physical adsorption. The values of ΔG_{ads} around -40 kJ·mol^{-1} or higher suggest a chemosorption.
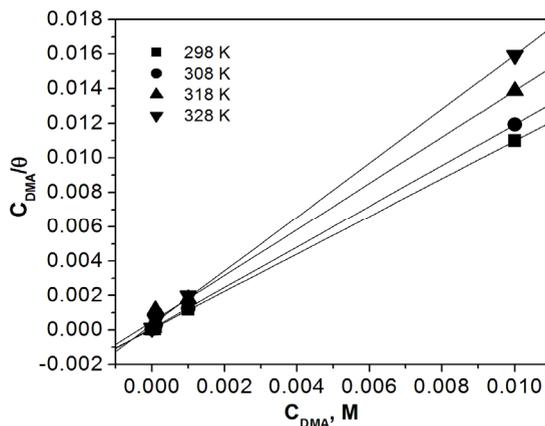
Figure 6. Langmuir's adsorption plots for DMA on the copper electrode surface in 0.5 M H_2SO_4 at different temperatures.

EIS results corroborated with polarization curve results proved direct involving of DMA in HER mechanism on the copper electrode as proton carrier from bulk to the solution/metal interface.

CONCLUSIONS

In this study, the catalytic effect of several organic amines on hydrogen evolution reaction (HER) was studied on copper electrode in 0.5 M H_2SO_4 at different temperatures. In order to obtain more information about catalytic effect of organic amines, kinetic parameters were determined from Tafel polarization curves, *e.g.*, Tafel slope (*b*), exchange current density (i_o). Based on these kinetic parameters, it was found that N,N-dimethylaniline (DMA) exhibited the best electrocatalytic effect.

The aspects regarding mechanism elucidation were discussed based on the molecular parameters of protonated amines. A larger dipole moment determined for N,N-dimethylanilinium (DMAH$^+$) showed that the orientation of these molecules are more favorable ordered on the electrode surface.

The value of the activation energy determined for 10^{-3} M DMA was 37% lower than that obtained in the absence of DMA. Also, electrochemical impedance spectroscopy (EIS) results showed a significant favorable effect of DMA concentration increasing on the rate of the charge transfer process for HER expressed by charge transfer resistance (R_{ct}). A great reducing of R_{ct} value was noticed with DMA concentration and temperature increasing.

A possible adsorption of DMA on internal Helmholtz layer of solution/electrode interface was found. In addition, the adsorption behavior of DMA on copper surface was studied by Langmuir adsorption isotherm model that fitted well the experimental data. The low negative values of the standard Gibbs free energy of adsorption at different temperature suggested a physical sorption of DMA on the copper electrode.

DMA acted as a proton carrier from bulk to the solution/metal interface and exhibited the catalytic activity towards the hydrogen evolution reaction.

EXPERIMENTAL SECTION

The chemicals used for this study *i.e.*, sulphuric acid (H_2SO_4), aniline ($C_6H_5NH_2$), N,N-diethylaniline (($C_2H_5)_2NC_6H_5$), N-ethylaniline ($C_6H_5NHC_2H_5$), N-methylaniline ($C_6H_5NHCH_3$), N,N-dimethylaniline ($C_8H_{11}N$), o-toluidine ($CH_3C_6H_4NH_2$), m-toluidine ($CH_3C_6H_4NH_2$) and p-toluidine ($CH_3C_6H_4NH_2$) (analytical grade) were purchased from Merck Company (Germany). The distilled water was used for all experiments. The experimental set-up consisted of a conventional three-electrode single-chamber glass cell and a PAR 2273 potentiostat/galvanostat equipped with PowerCV specific module for linear voltammetry. The potentiostat was connected with a platinum sieve counter electrode, Ag/AgCl reference electrode and a copper working electrode with 0.5 cm^2 surface area. All electrode potentials are reported with respect to Ag/AgCl. The working electrode surface was polished before each experiment with a soft abrasive paper and rinsed with distilled water. Luggin capillary was positioned very close to the electrode surface in order to avoid the ohmic drop through the electrolyte solution. Thermo Scientific DC 10 - thermostat was used to control the solution temperature in the range of 298-328 K (±0.1K). All solutions were deoxygenated thoroughly by purging with high purity nitrogen gas. Details of the calculation of the reversible potential E_{rev} (*vs.* the normal hydrogen electrode) for the HER in 0.5 M H_2SO_4 solution have been reported in our previous published paper [31].

EIS measurements were carried out using the FRA module of Biologic SP150, in the frequency range from 0.01 Hz to 100 kHz and AC voltage amplitude of 10 mV. For each spectrum 60 points were collected,

with a logarithmic distribution of 10 points per decade. The experimental electrochemical impedance data were fitted based on the electrical equivalent circuit by CNLS Levenberg – Marquardt procedure using ZView – Scribner Associates Inc. software.

ACKNOWLEDGMENTS

REFERENCES

1. I. Dincer, C. Acar, *International Journal of Hydrogen Energy*, **2014**, 1.
2. S. Sharma, S.K. Ghoshal, *Renewable Sustainable and Energy Reviews*, **2015**, *43*, 1151.
3. Y. Zhang, R. Wang, X. Lin, Z. Wang, J. Liu, J. Zhou, K. Cen, *Applied Catalysis B: Environmental*, **2015**, *166–167*, 413.
4. T. Kawada, H. Yamashita, Q. Zheng, M. Machida, *International Journal of Hydrogen Energy*, **2014**, *39*(35), 20646.
5. A.C. Tizzoni, N. Corsaro, C. D'Ottavi, S. Licoccia, S. Sau, P. Tarquini, *International Journal of Hydrogen Energy,* **2015**, *40*(11), 4065.
6. J.A. Allen, G. Rowe, J.T. Hinkley, S.W. Donne, *International Journal of Hydrogen Energy,* **2014**, *39*(22), 11376.
7. B. Pierozynski, *International Journal of Electrochemical Science*, **2011**, *6*, 63.
8. F. Safizadeh, E. Ghali, G. Houlachi, *International Journal of Hydrogen Energy,* **2015**, *40*, 256.
9. A. Survila, S. Kanapeckaite, J. Pileckiene, J. Budiene, *International Journal of Electrochem*istry, **2011**, 9.
10. A.A. Ismail, D.W. Bahnemann, *Solar Energy Materials and Solar Cells*, **2014**, *128*, 85.
11. C. Zamfirescu, I. Dincer, G.F. Naterer, *International Journal of Hydrogen Energy,* **2012**, *37*(12), 9537.
12. W. Yao, X. Song, C. Huang, Q. Xu, Q. Wu, *Catalysis Today*, **2013**, *199*, 42.
13. Z. Wang, R.R. Roberts, G.F. Naterer, K.S. Gabriel, *International Journal of Hydrogen Energy,* **2012**, *37*(21), 16287.
14. D. Praveen Kumar, N. Lakshmana Reddy, M. Mamatha Kumari, B. Srinivas, V. Durga Kumari, B. Sreedhar, V. Roddatis, O. Bondarchuk, M. Karthik, B. Neppolian, M.V. Shankar, *Solar Energy Materials and Solar Cells*, **2015**, *136*, 157.
15. W. Zhang, S. Wang, J. Li, X. Yang, *Catalysis Communications*, **2015**, *59*, 189.

16. J. Ji, L. Guo, Q. Li, F. Wang, Z. Li, J. Liu, Y. Jia, *International Journal of Hydrogen Energy,* **2015**, *40*(10), 3813.
17. T. Zhu, M.N. Chong, *Nano Energy*, **2015**, *12*, 347.
18. D. Sharma, A. Verma, V.R. Satsangi, R. Shrivastav, S. Dass, *International Journal of Hydrogen Energy*, **2014**, *39*(9), 4189.
19. M. Wang, Z. Wang, X. Gong, Z. Guo, *Renewable and Sustainable Energy Re*views, **2014**, *29*, 573.
20. D. Wang, Z. Pan, Z. Wu, Z. Wang, Z. Liu, *Journal of Power Sources*, **2014**, *264*, 229.
21. S.S.J. Aravind, M. Costa, V. Pereira, A. Mugweru, K. Ramanujachary, T.D. Vaden, *International Journal of Hydrogen Energy*, **2014**, *39*(22), 11528.
22. J. Ji, L. Guo, Q. Li, F. Wang, Z. Li, J. Liu, Y. Jia, *International Journal of Hydrogen Energy*, **2015**, *40*(10), 3813.
23. D. Wang, Z. Wang, C. Wang, P. Zhou, Z. Wu, Z. Liu, *Electrochemistry Communications*, **2013**, *34*, 219.
24. B.B. Li, S.Z. Qiao, X.R. Zheng, X.J. Yang, Z.D. Cui, S.L. Zhu, Z.Y. Li, Y.Q. Liang, *Journal of Power Sources*, **2015**, *284*, 68.
25. X. Xia, Z. Zheng, Y. Zhang, X. Zhao, C. Wang, *International Journal of Hydrogen Energy*, **2014**, *39*(18), 9638.
26. A.W. Jeremiasse, J. Bergsma, J.M. Kleijn, M. Saakes, C.J.N. Buisman, M.C. Stuart, H.V.M. Hamelers, *International Journal of Hydrogen Energy*, **2011**, *36*(17), 10482.
27. D. Hou, W. Zhou, X. Liu, K. Zhou, J. Xie, G. Li, S. Chen, *Electrochimica Acta*, **2015**, *166*, 26.
28. A.W. Jeremiasse, J. Bergsma, J.M. Kleijn, M. Saakes, C.J.N. Buisman, M.C. Stuart, H.V.M. Hamelers, *International Journal of Hydrogen Energy,* **2011**, *36*(17), 10482.
29. S. Meyer, A.V. Nikiforov, I.M. Petrushina, K. Köhler, E. Christensen, J.O. Jensen, N.J. Bjerrum, *International Journal of Hydrogen Energy*, **2015**, *40*(7), 2905.
30. M.P.M. Kaninski, V.M. Nikolic, T.N. Potkonjak, B.R. Simonovic, N.I. Potkonjak, *Applied Catalysis A: General*, **2007**, *321*, 93.
31. R. Cretu, A. Kellenberger, N. Vaszilcsin, *International Journal of Hydrogen Energy,* **2013**, *38*, 11685.
32. R. Cretu, A. Kellenberger, M. Medeleanu, N. Vaszilcsin, *International Journal of Electrochemical Science*, **2014**, *9*, 4465.
33. C.C. Vaduva, N. Vaszilcsin, A. Kellenberger, M. Medeleanu, *International Journal of Hydrogen Energy,* **2011**, *36*(12), 6994.
34. C.C. Vaduva, N. Vaszilcsin, A. Kellenberger, *International Journal of Hydrogen Energy,* **2012**, *37*, 12089.
35. C.C. Vaduva, "PhD. Thesis", Ed. Politehnica, Timisoara, **2013**.
36. M. Szycher, "Szycher's Handbook of Polyurethanes", CRC-Press, USA, **2013**.
37. C. Reichardt, "Solvents and Solvent Effects in Organic Chemistry", WILEY-VCH, Germany, **2003**.
38. S. Fletcher, *Journal of Solid State Electrochemistry*, **2009**, *13*, 537.
39. M.N. El-Haddad, *Carbohydrate Polymers*, **2014**, *112*, 595.
40. N. Abdulwali, F. Mohammed et al., *International Journal of Electrochemical Science,* **2014**, *9*, 6402.
41. A.M. Al-Bonayan, *International Journal of Electrochemical Science*, **2015**, *10*, 589.

Dedicated to prof. dr. I. C. Popescu
on the occasion of his 70th anniversary

ELECTROCHEMICAL CHARACTERIZATION OF TWO OLEAMIDE ANALOGUES ANTI-OBESITY AGENTS

CĂTĂLINA NEGUŢ (CIOATEŞ)[a,b], ELEONORA-MIHAELA UNGUREANU[a*], GEORGIANA-LUIZA ARNOLD[a], CONSTANTIN TĂNASE[b], LIVIU BÎRZAN[c]

ABSTRACT. Electrochemical characterization of two oleamide analogues was performed by cyclic voltammetry, differential pulse voltammetry, and rotating disk electrode voltammetry. Modified electrodes have been obtained by scanning the potential in the domain of the first oxidation peaks.

Keywords: *oleamide analogues, cyclic voltammetry, differential pulse voltammetry, rotating disk electrode voltammetry, modified electrodes*

INTRODUCTION

Many researches are nowadays dealing with elucidating of obesity molecular mechanism and developing new potent therapeutic agents with less secondary effects. Oleic acid amide (oleamide) and some of its structural analogues are amides of the naturally present in food fatty acids. These compounds occur also endogenously as signaling molecules with various biological effects depending on tissue type. The most studied biological activities of oleamides are the sleeping modulator effect, decreasing of pain perception, decreasing of body temperature, and regulator effects on cardiovascular system and lipid metabolism.

[a] *Faculty of Applied Chemistry and Materials Science, Politehnica University of Bucharest, 1-7 Polizu St., 011061, Bucharest, Romania*
[b] *National Institute for Chemical–Pharmaceutical Research and Development ICCF, 112 Vitan Av., 031299, Bucharest, Romania*
[c] *Institute of Organic Chemistry "C.D. Nenitzescu" of Romanian Academy, Splaiul Independentei 202B, PO Box 15-258, 71141 Bucharest, Romania*
[*] *Corresponding author: eleonoramihaelaungureanu@gmail.com*

N-(2-hydroxyethyl)oleamide (OEA) is an important analogue of oleamide; it is a fatty acid amide biosynthesized from oleic acid and phosphatidylethanol-amine mainly in brain, liver, adipocytes and small intestine [1, 2]. OEA acts on peroxisome proliferator-activated receptor alpha (PPAR-α) and less on cannabinoid receptors [3, 4]. Both endogenous and oral/parenteral administration of OEA induced a satiety signal leading to the decrease of food intake and body weight loss [3, 5]. This activity is opposed to that induced by the anandamide, (5Z,8Z,11Z,14Z)-N-(2-hydroxyethyl) icosa-5,8,11,14-tetraenamide, which is a similar amide that contains 4 double bonds and 3 double allylic positions. This antagonist induces a motivation for feeding and pleasure, activating mainly the cannabinoid receptors [6]. This difference could be also due to the gap between the oxidation potentials of the two amides, OEA possessing only one isolated double bond, while anandamide is much easier oxidized at the double allylic positions, making impossible the generation of hydrogen peroxide by PPAR-α. Therefore, we examined two compounds **1** and **2** (Fig. 1) with similar structures that have different oxidation capacities.

In this paper we present the results obtained in the study of the electrochemical profiles of compounds **1** and **2**, which were synthesized as promising oleamides analogues [7], similar to the natural active compounds useful for anti-obesity therapy.
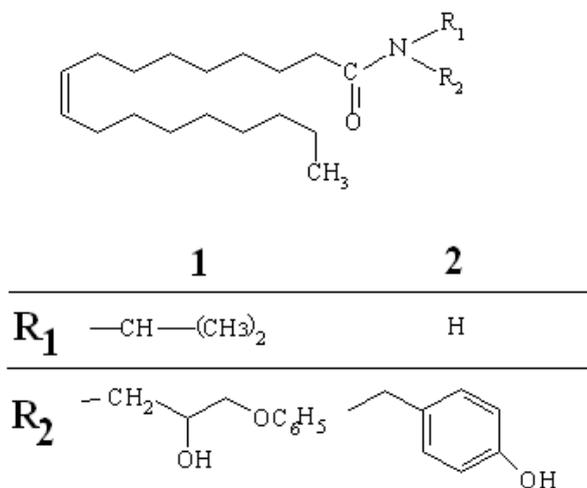
Figure 1. Structures of the investigated compounds

RESULTS AND DISCUSSION

The compounds **1** and **2** were synthesized from oleic acid and 1,1'–carbonyldiimidazole to give the oleyl-imidazole intermediate, which reacted with the corresponding amines according to the procedure previously described [7]. The characterization by IR, ^{1}H- and ^{13}C-NMR spectra confirmed the compounds structure.

The electrochemical behavior of these two oleamide analogues was studied in acetonitrile (CH_3CN) containing tetrabutylammonium perchlorate (TBAP) as supporting electrolyte, using stationary or rotating glassy carbon electrodes. The results of electrochemical experiments carried out in anodic scans by cyclic voltammetry (CV), differential pulse voltammetry (DPV) and rotating disk electrode voltammetry (RDE) are shown in Fig. 2. All curves were recorded individually, starting from the stationary potential in cathodic or anodic scans. No cathodic processes have been evidenced.

The anodic processes are denoted in the order in which they appear in the voltammograms (*eg* with 1.1 – 1.4 or with 2.1 – 2.5 for compounds **1** or **2**, respectively). Two main anodic processes (1.1 and 1.2 and 2.1 and 2.2, respectively) are noticed for all kind of curves: CV, DPV and RDE (Figure 2). They can be attributed to the specific oxidation processes of each oleamide.

The reaction mechanism which explains these peaks was previously studied when determining the phenols capacity to be antioxidants or promotors of lipide peroxidation. This behavior could make the difference between the treatment and the worsening of cancer [8]. The phenols possessing low oxidation potentials can easily quench the generated radical cations on the lipid double bonds; natural caffeic acid, but also alkylated phenols (if they do not contain electro withdrawing groups (EWGs) on the molecule) are effective. Unfortunately, the phenols substituted with EWGs or the anisoles have much higher oxidation potentials, and they behave even as catalyst in the electron transfer from the oleic double bond to the electrode. A better understanding of these processes could be achieved if the experiments are conducted using a buffer, which prevents the inherent solvent acidification by the TBAP oxidation [9]. At biological pH-s, the compound **2** would have had oxidation potentials lower than **1**, and compound **1** would not be affected by pH. This difference is induced by the capacity of the phenolic system to form relative stable semiquinone and then quinone (by hydration) forms [10].
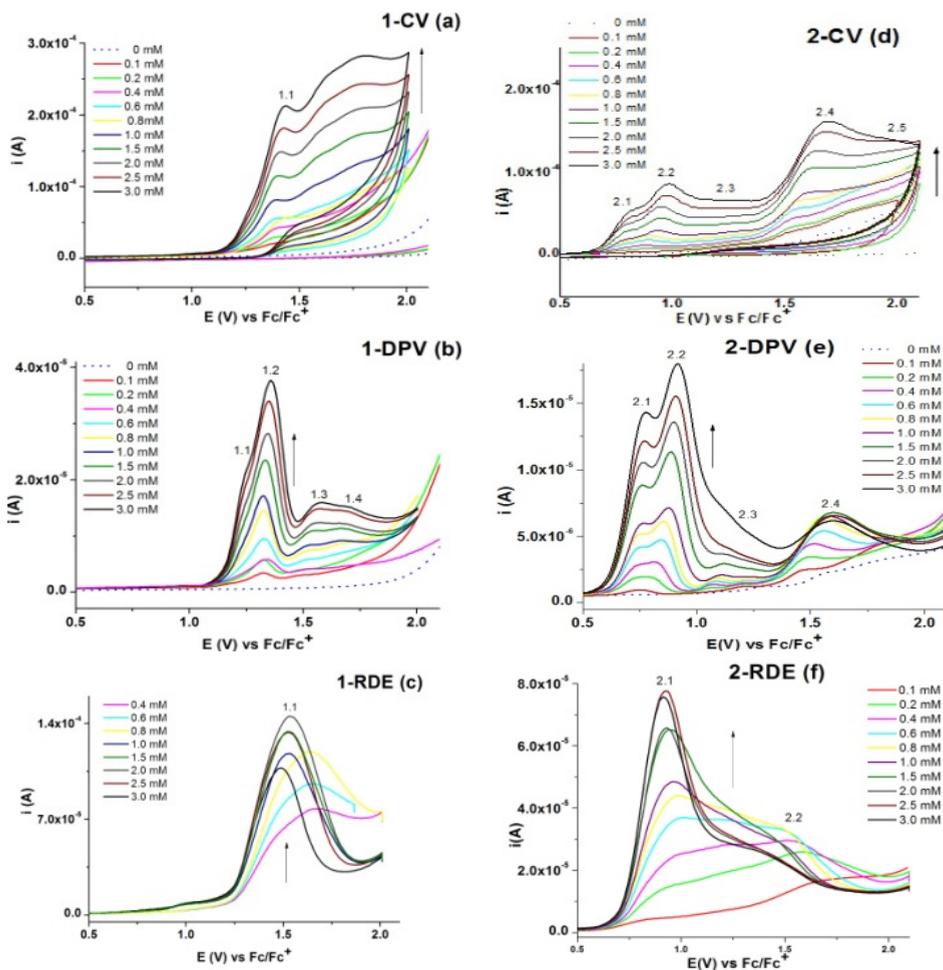
Figure 2. CV (a,d), DPV (b,e) and RDE (c,f) curves for **1** (a, b, c) and **2** (d, e, f) obtained for different concentrations of each compound

Analyzing the curves obtained in Figure 2 it can be concluded that oxidation of **2** occurs more readily than that of compound **1**. The oxidation processes are, respectively: phenol oxidation to *o*-semiquinone and then to *o*-quinone in compound **2**, and alkene and anisole oxidation to cation radicals (occurring at the same area of potentials) in compound **1**.

The influences of the scan rate and scan domain on the CV curves was also studied for the two compounds, and the obtained curves showed that all processes are irreversible (Figure 3).
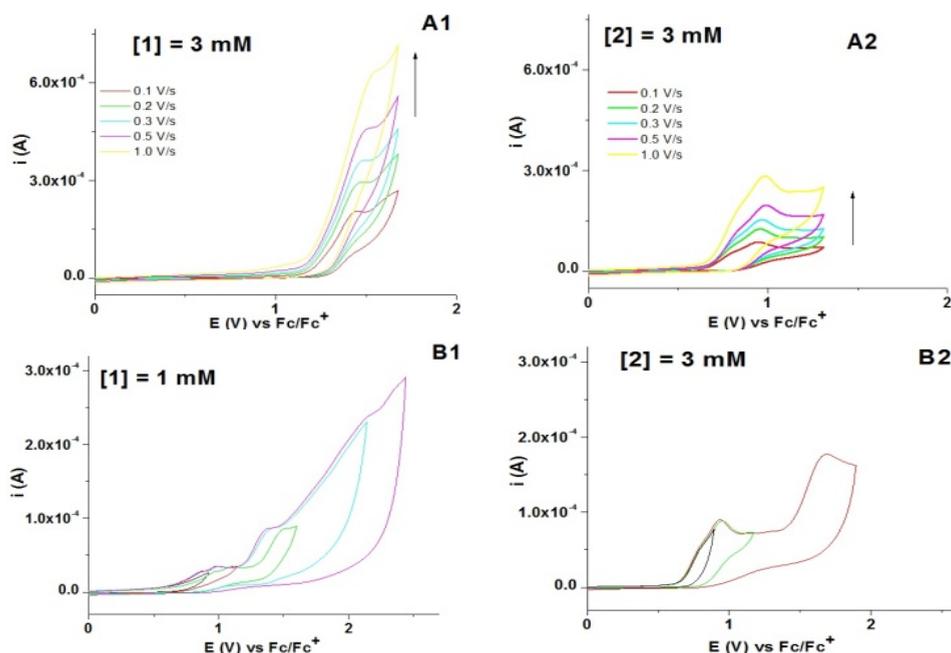
Figure. 3. CV curves at different scan rates (A1, A2) and various of scan domains (B1, B2) in the potential range of the first anodic peak for **1** and **2** in 0.1 M TBAP, CH$_3$CN

It can be seen from Figure 4 that dependences of peak currents on oleamide concentrations obtained from all methods are linear for both compounds in CV and DPV (Table 1), but parabolic or sigmoid, respectively, in RDE for compounds **1** or **2**. The last shapes are connected to the formation of insoluble products or films on the electrode surface from both oleamide analogues. It can be seen from Table 1 that correlation coefficients for the linear dependences of the peak currents on concentration of compound **1** or **2**, [**1**] or [**2**], respectively, are good.

It can be seen from figure 5 that by scanning the potential in the range of the first anodic peaks in solutions of **1** or **2** the currents decrease drastically in successive cycles, showing the electrode blocking. Modified electrodes have been obtained by cycling the potential between 0 and the potential of the first two peaks. The transfers of these modified electrodes in ferrocene solution have shown that the reversible ferrocene signal is deeply changed on modified electrodes being smaller in intensity and very flat, confirming the electrode blocking with an insulating layer.
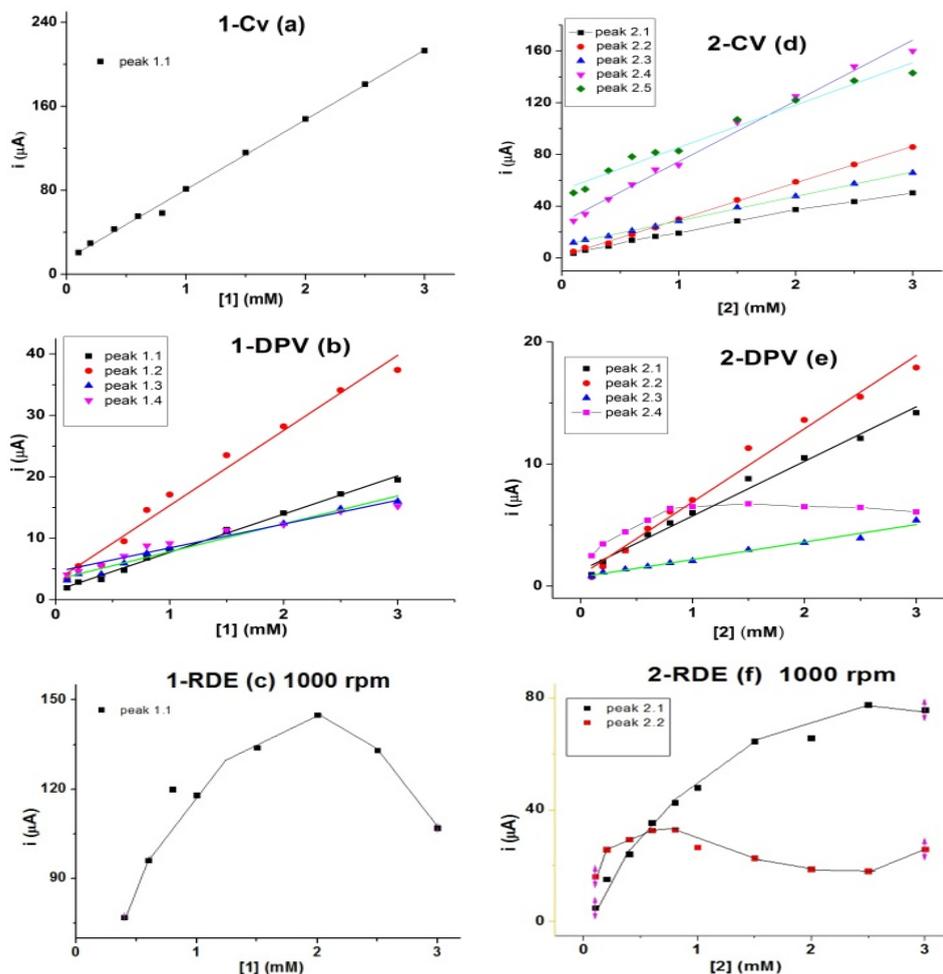
Figure 4. Dependences on concentration of the currents in CV, DPV and RDE

Table 1. Equations for the 1.1-1.4 and 2.1-2.3 peak currents (A) vs the corresponding oleamide concentration, [**1**] or [**2**] in mole/L

Compound	Method	Equation	Correlation coefficient
1	CV	$i_{peak\ 1.1} = 14.19 + 66.47 \cdot [\mathbf{1}]$	0.997
	DPV	$i_{peak\ 1.1} = 1.46 + 6.23 \cdot [\mathbf{1}]$	0.994
		$i_{peak\ 1.2} = 3.07 + 12.23 \cdot [\mathbf{1}]$	0.980
		$i_{peak\ 1.3} = 3.25 + 4.54 \cdot [\mathbf{1}]$	0.978
		$i_{peak\ 1.4} = 4.52 + 3.88 \cdot [\mathbf{1}]$	0.958

Compound	Method	Equation	Correlation coefficient
2	CV	$i_{peak\ 2.1} = 9.33 + 7.34 \cdot [2]$	0.995
		$i_{peak\ 2.2} = 1.48 + 28.28 \cdot [2]$	0.999
		$i_{peak\ 2.3} = 9.77 + 18.89 \cdot [2]$	0.999
		$i_{peak\ 2.4} = 27.43 + 46.97 \cdot [2]$	0.989
		$i_{peak\ 2.5} = 52.55 + 32.79 \cdot [2]$	0.973
	DPV	$i_{peak\ 2.1} = 1.26 + 4.47 \cdot [2]$	0.988
		$i_{peak\ 2.2} = 0.87 + 6.0 \cdot [2]$	0.984
		$i_{peak\ 2.3} = 0.73 + 1.44 \cdot [2]$	0.981
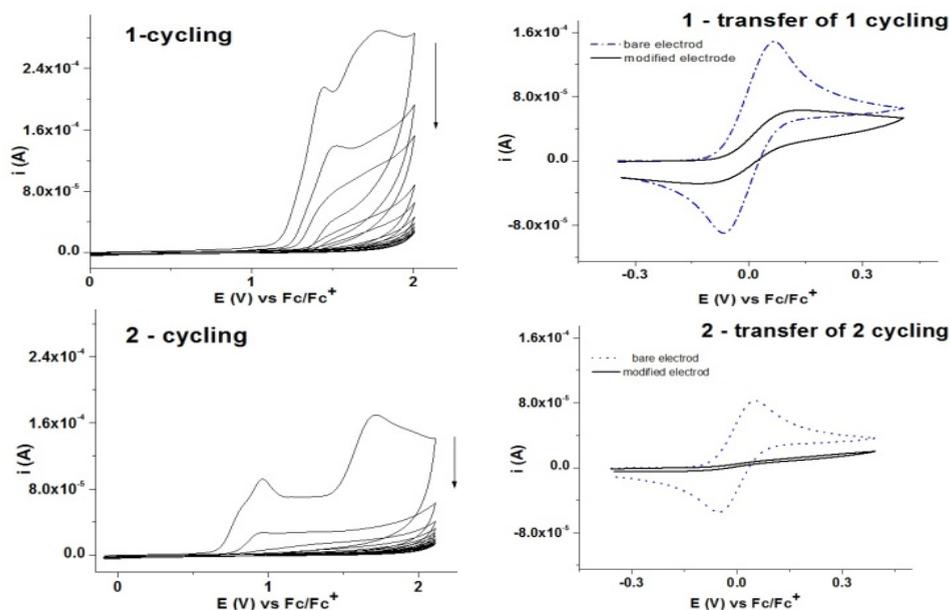
Figure 5. CV curves during successive cycles in milimolar solutions of **1** or **2** (**1-cycling** and **2-cycling**, respectively) in 0.1M TBAP, CH$_3$CN (left side), and the corresponding CV curves of ferrocene in 0.1M TBAP, CH$_3$CN solution on bare (dashed lines) and modified (full lines) electrodes (right side), obtained after the transfers of the electrodes prepared by scanning the potentials (20 cycles in solutions of **1** or **2** in 0.1M TBAP, CH$_3$CN, respectively)

Modified electrodes can be obtained either by scanning the electrode potential between 0 and the potential of the second main oxidation peaks, or by controlled potential electrolysis at potentials in the domain of the second main oxidation peaks.

Electrochemical characterization of oleamides **1** and **2** led to concordant results with those obtained for another oleamide having a similar structure, which has been investigated previously [11]. These investigated compounds show different electroactivities, evidenced by different potentials for the anodic peaks. This behavior is explained by the differences in their structures. In the present study, all electrochemical curves agree that compound **2** is oxidized easier then **1,** due to its phenolic structure.

CONCLUSIONS

The electrochemical behavior of two oleamide analogues was investigated in acetonitrile containing tetrabutylammonium perchlorate as supporting electrolyte. Two main anodic irreversible processes were identified by cyclic and differential pulse voltammetry. Scanning the potential in the range of the first anodic peak led to the coverage of the electrode with an insulating layer. This coverage was confirmed by rotating disk electrode curves. Modified electrodes can be easily obtained either by potential scans or by controlled potential electrolysis in the domain of the first two oxidation peaks.

The electrochemical studies of the two compounds performed by cyclic, differential pulse and rotating disk electrode voltammetries allowed highlighting the different features of the electrochemical behaviour of these two oleamide analogues in view of their potential anti-obesity action. The compound **1** has a higher oxidation potential, and it is prone to activate mainly the peroxisome proliferator-activated receptor alpha, while the compound **2** can act more as an activator of cannabinoid receptors, inducing hunger and pleasure. At the same time, if the concentration of hydrogen peroxide generated by peroxisome is too high, compound **1** seems not to have anymore antioxidant capacity, but even worse, it catalysis the oleoyl oxidation. The compound **2** can protect the organic tissue against the formation of radical cations in surplus. In this way, both compounds can act as potential anti-obesity agents. The corresponding tests are in progress.

EXPERIMENTAL SECTION

Oleamides **1** and **2** (Figure 1) were synthesized according to the procedure described in [6]. For electrochemical investigations acetonitrile and tetrabutylammonium perchlorate (TBAP) from Fluka were used (as received) as solvent and supporting electrolyte, respectively.

The electrochemical experiments were carried out using a PGSTAT 12 AUTOLAB potentiostat coupled to a three-compartment cell. The CV curves were generally recorded at 0.1V/s or at various rates (0.1 - 1V/s) when studying the influence of the scan rate. DPV curves were recorded at 0.01V/s with a pulse height of 0.025V and a step time of 0.2 s. RDE experiments were performed using Autolab RDE-2 rotating disk electrode at a scan rate of 0.01V/s, with rotating rates between 200 and 2000 rpm. The working electrodes were glassy carbon disks (diameter of 3 mm). There active surface was polished before each determination with diamond paste (0.25 μm). Ag/10 mM $AgNO_3$ in 0.1M TBAP, CH_3CN was used as reference electrode. The potential was referred to the potential of the ferrocene/ferricinium redox couple (Fc/Fc$^+$) which in our experimental conditions was +0.07V. A platinum wire was used as auxiliary electrode.

The electrochemical experiments were performed at 25ºC under argon atmosphere.

ACKNOWLEDGEMENTS

REFERENCES

1. Y.M. AlSuleimani, C.R. Hiley, *European Journal of Pharmacology*, **2013**, *702*, 1.
2. G. Petersen, C. Sorensen, P.C. Schmid, A. Artmann, M. Tang-Christensen, S.H. Hansen, *Biochim Biophys Acta*, **2006**, *1761*, 143.
3. J.Fu, F. Oveisi, S. Gaetani, E. Lin, D. Piomelli, *Neuropharmacology*, **2005**, *48* (8), 1147.
4. Y. Zhou, L. Yang, A. Ma, X. Zhang, L. Weijie, Y. Wushuang, C. Caixia, J. Xin, *Neuropharmacology*, **2012**, *63 (2)*, 242.
5. S. Gaetani, F. Oveisi, D. Piomelli, *Neuropsychopharmacology*, **2003**, *28*, 1311.
6. P Pacher, S Batkai, G Kunos, *Pharmacological Review,* **2006**, *58 (3)*: 389.
7. C. Tanase, C. Negut (Cioates), D.I. Udeanu, E.-M. Ungureanu, M. Hrubaru, C.V.A. Munteanu, S. P. Voicu, F. Cocu, A.N. Ionita, *Revista de Chimie*, **2014**, *65 (7)*, 768.
8. A. Simic, D. Manojlocvic, D. Segan, M. Todorovic, *Molecules*, **2007**, *12 (10)*, 2327.
9. J.L.N. Xavier, E. Ortega, J.Z. Ferreir, A.M. Bernardes, V. Perez-Herranz, *International Journal of Electrochemical Science* **2011**, *6*, 622.
10. T.A. Enache, A.M. Oliveira-Brett, *Journal of Electroanalytical Chemistry* (**2011**), *655 (1)*, 9.
11. C. Negut (Cioates), E.-M. Ungureanu, F. Cocu, C. Tanase, C. Draghici, C.V.A. Munteanu, *University Politehnica Scientific Bulletin, Series B, Chemistry and Materials Science*, **2014**, *76* (4), 173.

Dedicated to prof. dr. I. C. Popescu
on the occasion of his 70th anniversary

ELECTROCHEMICAL STUDIES ON MODIFIED ORGANO-SILANES COMPOSITE COATINGS FOR ALUMINIUM CORROSION INHIBITION

IOANA MAIOR[a], IOANA-ALINA CIOBOTARU[*], SIMONA CĂPRĂRESCU, ANCA COJOCARU, DĂNUȚ-IONEL VĂIREANU

ABSTRACT. The main objective of this study consists in developing a new anticorrosive protection coating for packaging industry based on deposition of organo-silanes composite film on the metallic material surface. Silane solutions (octyltrietoxysilane OTES and vyniltrietoxysilane VTES) modified with SiC and CeO_2 nanoparticles were applied on a 99.99% aluminium substrate and compared with a sample of aluminium commercially available package (can).
For the analysis of film composition and metal surface Fourier Transform Infrared Spectroscopy (FT-IR) and Scanning Electron Microscopy (SEM) were performed. The results highlighted the film's compactness and its adhesive properties, as well as the favourable effect of nanoparticles in tested coatings.
Corrosion tests on aluminium samples with and without protective coatings, as well as on commercially available aluminium cans were carried out in phosphoric acid 3M using open circuit potential, potentiodynamic curves and Electrochemical Impedance Spectroscopy (EIS) techniques.

Keywords: *corrosion, aluminium, phosphoric acid, silanes, nanoparticles, electrochemical impedance spectroscopy, FT-IR, SEM*

INTRODUCTION

In recent years, various studies have focused on food safety issues. Among them, food packaging has gained an increased interest. One of the most important features of food packaging materials is their ability to

---

[a] *"Politehnica" University of Bucharest, Faculty of Applied Chemistry and Materials Science, 1–7 Gh. Polizu Str., RO-011061 Bucharest, Romania*
[*] *Corresponding author: ioanaalinaciobotaru@yahoo.com*

remain neutral against the attacks from various additives contained in food (e.g. phosphoric acid as an acidity regulator included in fizzy drinks) or from food itself, where the pH is already low (e.g. citric acid, acetic acid). This fact may be translated and measurable as a corrosion resistance characteristic of the packaging material.

Among food packaging materials, aluminium has proven to be suitable for different types of food content [1] due to the formation of a protective film on the surface during exposure to atmospheric conditions or to different aqueous solutions [1–5] and therefore is used in a large variety of packaging materials [1, 6].

The aluminium oxide self-formed film on metal surface can act as a barrier during corrosion process in mild corrosive environments, but not in aggressive acid media [7, 8]. One of the most efficient methods to prevent metallic corrosion consists in applying films on the metallic substrate [7, 9] and, in addition, these coatings confer improved properties as mechanical strength or optical appearance [9].

An important factor that influences the interaction and the adhesion of films on metallic substrates is the pre-treatment of the substrate. Therefore, prior to the film deposition, surface pre-treatments play an important role in the bonding process [10, 11].

Chromate coating is a common anticorrosive treatment of aluminium alloys [12–14], but due to its high toxicity, in recent years studies have focused on alternative treatments [12], such as silanization, which is an environmentally compliant alternative [11, 15].

Silane coatings are obtained based on hydrolysis and condensation reactions that take place during film formation [16], by forming oxane bonds between metal and silane [17]. Silane coatings have good barrier properties, are easily applied [11] and high anti-corrosion efficiency [18]. They could be used as a single silane without topcoats for 6 month to 1 year, or as surface pre-treatments before painting [18].

The most commonly used coating technique is dip-coating [9] which consists in dipping the metal substrates into pre-hydrolyzed silane/ water/alcohol solution then drying and curing at a certain temperature [12].

Corrosion resistance of silane films can be improved by adding chemicals with good corrosion inhibitor properties [18] such as pre-treated layers (rare earth salts) or active layers (cerium salts) [16]. In order to achieve better anticorrosive resistance properties, the addition of nanoparticles to the surface silane films has been studied [16, 19, 20]. The nanoparticles can be synthesised in the films or added to the pre-treatment solutions. Silica nanoparticles used in silane films deposited on aluminium substrates lead to the improvement of the substrate corrosion properties [19].

In order to developing a new anticorrosive protection coating for packaging industry, the deposition of different organo-silanes composite film on the metallic material surface have been reported in this paper. OTES and VTES silane solutions modified with SiC and CeO_2 nanoparticles were applied on pure aluminium substrate and then compared with a sample of aluminium commercially available package (can). Corrosion tests on aluminium samples with and without protective coatings, as well as on aluminium cans were carried out in 3M phosphoric acid aqueous solution. From the analysis of film composition and of metal surface the results highlighted the film's compactness and its adhesive properties, as well as the favourable effect of nanoparticles in tested coatings.

RESULTS AND DISCUSSION

The composition of the silane films modified with nanoparticles was investigated by FTIR. Figure 1 depicts the FT-IR spectra of aluminium sheet without coating (Al blank or e.p.), aluminium samples coated with silane films with and without nanoparticles and also nanoparticles powder samples. All silane samples showed *peaks* at 1114–1100cm^{-1}, 968–902cm^{-1} and at 3303-3371cm^{-1} corresponding to Si–O–Si, Al–O–Si bonds formed between the silane film and aluminium surface, respectively –OH stretching vibration (Table 1). For silane films modified with SiC and CeO_2 nanoparticles -CH$_2$ corresponding *peaks* were recorded at 2858 and 2859cm^{-1}. -CH$_3$ stretching vibration *peaks* were recorded for all silane films at 2924cm^{-1} up to 2973cm^{-1}.

Table 1. FT-IR *peaks*

Bonds	Wavenumber, cm^{-1}					
	OTES	OTES SiC 3000	OTES CeO$_2$ 3000	VTES	VTES SiC 3000	VTES CeO$_2$ 3000
–OH	3.303	3.318	3.318	3.307	-	3.371
–CH$_3$	2.924	2.925	2.926	2.967	2.973	2.967
–CH$_2$	2.858	2.858	2.859	-	-	-
Si–O–Si	1.114	1.106	1.115	1.105	1.144	1.120
Al–O–Si	902	947	948	968	959	958
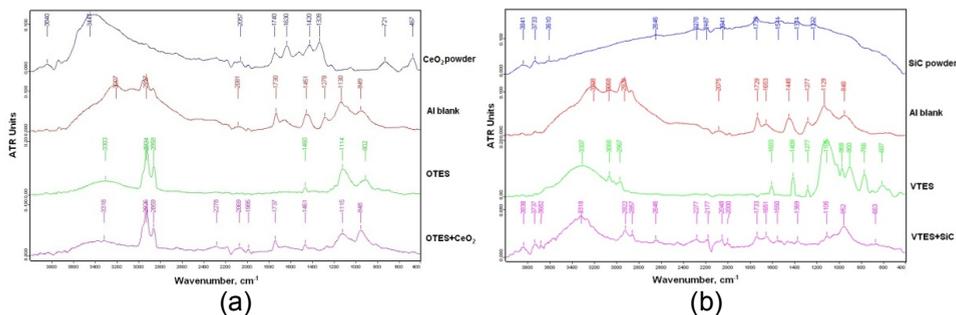
Figure 1. FT-IR spectra for Al e.p., Al OTES 5% and Al OTES 5% modified with CeO$_2$ (a) and for Al e.p., Al VTES 5% and Al VTES 5% modified with SiC (b)

The surface coating film was investigated by SEM analyses. In Figure 2 are shown SEM micrographs of silane films with and without nanoparticles.

Organic compounds chains exhibit a strong influence on the properties of composite films deposited on aluminium substrate. Synthesized films from octyl and vinyl precursors are forming clusters due to the association of these chains under hydrophobic forces. Films adhesion on aluminium depends on alcoxi-silane nature. A smooth surface is characteristic for silane film without nanoparticles, due to bi-diminesional structure with –CH$_3$ groups on silica surface.

As may be seen in Figure 2, CeO$_2$ and SiC nanoparticles are incorporated in silane films leading to relatively homogenous silane films.

In addition, synthesized silica nanoparticles exhibit a tridimensional structure with –OH groups. This structure is characterized by a high roughness.
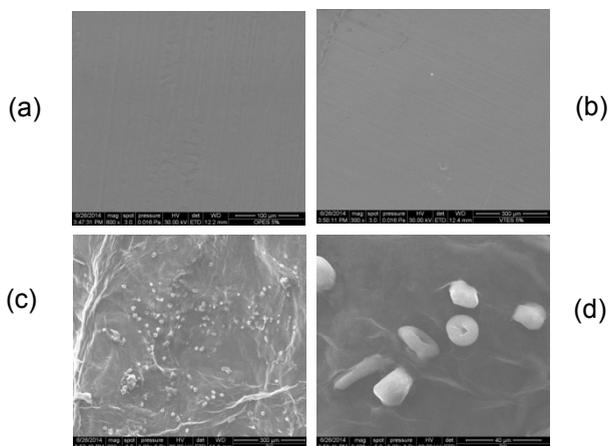
Figure 2. SEM micrographs of silane films deposited on aluminium substrate: (a) OTES 5%, (b) VTES 5%, (c) VTES 5% modified with CeO$_2$ and (d) VTES 5% modified with SiC

In Figure 3 are shown the variation of potential in time.

As shown in figure 3, initially, the potential decreases, and after 5 minutes increases to more electropositive values. After 20-25 minutes, it can be observed a stabilization of potential at higher values than for uncoated aluminium sample. For the blank aluminium sheet, the potential increases in time until it reaches a constant value, lower than the coated samples.

(a)   (b)
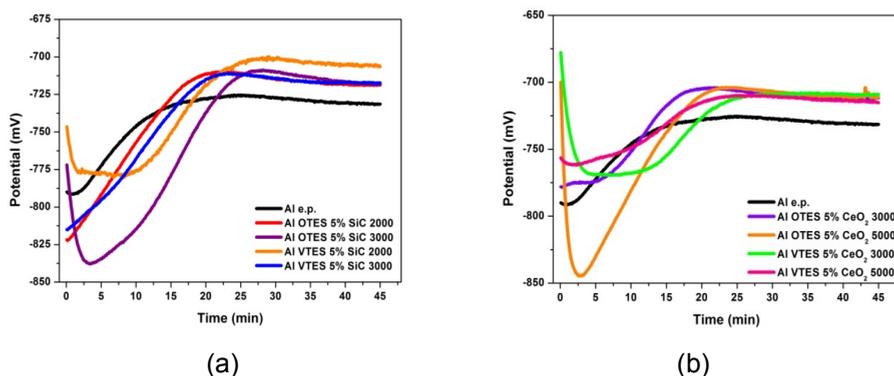
Figure 3. Variation of potential in time for Al e.p., Al can and Al with silanes modified with SiC (a) and with CeO_2 (b) in H_3PO_4 3M

In Figures 4–6 are presented the Nyquist plots registered in H_3PO_4 3M.
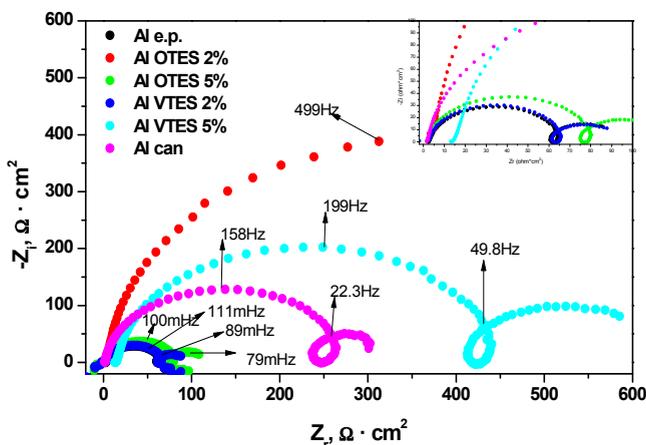
Figure 4. Nyquist plots for Al, Al with silane films and commercially available aluminium cans samples in H_3PO_4 3M

Nyquist plots also show that silane films modified with nanoparticles samples have higher polarization resistance than aluminium samples, indicating a charge transfer process which controls aluminium corrosion.

Rp is the polarization resistance at the electrode/solution interface and represents the diameter of the semicircle calculated from the circular regression applied to the Nyquist plots.

In this particular case, the polarization resistance was calculated using the circular regression applied to the experimental points, taking into consideration the points up to the second intersection of the semicircle with the real impedance axis.

Rp can be used as a quantitative parameter to compare the corrosion resistance of metals under various conditions. This parameter is used to describe the corrosion resistance of the investigated sample, a higher value indicating a better corrosion resistance.

Polarisation resistances of silane films modified with CeO_2, of VTES 2% and OTES 5% have smaller values than the commercially available aluminium cans. Higher polarisation resistance values than the commercially available aluminium cans were obtained for OTES 2%, VTES 5% and VTES 5% modified with SiC. Bode plots (Figure 5) confirm the estimated values of polarisation resistance from Nyquist plots. Also, they confirm the existence of two time constants corresponding to the two processes highlighted by the Nyquist plots.
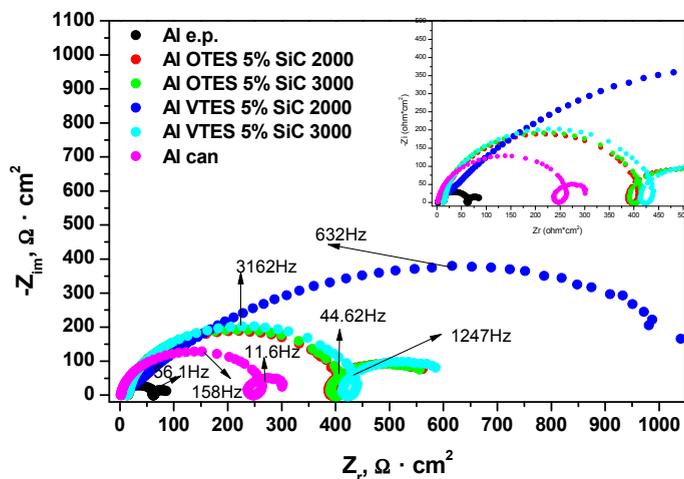
Figure 5.a. Nyquist plots for Al, Al with silane films modified with SiC and commercially available aluminium cans samples in H_3PO_4 3M.
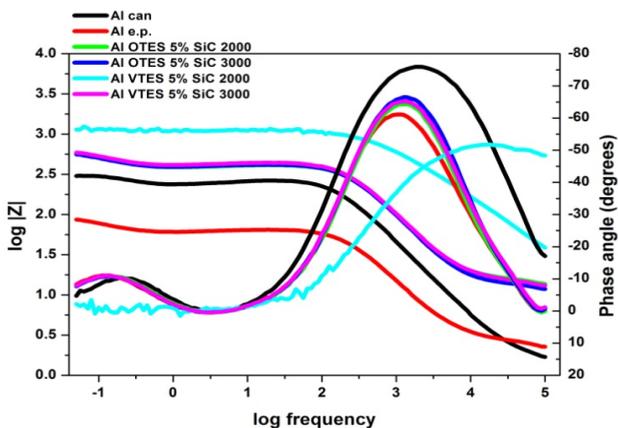
Figure 5.b Bode plots for Al, Al with silane films modified with SiC and commercially available aluminium cans samples in H_3PO_4 3M.
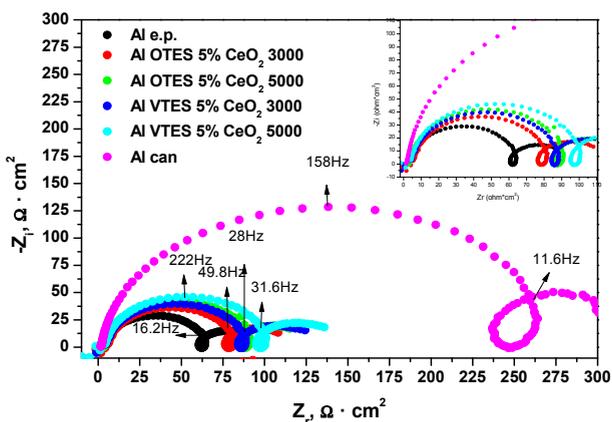
Figure 6. Nyquist plots for Al, Al with silane films modified with CeO_2 and commercially available aluminium cans samples in H_3PO_4 3M

The impedance plots consist of two capacitive loops at high and low frequencies and an inductive loop at medium frequencies. These loops are not perfect semicircles, which can be attributed to dispersion phenomena.

The high frequency capacitive loop is attributed to the charge transfer process during corrosion and to the formation of an oxide layer. The oxide layer can be considered a parallel circuit which consists of a resistance (due to ionic conduction) in oxide layer and a condenser (due to dielectric properties).
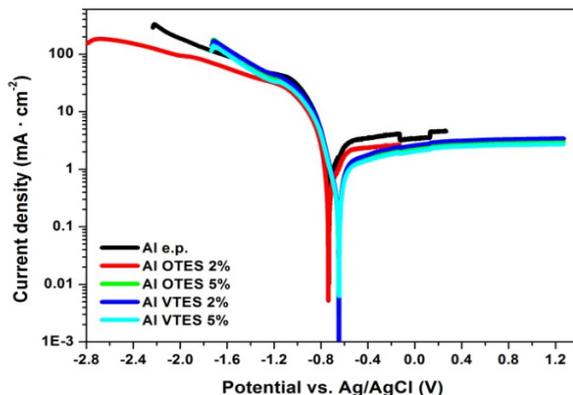
Figure 7. Potentiodynamic polarization curves for Al e.p., Al with silane films and commercially available aluminium cans in H_3PO_4 3M

This loop is attributed to interface reactions, mainly to a three–step aluminium oxidation at metal/oxide/electrolyte interface.

The medium frequencies inductive loop may be attributed to the relaxation of the charge intermediates adsorbed on the electrode surface similar findings are presented in details in [21]. The low frequency capacitive loop may be attributed to a change in the double layer capacitance due to the possible existence of an oxide layer on the metallic surface [22, 23].

(a)   (b)
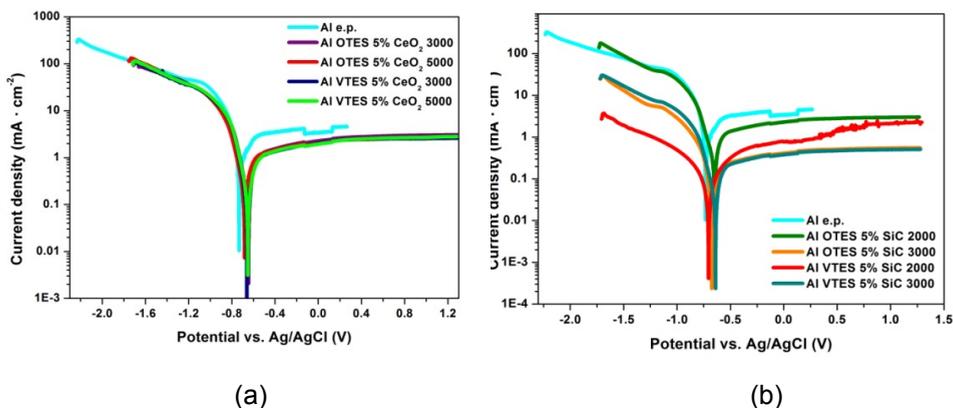
Figure 8. Potentiodynamic polarization curves for Al e.p., Al with silane films modified with CeO_2 (a) and SiC (b) and commercially available aluminium cans in H_3PO_4 3M

The efficiency of silane coatings on the corrosion reactions was determined by polarization techniques. Potentiodynamic polarization curves are plotted in figures 7 and 8. The potentiodynamic parameters such as corrosion potential (ε_{corr}), cathodic and anodic Tafel slopes (b_c and b_a), corrosion current density (i_{corr}), were obtained from Tafel plots and the inhibition efficiency values IE(%), were calculated using equation 1. The results are presented in Table 2.

Table 2. Electrochemical parameters calculated from Tafel polarization curves on aluminium in 3M phosphoric acid for different silane coatings

Samples	ε_{cor}, mV vs. Ag/AgCl	i_{cor}, µA·cm^{-2}	β_a, mV·dec^{-1}	$-\beta_c$, mV·dec^{-1}	p, mm·y^{-1}	IE,%
Al e.p.	−660	264.90	167.80	127.30	2.88	-
OTES 2%	−739	218.60	64.10	49.40	2.38	17.47
OTES 5%	−651	132.48	51.10	69.30	1.44	49.98
OTES 5% 2000 SiC	−676	16.24	54.70	47.10	0.18	93.86
OTES 5% 3000 SiC	−649	16.51	46.10	55.50	0.18	93.76
OTES 5% 3000 CeO$_2$	−634	107.12	48.10	65.00	1.16	59.57
OTES 5% 5000 CeO$_2$	−685	77.59	49.20	54.30	0.84	70.71
VTES 2%	−649	142.39	50.40	69.60	1.55	46.24
VTES 5%	−649	120.98	54.00	66.70	1.32	54.32
VTES 5% 2000 SiC	−717	12.22	48.90	56.20	0.15	95.38
VTES 5% 3000 SiC	−708	13.73	52.00	60.90	0.15	94.81
VTES 5% 3000 CeO$_2$	−663	62.75	49.80	51.90	0.68	76.31
VTES 5% 5000 CeO$_2$	−656	68.62	48.90	53.10	0.75	74.09

The inhibition efficiency was calculated using the following equation:

$$IE\,(\%) = \left(1 - \frac{i_{corr}}{i_{corr}^0}\right) \cdot 100 \qquad (1)$$

where i_{corr} and i_{corr}^0 are the corrosion current densities obtained in uninhibited and inhibited solutions, respectively. The corrosion rate was calculated using the following equation:

$$p\,(mm/year) = \frac{3270 \cdot M \cdot i_{corr}}{\rho \cdot Z} \qquad (2)$$

where 3270 is a constant that defines the unit of corrosion rate, i_{corr} is the corrosion current density in A cm^{-2}, ρ is the density of the corroding material (g cm^{-3}), M is the atomic mass of the metal and Z is the number of electrons transferred per atom.

The smallest value of the corrosion current was recorded for VTES 5% modified with 2000 µg/L SiC. Regardless of the nature of silane, for a concentration of 5% and for the maximum concentration of SiC (3000 µg/L), it can be observed a similar behaviour on both anodic and cathodic curve, leading to small values of the corrosion rate and to achieving the passivation state after a slow evolution in a shorter time (Figure 8).

There was no remarkable shift in the corrosion potential value (ε_{corr}) with respect to the uncoated aluminium sample. The maximum shift is less than ±85 mV. Both anodic and cathodic polarizations are influenced simultaneously and have a similar behaviour, which indicate the influence of coatings on both the anodic and the cathodic reactions.

CONCLUSIONS

FT-IR spectra confirmed the presence of functional groups –CH$_2$, –CH$_3$, –OH and also the presence of Si–O–Si and Al–O–Si bonds.

SEM micrographs confirmed the incorporation of nanoparticles in silane films that led to a certain roughness of films surface.

Electrochemical studies showed a better corrosion behaviour of aluminium with silane modified with SiC than the ones modified with CeO$_2$ in H$_3$PO$_4$ 3M. Aluminium with OTES 5% and 2000 SiC has a polarization resistance higher than the commercially available aluminium cans.

Nanoparticles concentration is an important factor in establishing the final properties of the film. The excess of nanoparticles can lead to opposite effects (VTES 5% modified with 5000 CeO$_2$ has a bigger value of corrosion current than VTES 5% modified with 3000 CeO$_2$).

EXPERIMENTAL SECTION

The aluminium sheets consisted of aluminium of electrolytic purity (Al 99.9%, with an active surface of $0.5cm^2$). Prior to deposition, the substrate was immersed in an alkaline solution (NaOH), then in distilled water, followed by cleaning with ethanol and distilled water using an ultrasonic apparatus. The coatings used in this study are silane solutions of octyltrietoxysilane – OTES and vyniltrietoxysilane – VTES, provided by Sigma Aldrich, modified with SiC and CeO_2 nanoparticles. The concentration of tested silane solutions were of 2 and 5% in ethanol. The maximum concentration of silane solutions were functionalized with SiC and CeO_2 of 2000, 3000 µg/L SiC, respectively 3000, 5000 µg/L CeO_2 concentrations (referred to as SiC 2000, SiC 3000, CeO_2 3000 and CeO_2 5000). The nanoparticles were dispersed in silanes by means of an ultrasonic apparatus. The silane films were deposited on the aluminium substrate by deep-coating procedure for 10 minutes.

The FT-IR spectra were recorded using a Fourier Transforms Infrared spectrometer (Tensor 37 Bruker) in transmission mode (ATR), in the spectral range of $400 - 4000$ cm^{-1}. Samples of nanoparticles powder were analysed mixed with KBr.

The surface morphology of silane films was examined on a SIRION Field Emission Scanning Electron Microscope (SEM) produced by FEI Co. Ltd.

Corrosion rate tests were carried out at room temperature ($24 \pm 2°C$) in 3M H_3PO_4 solution as a substitute (stimulant) for water-based food and drinks. The electrochemical measurements were carried out in a three-electrode configuration electrochemical cell consisting of a working electrode (the aluminium sheet with an active area equal to $0.5cm^2$), an Ag/AgCl saturated electrode (used as reference electrode, provided by Radiometer Analytical) and a platinum counter electrode (Radiometer Analytical, $1.13cm^2$ active area). These studies were performed with a VoltaLab 40 PGZ301 potentiostat, connected to a computer that uses VoltaMaster 4.0 software for data processing.

EIS measures the response of the electrochemical system within a frequency range of 100 kHz – 1Hz using a 10mV a.c. potential excitation. The open circuit potential was measured for over 45 minutes. Potentiodynamic polarization curves were plotted at a scan rate of 10mV/min, starting from cathodic potential.

REFERENCES

1. European Food Safety Authority, *Safety of aluminium from dietary intake,* The EFSA J., **2008**, *754*, 1.
2. M.K. Awad, M.S. Metwally, S.A. Soliman, El-Zomrawy, M.A. Bedair, *J. Ind. and Eng. Chem.*, **2014**, *20*, 796.
3. M. Whelan, J. Cassidy, B. Duffy, *Surface & Coatings Technology*, **2013**, *235*, 86.
4. M. Whelan, K. Barton, J. Cassidy, J. Colreavy, B. Duffy, *Surface & Coatings Technology*, **2013**, *227*, 75.
5. M.A. Amin, Q. Mohsen, O.A. Hazzazi, *Materials Chemistry and Physics*, **2009**, *114*, 908.
6. L. Bouchama, N. Azzouz, N. Boukmouche, J.P. Chopart, A.L. Daltin, Y. Bouznit, *Surface and Coatings Technology*, **2013**, *235*, 676.
7. Y. Wang, Y. Li, F. Wang, *E-Journal of Chemistry*, **2012**, *9*, 435.
8. X. Li, S. Deng, X. Xie, *Corrosion Science*, **2014**, *81*, 162.
9. D. Wang, G.P. Bierwagen, *Progress in Organic Coatings*, **2009**, *64*, 327.
10. W.J. van Ooij, D. Zhu, M. Stacy, A. Seth, T. Mugada, J. Gandhi, P. Puomi, *Tsinghua Science and Technology*, **2005**, *10(6)*, 639.
11. J.B. Bajat, V.B. Miskovic-Stankovic, Z. Kacarevic-Popovic, *Corrosion Science*, **2008**, *50*, 2078.
12. J.M. Hu, L. Liu, J.Q. Zhang, C.N. Cao, *Electrochimica Acta*, **2006**, *51*, 3944.
13. B. Valdez, S. Kiyota, M. Stoytcheva, R. Zlatev, J.M. Bastidas, *Corrosion Science*, **2014**, *87*, 141.
14. L.M. Palomino, P.H. Suegama, I.V. Aoki, M.F. Montemor, H.G. De Melo, *Corrosion Science*, **2009**, *51*, 1238.
15. J.M. Hu, L. Liu, J.Q. Zhang, C.N. Cao, *Progress in Organic Coatings*, **2007**, *58*, 265.
16. L. Liu, J.M. Hu, J.Q. Zhang, C.N. Cao, *Electrochimica Acta*, **2006**, *52*, 538.
17. G. Pan, D.W. Schaefer, *Thin Solid Films*, **2006**, *503*, 259.
18. P.H. Suegama, A.A.C. Recco, A.P. Tschiptschin, I.V. Aoki, *Progress in Organic Coatings*, **2007**, *60*, 90.
19. M.F. Montemor, M.G.S. Ferreira, *Progress in Organic Coatings*, **2008**, *63*, 330.
20. P.H. Suegama, V.H.V. Sarmento, M.F. Montemor, A.V. Benedetti, H.G. de Melo, I.V. Aoki, C.V. Santili, *Electrochimica Acta*, **2010**, *55*, 5100.
21. A. Lasia, Electrochemical Impedance Spectroscopy and Its Applications, in Modern Aspects of Electrochemistry, B.E. Conway, J. Bockris, and R.E. White, Eds., *Kluwer Academic/Plenum Publishers*, New York, **1999**, *32*, 143-248.
22. D. Prabhu, P. Rao, *Journal of Environmental Chemical Engineering*, **2013**, *1*, 676.
23. A.A. Mohammed, Q. Mohsen, O.A. Hazzazi, *Materials Chemistry and Physics*, **2009**, *114*, 908.

Dedicated to prof. dr. I. C. Popescu
on the occasion of his 70th anniversary

ELECTROCHEMICAL BEHAVIOUR OF THE NEW HETEROCYCLIC PYRIDINIUM LIGANDS

ANDREEA CÂRÂC[a,b], RICA BOSCENCU[a],
RODICA MIHAELA DINICĂ[b], GETA CÂRÂC[b,*]

ABSTRACT. New heterocyclic pyridinium compounds as N,N' di-(p-bromophenacyl)-4,4'-bipyridinium dibromide (Lr) and N,N' di-(p-bromophenacyl)-1,2-bis(4-pyridinium)-ethane dibromide (Lm) were investigated applying cyclic voltammetry to evaluate the electrochemical behaviour. The stability of new heterocyclic pyridinium compounds in aq. media depends on pH and the dependence was correlated with spectrophotochemical data. Ethylenic group from Lm induces changes on the stability and on the electrochemical performances of the ligand. The quasireversible process on electron transfer between functional groups depends on pH and also on the scan rates of the potential applied. The alkaline pH of a media is more favorable than acidic pH for the ligands stability and the electron transfer process on platinum electrode. The study of the redox potential on the two ligands indicates the role as mediator candidate in the reduction mechanism. We believe that the present work will stimulate the investigations of the chemical features of ligands and their role in biological and medicinal chemistry.

Keywords: *pyridinium compounds, electrochemical, aq. media, cyclic voltammetry*

INTRODUCTION

The concept of molecules with biologic properties is very interesting and opens an important field on research in molecular biology and

---

[a] *University of Medicine and Pharmacy "Carol Davila", Faculty of Pharmacy, Department of Medicinal Chemistry, 6 Traian Vuia Str., RO-020022, Bucharest, Romania*
[b] *"Dunarea de Jos" University, Faculty of Sciences and Environment, Department of Chemistry, Physics and Environment, 47 Domneasca Str., RO-800008, Galati, Romania*
[*] *Corresponding author: getac@ugal.ro*

pharmacology. Quaternary ammonium salts and their variously substituted derivatives are important biological agents and have found applications in different fields [1-3]. An increasing attention is given to the synthesize and characterization of the new pyridinium derivates based on their wide range of interesting properties such as their ability to easily functionalise at the nitrogen heterocyclic atom in order to obtain useful compounds for biological and industrial applications [4-9]. Furthermore, their application in gene delivery, pharmaceutics, polymerization stand on their ability to be employed as electron carriers, model system in photosynthesis, neuromuscular agents, enzyme inhibitors, antimicrobial agents, initiators of cationic polymerization and phase transfer agents was reported [5, 7-9]. Pyridinium derivates were found to be ionic liquids whereas others compounds, named viologens (4,4'-bipyridinium salts) demonstrated electrochromic properties [10].

We previously reported the synthesis of a novel series of heterocyclic compounds with nitrogen using an efficient synthesis through N-alkylation of pyridinium substituted nucleus with reactive halides. The structures of the compounds were fully characterized using IR, ^{1}H-NMR, MS and elemental analysis. In addition, their thermal stability was determined using the thermogravimetric analysis [3, 11-12]. The elucidation of the electro-changes of the synthesized compounds is useful for the electrochemical investigation [13]. Compounds can be used as biological redox indicators, electrochemical sensors, electronic transporters and precursors for compounds such as indolizines, biologically active compounds which can serve as potential markers and fluorescent ligands for estrogen receptors [14-20]. This research also helps us to understand the mechanism of cycloadditon of these ligands with dipolarophils for obtaining indolizine compounds [21]. The behaviour of the compounds bearing aryl substituents on the quaternarized nitrogen atoms has been examined showing that the spectroscopic and electrochemical properties are fine tuned by the nature of the nitrogen ring [22]. These quaternisation reactions will be done in aq. media. The redox potentials of the compounds are interesting for determining the donor - acceptor properties of the radicals [23]. Another aspect that we will study in the future would be understanding reactions of cycloaddition and substitutions, realized in aq. media [24-25]. Viologens compounds present a significant interest due to their changing properties and colour connected to the reaction medium [11-12]. In this work, the electrochemical behaviour of two pyridinium heterocyclic compounds has been recorded for the first time by cyclic voltammetry in aq. media.

RESULTS AND DISCUSSION

Stability of ligands

The synthesized compounds were N,N' di-(p-bromophenacyl)-4,4'-bipyridinium dibromide (named rigid Ligand-Lr) and N,N' di-(p-bromophenacyl)-1,2-bis(4-pyridinium)-ethane dibromide (named mobil Ligand-Lm) [3]. The stability of ligands derived from 4,4'-bipyridil (Lr) and 1,2-bis(4-pyridil)-ethane (Lm) respectively was performed by spectrophotometric analysis and open circuit potential (OCP) measurements. The aq. compounds (0.1 mM) were prepared and the analysis was conducted by adjusting the pH between the range of 3 and 11. Solutions shown variable colours depending on pH, beginning from light yellow to violet (N,N' di-(p-bromofenacyl)-4,4'-bipyridinium dibromide (Lr) and orange (N,N' di-(p-bromofenacyl)-1,2-bis(4-pyridinium)-ethane dibromide (Lm). A discoloration of the solution was observed when the ligand concentration was lower than 10^{-5} M.

The UV/VIS spectra of aq. solutions were analyzed at 264 nm (λ_{max}) [3, 25] with the purpose to study the initial stability and after 24 hours (Figure 1). The highest absorbance are registered for Lr on pH 3 (weak yellow colour) and pH around 7 (weak violet colour) when protonated species are formed. Fresh aq. Lr solution presents most stable form in lower alkaline medium (pH around 8). On the other hand, Lm is more stable in lower acidic medium (pH around 6) and the dication form is unstable in alkaline media. This behaviour suggests the presence of the anionic species AH^- at the addition of base excess and transition from AH_2 to AH^-.
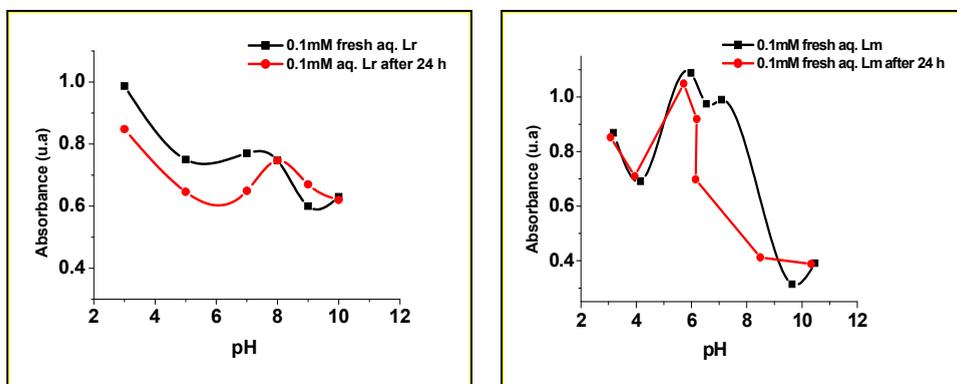
Figure 1. Overview of absorbance *vs.* pH of aq. Lr and Lm.

The ligands solutions kept at room temperature shown after 24 hours a slightly absorbance change; for Lr decreases with about 2 units. The electro-oxidation process is more active due to favourable dynamic

acid-basic equilibrium of the electrons transfer reaction from the dication to produce radical cation (AH$^{\cdot}$), and then neutral specie. At the same time Lm indicates stability in acidic medium (till pH 6), but an evident decrease of absorbance values in neutral and alkaline medium. This behaviour could be explained by the ethylenic group from Lm, that is more favourable for some cycloarrangement additions in alkaline than in acidic media.

The absorbance from UV/VIS spectra are well correlated with OCP measurements. Bispyridinium compounds are organic oxidants and electrochemical techniques are useful to allow the characterization of the electro-oxidation behaviour of electroactive species, to establish the redox potential and to predict the reaction mechanism. The electrochemical investigations of each aq. ligand (0.1 mM) began with monitoring of OCP from fresh solutions (pH acid). Measurements at neutral and alkaline pH were also performed by adjusting pH using buffer solutions. OCP measurements were performed again after 24 hours, 120 hours and respectively 168 hours (7 days) in order to evaluate the electrochemical stability of the acidic - basic equilibrium and electro-oxidation process of compounds kept in closed bottles in the refrigerator (4°C).

Although, initially the aq. ligands presented a difference about 0.5 pH units no significant differences between OCP values (± 2 mV) were found. OCP was around +72 mV *vs.* SCE for fresh aq. ligands. The open potential was also measured for the synthesized salts precursors (0.1 mM) by dissolving them in aq. media. The precursors 4,4-bipyridil (for Lr) presents a E_{WE} = +69 mV *vs.* SCE and 1,2 - bis (pyridil) ethane (for Lm) have a potential of E_{WE} = +75 mV *vs.* SCE which does not indicate essential modifications compared with the new ligands obtained.

After 24 hours a difference of about of 30 mV between the acid aq. ligands was measured for the OCP values; Lr indicates +45 mV *vs.* SCE and Lm indicate + 63 mV *vs.* SCE as a result of their structures. The fresh Lm solutions shown larger variations of OCP values for the entire pH range because it is more unstable due to the position of ethylenic group in base excess. Meanwhile Lr which does not have the ethylene group in its structure is more stable at the same conditions.

In time the OCP data for Lr showed lower variations. Aq. Lr indicates a more positive electro-oxidation potential for the fresh aqueous solutions of pH 6, similar with the solutions kept for 7 days having neutral or alkaline pH. Thus Lr is a more powerful oxidant with greater stability in time and its property is also kept at neutral and alkaline pH. A significant difference was observed for the fresh aq. Lm (pH 5.50) in time, a decrease with 10 mV. Anyway, at the neutral and alkaline pH OCP values for Lm indicated larger variations than those at acidic pH.

Thus, OCP values sustain the ligands structure shown in Scheme 1 and explain their stability as confirmed by the spectrophotochemical measurements. The data results are helpful to provide an explanation for the proposed electro-oxidation mechanism of the ligands but are insufficient data for the reaction kinetics in aq. solutions.

Cyclic voltammograms measurements

The electrochemical measurements give information on the electrochemical state of the organic compounds on the working electrode in an active or passive state. CV provides information about the redox couples and this remains the most attractive gain of this technique [26]. CVs data are useful for the presence of the protoned/deprotonated structures and supply information about the kinetics of reactions. A series of CVs measurements were obtained in aq. media of the ligands at variable pH from acidic to alkaline range and different scan rates of the potential applied.

Effect of the pH

The pH has an important role for the organic compounds as a result of the proton concentration from aq. media. Changes in CVs are the result of the different ligand structures in aq. solutions with variable pH (Figure 2 and 3). The shapes can explain the influence of functional groups from the ligand molecule in aq. media correlated with their stability in time, depending on pH.
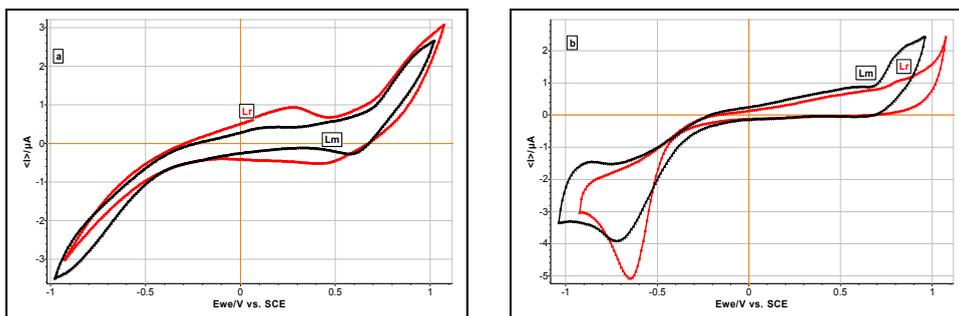
Figure 2. Cyclic voltammograms in aq. Lr and Lm from fresh solutions with initial pH (a) and at pH 9.0 (b); E = ± 1.0 V *vs.* SCE, from a negative direction, scan rate 100 mVs^{-1}(a), scan rate 50 mVs^{-1}(b).

A similar behaviour appears in the redox process on platinum electrode in both compounds mainly for the anodic current peak. The corresponding peak of the initiation of the anodic oxidation indicates that at least a prototropic couple (AH$_2^-$/AH$^-$) of the organic compounds is present. The anodic current peak (i$_a$) around of + 300 mV *vs.* SCE is more evident for Lr and it appears diminished for Lm, with a difference of 0.5 µA and shifted to a less positive potential.

The voltamogramms sustain the electrons transfer between functional groups of ligands and the prototropic couple, depending on the pH of the solution. If the pH solutions are changed the typical voltammograms will be observed. Figure 2b shows the voltammograms of aq. ligands at pH of 9.0 indicate the electron transfer by characteristic cathodic peak on Pt electrode which is similar in both salts under the same potential conditions and scan rates applied (E = 1 V; 50 mVs^{-1}). Lm indicates a slight modification to more negative potential as a result of a favourable rearrangement of ethylenic group present in the structure. An anodic peak can be observed related with the oxidation of Lr to Lr product (radical anion), as an irreversible process due to its higher reactivity. The compounds described by CVs measurements could be more complex and show more than a single redox transaction. Water as proton acceptor suggests that in this case, the proton charge is delocalized over the primary shell of water molecules firmly formed around the pyridinium ligand. Lr indicates an evident reduction process in the alkaline domain (around pH 9), having quite a different behaviour, compared to the acidic and neutral domains (Figure 3a). The scan rate also remains an important condition in these electron transfers (Figure 3b). In alkaline pH, the current peak is shifted to more positive potential around +800 mV while in cathodic reduction is an intensive active process. At the same time Lm does not indicate an obvious electro-oxidation transformation (Figure 4).
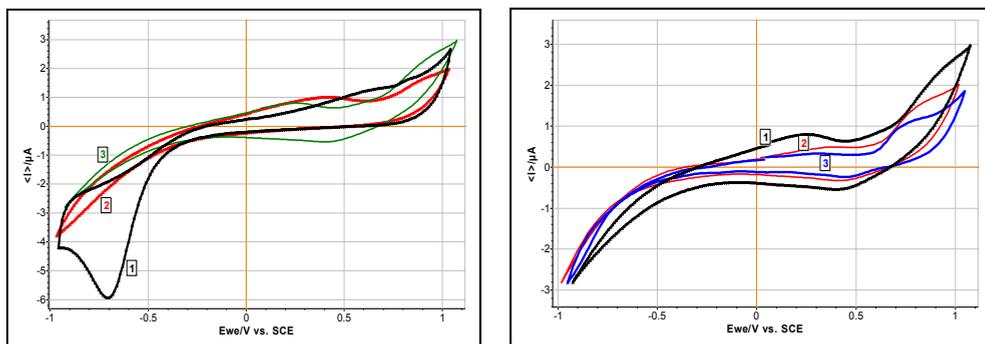
Figure 3 (a). Cyclic voltammograms measured in aq. Lr ranging pH: 9.0 (1); 7.0 (2) and 6.0 (3); E = 1 V, scan rate 100 mV s^{-1}. (**b**) Cyclic voltammograms measured in aq. fresh Lr (pH 6.0) at different scan rate: 100 mVs^{-1}(1); 50 mVs^{-1}(2) and 20 mVs^{-1}(3), E = 1 V.

It is evident that in the cathodic process on Pt electrode and at alkaline pH the deprototropic conjugate couple (from AH$^-$ to AH) changes slower in comparison with acid and neutral pH. A blockage of the electron transfer by adsorption on Pt substrate of the reduced pyridinium ligands can suggest this behaviour.

Effect of the potential scan rate

There are registered CVs on platinum electrode for both aq. ligands (0.1 mM) at different scan rates (100 – 20 mVs^{-1}) for E = 1 V (Figures 3b and 4a). No significant shifts were observed in the redox potential when the scan rate was increased from 20 to 100 mVs^{-1}in CVs of fresh aq. Lr at 6.00 pH (Figure 3b). Moreover, an increase of the anodic current was obtained when the scan rate was higher as an effect of faster prototropic conjugate in the form of $AH_2/AH^{-}\cdot$or AH^{-}/AH_2 from ylides stage that immediately formed when a potential is applied [25].
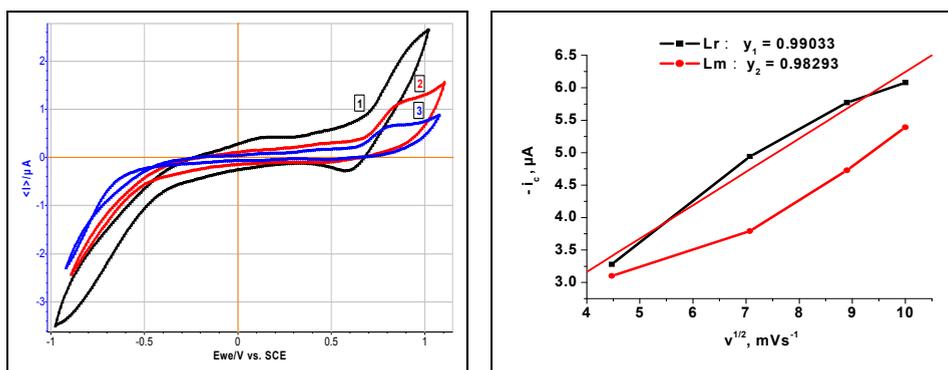
Figure 4 (a). Cyclic voltammograms in aq. fresh Lm (pH 5.50), at different scan rate: 100 mVs^{-1} (1); 50 mVs^{-1} (2) and 20 mVs^{-1} (3), E = 1 V. **(b).** Plot of cathodic current *vs.* square root of scan rates.

The cathodic peak position obtained at 100 mVs^{-1} corresponds to the redox changes from potential (E_{pc}) of + 350 mV for Lr to the potential of + 600 mV for Lm (Figure 4a). A comparative study of aq. alkaline pH shows the different behaviour between the pyridinium heterocyclic ligands. The electrochemical parameters are presented in Table 1.

Table 1. Electrochemical data *vs.* scan rate of the potential applied for aq. pyridinium ligands at pH 9.00.

scan rate (mV·s^{-1})	- E_{pc} (mV *vs.* SCE)		- i_c (µA)		E_{pa} (mV *vs.* SCE)		i_a (µA)	
	Lr	Lm	Lr	Lm	Lr	Lm	Lr	Lm
100	670	901	6.08	5.39	910	876	2.85	2.35
80	652	886	5.65	4.73	880	780	2.54	2.27
50	647	874	4.94	3.79	790	760	1.66	2.15
20	613	818	3.28	3.10	690	660	1.45	1.87

The reduction peak of ligands was significantly shifted towards a more negative potential, whereas a small shift in the oxidation peak was obtained at aq. Lr. Lm presents a different potential between the anodic peak and the cathodic peak that is considered an effect of quasireversible redox process of electrons transfer, due to presence of the ethylenic group. Both ligands show characteristic peaks as a result of electron transfer between the functional groups, more evident on cathodic range at alkaline solutions. The cathodic peak at very lower potentials cannot be clearly assigned to reduction (Figure 4b).

Assuming that the electron transfer rate is faster, the current i_a is measured while the potential decreases and it will be directly related to the diffusion rate of oxidized species on the Pt surface, by the flux governed by Fick law [26]. Thus, the oxido-reduction process involves a transfer of hydrogen proton and electron transfer of pyrididium ligands functioning as mediators in the aq. media. The peak is characterized by E_p, i_a and there is a shift peak while the pH increase.

The pyridinium ligands generate some current waves in cyclic voltammogram which are described as two typical one-electron transfer steps. The first step is reduction of AH_2 (AH_2/AH^-) and the second step is the role of electron carrier of pyridinium ligand ($AH^-/AH^{·-}$). To explain this behaviour, a mechanism can be proposed when a catalytic reduction of the H^+ ion takes place via a neutral (alkaline) an intermediate of 1 H adsorbed on the Pt electrode in aq. media. The addition of proton donor produces changes, not only to the electroactive species, but also to the overall mechanism of reaction, making it simultaneous. Aq. alkaline ligands indicate an electron transfer irreversible, confirmed also by the cathodic peak on electrode, which is more evident on Lr than on Lm; it is a well correlation that ligands has different mechanism depending on aq. pH.

CONCLUSIONS

Pyridinium heterocycle ring of dibromide ligands having as difference an ethylenic group in their structure have been synthesized and the electrochemical properties have been explored. The stability of the acidic - basic activity of solutions depends on pH.

Spectrophotochemical absorbance registered in different solutions, fresh and kept at constant temperature indicates that pH 6-7 is better for stability of aq. ligands. The open circuit potential is a useful tool to characterize the ligands stability in aqueous media on Pt electrode. CV has been applied to characterize the electron transfer of aq. pyridinium ligands and the possibility to become a useful mediator. Electrochemical measurements offer

the possibility to study the redox potential and the influence of pH and scan rates applied.

A good correlation was found between the electro-oxidation potential and the stability in aq. media of the ligands at acidic and neutral pH. Moreover, at alkaline pH, the pyridinium ligands indicate a difference taking into account the acidic-basic and electrochemical properties which might result from the most favourable arrangement.

The presence of the ethylenic group diminishes this effect as a result of more cyclofavourable addition in alkaline pH. We believe that the present work will stimulate the investigations; CV can be used to characterize the reduction ability and electrochemical behaviour of the compounds as pyridinium ligands and their role in biological chemistry. This study helps us better understand the ligands mechanism in aq. media and our purpose is to use them in cycloaddition to obtain indolizines in catalytic systems and for the synthesis of new Ln complexes.

EXPERIMENTAL SECTION

The pyridinium salts were prepared starting from 4,4 bipyridil (for Lr) and 1,2 - bis (pyridil) ethane (for Lm) and phenacyl bromide by substitution reactions as it was mentioned in reference 3 Scheme 1. All chemical reagents were commercially available of analytical grade with maxim purity (Merck) and were used without further purification.
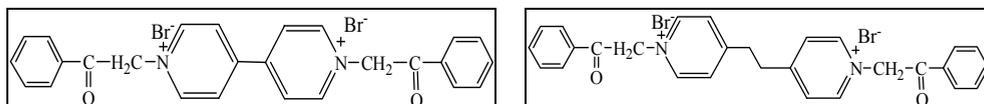
Scheme 1. *Structure of bipyridinium salts Lr and Lm.*

Both dibromide ligands solutions (0.1 mM) were prepared using deionized water (1.6 µS cm^{-2} - measured with Milli-Q Millipore Losheim France). The Lr solution presents initially a pH of 6.0 and Lm a pH of 5.50. The pH adjustment of solutions for a neutral and alkaline media was made using different buffer solutions, according with [20, 27].

The electrochemical behaviour of ligands (0.1 mM) as deaerated aq. solutions, using KCl 0.1 M as support electrolyte was examined by cyclic voltammetry (CV) at 20°C (Biologic SP-150, with EC-Lab® Express v 9.46 software): three-electrode cell (20 mL capacity): WE -platinum (1.6 mm^2) with a platinum auxiliary electrode, and an saturated calomel reference electrode RE (E_{SCE} = 0.241 V *vs.* SHE). The potential range of E = 1 V *vs.* SCE from a negative direction. Scan rates were: 100 mVs^{-1}, 80 mVs^{-1}, 50 mVs^{-1} and 20 mVs^{-1}.

The measurements were repeated for five times to mark the significant changes that might appear. Three types of solutions were analyzed: fresh-made solutions (lower acidic pH), neutral and alkaline solutions by controlling their pH using buffering solution. The measurements were registered and after 24 hours, 120 and respectively 168 hours (7 days) to relive the electrochemical behaviour of the ligands in time. The aq. solutions were kept in closed bottle refrigerator at 4°C.

ACKNOWLEDGMENTS

REFERENCES

1. A.D. Knauft, *Effect Weed Technology,* **2012**, *4*, 866.
2. R.J. Dinis-Oliveira, P. Guedes de Pinho, A.C. Silva Ferreirad, M.S. Silvae, A.C. Afonso, M. de L. Bastos, F. Remiao, J. Alberto Duarte, F. Carvalho, *Toxicology*, **2008,** *249,* 130.
3. I. Druta, R.M. Dinica, E. Bacu, M. Andrei, *Analele Stiintifice ale Universitatii "Al.I. Cuza" din Iasi, seria Chimie*, 1**998**, *6*, 19.
4. L. Ruhlmann, J. Hao, Z. Ping, A. Giraudeau, *Journal of Electroanalytical Chemistry,* **2008**, *621*, 22.
5. A. Schiller, B. Vilozny, R.A. Wessling, B. Singaram, *Analytical Chimica Acta*, **2008**, *62,* 203.
6. J.K. Clark, P. Cowley, A.W. Muirb, R. Palin, E. Pow, A.B. Prossera, R. Taylora, M.Q. Zhang, *Bioorganic & Medicinal Chemistry Letters*, **2002**, *12,* 2565.
7. E.L. Clennan, *Coordination Chemistry Reviews,* **2004**, *248,* 477.
8. J. Pernak, J. Kalewska, H. Ksycinska, *European Journal of Medicinal Chemistry,* **2001**, *36*, 899.
9. R.M. Dinica, F. Marchetti, C. Pettinari, B.W. Skelton, A.H. White, *Inorganic Chimica Acta,* **2007**, *360*, 2609.
10. N.M. Rowley, R.J. Mortimer, *Science Progress,* 2**002**, *85*, 243.
11. B. Furdui, R.M. Dinica, M. Demeunynck, M.I. Druta, Al. Vlahovici, *Revue Roumaine de Chimie,* **2007**, *52*, 633.
12. R.M. Dinica, B. Furdui, G. Bahrim, M. Demeunynck, *Revue Roumaine de Chimie,* **2008,** *53,* 21.
13. R. Palin, J.K. Clark, P. Cowley, A.W. Muir, E. Pow, A.B. Prosserv, R. Taylor, M.Q. Zhang, *Bioorganic & Medicinal Chemistry Letters*, **2002**, *12,* 2569.
14. M. Eda, M.J. Kurth, *Tetrahedron Letters*, **2008**, *42*, 2063.
15. D.H. Evans, *Chemistry Review*, **2001**, *108,* 2113.

16. E.F.V. Scriven, *Chemistry Society Reviews*, **1983**, *12*, 129.
17. J. Pernak, J. Rogoźa, *Arkivoc (Archive for Organic Chemistry),* **2000**, *1*, 889.
18. A.F. Elmosallamy, M, *Analytical Science*, **2004**, *20,* 285.
19. V. Causin, G. Saielli, *Journal of Molecular Liquid*, **2009,** 14541.
20. A. Albert, E.P. Sergeant, "The Determinations of Ionization Constants. A Laboratory Manual", London: Chapman and Hall, **1971**.
21. M. Jiang, E. Sak, K. Gentz, A. Krupski, K. Wandelt, *European Journal of Chemical Physics and Physical Chemistry,* **2010**, *11*, 1542.
22. W. Silva, *Heterocycles,* **1991**, *32,* 11.
23. F. Teplý, M. Čížková, P. Slavíček, V. Kolivoška, J. Tarábekv, M. Hromadováv, L. Pospíšil, *Journal of Physics Chemistry C*, **2012**, *116*, 3779.
24. V. Kolivoška, M. Gál, L. Pospíšil, M. Valášek, M. Hromadová, *Physical Chemistry Chemical Physics,* **2011**, *13,* 11422.
25. B. Furdui, R.M. Dinica, A. Tabacaru, C. Pettinari, *Tetrahedron,* **2012**, *68*, 6164.
26. A.M.O. Brett, M.E. Ghica, *Electroanalysis*, **2003**, *15,* 1745.
27. W.G. Phillips, W.K. Ratts, *Journal of Organic Chemistry*, **1970**, *35*, 3144.

Dedicated to prof. dr. I. C. Popescu
on the occasion of his 70th anniversary

DETERMINATION OF COPPER IN ORANGE JUICE BY VOLTAMMETRIC TECHNIQUE: A COMPARATIVE STUDY OF SAMPLE PREPARATION METHODS

MARIAME COULIBALY[a,b,*], ALFRED N'GUESSAN YAO[a], DRISSA BAMBA[a], MAMIA EL RHAZI[b]

ABSTRACT. In the present work, carbon paste electrodes (CPE) modified with conducting polymers (1,8-diaminonaphthalene, 1,8-DAN) combined with rotating disk electrode (RDE) was applied to determine copper in orange juice samples. Copper (II) was preconcentrated at open circuit potential on the modified electrode. Then, the preconcentrated metals were oxidized by scanning the potential of the electrode from -0.4 to 0 V using differential pulse anodic stripping voltammetry (DPASV). Samples were analyzed with and without previous treatment. The current peak was high in orange juice sample digested with wet ashing and dry ashing procedures compared to those in sample without pretreatment. The wet ashing procedure was chosen for the digestion of orange samples because it required shorter time. The results obtained were validated by inductively coupled plasma atomic emission spectroscopy (ICP-AES).

Keywords: carbon paste electrode, 1,8-diaminonaphtalene, differential pulse anodic stripping voltammetry, rotating disk electrode, orange juice

INTRODUCTION

Fruits are known as good for health because they are sources of vitamin C, carotenoids, minerals and various kinds of antioxidants. However in production process, the quality of fruit products (juice) can be affected with increasing concentration of toxic compounds and environmental pollutants especially heavy metals.

---

[a] *Ecole Normale Supérieure, Laboratoire des Sciences Physiques Fondamentales et Appliquées, 08 BP 10 Abidjan, Republic of Côte d'Ivoire*
[b] *Laboratoire d'Électrochimie et de Chimie Physique Faculté des Sciences et Techniques, BP146, Mohammedia, Morocco*
[*] *Corresponding author: mamecoul2002@yahoo.fr*

Copper is important as an essential trace element in biological systems [1]. Acute copper poisoning occurs when several grams of copper salt are ingested. The maximum tolerable daily intake for copper is 0.5 mg per kg body weight [2]. Wilson's disease is a prototypical disease caused by copper toxicosis, affecting first the liver and later the central nervous system, kidneys and eyes. Monitoring trace or ultra trace copper in canned juice is very important. For this reason, a sufficiently selective and sensitive method for reliable determination of copper would be of great interest. Commonly, the analytical methods for the quantification of heavy metals are neutron activation analysis (NAA), atomic absorption spectrometry (AAS), inductively coupled plasma-mass spectrometry (ICP-MS) and inductively coupled plasma atomic emission spectroscopy (ICP-AES), which are also used for the analysis of copper in juices [3,4].

The electrochemical technique, especially stripping voltammetry for the trace analysis of metal ions, obtained considerable interest because of its low cost, easy operation, good sensitivity, high selectivity and accuracy [5]. It is well known that voltammetric methods coupled with hydrodynamic sensors is very advantageous. The rotating-disk electrode technique allows mass transport control, providing thus higher levels of sensitivity and very low detection limits [6].

The use of carbon paste electrodes CPEs in analytical chemistry has attracted considerable attention in recent years especially, chemically modified carbon paste electrodes (MCPE) [7-9]. Complexation reactions with organic or inorganic reagents in carbon paste electrodes (CPE) have been reported [10–12]. The poly (1,8-DAN) incorporated in carbon paste electrode leads to a conducting polymer able to form complex with copper [13]. This polymer has been used for detection of lead and copper in water [13, 14]. In addition, it was showed that metal ions, which can compete for complexation at binding sites on the poly (1,8-DAN) film, are lead, mercury, zinc or iron. The interference can be eliminated using appropriate masking agent.

The aim of the present study was to apply carbon paste electrode modified with poly (1,8-DAN) for the determination of copper in orange juice samples, with and without pretreatment of the juice. In this article, we address the detection issues of copper in food samples that occur when MCPE is used after different treatment methods.

RESULTS AND DISCUSSION

Synthetic Cu^{2+} solutions analysis

The surfaces of fresh MCPEs were immersed in aqueous solution under rotation of the electrode. The preconcentration of Cu^{2+} was carried

out under open circuit. Following the preconcentration step at open circuit potential, the rotation of electrode was stopped and the solution was left to equilibrate for 30 s. An initial potential of –0.6 V was applied for an appropriate time and then scanned from –0.4 V to 0 V using differential pulse anodic stripping voltammetry. An anodic peak at –0.2 V (*vs.* ECS) was observed (see figure 1). No deaeration of the solution was required. The preliminary studies of copper accumulation have been performed on bare electrode and on modified electrode. In the same solution and under the same conditions, the results show that an anodic stripping peak at –0.2 V was observed for CPE (1.3 µA) and a well defined stripping peak was observed at the same potential on MCPE (11.5 µA) [14]. It is important to mention that the bare carbon paste electrodes were found to be less efficient and less reproducible compared to the modified electrode. Because of complexity of matrix, the copper content was always determined by the multiple standard addition method, each data point used was the average of at least five distinct measurements.

Calibration curve

Using the chosen optimized condition a calibration graph for the determination of Cu (II) was constructed for a concentration range 0.1 – 250 ppb. The calibration plot in Figure 1 is linear from 0.1 – 250 ppb with R^2= 0.9998.
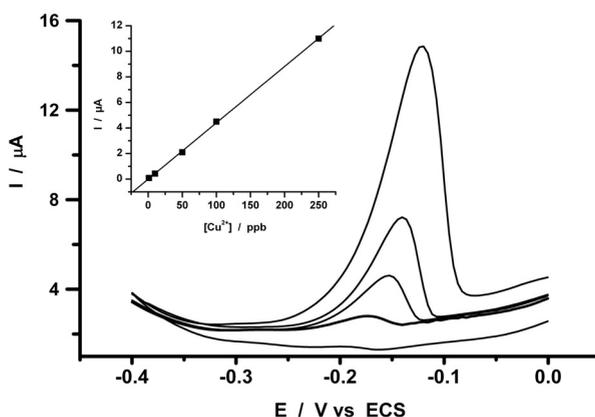
Figure 1: Calibration plot for copper (II) in 0.1 M L^{-1} HCl, preconcentration time 180 s, initial potential –0.6 V, potential step height 10 mV, pulse amplitude 50 mV, duration of 50 ms, speed of rotation 300 rpm. Concentration range 0.1 to 250 ppb.

The detection limit of Cu (II) was 0.05 ppb based on three times blank noise (3σ). The relative standard deviation of six determinations was 4.7% at 100 ppb.

Determination of copper in orange juice samples without pretreatment

The method proposed was applied to the determination of copper in orange juice samples, where possible interferences due to the complexity of the matrix could appear. No copper traces were found when the proposed procedure was used in the range of 0.1 to 250 ppb. Samples don't contain copper or, matrix complexity does not allow copper detection. Fruits contain acids such as: citric, tartaric, and malic acids that have the power of chelating heavy metals. In general, the concentration of metals in fruit juice and orange juice in particular depends on several factors related to the geographical origin of oranges [15], contamination by fertilizers, pesticides, the industrial process or the acidity. Tufuor et al. [16] have detected any trace of copper in orange juice samples by ICP-AES. However, the concentration of copper in orange juices available in the Polish market was determined using AAS by Krejpcio et al., the results show of copper concentrations ranging from to 47 to 1750 ppb [17].

Then, a new calibration graph was constructed in the concentration range 100 ppb to 1 ppm. The equation of calibration plot was $I/A = -19.02 + 30.76[Cu^{2+}]/\mu g\ L^{-1}$ with a regression coefficient of 0.996. Then, five replicate determinations of Cu (II) in spiked orange juice samples were carried out using the standard addition method. Table 1 summaries the recoveries of the results obtained from five replicate determinations of 500 ppb in an orange juice sample. A recovery between 98% and 118% were obtained and show that the procedure can be applied for the determination of Cu (II) in orange juice with a concentration above 500 $\mu g\ L^{-1}$. The minimum concentration of copper determined is 500 $\mu g\ L^{-1}$, which is within the safe limit set by World Health Organization (WHO), *i.e.* 3000 $\mu g\ L^{-1}$ [18]. This method based on stripping voltammetry could be used to detect copper in assessment of orange juices quality.

Table 1. Recovery data for copper (II) ($\mu g\ L^{-1}$) obtained for orange juice samples without pretreatment.

Sample	$[Cu^{2+}]$ add / $\mu g\ L^{-1}$	$[Cu^{2+}]$ found / $\mu g\ L^{-1}$	Recovery / %
S_1	500	590	118
S_2	500	490	98
S_3	500	535	107
S_4	500	~500	100
S_5	500	~500	100

Detection of copper in orange juice after pretreatment

Under the conditions reported in calibration section, MCPEs were applied to the analysis of orange juice samples after pretreatment (wet ashing and dry ashing).

Considering the safe limit set by WHO, *i.e.* 3 mg L^{-1} and the limit of detection of DPV method developed 0.05 µg L^{-1} we determined the concentration of copper recovered from five samples of orange juice spiked with 0.2 mg L^{-1} of copper treated by wet-ashing method analyzed by DPASV and by ICP-AES. In the Table 2, the results of copper determination in five juice samples obtained by DPASV and validated by ICP-AES method have been presented; the obtained recoveries were ranging from 95 to 98%.

Table 2. Detection of Cu (II) concentration in five orange samples treated by wet-ashing method, analyzed by DPASV and by ICP-AES.

amples	[Cu^{2+}] by DPASV µg L^{-1}	[Cu^{2+}] by ICP-AES µg L^{-1}	Recovery %
S1	186 ± 4.7	198	94
S2	182 ± 5.6	192	95
S3	192 ± 4.5	197	97
S4	208 ± 4.2	212	98
S5	205 ± 6.3	218	94

These results show that it was possible to use DPASV on CPE modified by poly (1,8-DAN) film in order to determine low concentration of copper by a judicious choice of the experimental conditions and after pretreatment. The comparison between DPASV method and ICP-AES method shows that there is satisfactory agreement between the two techniques.

Table 3 presents the results of copper concentrations in five orange juice samples obtained using wet ashing and dry ashing digestion methods. The simple comparison between these two pretreatment methods shows that the wet ashing treatment provides the same recoveries obtained for dry ashing method. However, the wet ashing treatment requires a very short time than the dry ashing method.

Table 3. Results for the determination of Cu (II) concentration in orange juice samples treated by dry ashing and wet ashing digestions methods.

Samples	[Cu^{2+}] by wet ashing / µg L^{-1}	[Cu^{2+}] by dry ashing / µg L^{-1}
S1	186 ± 4.7	182 ± 2.7
S2	182 ± 5.6	175 ± 4.5
S3	192 ± 4.5	178 ± 5.2
S4	208 ± 4.2	205 ± 4.6
S5	205 ± 6.3	198 ± 3.4

CONCLUSIONS

In this paper, we applied a novel method to determine copper in juice; it has been proved that carbon paste electrode modified with poly (1,8-DAN) can be used for the determination of copper in orange juice samples. However for the determination of low concentration, the sample pretreatment is necessary. Moreover, DPASV can be certainly a good alternative to spectroscopic methods owing to its inexpensive instrumentation and the simple operation. In addition, Copper levels in the samples analyzed were within the limit set by WHO and therefore pose no threat to public health.

EXPERIMENTAL SECTION

Reagents

All chemicals were of analytical grade. 1,8-DAN was purchased from Sigma. Copper sulphate was obtained from Riedel-de Héan. Solutions were prepared with distilled water. Standard copper (II) stock solution was prepared by dissolving $CuSO_4$ in water. Diluted copper standards for optimization studies were prepared from this solution. All experiments were carried out at room temperature (25°C). A solution of 0.1 M HCl served as supporting electrolyte.

Electrochemical measurements

Electrochemical experiments were carried out with an Autolab PGSTAT 10 potentiostat (Ecochemie, Utrecht Netherlands) controlled by 4.8 software. A rotating disk carbon paste and a rotating disk modified carbon paste electrode were used as working electrode (WE, Φ = 3 mm). A rotating disk electrode was used during the preconcentration step. A saturated calomel electrode (SCE) was used as the reference electrode (RE) and a platinum wire was used as the counter electrode (CE). The pH was adjusted using a Fisher Scientific Accumet AB15 BASIC pH meter. Analysis ICP-AES were carried out using an Ultima 2 Jobin Yvon Model spectrometer.

Preparation of electrodes

The modified carbon paste electrode (MCPE) was prepared by thoroughly mixing weighed amounts of monomer (0.1 g of 1,8-DAN dissolved in a small quantity of acetonitrile) with 1 g of graphite powder and 0.3 mL of paraffin oil until a uniformly wetted paste was obtained. The mixture was kept at room temperature for one day to let the solvent evaporate. After that, the paste was inserted into the cavity of the electrode. The electrode surface could be renewed by simple extrusion of a small amount of paste from the tip of the electrode. Otherwise, before each use the electrode surface, it was rubbed with a piece of paper until a smooth surface was observed.

Sample preparation

Five samples of orange juice from Morocco were purchased on the market of Mohammedia. For the determination of copper by the proposed method in juice, three ways were used.

Procedure a: The sample were filtered through a membrane (0.45 µm), diluted and adjusted to pH < 2, without any other pretreatment.

Procedure b: Pretreatment of orange juice was performed using an oxi-acidic mixture of 5ml HNO_3 (67%) and 5 ml of H_2O_2 (37%) for 25 ml of sample. This mixture was heated until all the organic matter was destroyed. The final solution was transferred to a 50 ml volumetric flask. After that, 5 ml of acetate buffer (1 M) was added. The pH of mixture was adjusted at 2 and diluted with distilled water until 50 mL.

Procedure c: orange juice samples were submitted to degasification by heating reflux during 40 min under 120 °C. After that, 5 ± 0.5 g of sample was placed in a high form porcelain crucible. The furnace temperature was slowly increased from room temperature to 550 °C in 1 h. The samples were ashed for about 24 h until a white ash residue was obtained. The residue was dissolved in 5 ml of HNO_3 (25%, v/v) and the mixture, when necessary, was heated slowly to dissolve the residue. The solution was transferred to a 50 ml volumetric flask. The pH of mixture was adjusted at 2 and diluted with distilled water until 50 mL.

ACKNOWLEDGMENTS

REFERENCES

1. G. Barceloux, *Clinical Toxicology*, **1999**, *37*, 217.
2. *** - "Evaluation of certain food additives and contaminants (Twenty-sixth report of the Joint FAO/WHO Expert Committee on Food Additives)", *WHO Technical Report Series, No. 683,* **1982**.
3. H. Ofori, M. Owusu, G. Anyebuno, *Journal of Scientific Research and Reports*, **2013**, *2,* 423.
4. C.M.A. Iwegbue, S.O. Nwozo, E.K. Ossai, G.E. Nwajei, *American Journal of Food Technology,* **2008**, *3,* 220.
5. P.J.S. Barbeira, L.H. Mazo, N.R. Stradiotto, *Analyst*, **1995**, *120*, 1647.

6. C.A. Wijayawardhana, S. Purushothama, M.A. Cousino, H.B. Halsall, W.R.J. Heineman, *Journal of Electroanalytical Chemistry*, **1999**, *468*, 2.
7. M. Elyasi, M.A. Khalilzadeh, H. Karimi-Maleh, *Food Chemistry,* **2013**, *141*, 4311.
8. H. Karimi-Maleh, P. Biparva, M. Hatami, *Biosensors and Bioelectronics, 2013, 48*, 270.
9. M.R. Shahmiri, A. Bahari, H. Karimi-Maleh, R. Hosseinzadeh, N. Mirnia, *Sensors and Actuators B*, **2013**, *177*, 70.
10. R.M. Takeuchi, A.L. Santos, P.M. Padilha, *Analytica Chimica Acta*, **2007**, *584*, 295.
11. M.G. Enass, *Talanta*, **2010**, *82*, 646.
12. B.S. Sherigara, Y. Shivaraj, R.J. Mascarenhas, *Electrochimica Acta*, **2007**, *52*, 3137.
13. S. Majid, M. El Rhazi, A. Aziz, *Microchimica Acta*, **2003**, *143*, 195.
14. M. Coulibaly, M. El Rhazi, I. Adraoui, *Journal of Analytical Chemistry,* **2009**, *64*, 632.
15. K. Robards, M. Antolovich, *Analyst,* **1995**, *120*, 1.
16. J.K. Tufuor, J.K. Bentum, D.K. Essumang, J.E. Koranteng - Addo, *Journal of Chemical and Pharmaceutical Research,* **2011***, 3*, 397*.
17. Z. Krejpcio, S. Sionkowski, J. Bartela, *Polish Journal of Environmental Studies,* **2005***, 14*, 877.
18. *** - "Guidelines for drinking water quality. Recommendations", 1st Ed., WHO, Geneva, **1985**, vol. 1, 130 p.

Dedicated to prof. dr. I. C. Popescu
on the occasion of his 70ᵗʰ anniversary

CHARACTERIZATION OF A MODIFIED GRAPHITE ELECTRODE OBTAINED BY HEMIN ELECTROPOLYMERISATION

GRAZIELLA L. TURDEAN[a*]

ABSTRACT. A new modified electrode (G/polyHm) was obtained by electropolymerisation of iron (III) protoporphyrin (IX) (hemin, Hm) at the surface of a graphite electrode (G), by repetitive scanning the potential between -0.85 and 0 V *vs.* Ag/AgCl,KCl$_{sat}$. The cathodic peak revealed by linear sweep voltammetry at the electrode in phosphate buffer, pH 8, corresponds to one electron transfer process occurring at the Hemin(Fe^{3+})/ Hemin(Fe^{2+}) metallic center of the immobilized hemin. All the estimated electrochemical parameters are in accordance with the values reported for immobilized hemin. The electrode exhibits electrocatalytic properties towards the H_2O_2 and NO_2^- reduction, respectively, proving an enzyme-like behaviour of the immobilised hemin, characterised by hyperbolic Michaelis Menten behaviour, when increasing concentrations of substrate were added, irrespective of the scan rate used.

Keywords: *iron (III) protoporphyrin (IX), linear sweep voltammetry, hydrogen peroxide, nitrite*

INTRODUCTION

Over the past several decades, the greatest interest of the electrochemical investigation techniques is to use a tailor made chemically modified electrode (CME) for the determination of organic and inorganic compounds in sensitive and selective analytical applications [1-3]. According to IUPAC definition [4], the distinguishing feature of a CME is that a generally quite thin ionic or polymeric film of a chemical modifier is bonded to or

---

[a] *"Babeş-Bolyai" University, Faculty of Chemistry and Chemical Engineering, Chemical Engineering Department, 11 Arany Janos St., 400028 Cluj-Napoca, Romania*
[*] *Corresponding author: gturdean@chem.ubbcluj.ro*

coated on the surface of an electrode made of a conducting or semiconducting material. This endows the electrode, with the specific and/ or desirable properties of the film in a rational, chemically designed manner. CME can be obtained by (1) chemisorption, (2) covalent bonding, (3) polymer film coating, or (4) composite mixture. Polymer film-coated electrodes may be further subdivided by the process type used to apply the film: (i) dip-coating, (ii) solvent evaporation, (iii) spin coating, (iv) electrochemical deposition, (v) electrochemical polymerization, (vi) radiofrequency polymerization, (vii) cross-linking. There are several reasons for the use of polymer modification derived from the relevant polymer-film properties: (a) the stability (consisting in the multi-layer resistance to degradation compared with the monolayers), (b) the permeability of various species to penetrate the polymer matrix, (c) the site population measured by the concentration of some designated chemical sites within the polymer film (e.g., the electrochemical responses of the multiple layers of redox sites are larger) and (d) the conductivity of the polymer film which may transport electrons (propagate charge) by localized site-site hopping (electron self-exchange) or by an electron delocalization mechanism, when highly conjugated polymer chains are present. Due to the lack of sufficient knowledge regarding the structure and properties of polymer films and the morphological changes that they undergo when subjected to various chemical, electrochemical and physical processes the mechanism of mass transport and electron transfer is not completely explained [4, 5].

In order to exert more direct control over the chemical architecture of an electrode surface/interface, research in the development of CMEs prepared by electropolymerization, offers a unique strategy to obtain homogeneous and reproducible immobilization of a redox modifier with various degrees of electrochemical activity onto electrode surface, a strong adherence to electrode surface, and a chemical stability of the film [6-8].

Used in numerous electronic and electrochemical devices, metalloporphyrins derivatives are ubiquitous organometallic compounds (containing Mn [9], Fe [2, 9,10], Ni [11]) having attractive physico-chemical properties due to their ability to vary their oxidation states without changing their molecular structure. The electrochemical activity towards a given reaction is primarily monitored by the metal center coordinated to the porphyrin ring as well as, to some extent, by the substituents of the porphyrin molecule [2].

As all iron derivatives, iron protoporphyrin IX (hemin, Hm) uses as electron source the reversible $Hemin(Fe^{3+})/Hemin(Fe^{2+})$ redox couple and shows strong electrocatalytic properties in the presence of many small molecules such as hydrogen peroxide [10, 12-14], oxygen [12], nitrite [10, 12, 13, 15], nitric oxide [2, 9, 10, 12], l-tyrosine [12], organohalides [9], tryptophan and its derivatives [9], and for superoxide [9].

Literature presents hemin coated electrode obtained either by electropolymerisation of metalloporphyrins derivatives [2, 9] or by various methods mentioned above. In terms of enhanced sensitivity, selectivity and stability of the fabricated electrodes when detecting the same analyte, the observed differences, can be attributed to the differences between the fabrication methods [16].

The aim of this paper is to investigate the electrocatalytic and analytical performances of a hemin thin film obtained by electropolymerization on a graphite electrode (G/polyHm), for the catalytic reduction of hydrogen peroxide and nitrite, using linear sweep voltammetry as investigation technique.

RESULTS AND DISCUSSION

Electrochemical characterization of the G/polyHm electrode

Figure 1 shows a typical cyclic voltammogram of 0.5 mM hemin in 0.05 M TRIS buffer + 0.1M KBr (pH 8) as supporting electrolyte on bare G electrode at a scan rate of 0.05 V s^{-1}. The quasi-reversible redox peak (Ia/Ic) pairs of hemin recorded at ca. −0.43 V $vs.$ Ag/AgCl, KCl$_{sat}$ corresponds to the Hemin(Fe^{3+})/Hemin(Fe^{2+}) redox couple.
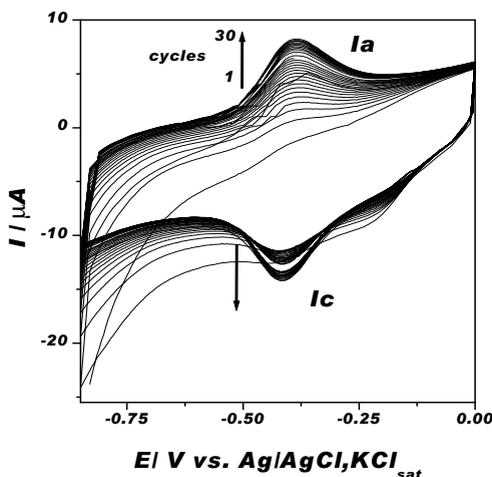
Figure 1. Preparation of G/polyHm modified electrode by cyclic voltammetry. Experimental conditions: 0.5 mM Hm in 0.05 M TRIS buffer + 0.1 M KBr, pH 8; starting potential, -0.85 V $vs.$ Ag/AgCl,KCl$_{sat}$; scan rate, 0.05 V s^{-1}; number of cycles, 30; dearerated solution (with N$_2$).

Repetitive scanning in the reduction potential window results in the electrodeposition and growth of a hemin-based electroactive film, as evidenced by the gradual increase in the peak currents. The electroactive film obtained by electropolymerization (G/polyHm) appears as a stable, deeply colored thin film.

Similar current increase was reported in literature for the electropolymerization in the oxidative window of hemin derivatives [9, 17].

Comparing the electrochemical behavior of G and G/polyHm in phosphate buffer, at 0.005 V s^{-1}, the last electrode emphasis a reduction peak corresponding to the single electron transfer into the metallic center Hemin(Fe^{3+})/Hemin(Fe^{2+}) of the immobilized hemin (Figure 2).

The electrochemical parameters of the G/polyHm modified electrode (Figure 2) are E_{pc} = -0.45 *vs.* Ag/AgCl,KCl$_{sat}$, I_{pc} = 5.76 µA at 0.05 V s^{-1}, parameters which are in accordance with those reported in literature for immobilized hemin using other techniques [13-15].

As expected for a surface confined redox couple [18], in the scan rates ranging from 0.005 - 0.100 V s^{-1} the peak currents (I_{pc}) increase linearly with the scan rate (v) and not with v$^{1/2}$ (Figure 2, inset). The slope of the dependency: log I = (1.6 $\pm$ 0.02) + (0.65 $\pm$ 0.01)log v, R^2 = 0.9994, n = 5 points, is considered a relevant criterion helping to distinguish between the adsorbed (slope $\sim$1) or dissolved (slope $\sim$0.5) redox couples, confirming the slow adsorption of the hemin on the electrode surface.
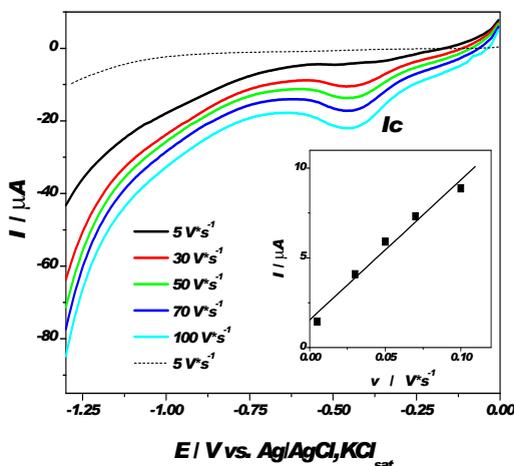
Figure 2. Voltametric response of G (thin dash line) and G/polyHm (thick lines) electrode at different scan rate. Inset: I *vs.* v dependence. Experimental conditions: electrolyte, 0.05 M phosphate buffer + 0.1 M KBr, pH 8; starting potential, 0 V *vs.* Ag/AgCl,KCl$_{sat}$; dearerated solution (with N$_2$).

The electrocatalytic behavior of G/polyHm electrode
Case of hydrogen peroxide.

It is well-known that hydrogen peroxide undergoes peroxidase-mediated reduction *via* both mediated electrochemical reaction and direct electron transport at a potential close to 0.0 V *vs.* Ag/AgCl or at the mediator redox potential. As consequence, detection of hydrogen peroxide *via* peroxidase-catalyzed reaction is preferred, and many biosensors involving the participation of hydrogen peroxide have been developed based on this reaction scheme [19]. Detailed investigation on the electrocatalytic reduction of H_2O_2 at the surface of bare G and G/polyHm were made, as shown in Figure 3A and 3B, respectively.
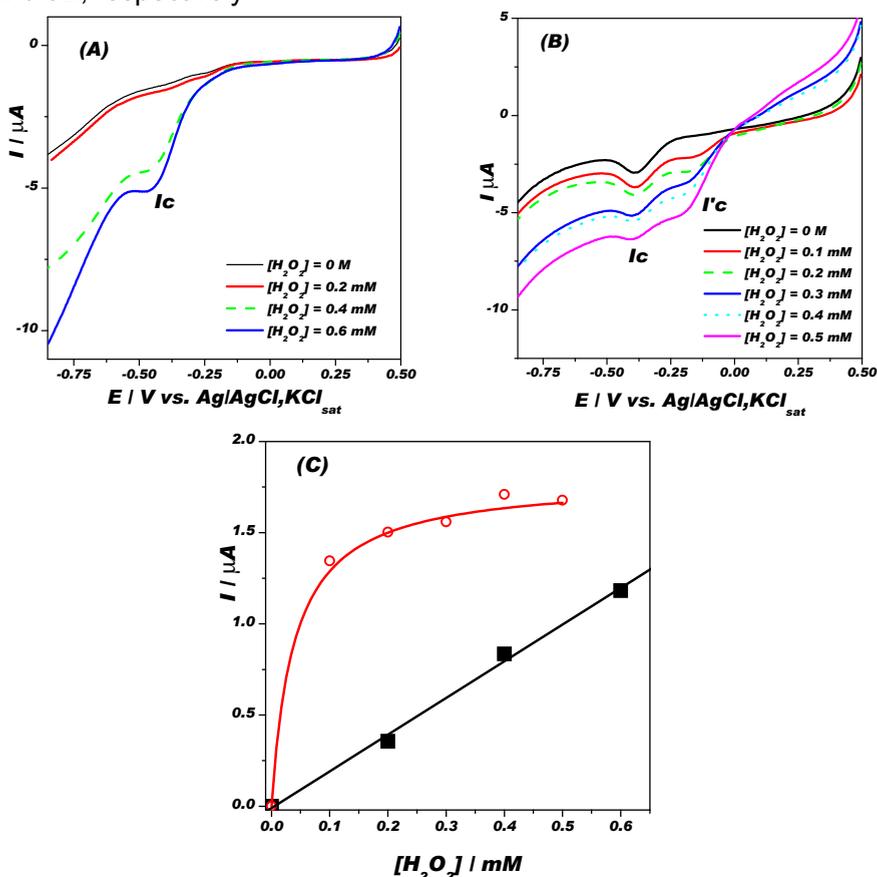
Figure 3. Linear scan voltammograms at G (A, ■) and G/polyHm (B, ●) modified electrode for different concentrations of H_2O_2 and the corresponding calibration curves for peak Ic (C). Experimental conditions: electrolyte, 0.05 M phosphate buffer + 0.1 M KBr, pH 8; scan rate, 0.02 V s^{-1}; starting potential, +0.5 V *vs.* Ag/AgCl,KCl$_{sat}$; dearerated solution (with N$_2$).

As can be seen, the augmentation of the current intensity maybe attributed to the excellent catalytic activity of hemin present on the electrode surface. Comparing with the bare G electrode where the H_2O_2 reduction occurs in one step, at G/polyHm modified electrode a two steps mechanism is observed (peaks Ic, I'c). The following schemes describe the simplified and possible mechanism for the electrochemical catalytic reaction [20]:

$$\text{Hemin(Fe}^{3+}) + H_2O_2 \rightarrow \text{Compound I (Fe}^{4+}= O) + H_2O \qquad (1)$$

$$\text{Compound I (Fe}^{4+}= O) + H^+ + e^- \rightarrow \text{Compound II} \qquad (2)$$

$$\text{Compound II} + H^+ + e^- \rightarrow \text{Hemin(Fe}^{3+}) + H_2O \qquad (3)$$
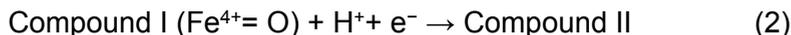
The analytical parameters of the detection of H_2O_2 at bare G electrode were: sensibility (slope of the calibration curve Figure 3C) is 2.15 ± 0.44 mA/M ($R^2 = 0.9897$, n = 4), linear range from 0.1 mM to 0.6 mM, with a detection limit of 0.1 mM. Also, for the detection of hydrogen peroxide *via* enzyme-like catalyzed reaction, the response of the G/polyHm modified electrode follows a Michaelis Menten hyperbolic mechanism having the following kinetic parameters: $K_{M,app} = 0.04 \pm 0.01$ mM and $I_{max} = 1.8 \pm 0.2$ µA, ($R^2 = 0.9968$, $\chi^2 = 0.0017$, n = 6). In this case, the sensibility (calculated as $I_{max}/K_{M,app}$ ratio) is 45.5 ± 0.2 mA/M, which is higher than the value obtained for the bare G, proving the electrocatalytic behavior of immobilized hemin. As expected the detection limit for G/polyHm modified electrode is lower, 0.05 mM (Figure 3C). The obtained values are also in accordance with the literature data [13, 14].

Case of nitrite

The electrocatalytic reduction of nitrite was also studied at both G bare and G/polyHm electrode. The Figures 4A-B show the cyclic voltammograms in phosphate buffer (pH 8.0) upon addition of increasing concentrations of $NaNO_2$. In the reduction potential window, the nitrite is not electroactive, therefore no peak is shown when the hemin is absent (Figure 4A). At low enough scan rate values, in the presence of immobilised Hm (Figure 4B) the reduction mechanism consists of two steps.

In agreement with the literature data, several sequential reduction pathways have been proposed [13, 15, 21, 22]. As example, the first step of the catalytic process involves the formation, in neutral aqueous solution, of an iron-nitrosyl complex as the consequence of the metal-centered Hemin(Fe^{3+})/Hemin(Fe^{2+}) reduction, followed by nitrite binding (peak IIc placed at about –0.7 V *vs.* Ag/AgCl, KCl_{sat}), according to equations 4-5:

$$[\text{Hemin(Fe}^{3+})]^+ + e^- \rightarrow [\text{Hemin(Fe}^{2+})] \qquad (4)$$

$$[Hemin(Fe^{2+})] + HONO + H^+ \rightarrow [Hemin(Fe^{2+})\,(NO^+)]^+ + H_2O \qquad (5)$$

These steps are then followed by the reduction of the iron-nitrosyl adduct (peak IIIc at about –0.9 V *vs.* Ag/AgCl, KCl$_{sat}$) according to equation 6:

$$[Hemin(Fe^{2+})(NO^+)]^+ + e^- \rightarrow [Hemin(Fe^{2+})(NO^\bullet)] \qquad (6)$$
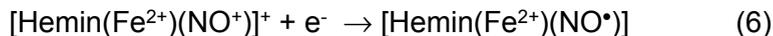
Also, it is worth to mention that no clear direct evidence regarding the presumed above-cited reduction process and no accurate overall catalytic process were established in literature [15, 21].
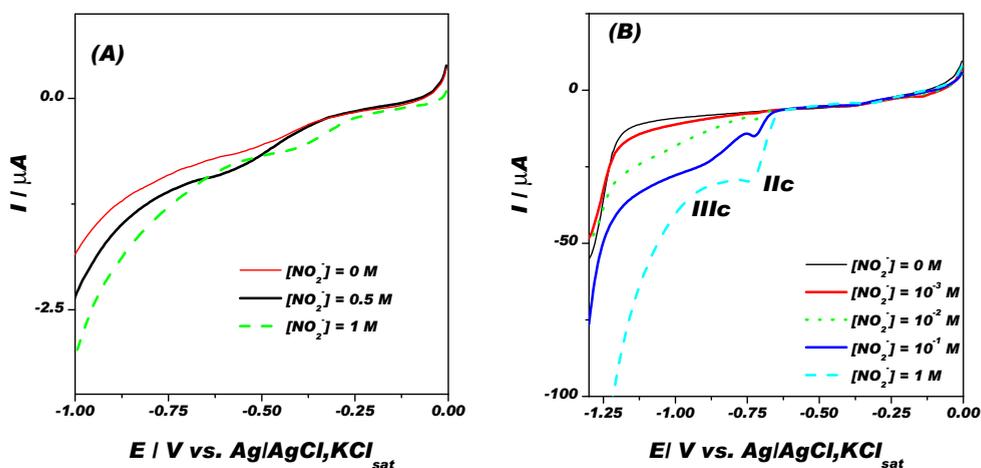
Figure 4. Linear scan voltamogramms at G (A) and G/polyHm (B) modified electrode for different concentrations of NO$_2^-$. Experimental conditions: electrolyte, 0.05 M phosphate buffer+ 0.1 M KBr, pH 8; scan rate, 0.02 V s^{-1}; starting potential, 0 V *vs.* Ag/AgCl,KCl$_{sat}$; dearerated solution (with N$_2$).

At different scan rates, the behavior of the G/polyHm obeys a Michaelis Menten hyperbolic equation (Figure 5), having the kinetic parameters summarized in Table 1.

As expected, the sensibility to nitrite detection of the G/polyHm electrode increases with the increase of the scan rate. However, a scan rate of 0.02 V s^{-1} is appropriate to evidence the intermediates of the two reduction steps.
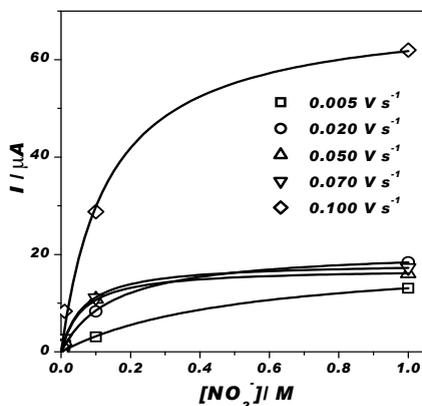
Figure 5. Calibration curve for G/polyHm modified electrode for different scan rate. Experimental conditions: see Figure 4.

Table 1. Kinetic parameters for the detection of NO_2^- at G/polyHm modified electrode. Experimental conditions: see Figure 5.

v / $V s^{-1}$	$K_{M, app}$ / M	I_{max} / μA	S^* / $\mu A/M$	R / n
0.005	0.52 ± 0.180	19.85 ± 2.74	38.30 ± 0.62	0.9961 / 5
0.020	0.15 ± 0.010	21.10 ± 0.63	142.18 ± 0.22	0.9990 / 5
0.050	0.06 ± 0.004	17.15 ± 0.28	281.82 ± 0.28	0.9996 / 5
0.070	0.06 ± 0.003	18.34 ± 0.20	287.16 ± 0.34	0.9998 / 5
0.100	0.13 ± 0.020	70.09 ± 3.29	519.82 ± 0.58	0.9975 / 5

*sensitivity calculated as $I_{max}/K_{M,app}$ ratio.

CONCLUSIONS

A new modified electrode (G/polyHm) was obtained by electropolymerisation of iron (III) protoporphyrin (IX) at the surface of a graphite electrode, by continuous scanning in the reduction potential window ranging between -0.85 to 0 V *vs.* Ag/AgCl,KCl$_{sat}$. The recorded redox process corresponds to a single electron transfer process into the metallic center Hemin(Fe^{3+})/Hemin(Fe^{2+}) of the immobilized hemin on the new electrode, and was compared with the electrochemical behavior in phosphate buffer pH 8 of bare graphite (this work) or with other modified electrode (in cited literature). Also, the influence of the scan rate on the linear sweep voltammograms recorded at the electrode confirms the adsorption of hemin on the electrode surface (slope of log I_{pc} *vs.* log v higher than 0.5).

The electrode exhibits electrocatalytic properties towards the H_2O_2 and NO_2^- reduction, respectively, proving an enzyme-like behaviour of the immobilised hemin, characterised by hyperbolic Michaelis Menten behaviour, when increasing concentrations of substrate were added.

EXPERIMENTAL SECTION

Reagents

Hemin, iron (III) protoporphyrin (IX) chloride (Hm), tris (hydroxymethyl) aminomethane (TRIS), sodium nitrite and hydrogen peroxyde (30%) were purchased from Fluka, Sigma–Aldrich GmbH and Merck, respectively. A stock solution of 0.5 mM Hm was prepared by dissolving the appropriate amount of salt in 0.05 M TRIS chloride containing 0.1 M KBr buffer (pH 10.5). The 0.05 M phosphate buffer solution containing 0.1 M KBr (pH 8.0) was prepared from appropriate amounts of KH_2PO4 and K_2HPO4 (supplied by Sigma–Aldrich GmbH). The pH of used electrolytes was adjusted by using H_3PO_4 and NaOH (Sigma–Aldrich GmbH). Deionized water was used for preparing all solutions.

Equipments

All electrochemical measurements were carried out using a computer controlled AMEL 433 trace analyzer (AMEL, Milan, Italy).

The standard uncompartment cell was equipped with a Pt counter electrode, a $Ag/AgCl,KCl_{sat}$ reference electrode (Radiometer, France), and a working electrode made of spectral graphite (Ringsdorff-Werke Gmbh, Bonn-Bad Godesberg, Germany) (diameter 0.3 cm). In order to remove the dissolved oxygen, highly purified nitrogen gas was purged into the working solution for at least 15 minutes prior to the experiment. During the measurements, the oxygen-free atmosphere was maintained using a continuous N_2 flow over the solution. All experiments were performed at room temperature (25 ± 2 °C). A combined type pH glass electrode connected to a digital pH meter type AMEL 338 (AMEL, Milan, Italy) was used for the pH measurements.

Preparation of G/poly-Hm modified electrode

Before Hm deposition, the graphite disc electrode was mirror-polished with 1.0, 0.3, 0.05 μm α-Al_2O_3 paste (Buehler, Evanston, IL, USA). Then, the electrodes were ultrasonicated for 2 minutes. The cleanness of the graphite electrode surface was checked by performing cyclic voltammograms in 0.05 M phosphate buffer + 0.1 M KBr (pH 8), between -0.6 and 0.6 V *vs*. Ag/AgCl, KCl_{sat} at 20 mV/s.

The thin film of hemin was electropolymerized on the graphite surface (G/polyHm) from a 0.5 mM hemin dissolved in a mixture of 0.05 M TRIS chloride containing 0.1 M KBr buffer (pH 10.5). The graphite electrode was immersed in the hemin solution and continuously cycled between -0.85 V and 0 V *vs*. Ag/AgCl,KCl$_{sat}$ in oxygen–free atmosphere, at 0.05 V s^{-1}, for 30 cycles. After each modification, the electrode was thoroughly rinsed with distillated water to remove excesses. Between measurements, the modified electrodes were kept at 4 °C.

REFERENCES

1. J.-M. Zen, A.S. Kumar, D.-M. Tsai, *Electroanalysis*, **2003**, *15*, 1073.
2. J.A. Bennett, K.L. Sterling, and J.E. Pander III, *ECS Electrochemistry Letters*, **2013**, *2*, H37-H39.
3. A. Eftekhari, *Analytical Letters*, **2001**, *34(4),* 541.
4. R.A. Durst, A.J. Bäumner, R.W. Murray, R.P. Buck, C.P. Andrieux, *Pure Applied Chemistry,* **1997**, *69,* 1317.
5. J. Labuda, M. Vaníčková, M. Bučková, E. Korgová, *Chemical Papers,* **2000***, 54*(2), 95.
6. K.L. Brown, S.B. Gray, *International Journal of Chemistry*, **2010**, *2*, 3, www.ccsenet.org/ijc.
7. A.A. Ciucu, *Journal Biosensors & Bioelectronics*, **2014**, *5,* 154*,* http://dx.doi.org/10.4172/2155-6210.1000154.
8. V.S. Vasantha, S.-M. Chen, *Journal of the Electrochemical Society,* **2005**, *152,* D151.
9. S.F. Peteu, T. Bose, M. Bayachou, *Analytica Chimica Acta*, **2013***, 780, 81.*
10. H.L. Zou, B.L. Li, H.Q. Luo, N.B. Li, *Sensors and Actuators B*, **2015**, *207*, 535.
11. R. Carballo, A.L. Rinaldi, P.C. Dabas, I.N. Rezzano, *Bioelectrochemistry*, **2015**, *104*, 51.
12. H. Song, Y. Ni, S. Kokot, *Analytica Chimica Acta*, **2013**, *788*, 24.
13. G.L. Turdean, I.C. Popescu, A. Curulli, G. Palleschi, *Electrochimica Acta*, **2006**, *51*, 6435.
14. G.M. Mares, G.L. Turdean, I.C. Popescu, *Studia UBB Chemia*, **2013**, *58,* 105.
15. G.L. Turdean, C. Fărcaş, A.F. Palcu, M.S. Turdean, *Studia UBB Chemia,* **2008**, *53,* 105.
16. A. Fagan-Murphy, M.C. Allen, B.A. Patel, *Electrochimica Acta*, **2015**, *152*, 249.
17. J.N. Younathan, K.S. Wood, T.J. Meyer, *Inorganic Chemistry*, **1992** *31*, 3280.
18. A.J. Bard, L.R. Faulkner, "Electrochemical Methods", Wiley-VCH, New York, 2001, p. 231.
19. P.C. Pandey, B. Singh, R.C. Boro, C.R. Suri, *Sensors and Actuators B,* **2007***,122,* 30.
20. Y. Zhang, Z. Xia, H. Liu, M. Yang, L. Lin, Q. Li, *Sensors and Actuators B*, **2013**, *188*, 496.
21. D. Mimica, J.H. Zagal, F. Bedioui, *Electrochemistry Communications*, **2001**, *3*, 435.
22. T. Lotzbeyer, W. Schuhmann, H.-L. Schmidt, *Bioelectrochemistry and Bioenergetics*, **1997**, *42*, 1.

Dedicated to prof. dr. I. C. Popescu
on the occasion of his 70th anniversary

INHIBITION EFFECT OF SOME THIADIAZOLE DERIVATIVES ON BRONZE CORROSION

ILEANA ROTARU[a], SIMONA VARVARA[b,*], LIANA MARIA MURESAN[a]

ABSTRACT. The anticorrosive properties of two thiadiazole derivatives, namely 5 amino-1,2,4- thiadiazole (AT) and 2,5 diamino-1,3,4- thiadiazole (DAT) on bronze corrosion in a complex electrolyte at pH=4 has been studied by open-circuit potential, potentiodynamic polarization, and electrochemical impedance spectroscopy measurements. The results of electrochemical investigations showed that both thiadiazole derivatives protect to some extent the bronze surface from corrosion. In the investigated experimental conditions, the highest inhibition efficiencies values were around 71.3 % and 81.6 % in the presence of 1 mM AT and 10 mM DAT, respectively. The inhibition efficiencies of the organic compounds obtained by electrochemical impedance spectroscopy are in agreement with those obtained from polarization technique.

Keywords: bronze, corrosion, thiadiazole derivatives, electrochemical impedance spectroscopy, polarisation curve

INTRODUCTION

Bronze is a relatively noble alloy but its corrosion resistance diminishes when the aggressive solution concentration increases.

Organic inhibitors have the ability to form protective films on the surface of the metal that lead to a remarkable decrease in the corrosion rate by slowing down the anodic and/or cathodic processes [1].

---

[a] *Department of Chemical Engineering, "Babes-Bolyai" University, 11 Arany Janos St., 400028 Cluj-Napoca, Romania.*

[b] *Department of Exact Sciences and Engineering, "1 Decembrie 1918" University, 11-13 Nicolae Iorga St., 510009 Alba-Iulia, Romania.*

[*] *Corresponding author: svarvara@uab.ro*

Heterocyclic compounds with polar functional groups and conjugated double bonds [2, 3-5] have been reported as efficient corrosion inhibitors of copper and its alloys, in various media. The inhibition effect of these organic molecules is usually attributed to their adsorption to the metallic surface. Polar functional groups are considered to be the reaction center that stabilizes the adsorption process [6].

Azole derivatives are well-known corrosion inhibitors for copper and its alloys since they contain nitrogen and sulphur atoms which could coordinate Cu(0), Cu(I) or Cu(II) through the lone pair electrons forming copper–azole complexes [7]. These complexes are generally believed to be polymeric in nature and form an adherent protective film on the electrodic surface, which acts as a barrier to aggressive ions from the corrosive solution.

Recently, various thiadiazole derivatives, *i.e.* 2-amino-5-mercapto-1,3,4-thiadiazole [8-10], 2-amino-5-ethylthio-1,3,4-thiadiazole [11,12] 2-amino-5-ethyl-1,3,4-thiadiazole [13], 2-methyl-5-mercapto-1,3,4-thiadiazole [10], 2-acetamino-5-mercapto-1,3,4-thiadiazole [14, 8], 2-mercapto-5-amino-1,3,4 thiadiazole; 2-mercapto-5-acetylamino-1,3,4-thiadiazole; 2-mercapto-5-methyl-1,3,4-thiadiazole and 2-mercapto-5-phenylamino-1,3,4-thiadiazole [15] have been reported as efficient inhibitors for bronze corrosion in different corrosive media.

Since thiadiazole derivatives are innoxious and inexpensive compounds, in the present paper, we continued our early work in the field [15] by investigating the anticorrosive properties of two new thiadiazole derivatives, namely 5 amino-1,2,4- thiadiazole (AT) and 2,5 diamino-1,3,4-thiadiazole (DAT) on bronze corrosion in a complex solution simulating a corrosive acid rain in a polluted urban environment, at pH =4. It should be noted that the above-mentioned organic compounds have never been tested before as corrosion inhibitors for bronze.

In order to evaluate the inhibiting effect of AT and DAT on bronze corrosion, conventional electrochemical techniques, such as open-circuit potential, potentiodynamic polarisation and electrochemical impedance spectroscopy (EIS) were used.

RESULTS AND DISCUSSIONS

Open circuit potential measurements

The evolution of the open-circuit potential (E_{oc}) for bronze over 1 hour immersion in the corrosive solution at pH = 4, in the absence and presence of different concentration of thiadiazole derivatives is illustrated in Figure 1.
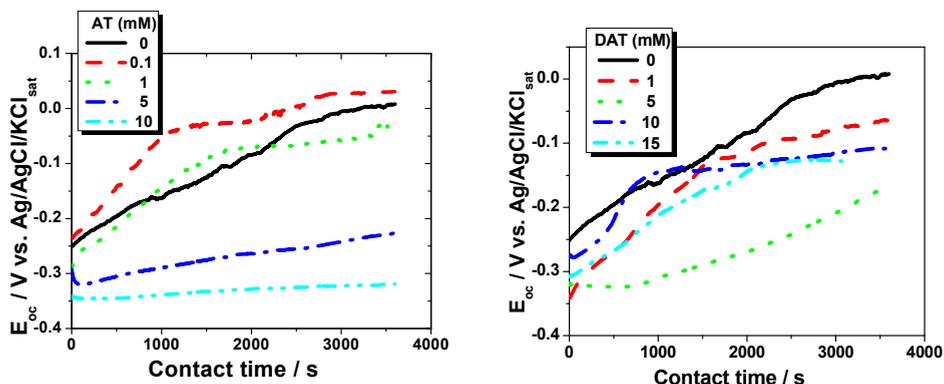
Figure 1. Time-variation of the open-circuit potential for bronze during its immersion in the corrosive media (pH 4), in the absence and in the presence of thiadiazole derivatives at various concentrations.

The values of E_{oc} for bronze corrosion in the presence of different concentrations of AT and DAT are presented in Table 1.

Table 1. Open-circuit values for bronze in the corrosive solution (pH 4) in the absence and in the presence of different concentrations of thiadiazole derivatives

Inhibitor conc. (mM)	E_{oc} (V$vs.$Ag/AgCl/KCl$_{sat}$)
0	0.008
AT	
0.1	0.031
1	-0.031
5	-0.227
10	-0.319
DAT	
1	-0.058
5	-0.170
10	-0.108
15	-0.130

The results in Table 1 show that, with the exception of 0.1mM AT, the E_{oc} values in the presence of both investigated thiadiazole derivatives are shifted towards negative values comparing to the value obtained in the inhibitor-free electrolyte, indicating that these organic compounds have stronger effect on oxygen cathodic reduction than on the copper dissolution.

Polarization curves

Fig. 2 presents the cathodic and anodic polarization curves obtained for bronze corrosion in the absence and in the presence of various concentrations of thiadiazole derivatives.
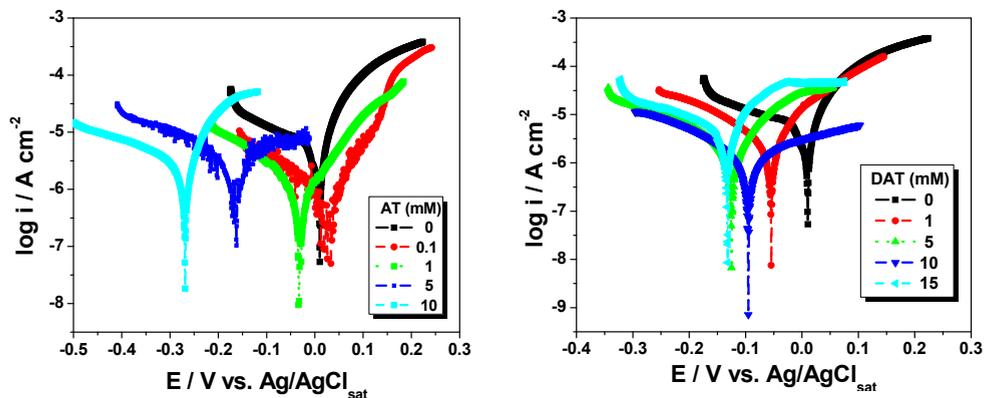
Figure 2. Anodic and cathodic polarization curves for bronze corrosion obtained in the absence and in the presence of different concentrations of AT and DAT in the corrosive solution at pH 4.

The kinetic parameters including the corrosion potential (E_{corr}), corrosion current density (i_{corr}), anodic Tafel slopes (β_a) and cathodic Tafel slopes (β_c) have been determined from the polarization curves by Tafel extrapolation method and their values are presented in Table 2.

The inhibition efficiency (z) values also listed in Table 2 were calculated using the following equation:

$$z = \frac{i_{corr}^0 - i_{corr}}{i_{corr}^0} \times 100 \, [\%] \tag{1}$$

where i_{corr}^0 and i_{corr} are the values of the corrosion current densities in absence and in presence of thiadiazoles, respectively.

It is noticeable in Figure 2 that the increase in the concentration of thiadiazole derivatives reduces both the cathodic and anodic current densities. Except for the case of 0.1 mM AT, the addition of the two thiadiazole derivatives in the corrosive solution shifts the corrosion potential values to negative direction, as compared to the blank solution, suggesting that AT and DAT inhibits mostly the cathodic process, even though the anodic current densities also decreased. This behavior may be attributed to

the adsorption of the organic molecules on the bronze surface through the lone pair of electrons of -N and -S atoms and as a protonated species. As thiadiazole derivatives contain sulphur, they probably self-assemble on the bronze surface forming a protective film. The possible protonation equilibrium of thiadiazole derivatives which may occur in strong acidic media is presented (particularization for DAT) in Figure 3.
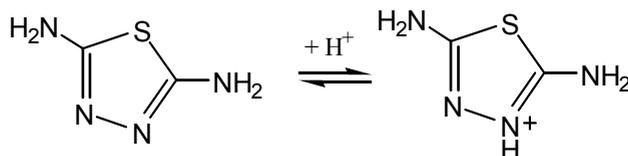
Figure 3. Protonation equilibrium for DAT

Table 2. Kinetic parameters for bronze corrosion in the absence and in the presence of different concentrations of thiadiazole derivatives in the corrosive solution at pH 4.

Inhibitor conc. (mM)	E_{corr} (V vs. Ag/AgCl/ KCl$_{sat}$)	i_{corr} (μA/cm^2)	$\|\beta_c\|$ (mV/dec)	β_a (mV/dec)	z (%)
0	-0.102	3.7	242.2	299.8	-
AT					
0.1	0.026	1.4	206.1	80.92	62.2
1	**-0.031**	**1.3**	**176.6**	**117.2**	**64.9**
5	-0.163	2.3	188.8	188.3	37.8
10	-0.279	2.9	213.8	102.1	21.6
DAT					
1	-0.057	1.3	266.9	127.9	64.9
5	-0.124	1.2	173.7	116.2	67.6
10	**-0.089**	**0.8**	**187.6**	**217.1**	**78.4**
15	-0.138	3.2	249.5	123.3	13.5

The changes of the cathodic (β_c) and anodic (β_a) Tafel slopes in the presence of thiadiazole derivatives suggests that the kinetics of both anodic and cathodic processes is affected by the presence of AT and DAT in the corrosive solution, but no definite trend was observed in the shift of (β_c) and (β_a) values.

From Table 2 one can notice that the maximum anticorrosive effectiveness of the thiadiazole derivatives on bronze was attained in the presence of 1 mM AT (64.9%) and 10 mM DAT (78.4%). Nevertheless, in the case of both investigated thiadiazole compounds, a further increase of their concentrations leads to a decrease of the inhibiting efficiency values.

Electrochemical impedance spectroscopy measurements

The Nyquist diagrams of bronze in the corrosive solution in the absence and in the presence of various concentrations of thiadiazole are given in Figure 3. These curves have been obtained after 1 h immersion of the bronze electrode in the corresponding electrolytes.
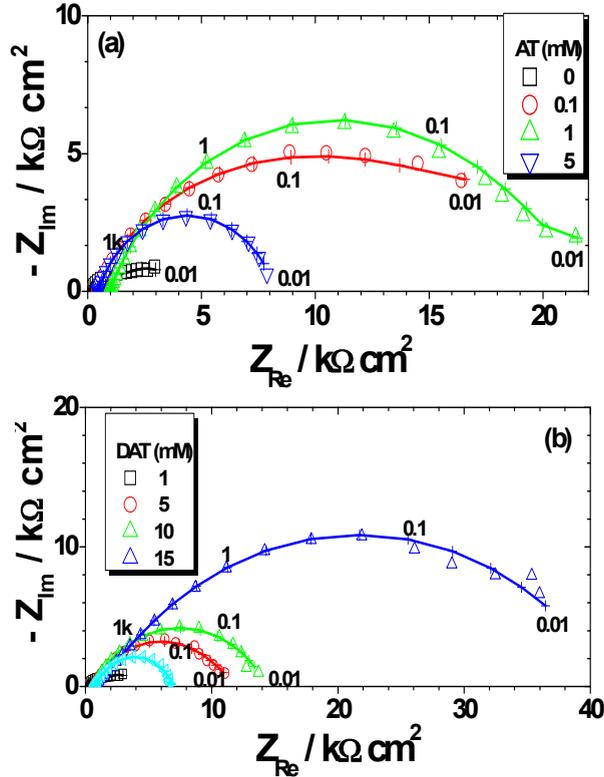
Figure 3. Nyquist plots of bronze electrode in the corrosive solution (pH 4), in the absence and in the presence of different concentrations of AT (a) and DAT (b). The symbol (—+—) corresponds to the simulated spectra. Frequencies are expressed in Hz.

The impedance diagrams exhibit a capacitive behavior with depressed loops in the whole frequency range, both in the absence and in the presence of AT and DAT. The increases of the capacitive loops diameters in the presence of the thiadiazole derivatives as compared to the blank solution is an indicative of the inhibition extent of the bronze corrosion process.

In the impedance diagrams from Figure 3, two capacitive loops could be observed although their separation is not always clear. Consequently, the equivalent circuit used for fitting experimental data is presented in Figure 4.
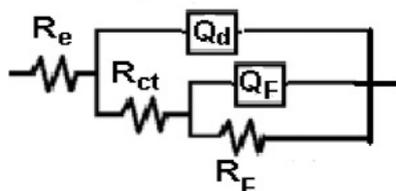
Figure 4. Equivalent electrical circuit used for computer fitting of the experimental data

The high-frequency loop was attributed to the charge transfer resistance and to the double-layer capacitance, while the low frequency loop was associated with the redox process taking place at the electrode surface, most probably involving the corrosion products (*i.e.* Cu(0) and Cu(I)), in accordance with other authors view [16]. In order to get more accurate fit of experimental data, the elements represented in the circuit from Figure 4 as capacitors were actually fitted as constant phase elements (CPEs) represented by the terms, *Q* and *n.* Constant phase elements have already been widely used [17, 18] to account for the deviations brought by the surface roughness of electrode, inhibitor adsorption, the presence of the impurities etc.

The impedance of the CPE is given by the following equation [19]:

$$Q = Z_{CPE(\omega)} = [C(j\omega)^n]^{-1} \qquad (2)$$

where *j* is an imaginary number and *ω* is the angular frequency in rad s^{-1}; depending on the value of the exponent *n*, CPE could be a resistor with the resistance, *R* (*n = 0*); a capacitor with the capacitance, *C* (*n = 1*); a Warburg impedance, W (*n = 0.5*) or an inductance, L (*n = -1*).

In order to compare the pseudo-capacitance values for bronze corrosion at various concentrations of thiadiazole derivatives, the values of CPEs were recalculated using the equation:

$$C = [R^{1-n}Q]^{1/n} \qquad (3)$$

Figure 3 demonstrates that the experimental and calculated impedance spectra obtained in the absence and in the presence of thiadiazole derivatives superimpose almost perfectly, confirming the validity of the adopted equivalent circuit. The results obtained for different parameters with respect to the thiadiazole derivatives concentrations are presented in Table 3.

In the absence of the inhibitors, the corrosion process leads to a rough electrodic surface and, consequently, to a high value of the double layer capacitance. The decreases of the C_d values in the presence of both investigated thiadiazole derivatives suggests that these compounds act by

adsorption at the metal/solution interface. The charge transfer resistance, R_{ct} increases when AT and DAT are added to the corrosive solution which could be related to the inhibiting proprieties of these compounds on bronze dissolution. This effect is improved upon increasing thiadiazole derivatives concentration up to certain values. For instance, the highest values of R_{ct} were obtained in the presence of 1 mM AT and 10 mM DAT. However, the increases of the thiadiazole derivatives concentration leads to a decrease of the charge transfer resistance values probably due to the deterioration of the adsorbed layer. The decreases of the protective effect at high concentration of inhibitors was already reported in the literature in the case of amino acids [1] and azole compounds [4].

It can also be noticed that the R_F values become greater in the presence of AT and DAT, while the C_F values decrease. Based on these observations it was assumed that the occurrence of the adsorbed inhibitors on the electrodic surface might impede the corrosion products formation. Furthermore, AT and DAT could stabilize the species covering the electrode which became less susceptible to redox processes and hence providing an enhanced protection of the bronze [20].

According to K. Marusic et al. [16], in presence of a redox process taking place at the electrodic surface, the polarization resistance, R_p calculated as the sum of R_{ct} and R_F is the parameter more closely correlated with the corrosion rate. This relationship was demonstrated in the case of bronze corrosion, when an electrochemical reaction following the Tafel law takes place at the electrodic surface, in addition to the charge transfer.

Table 3. Electrochemical parameters of bronze corrosion in the corrosive solution (pH 4) obtained in the absence and in the presence of different concentrations of thiadiazole derivatives

Inhib conc (mM)	R_e kΩ cm²	R_{ct} kΩ cm²	Q_d µF s^{n-1} cm^{-2}	n_d	C_d µF cm^{-2}	R_F kΩ cm²	Q_F µF s^{n-1} cm^{-2}	n_F	C_F µF cm^{-2}	R_p kΩcm²	z %
0	0.36	1.4	10.5	0.62	74.9	4.8	1410	0.70	3420	6.2	-
AT											
0.1	0.40	5.4	50.5	0.73	31.1	10.6	60.8	0.76	42.8	16.0	61.3
1	0.27	7.6	29.1	0.73	16.5	13.9	5.2	0.69	1.6	21.5	**71.3**
5	0.45	2.1	42.3	0.80	23.0	6.7	4.5	0.81	1.9	8.8	29.9
DAT											
1	0.67	5.7	50.5	0.81	37.7	6.8	50.5	0.81	39.3	12.5	50.6
5	0.72	7.1	36.3	0.77	24.2	7.3	48.9	0.76	35.3	14.4	57.0
10	0.76	9.3	26.34	0.62	11.1	24.2	8.4	0.80	5.7	33.5	**81.6**
15	0.73	2.9	23.3	0.82	12.9	4.1	25.9	0.83	16.4	7.0	11.3

$^*R_p = R_{ct} + R_F$

It can be observed from Table 3 that the R_p value increases in the presence of AT and DAT this effect is more pronounced at certain concentrations of thiadiazole derivatives, namely 1 mM AT and 10 mM DAT, respectively.

The inhibition efficiency values, *z* were calculated from the polarisation resistance values, R_p, according to the following equation:

$$z = \frac{R_p - R_p^0}{R_p} \cdot 100 \ [\%] \qquad\qquad (4)$$

where R_p and R_p^0 are the polarisation resistances in electrolytes with and without organic compounds, respectively.

In the investigated experimental conditions, the highest inhibition efficiencies values obtained in the presence of the 1 mM AT and 10 mM DAT were 71.3% and 81.6%, respectively.

CONCLUSIONS

In the present paper, open circuit potential, potentiodynamic polarization and electrochemical impedance spectroscopy measurements were used to investigate the anticorrosive effect of two new thiadiazole derivatives, namely, 5 amino-1,2,4- thiadiazole (AT) and 2,5 diamino-1,3,4-thiadiazole (DAT) on bronze in a corrosive solution at pH 4. The results can be summarized as follows:

1. AT and DAT protect to some extent surface of bronze against corrosion and lead to a decreases of the corrosion rate with respect to the blank solution.

2. Potentiodynamic polarization results revealed that both thiadiazole derivatives appears to have a more pronounced inhibiting effect on the oxygen cathodic reduction than on the copper dissolution process, as attested by the significant shift of the corrosion potential towards negative values. However, they causes a decrease of both anodic and cathodic current density values.

3. The (2RC) equivalent-electrical-circuit was successfully used for modeling the bronze/electrolyte interface and the corresponding surface processes, both in the absence and in the presence of thiadiazole derivatives.

4. In the investigated experimental conditions, the highest inhibition efficiencies values were 71.3% and 81.6% in the presence of 1 mM AT and 10 mM DAT, respectively. The inhibition efficiencies of the tested compounds obtained by electrochemical impedance spectroscopy are in agreement with those obtained from polarization technique.

EXPERIMENTAL SECTION

The two thiadiazole derivatives used in this research were synthesized in the laboratory following a procedure previously reported [21].

Chemical formula, molecular mass and molecular structure of the investigated thiadiazole derivatives are presented in Table 4.

All the solutions containing thiadiazole derivatives were prepared using distilled water and ethanol (90:10, v:v) from which appropriate volumes were introduced into the corrosive medium in order to obtain concentrations of 0.1; 1, 5, 10 or 15 mM, depending on the compound's solubility limit.

A complex electrolyte was used as synthetic acid rain at pH 4. The composition of this electrolyte is 31.85 mg/L H_2SO_4 + 46.2 mg/L $(NH_4)_2SO_4$ +31.95 mg/L Na_2SO_4 + 15.75 mg/ L HNO_3 + 21.25 mg/L $NaNO_3$ + 84.85 mg/L NaCl [1]. All solutions were prepared using analytical grade reagents (Merck) and distilled water.

Table 4. Structural and molecular formulas of the investigated thiadiazole derivatives

Thiadiazole (Abbreviation)	Formula/ Molecular weight (g/mol)	Structure
5 amino-1,2,4- thiadiazole (AT)	$C_2H_3N_3S$ M= 101.16	
2,5 diamino-1,3,4- thiadiazole (DAT)	$C_2H_4N_4S$ M=116.15	
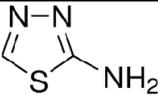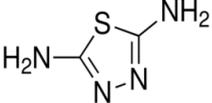
The working electrode was made of bronze with the chemical composition presented in Table 5.

To avoid the electrolyte infiltration, the working electrode was made of a bronze cylinder rod that was first covered with a cataphoretic paint layer and cured at 150 ^{0}C for 15 min. Then, the bronze cylinder was embedded into an epoxy resin leaving only a circular cross section (0.283 cm^2) in contact with the corrosive solution. Prior to use, the bronze surface was mechanically polished using emery paper of 600, 800, 1200, 2400, and 3600 granulation and consecutively rinsed with distilled water. The surface was also polished with Al_2O_3 powder (0.05 µm), and rinsed with distilled water. The last step in preparing the electrode for experiments was immersing it in a 1:1 mixture of distilled water and ethanol and ultrasonicatting it for 10 minutes.

A three-electrode cell was used for the electrochemical experiments. The counter-electrode was a platinum grid and an Ag/AgCl/ KCl$_{sat}$ electrode was used as reference electrode.

Table 5. Chemical composition (% at) of the bronze working electrode

Cu	Sn	Pb	Zn	Ni	Fe	S
94.03	3.31	0.24	1.44	0.25	0.22	0.51

Electrochemical experiments were performed at room temperature, using a a PAR model 2273 potentiostat controlled by a PC computer. Before each experiment, the bronze electrode was left at the open circuit potential for 1 hour in the corrosive solution.

Polarization curves were recorded at constant sweep rate of 10mV/min and scanning range was from - 200 to +200 mV with respect to the open circuit potential.

Electrochemical impedance measurements were carried out at the open-circuit potential after 1 h immersion of the bronze electrode in the corrosive solution. The impedance spectra were acquired in the frequency range 10 kHz to 10 mHz at 5 points per hertz decade with an AC voltage amplitude of ±10 mV.

The impedance data were interpreted based on equivalent electrical circuits, using the ZSimpWin V3.21 software for fitting the experimental data.

REFERENCES

1. K.M. Ismail, *Electrochemical Acta*, **2007**, *52*, 7811.
2. H. Otmacic, E. Stupnisek-Lisac, *Electrochemical Acta*, **2003**, *48*, 985.
3. I. Epelboin, M. Keddam, H. Takenouti, *Journal of Applied Electrochemistry*, **1972***, 2*, 71.
4. P. Gupta, R.S. Chaudhary, T.K.G. Namboodhiri, B. Prakash, *British Corrosion Journal*, **1982**, *17*, 136.
5. M.M. Antonijevic, M.B. Petrovic, *International Journal of Electrochemical Science,* **2008**, *3*, 1.
6. M.A. Elmorsi, A.M. Hassanein, *Corrosion Science*, **1999**, *41,* 2337.
7. M. Scendo, D. Poddebniak, J. Malyszko, *Journal of Applied Electrochemistry*, **2003**, *33*, 2337.
8. G. Brunoro, A. Friganani, A. Colledan, C. Chiavari, *Corrosion Science*, **2003**, *45*, 2219.
9. R. Yonda, H. Nishishara, K. Aramaki, *Corrosion Science*, **1988**, *28*, 87.

10. I. Ignat, S. Varvara, L. Muresan*, Studia UBB Chemia* **2006**, *LI, 1*, 127.
11. O. Blajiev, A. Hubin, *Electrochemical Acta*, **2004**, *49,* 2761.
12. E.M. Sherif, *Applied Surface Science,* **2006**, *252*, 8615.
13. E.M. Sherif, S.-M. Park, *Electrochemical Acta*, **2006**, *51,* 6556.
14. F.M. Al-Kharafi, *Corrosion Science,* **1988**, *28*, 163.
15. S. Varvara, L.M. Muresan, K. Rahmouni, H. Takenouti*, Corrosion Science,* **2008**, *50,* 2596.
16. K. Marusic, H. Otmačić Ćurković, H. Takenouti, *Electrochimica Acta*, **2011**, *56*, 7491.
17. L. Larabi, O. Benali, S.M. Mekelleche, Y. Harek*, Applied Surface Science,* **2006**, *253,* 1371
18. M. Kissi, M. Bouklah, B. Hammouti, M. Benkaddour, *Applied Surface Science,* **2006**, *252,* 4190.
19. I.D. Raistrick, J.R. MacDonald, D.R. Franceschetti, "The electrical analogs of physical and chemical processes", J.R. MacDonald (Ed.)," Impedance Spectroscopy Emphasizing Solid Materials and Systems", John Wiley & Sons, New York, **1987**, 27.
20. R. Bostan, S. Varvara, L. Găină, L.M. Mureşan, *Corrosion Science*, **2012**, *6*, 275.
21. H. Otmacic Curkovic, E. Stupnisek-Lisac, H. Takenouti, *Corrosion Science,* **2010**, *52,* 398.

Dedicated to prof. dr. I. C. Popescu
on the occasion of his 70th anniversary

GALVANOSTATIC GRAPHITE ELECTROACTIVATION FOR HYDROGEN PEROXIDE ELECTROSYNTHESIS BY MULTI-SEQUENCE AND AUTO-ADAPTIVE TECHNIQUES

CODRUŢA AURELIA VLAIC[a], SORIN-AUREL DORNEANU[b,*]

ABSTRACT. Electrochemical oxidation/reduction of carbonaceous electrodes represents a simple and inexpensive way for in-situ electroactivation (EA), increasing the electrocatalytic activity toward hydrogen peroxide electrosynthesis (HPE). In this context, our previous results obtained by cyclic hydrodynamic voltammetry (CHV) and an original potentiostatic multi-sequence electroactivation technique (MSET) revealed that the graphite anodization followed by the surface partial reduction has a positive effect upon the HPE efficiency. Unfortunately, CHV is not suitable for industrial approaches and the use of MSETs in potentiostatic mode induces prohibitive electrical energy consumptions during the EA steps. In order to overcome these drawbacks, in this work, new galvanostatic MSETs were designed and tested in hydrodynamic controlled conditions using a Pt/graphite wall-jet ring disk electrode system. The galvanostatic approach diminished significantly the electrical energy used for graphite EA (under 30 % from the global consumption) and improved HPE efficiency up to 35 % compared to the unmodified graphite. The best results were obtained when original auto-adaptive protocols were used. Finally, in the attempt to eliminate the energy waste during the EA steps, we proposed the use of a symmetrical divided reactor with periodic inversion of the electrodes function and the feasibility of this idea was also tested with very promising results.

Keywords: hydrogen peroxide electrosynthesis, graphite electroactivation, wall-jet ring disk electrode, auto-adaptive techniques

[a] *Technische Universität Ilmenau, Electrochemistry and Electroplating Group, Gustav-Kirchhoff-Str. 6, 98693 Ilmenau, Germany*

[b] *Babes-Bolyai University, Faculty of Chemistry and Chemical Engineering, 11 Arany Janos str., RO-400028, Cluj-Napoca, Romania*

[*] *Corresponding author: dorneanu@chem.ubbcluj.ro*

INTRODUCTION

Hydrogen peroxide (H_2O_2) represents a potential energy carrier and is also widely used in almost all industrial areas, particularly in the chemical industry and environmental protection. At industrial scale, the H_2O_2 is mainly produced by the anthraquinone oxidation process (AOP), but this multi-step technology requires complex equipments and significant energy input, and generates large amounts of waste [1]. Moreover, the transport, storage, and handling of bulk H_2O_2 involve hazards and escalating expenses. In this context, during the last decades, significant efforts have been dedicated to develop efficient and on-site/in-situ H_2O_2 production technologies, which can considerably reduce the cost for synthesis, separation, transport, storage and handling [2]. A first alternative to the AOP involve the direct synthesis of H_2O_2 from H_2 and O_2 using plasma reactors [3] or various catalysts [4, 5]. These methods allow a decentralized production of H_2O_2 in continuous mode but their implementation is difficult due to the potential risk of H_2/O_2 gas mixture explosion. Another extremely studied alternative is the hydrogen peroxide electrosynthesis (HPE) by the partial electroreduction of O_2. For the HPE process, diverse models of electrochemical cells were proposed: divided [6-8] or undivided [9-11] batch reactors, filter-press [12], flow-trough [13] or wall-jet [14] micro-reactors, H_2/O_2 fuel cells [15, 16] or solid polymer electrolyte electrolyzer [17]. In the great majority of the above cited studies, the cathode was made of modified or unmodified carbonaceous materials, in different forms, like compact (bare or plate), porous, reticulated, felt, granular, powder or gas diffusive composite membranes. Comparing to the other cathodic materials, the compact graphite electrodes present major advantages (facile production at low costs, high electrical conductivity and mechanical robustness), allowing the design of small scale plants for on-site and in-situ wastewater treatment and drinking water disinfection. In order to counteract the low specific surface of compact graphite, consistent studies were dedicated to increase it electrocatalytic activity toward HPE by physical, chemical or electrochemical modification [18, 19].

In this context, our previous results [20] obtained by cyclic hydrodynamic voltammetry (CHV) and by an original potentiostatic multi-sequence electroactivation technique (MSET) revealed that the compact graphite anodization followed by the partial reduction of its surface induces an increase of around 50 % in HPE efficiency comparing to the value evaluated on unmodified graphite. Unfortunately, CHV is not suitable for industrial approaches and, using the MSET in potentiostatic mode, the amount of electricity used for electroactivation (EA) steps was around 100 times larger than that employed for HPE.

In order to overcome these drawbacks, in the present work, new galvanostatic MSETs were designed and tested in hydrodynamic controlled conditions using a Pt-graphite wall-jet ring disk electrode (WJRDE) system. In this manner, the electrical charge (Q_{EA}) used for graphite EA diminished

below 30 % from the global charge consumption (Q_G), and HPE efficiency increased up to 35 % against the unmodified graphite, the best result being obtained using original auto-adaptive MSETs. Supplementary, in the attempt to eliminate the energy waste during the EA steps, we propose a symmetrical divided reactor with periodic inversion of the electrodes and compartments functions and the feasibility of this new design was also tested at the WJRDE scale with very promising results.

RESULTS AND DISCUSSION

Constant current HPE tests

Because the graphite activation by potentiostatic MSETs had relative modest results upon HPE global efficiency, we decide to test similar protocols, but in galvanostatic conditions, taking into account that the galvanostatic approach is more feasible for potential industrial applications.

The necessity of graphite surface periodic activation was proved by two preliminary long duration HPE experiments (results not shown) at a constant current value and a volume flow rate (V_F) of 1.42 mL/min. In the first test, imposing a disc current (I_d) of -13 μA (corresponding to the maximal HPE efficiency evaluated by CHV), the recorded ring current (I_r) slowly decreased and, consequently, the current efficiency (CE) diminished from 57% to 54% after one hour. Similarly, during the second experiment, carried out at I_d = -15 μA (value corresponding to the beginning of 4 electrons oxygen reduction process), the initial CE value of 64 % decreased rapidly to 46% and 39 % after 50 min. and 100 min, respectively. The CE values were calculated using the following equation:

$$CE\,(\%) = 100 \cdot I_r \,/(I_d \cdot N) \qquad (1)$$

where N is the collection efficiency of the WJRDE ensemble.

In both cases, the CE decrease can be explained by the disk potential (ε_d) shift to negative values due to the continuous modification of graphite surface in an air saturated strong alkaline solution [21], which favors the total O_2 reduction via the 4 electrons pathway.

Galvanostatic EA/HPE using fixed parameters MSETs

These new galvanostatic experimental protocols were designed in the idea of periodical graphite EA during the HPE process using a train of rectangular current pulses with constant intensities and durations, fixed by user. For each EA/HPE cycle, the applied signal includes three current pulses, corresponding to the already mentioned processes: anodisation step (AS), partial reduction step (PRS) and H_2O_2 production step (PS).

During the first set of measurements, performed at V_F = 1.42 mL/min, we tried to establish the best experimental parameters for the EA sequences. Currents of +100 and +150 µA (I_{AS}) were imposed trough the graphite disc electrode during the AS and of -100 and -150 µA (I_{PRS}) for the PRS, respectively. Different ratios between AS duration (T_{AS}) and PRS duration (T_{PRS}) were also tested: 2:2, 3:1, 4:2 and 2:1.5 (s:s) in order to reach the optimum EA potentials. Based on these experiments, we found that the best combination consisted in an AS of 2 s at +100 µA followed by a PRS of 1.5 s at -100 µA. Starting from these parameters, we initiated an optimization study concerning the duration of PS (T_{PS}) through 30 consecutive cycles for each experiment. Different T_{PS} values of 20 s, 60 s and 120 s wee tested and the best results were obtained for a T_{PS} of 60 s, the recorded signals being presented in Figure 1.
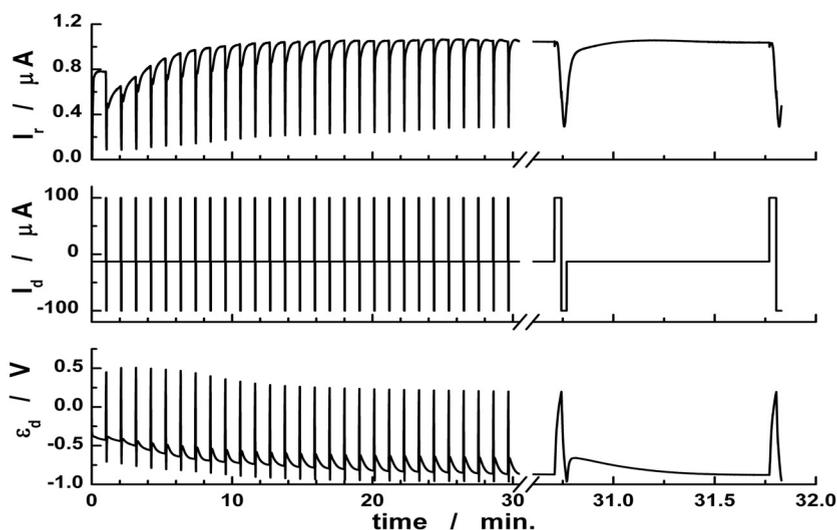
Figure 1. The influence of the disk applied current (I_d) on the recorded disc potential (ε_d) and ring current (I_r) for 30 cycles of galvanostatic EA and HPE. (T_{AS} = 2 s; I_{AS} = +100 µA; T_{PRS} = 1.5 s; I_{PRS} = -100 µA; T_{PS} = 60 s; I_{PS} = -13 µA)

It can be noticed that, at the end of the first four cycles of EA/HPE, ε_d did not decrease enough to reach the adequate potential value (near -0.8 V) for partial reduction of the active centers. As a consequence, during the cycles 2 to 4, the CE of HPE is inferior to that obtained in the first PS, corresponding to the unmodified graphite electrode. Starting from the fifth cycle, the ε_d reached adequate negative values for partial reduction and the I_r values increased largely, proving the HPE efficiency enhancement due to this original technique of graphite galvanostatic EA.

From another point of view, it is worth to note that, comparing to potentiostatic MSETs, the values of Q_{EA} decreases at reasonable values, representing around 30 % from the Q_G value. Moreover, the HPE efficiency increases with approx. 35 % in respect to the values evaluated on unmodified graphite electrode.

The downside of these EA protocols consists in the fact that, after more than 20 consecutive cycles, the ε_d values during the PRS and PS became too negative and, consequently, the HPE efficiency started to diminish due to the total oxygen reduction and the subsequent reduction of the electrosynthetized H_2O_2. In order to overcome this inconvenient, we designed new EA galvanostatic protocols, described below.

Galvanostatic EA/HPE using auto-adaptive MSETs

The previous results showed that the galvanostatic EA of graphite using a fixed time MSETs did not allow us to control rigorously, in each step, the evolution of ε_d values during the long time experiments. This fact is caused by the continuous modification of the electrode surface and, consequently, the EA and HPE parameters must be permanently readjusted. Aiming to accomplish these requirements, the initially designed LabView application, based on programmable fixed time sequences, was modified in order to allow an auto-adaptive control of steps duration. Practically, for each programmed sequence, the experimenter can set both the maximal duration and one limitative (maximal or minimal) value for other three recorded electrical parameters (ε_d, I_d or I_r). Depending on the electrochemical system evolution, the software detects the occurrence of the first limitative condition (time or the selected electrical parameters), stops the current sequence and jumps to the next programmed sequence.

Using the new designed auto-adaptive protocol, we started an optimization study, fixing T_{PS} at 60 s and I_{PS} at -13 µA, and setting different limitative ε_d values: maximum of +0.5 V or +0.6 V for the AS ($\varepsilon_{AS, MAX}$) and minimum of -0.7 V, -0.8 V or -0.9 V for the PRS ($\varepsilon_{PRS, MIN}$). In order to accelerate the EA processes, I_{AS} and I_{PRS} were fixed at increased values of +150 and -150 µA, respectively. Based on this set of experiments, we conclude that the best limitative ε_d values were +0.5 V for $\varepsilon_{AS, MAX}$ and -0.8 V for $\varepsilon_{PRS, MIN}$. From the obtained results, presented in Fig. 2, a progressive enhancement of the HPE efficiency up to 35 % was estimated. Moreover, this auto-adaptive protocol allows the reduction of the Q_{EA} value at around 20 % from Q_G. In order to validate these optimized parameters, the experiment was repeated in duplicate for 20 and 30 successive cycles, the obtained values being quasi-identical.

Considering the favorable results obtained by the auto-adaptive galvanostatic EA, supplementary long duration experiments (100 cycles) were carried out for the T_{PS} optimization, values of 60, 80, 100, 120 and

140 s being tested. The obtained results, summarized in Table 1, reveal that the optimal T_{PS} value is 100 s, when the global current efficiency (CE_G) reaches a reasonable value of 67 % and the percent of Q_{EA} against Q_G ($Q_{EA/G}$) decreases to 14 %. CE_G and $Q_{EA/G}$ were calculated as:

$$CE_G = 100 \cdot Q_R /(Q_G \cdot N) \qquad (2)$$

$$Q_{EA/G} = 100 \cdot Q_{EA} /Q_G \qquad (3)$$

were Q_R is the integral electric charge recorded for the ring electrode.
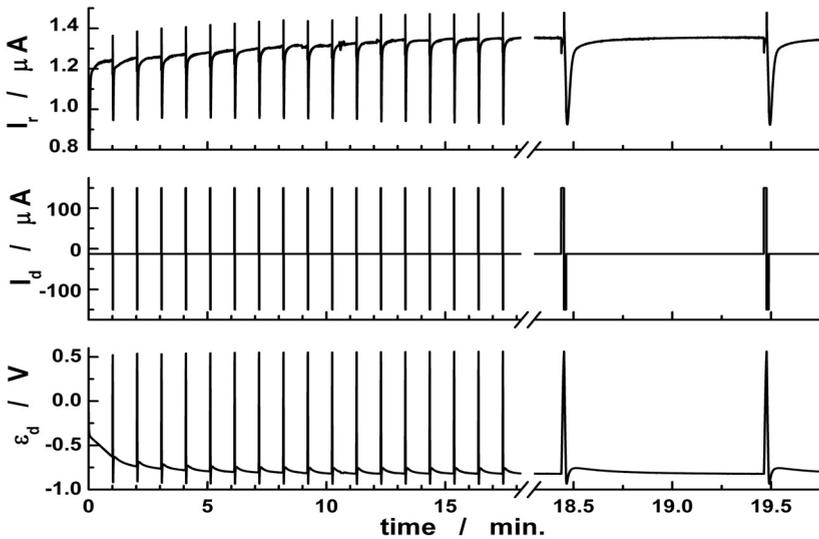
Figure 2. The evolution of I_r, I_d and ε_d during 20 cycles of galvanostatic auto-adaptive EA and HPE. (V_F = 1.42 mL/min.; $\varepsilon_{AS,\,MAX}$ = +0.5 V; $\varepsilon_{PRS,\,MIN}$ = -0.8 V; T_{PS} = 60 s; I_{AS} = +150 µA; I_{PRS} = -150 µA; I_{PS} = -13 µA)

Table 1. Influence of T_{PS} over global current efficiency (CE_G) and EA charge percentage ($Q_{EA/G}$) during the auto-adaptive galvanostatic EA and HPE

T_{PS} (s)	60.00	80.00	100.00	120.00	140.00	Auto
Q_G (mC)	98.66	140.02	151.15	176.93	221.28	132.79
Q_R (mC)	4.55	7.05	11.11	10.90	13.96	10.18
Q_{EA} (mC)	20.66	36.02	21.15	20.93	39.28	15.72
$Q_{EA/G}$ (%)	20.94	25.73	**13.99**	11.83	17.75	**11.84**
CE_G (%)	41.94	45.77	**66.85**	56.03	57.34	**69.72**

A supplementary test using the galvanostatic auto-adaptive EA and HPE was performed at $\varepsilon_{AS, MAX}$ = +0.6 V and $\varepsilon_{PRS, MIN}$ = -1.0 V, and limiting the PS at T_{PS} = 500 s or until ε_d decrease under -0.8 V. In these conditions, as indicated in the last column of Table 1, CE_G reaches an improved value of ~70 % and the $Q_{EA/G}$ decreases below ~12 %, proving the feasibility on this original protocol for graphite EA and HPE.

Galvanostatic electroactivation using symmetrical rectangular signal

As pointed before, the galvanostatic auto-adaptive EA and HPE protocols present many advantages, but a small quantity of electricity is still wasted for the EA steps. In order to overcome this drawback, we intend to design and use a symmetrical divided reactor with periodic inversion of the electrodes functions. This approach was based on the idea that, when one electrode is anodised, simultaneously, on the other electrode occurs the partial reduction of surface and, afterwards, the HPE process could take place. Subsequently, switching simultaneously the electrodes polarities and electrolytes flows, the processes would interchange, allowing a periodic reactivation of the graphite electrode without energy wasting. In order to confirm the feasibility of this new design, several tests were accomplished using the WJRDE system and a symmetrical rectangular signal. Practically, pulses of equal duration but with different symmetric (positive and negative) current values were applied to the disc electrode, at two values of V_F (1.5 and 10 mL/min.). An example of recorded data for V_F = 10 mL/min is presented in Figure 3.
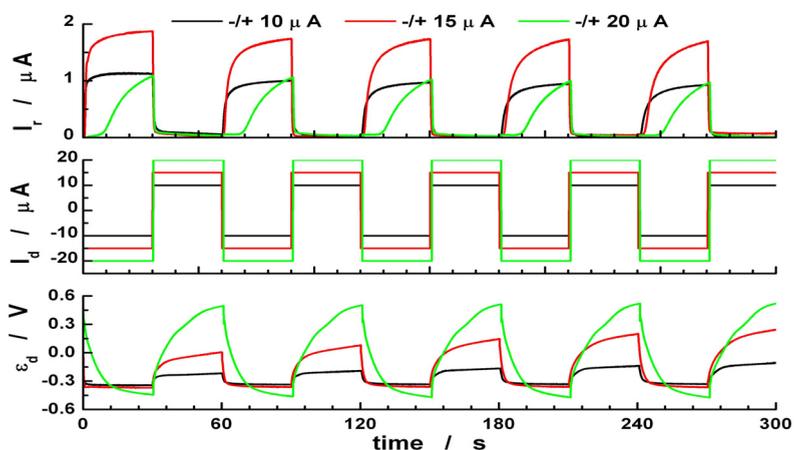
Figure 3. Example concerning the evolution of I_r, I_d and ε_d recorded with the WJRDE system at V_F = 10 mL/min. for symmetrical current pulses

Reference data were also recorded in asymmetric mode (without activation), meaning that the disc current was switched only between 0 and the negative value. The calculated values of CE for different experimental conditions are centralized in Table 2.

Table 2. HPE current efficiency (%) evaluated in different experimental conditions using galvanostatic pulses of equal duration

Pulse shape	Pulses intensity (µA)[*]					V_F (mL/min)	Pulse width (s)
	10	13	15	20	25		
Symmetric	55.5	68.5	58.4	43.6	-	1.5	60
Asymmetric	61.5	-	66.6	66.9	65.2	10	30
Symmetric	71.5	-	85.1	38.5	-	10	30
Symmetric	-	-	89.7	-	-	10	60

[*] +/- for symmetric or 0/- for asymmetric pulses

The data included in Table 2 indicate that, at V_F = 1.5 mL/min., a maximal CE value of 68.5 % was obtained for symmetrical current pulses of ±13 µA. The increase of V_F at 10 mL/min. enhances the CE of HPE on inactivated graphite (asymmetric mode) up to 66.9 % for current pulses of -20 µA. At the same V_F of 10 mL/min., the CE for the HPE process attained maximum values of 85.1 % and 89.7 % when symmetrical current pulses of ±15 µA were applied for durations of 30 and 60 s, respectively. These very promising results encourage us to implement this protocol on a pilot scale reactor.

CONCLUSIONS

In order to increase and maintain the HPE efficiency on compact graphite electrodes, we designed new techniques for in-situ galvanostatic EA. These protocols include two essential sequences, corresponding to the electrode surface oxidation followed by a partial reduction step. All the measurements were performed in hydrodynamic controlled conditions using a Pt/graphite WJRDE system, that allow the instant monitoring of the experimental parameters and process efficiency. The necessity of periodic EA was confirmed by two preliminary HPE experiments at constant current values, both of them revealing a permanent and significant CE decrease after a prolonged electrolyze. Consequently, several multi-sequence electroactivation techniques were designed and tested in galvanostatic conditions. For the beginning, trains of rectangular pulses of fixed currents and periods were applied to the disc electrode as exciting signal. Using this type of EA/HPE protocol, the amplitude and duration of the current pulses were optimized in order to maximize the HPE efficiency. At the best combination

of experimental parameters (pulses of +100, -100 and -13 µA for durations of 2, 1.5 and 60 s, respectively), the values of $Q_{EA/G}$ decreases under 30 % and the HPE efficiency increases with approx. 35 % beside the unmodified graphite.

Because the protocols based on rectangular pulses of fixed currents and periods did not allow a rigorous control of the ε_d evolution during the prolonged experiment, the experimental parameters must be permanently re-adjusted. For solving this problem, the initially designed Labview application was modified in order to allow an auto-adaptive control of steps duration. Using this new protocol, after an intensive optimization study, $Q_{EA/G}$ can be diminished below 12 % while CE_G can increase up to 70 %.

Finally, in the attempt to eliminate the energy waste during the EA steps, we proposed a symmetrical divided reactor with periodic inversion of the electrodes and functions. The feasibility of this new design was tested using the WJRDE system and symmetric current pulses. In these conditions, the preliminary results indicate the possibility to increase of HPE efficiency up to 90 %, without inutile energy consumption.

For future developments, the best experimental parameters will be transferred on a micro-pilot scale electrochemical reactor in order to validate the very promising obtained results. Moreover, due to the extreme flexibility of the new developed multi-sequence techniques, these will be implemented for other electrochemical processes that require similar protocols such as electrodeposition, electrosynthesis etc.

EXPERIMENTAL SECTION

All the electrochemical measurements were carried out in controlled hydrodynamic conditions, using the experimental setup described in detail in our previous work [20]. Briefly, it includes a wall-jet cell (WJC) equipped with a Pt/graphite ring-disc electrode (RDE), a peristaltic pump (Reglo Analog, Ismatec, Switzerland) and a fully computer controlled home-made bipotentiostat. All designed and used applications for data acquisition and experiment control were elaborated using the LabView 8.5 software. In the WJC, the distance between the injector and disc electrode was fixed at 1 mm in order to achieve a planar laminar flow. The collecting efficiency (N) was evaluated using a 10 mM $K_4[Fe(CN)_6]$ solution in 1 M NaOH as supporting electrolyte and values of 0.11 and 0.13 were obtained at V_F of 1.42 and 10 mL/min., respectively. For HPE experiments, an air saturated ([O2] ~ 8 ppm) 1 M NaOH aqueous solution was pumped in the WJC at V_F of 1.42 or 10 mL/min. Before each set of experiments, the RDE surface was polished on waterproof emery paper of 1200 grit (Struers, Denmark) and intensively washed with doubly distilled water. In order to reduce the background value of I_r, the Pt ring electrode was pre-oxidized at +0.8 V for 10 s before each experiment. All measurements were performed at room temperature (25 ± 1 ^{o}C).

ACKNOWLEDGMENTS

REFERENCES

1. J.M. Campos-Martin, G. Blanco-Brieva, J.L.G. Fierro, *Angewandte Chemie - International Edition*, **2006**, *45*, 6962.
2. Y. Liu, X. Quan, X. Fan, H. Wang, S. Chen, *Angewandte Chemie - International Edition*, **2015**, *54(23)*, 6837.
3. Y. Yi, J. Zhou, H. Guo, J. Zhao, J. Su, L. Wang, X. Wang, W.Gong, *Angewandte Chemie - International Edition*, **2013,** *52*, 8446.
4. R. Dittmeyer, J.-D. Grunwaldt, A. Pashkova, *Catalysis Today*, **2015**, *248*, 149.
5. J.K. Edwards, S.J. Freakley, R.J. Lewis, J.C. Pritchard, G.J. Hutchings, *Catalysis Today*, **2015**, *248*, 3.
6. E.L. Gyenge, C.W. Oloman, *Journal of Applied Electrochemistry*, **2001**, *31*, 233.
7. G.A. Kolyagina, V.L. Kornienkoa, Yu. A. Kudenkob, A.A. Tikhomirovb, S.V. Trifonovb, *Russian Journal of Electrochemistry*, **2013**, *49(10)*, 1004.
8. G.A. Kolyaginz, V.L. Kornienko, *Russian Journal of Electrochemistry*, **2014**, *50(8)*, 798.
9. L. Zhou, Z. Hu, C. Zhang, Z. Bi, T. Jin, M. Zhou, *Separation and Purification Technology*, **2013**, *111*, 131.
10. Y. Sheng, Y. Zhao, X. Wang, R. Wang, T. Tang, *Electrochimica Acta*, **2014**, *133*, 414.
11. G. Xia, Y. Lu, H. Xu, *Electrochimica Acta*, **2015**, *158*, 390.
12. M. Giomo, A. Buso, P. Fier, G. Sandona, B. Boyec, G. Farnia, *Electrochim. Acta,* **2008**, *54*, 808.
13. Q. Li, C. Batchelor-McAuley, N.S. Lawrence, R.S. Hartshorne, C.J.V. Jones, R.G. Compton, *Journal of Solid State Electrochemistry*, **2014**, *18(5)*, 1215.
14. P. Ilea, S.A. Dorneanu, I.C. Popescu, *Journal of Applied Electrochemistry*, **2000**, *30*, 187.
15. E. Lobyntseva, T. Kallio, N. Alexeyeva, K. Tammeveski, K. Kontturi, *Electrochimica Acta,* **2007**, *52*, 7262.
16. T. Murayama, S. Tazawa, S. Takenaka, I. Yamanaka, *Catalysis Today*, **2011**, *164(1)*, 163.
17. J. Choi, S.H. Hwang, J. Jang, J. Yoon, *Electrochemistry Communications*, **2013**, *30*, 95.
18. A.R. Khataee, M. Safarpour, M. Zarei, S. Aber, *Journal of Electroanalytical Chemistry*, **2011**, *659(1)*, 63.
19. I. Kocak, M.A. Ghanem, A. Al-Mayouf, M. Alhoshan, P.N. Bartlett, *Journal of Electroanalytical Chemistry*, **2013**, *706*, 25.
20. Vlaic, S. A. Dorneanu, P. Ilea, *Studia UBB Chimia*, **2011**, *LIV(2)*, 167.
21. R. Berenguer, J.P. Marco-Lozar, C. Quijada, D. Cazorla-Amorós, E. Morallón, *Carbon*, **2009**, *47*, 1018.

Dedicated to prof. dr. I. C. Popescu
on the occasion of his 70th anniversary

THE EFFECTIVENESS OF WAX IN PROTECTION OF BRONZES COVERED WITH ARTIFICIAL PATINA IN OUTDOOR EXPOSURE

JULIETA DANIELA CHELARU[a], LUCIAN BARBU-TUDORAN[b], LIANA MARIA MURESAN[a*]

ABSTRACT. Lately there is a major concern about the preservation of artificial patina applied on the art objects made of bronze. These studies are important in the restoration and conservation of bronze monuments exposed outdoor. In this context the present work aims studying the efficiency of wax-based films (WF) on the protection of two artificial patina (brown and golden) in a solution containing Na_2SO_4 and $NaHCO_3$ (pH 5) simulating an acid rain. The protective effect of the artificial patina with / without wax-based films was investigated by electrochemical and non-electrochemical methods. The chemical composition of the golden artificial patina/ Carnauba wax layer was determined by X - ray fluorescence analysis, and the morphology was determined by SEM - EDX cartographies. The results have shown that both artificial patinas exerted an anticorrosion protective effect on bronze and the wax improved even more the corrosion resistance. The protection conferred by the golden artificial patina was significantly improved by using Carnauba wax (Cw) and a corrosion inhibitor (2 - mercapto - 5 acetylamino - 1, 3, 4 - thiadiazole).

Key words: bronze, artificial patina, corrosion inhibitor, Carnauba wax.

INTRODUCTION

Outdoor bronze artworks have aesthetic and often historic value. It is therefore necessary to protect them against aggressive agents. Long

---

[a] *Department of Chemical Engineering, "Babes-Bolyai" University, 11 Arany Janos St., 400028 Cluj-Napoca, Romania.*
[b] *Biology and Geology Department, „Babes-Bolyai" University, Piata Unirii 31, 400098, Cluj-Napoca, Romania*
[*] *Corresponding author: limur@chem.ubbcluj.ro*

term conservation of outdoor bronze sculptures involves formation of artificial patinas on bronze surface, which additionally confer to artistic objects a pleasant aesthetic aspect [1, 2]. For more protection are used corrosion inhibitors [3 - 9], waxes and lacquers [10, 11] which are applied on the surface of patinated bronze. The advantage of the wax-bases films is that they do not modify the patina color [11], while some corrosion inhibitors such as benzotriazole change and blacken it [12].

In order to confer a pleasant esthetical aspect to bronze surfaces, in the past the sculptors prepared artificial patina by using flowers of sulphur (for dark brown color), copper nitrate (for light green) and copper sulphate (for reddish color). In a previous study [13] the authors examined the electrochemical behavior of bronze treated with these compounds in an environment that simulated acid rain. Accelerated corrosion tests revealed that the investigated patinas have a limited protection effect on bronze corrosion. The patina layers were not enough compact and uniform. Moreover, after the corrosion tests, the patina showed limited adherence to the bronze surface.

In this context, in order to improve the corrosion resistance of patinated bronze, the aim of this paper was to investigate comparatively the protective effect of two new artificial patinas (brown and golden) prepared by chemical methods on bronze CuSn8 surface, in the absence and in the presence of wax-based films (WF). Additionally, the efficiency of golden patina was investigated in the presence of Carnauba wax (Cw) and two corrosion inhibitors (benzotriazole (BTA) and 2 - mercapto - 5 acetylamino - 1, 3, 4 – thiadiazole (MAcT)). The anticorrosion effect of the all protective layers was investigated by electrochemical methods in a solution containing Na_2SO_4 + $NaHCO_3$ (pH 5) that simulated an acid rain in urban environment. The protective effect of artificial patinas was comparatively investigated by electrochemical and non - electrochemical methods.

RESULTS AND DISCUSSION

To conduct the studies, a contemporary bronze CuSn8 was selected, of the following composition: 90.18 % copper, 8 % tin, 0.8 % zinc, 1 % lead and 0.02 % aluminum.

Polarization measurements

Firstly the electrochemical behavior of electrodes covered with brown and golden patina has been studied. To determine the kinetic parameters of the corrosion process, polarization curves were recorded in the potential range of ± 200 mV *vs.* ocp (Figure 1-a). Secondly, the Tafel polarization curves for bronze electrodes covered with artificial patina in presence of

WF protection (Figure 1-b) were recorded. Finally, the electrodes covered with golden patina in the presence of Carnauba wax and corrosion inhibitors (BTA and MAcT) (Figure 1-c) were investigated.

The the corrosion kinetic parameters values were determined from the polarization curves by Tafel interpretation and the results are presented in Table 1. The polarization resistance R_p values for each electrode, calculated as the inverse of the slope of linear polarization curves (± 20 mV vs. OCP), are also shown in Table 1.
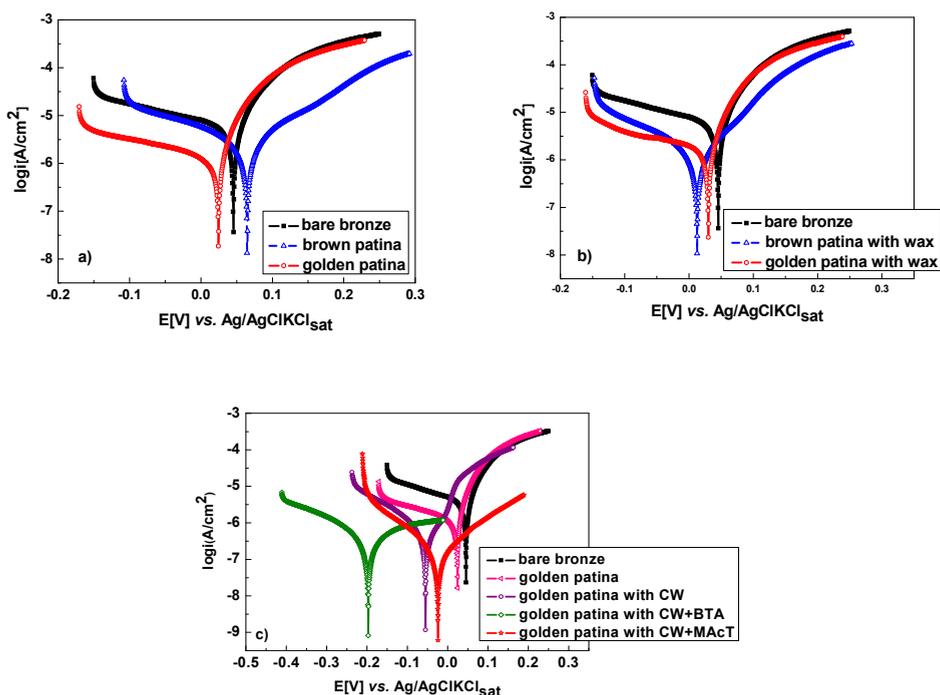
Figure 1. The polarization curves (± 200 mV vs. OCP) for the bronze covered with: brown and golden artificial patina (a); artificial patina (brown and golden) with WF (b); golden artificial patina with Cw in the absence and in the presence of inhibitors (c); Experimental conditions: corrosion solution, Na_2SO_4 + $NaHCO_3$ (pH 5); potential scan rate, 10 mV / min.

The protection efficiencies (PE) conferred by different treatments (artificial patinas and waxes) were calculated from the corrosion current densities (i_{corr}) according to the equation:

$$PE[\%] = \frac{i_{corr}^0 - i_{corr}}{i_{corr}^0} x100$$

where: i_{corr}^0 - represents the corrosion current density for bare bronze and i_{corr} -represents the corrosion current density for bronze covered with artificial patina / WF / inhibitor.

Table 1. Corrosion process parameters for the examined samples in 0,2 g/L $NaSO_4$ + 0,2 g/L $NaHCO_3$ (pH = 5)

Electrode	E_{corr} [mV vs Ag/AgCl]	i_{corr} [µA/cm²]	β_a [mV/decade]	- β_c [mV/decade]	R_p [kΩcm²]	PE [%]
Bare bronze	46	5.36	46	284	2.06	-
Brown patina	65	2.75	85	134	5.38	48.69
Golden patina	25	1.54	27	188	5.60	71.26
Brown patina / WF	13	1.69	71	111	4.39	68.47
Golden patina / WF	30	1.46	33	224	3.39	72.76
Golden patina / Cw	-55	0.22	53	56	3.60	95.90
Golden patina / Cw / BTA	-197	0.32	243	159	32.26	**94.03**
Golden patina / Cw / MAcT	-24	0.08	83	72	148	**98.51**

β_a and β_c are the Tafel coefficients

Artificial patinas

As expected, the lowest corrosion resistance, was obtained in case of bare bronze (R_p = 2.06 kΩcm², i_{corr} = 5.36 µA/cm², Table 1). The results have shown that both artificial patinas (brown and golden) improve the corrosion resistance of bronze, but their protection efficiencies are not spectacular. The best protection efficiency was exerted by the golden patina (71.26 %).

Artificial patinas with WF

In the presence of WF, it is observed in all cases a slight improvement in the protective properties of the patina layers and a decrease of the corrosion current density. Thus, the results reveal that the highest corrosion resistance was noticed in the case of the electrode coated with golden patina and WF (R_p=4.39 kΩcm², i_{corr}= 1.46 µA/cm²), followed by the electrode covered with brown patina and WF (Table 1). By comparing these results with those recorded for bronze covered only with artificial patina layers, it can be concluded that the wax plays a role of barrier against corrosion enhancing the protective effect exerted by the patinas.

Golden patina with Carnauba wax (Cw)

A comparison of the results obtained with two different waxes applied on the same type of patina was performed in the case of golden

patina. The analysis of data obtained in this case (Table 1) shows that by applying a layer of Cw on the bronze surface covered with golden patina, there is a considerable improvement of anticorrosion properties. It should be also mentioned that Carnauba wax exerted a more pronounced inhibiting effect than WF.

In order to explore the possibility of improving even more the corrosion resistance of the bronze samples, a thiadiazole derivative (MAcT) was dissolved in the corrosion solution in a concentration of 1mM / L [14]. In this case, the bronze covered with golden patina and Cw gave the best results (R_p = 148 kΩcm^2, i_{corr}= 0.08 µA/cm^2) confirming that the thiadiazole derivative acts as an effective corrosion inhibitor. The spectacular rise of resistance polarization in this case is not only due to the fact that Cw layer forms a physical barrier against corrosion, but also to the synergistic effect that appear in the simultaneous presence of the inhibitor and the Cw layer on the bronze surface covered with golden patina. This synergistic effect may be due to chemical reactions that take place between participants and creates on the bronze surface covered with golden patina an effective barrier.

It should also be noted that the MAcT was proved to be a better corrosion inhibitor than BTA, which is a remarkable fact, given its non-toxic nature and its accessibility.

Morphological characterization

The SEM image of the bare bronze surface (Figure 2) shows that the surface is homogeneous, without slag inclusions or foreign material. However, there are some points with Pb segregation (see arrow).
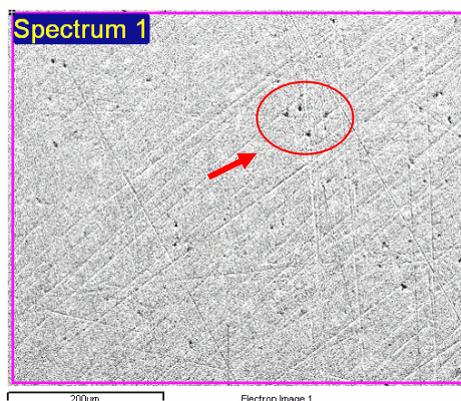
Figure 2. SEM image obtained on surface of bronze before the application of artificial patina
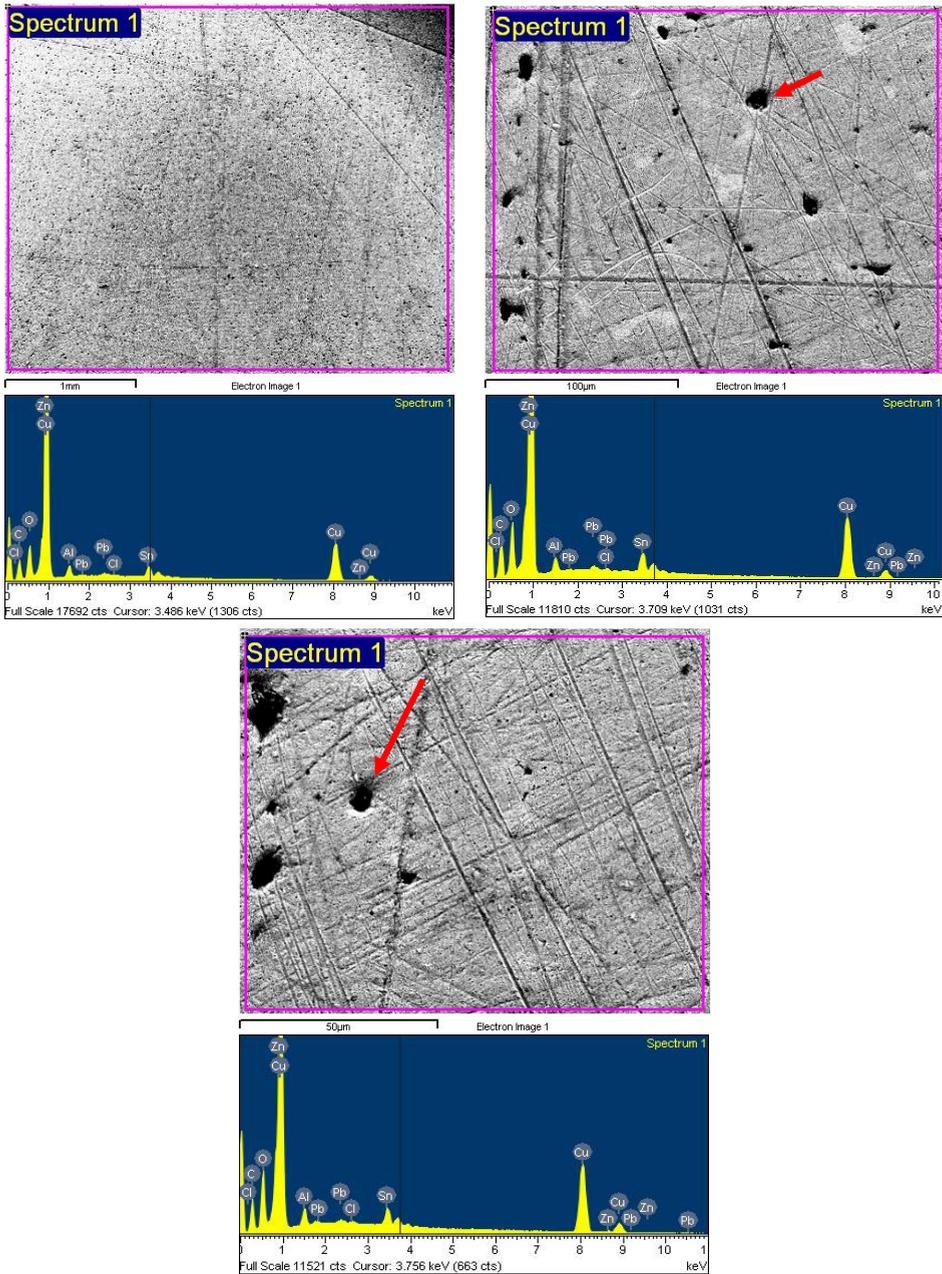
Figure 3. SEM / EDX results obtained on the bronze surface covered with golden artificial patina, after corrosion tests

The chemical treatment applied to form the golden patina led to a sparingly soluble and adherent film (Table 3, last column). After the corrosion tests, the bronze surface covered with golden patina has not suffered major depreciations and its color has not significantly changed (results not shown).

In order to determine the morphology and the chemical composition of the golden patina layer after one hour of immersion SEM - EDX analysis was performed at different points of the bronze's surface and results are presented in Figure 3 and Table 2.

Analyzing the SEM images from Fig. 3 it can be observed a uniform distribution of the corrosion products all over the surface and the existence of some black points (see arrow) in the patina layers, existing on bare bronze too (Fig. 2). As already mentioned, these points are due to lead segregation during casting. The bronze surface is not covered with a thick corrosion products layer and compared with bare bronze's surface there are not major modifications.

As can be seen from Table 2, the distribution of the chemical elements in the corrosion products all over the surface is uniform. The EDX analysis in different points indicated the presence of copper, oxygen, carbon, zinc and tin, whereas Al, Pb and Cl were present as minor elements. The presence of O and C in high concentrations led to the conclusion that the corrosion products layer is mainly composed of oxides and carbonates. The presence of zinc in the corrosion products layer in higher concentration than in the bronze substrate is due to the phenomenon of bronze dezincification [15] which is explained elsewhere [16].

Table 2. Elemental composition [%] of the corrosion products formed at different points of the bronze surface covered with golden artificial patina, determined by EDX analysis

	C [%]	O [%]	Al [%]	Cl [%]	Cu [%]	Zn [%]	Sn [%]	Pb [%]
1	15.09	9.82	1.63	-	64.76		5.53	0.96
2	15.29	9.36	1.38	0.21	65.19	2.03	5.69	0.85
3	13.50	9.16	1.45		68.02	2.16	4.83	0.70

The uniform distribution of the chemical elements on the bronze surface covered with golden patina after the corrosion tests can be also observed in Figure 4.

Based on SEM / EDX analysis it can be concluded that the thin, continuous, adherent and chemically homogenous corrosion products layer formed in the presence of golden patina is responsible for the better corrosion resistance of the bronze samples covered with this type of patina.
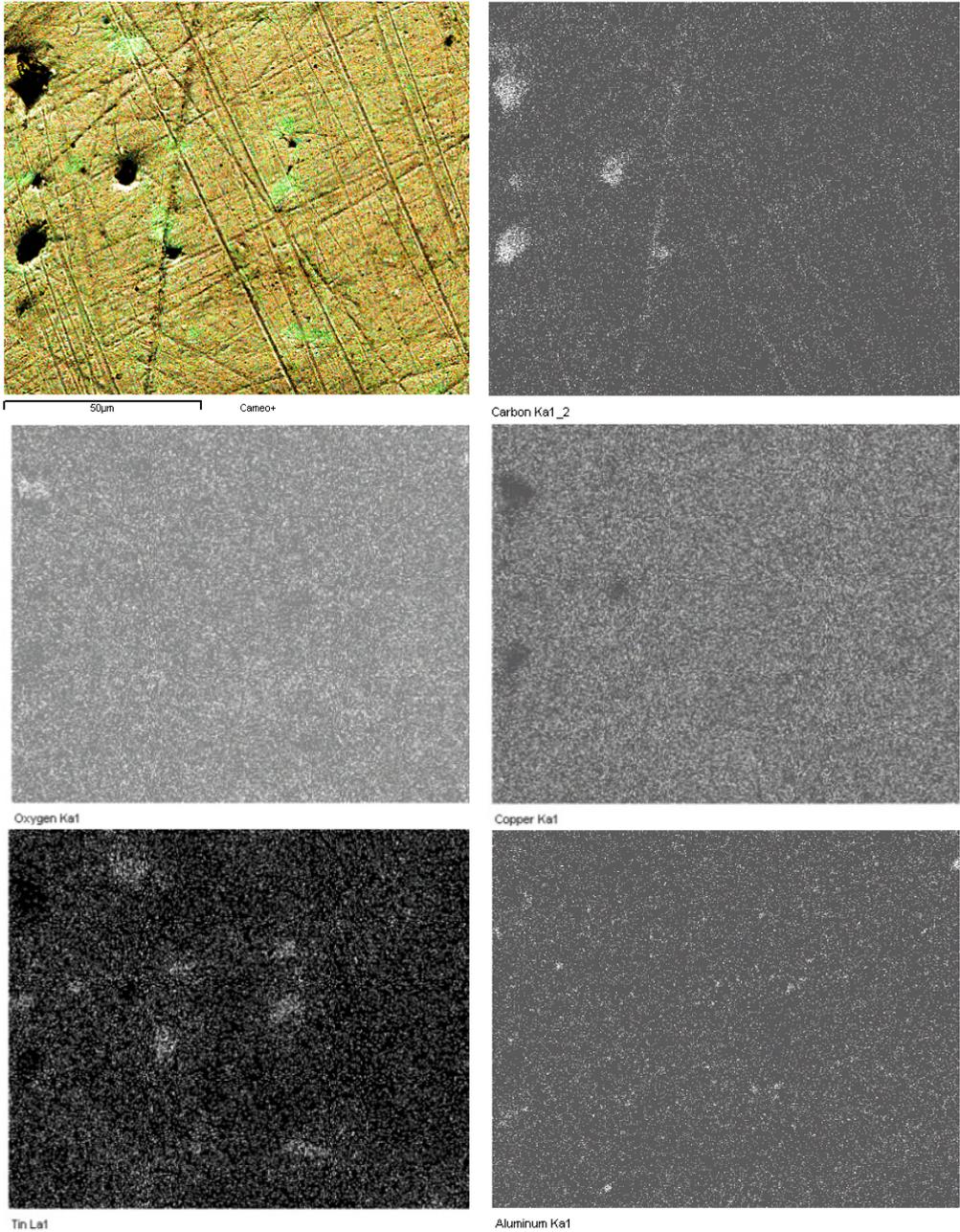
Figure 4. Mapping results obtained on surface of bronze electrode covered with gold artificial patina, after corrosion tests. X-ray maps for C, O, Cu, Sn, Al.

CONCLUSIONS

The corrosion properties of bronze covered with brown and golden artificial patinas (chemically formed on bronze surface) were investigated in a solution of Na_2SO_4 and $NaHCO_3$ (pH 5) which simulated an urban acid rain. The artificial patinas (brown and golden) were applied by chemical methods. For additional protection wax-based films were used.

Based on SEM / EDX analysis it can be concluded that in the presence of golden patina the corrosion products layer formed is thin, continuous, adherent and chemically homogenous and is mainly composed of copper and tin compounds (oxides and carbonates).

The artificial patinas improve the corrosion resistance of bronze. Both types of patinas can be recommended for protection of works of art, especially in the presence of wax-based films.

The best protection efficiency was exerted by golden patina with Cw when corrosion inhibitors (BTA and MAcT) were used. The maximum protective effect was noticed in case of the golden patina with Cw in presence of MAcT (98.51 %).

EXPERIMENTAL

Electrodes

The working electrodes made of bronze CuSn8, cylindrically shaped, were placed in a PVC tube, while the sealing was assured with epoxy resin. In this way, the surface of the electrode exposed to the solution was disk - shaped, with a surface S = 2.00 cm^2. For electrical contact, a metal rod was attached. On these electrodes, patina was applied chemically.

Patinas

Artificial patinas were prepared (on the polished bronze surface) in several steps, using the solutions mentioned in Table 3.

The stages in the patination process were:
- Polishing the electrode surface;
- Degreasing in acetone
- Immersion in solution (see Table 3) (T, t);
- Washing with distilled water;
- Drying with ethyl alcohol;
- Applying of a protective solution (wax - based)

Table 3. Substances used to create artificial patina

Patina color	Chemical composition of the solution	Chemical formula	Quantity [g/L]	Duration of imersion / temperature	The working electrode
Brown	Copper sulphate	$CuSO_4$	60	3 - 5 minutes / 90 - 100 ºC	
	Potassium permanganate	$KMnO_4$	7		
Golden	Sodium hydroxide	$NaOH$	50	7 - 15 minutes / 30 ºC	
	Oxalic acid	$C_2H_2O_4$	30		
	Copper sulphate	$CuSO_4$	50		
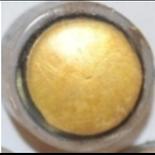
Wax – based films (WF)

For an additional protection of all artificial patinas a mixture of beeswax (25 %) and anticorrosive oil (75 %) was used. In the case of golden patina Carnauba wax (Cw) was also used. To apply the Cw on bronze surface the wax was melted around 85 ºC and mixed with „white spirit" [1].

Corrosion inhibitors

The inhibitors used in the experiments were benzotriazole (BTA) (Sigma Aldrich) and a non - toxic thiadiazole derivative, respectively 2 - mercapto - 5 acetylamino - 1, 3, 4 - thiadiazole (MAcT, from Sigma Aldrich). The molecular structure of the two compounds is shown in Figure 5. The inhibitors were dissolved in the corrosion solution at a concentration of 1mM / L, considered optimal according to some studies [14, 17].

a)   b)
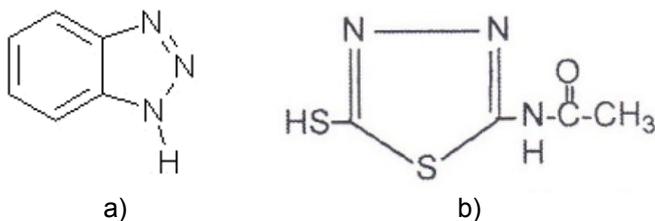
Figure 5. The molecular structure of the a) benzotriazole, b) 2 - mercapto - 5 acetylamino - 1, 3, 4 – thiadiazole

Experimental investigation

The morphology of corrosion products layer formed on the electrodes surface was examined with a scanning electron microscope (SEM; Scanning Jeol JEM5510LV (Japan) coupled with Oxford Instruments EDX Analysis System Inca 300 (UK) at 15kV and spot size 39 µm).

The electrochemical corrosion measurements were performed on a PC – controlled electrochemical analyzer AUTOLAB - PGSTAT 10 (Eco Chemie BV, Utrecht, The Netherlands) using a three electrodes cell containing a working electrode (bronze), an Ag/AgCl/KCl$_{sat}$ electrode as reference electrode and a platinum counter electrode. Anodic and cathodic polarization curves were recorded in a potential range of ± 20 mV (for Rp determination) and of ± 200 mV *vs.* the value of the open circuit potential (for Tafel interpretation), with a scan rate of 10 mV / min, after 1 hour immersion in the corrosive solution.

The electrolyte solution for corrosion measurements was 0.2 g / L Na_2SO_4 + 0.2 g / L $NaHCO_3$ acidified to pH = 5 by the addition of a dilute sulphuric acid at room temperature.

REFERENCES

1. H. Otmačič - Ćurković, T. Kosec, K. Marušić, A. Legat, *Electrochimica Acta*, **2012**, *83*, 28-39.
2. P. Kipper, Patina for Silicon Bronze, Regal Printing, Hong Kong, **2003**.
3. J.D. Chelaru, L.M. Mureşan, *Studia UBB Chemia*, **2014**, *59*, 91-102.
4. K. Marušić, H. Otmačić - Ćurković, Š. Horvat - Kurbegović, H. Takenouti, E. Stupnišek - Lisac, *Electrochimica Acta*, **2009**, *52*, 7106-7113.
5. L. Mureşan, S. Varvara, E. Stupnišek - Lisac, H. Otmačič, K. Marušić, S. Horvat - Kurbegović, L. Robbiola, K. Rahmouni, H. Takenouti, *Electrochimica Acta*, **2007**, *52*, 7770-7779.
6. E. Cano, D. Lafuente, Published by Woodhead Publishing Limited, **2013**, 570-594.
7. S.H. Zaferani, Majid Sharifi, D. Zaarei, M.R. Shishesaz, *Journal of Environmental Chemical Engineering,* **2013**, 1, 652-657.
8. A.A. Nazeer, E.A. Ashour, N.K. Allam, *Materials Chemistry and Physics*, **2014**, *144*, 55-65.
9. A. Balbo, C. Chiavari, C. Martini, C. Monticelli, *Corrosion Science*, **2012**, *59*, 204-212.
10. T. Kosec, H. Otmačič - Ćurković, A. Legat, *Electrochimica Acta*, **2010**, *56*, 722-731.
11. Kosec, A. Legat, I. Milosev, *Progress in Organic Coating*, **2010**, *69*, 199-206.
12. R.B. Faltermeier, *Studies in Conservation*, **1998**, *44*, 121-128.
13. J.D. Chelaru, L.M. Mureşan, V.F. Soporan, O. Nemeş, T. Kolozsi, *International Journal of Conservation Science*, **2011**, *2*, 109-116.

14. S. Varvara, L.M. Mureşan, K. Rahmouni, H. Takenouti, *Corrosion Science*, **2008**, *50*, 2596-2604.
15. L. Campanela, O. Colacicchi Alessandri, M. Ferretti, S.H. Plattner, *Corrosion science*, **2009**, *51*, 2183-2191.
16. J.D. Chelaru, L.M. Mureşan, *Studia UBB Chemia*, **2013***, 58*, 173-182.
17. A. Dermaj, N. Hajjaji, S. Joiret, K. Rahmouni, A. Srhiri, H. Takenouti, V. Vivier*, Electrochimica Acta*, **2007**, *52*, 4654-4662.

Dedicated to prof. dr. I. C. Popescu
on the occasion of his 70th anniversary

REMOVAL OF COPPER FROM DILUTED AQUEOUS SOLUTIONS USING AN IMINODIACETIC ACID CHELATING ION-EXCHANGE RESIN IN A FIXED-BED COLUMN

IRINA BLEOTU[a], EMILIA GÎLCĂ[a], SORIN-AUREL DORNEANU[a,*], COSMIN CĂȚĂNAȘ[a], PETRU ILEA[a]

ABSTRACT. In this study, the copper removal was investigated in a fixed-bed column using a iminodiacetic acid chelating ion exchange resin (Purolite S930Plus).The influence of the resin bed height (3-6 cm) over the removal process was evaluated at a flow rate of 5 mL/min and initial Cu(II) concentration of 0.8 mM. The obtained results were analysed by linear regression using the most common sorption kinetic models such as Yoon-Nelson, Adam-Bohart, and Clark. The experimental data were in good agreement with Yoon and Nelson model. Also, scanning electron microscopy (SEM) and energy dispersive X-ray spectroscopy (EDS) were employed to study the morphologies and the composition of the resin surface before and after sorption. The column regeneration studies were performed using 3 N H_2SO_4 solution. The tested resin presented a good regeneration capacity and can be successfully used to remove copper ions from diluted wastewaters.

Keywords: Copper removal, Fixed-bed column, Kinetics, Regeneration

INTRODUCTION

The presence of heavy metals in effluents discharged from different activities can cause serious environmental problems, because of theirs non-biodegradability and long persistence [1].

Copper is one of the metals used extensively in the technological sphere, along with other heavy metals such as lead and chromium [1]. The

[a] *Babeş-Bolyai University, Faculty of Chemstry and Chemical Engineering, 11 Arany Janos str., RO-400028, Cluj-Napoca, Romania.*
* *Corresponding author: dorneanu@chem.ubbcluj.ro*

most common methods to treat these wastewaters in order to remove the copper ions are: flotation, solvent extraction, adsorption, cementation, ion exchange, ultrafiltration and electrochemical methods [2-5].

Among these methods, the ion exchange process has been successfully used for heavy metals removal. Moreover, the resins present the ability to adsorb and desorb metals for several cycles.

According to the literature, numerous studies regarding the ion exchange process can be found but many of them are still in the optimization phase in order to improve the affinity and selectivity of the resins [6, 7]. The sorption experiments performed in batch conditions can be easily used in the laboratory study, but are not appropriate for industrial applications because of the large volume of wastewaters that have to be processed [8]. Therefore, the fixed-bed column studies can be used due to their simplicity, ease of handling and operation [8-10].

In this case, the concept of breakthrough curve [8, 11-13] can be applied, analyzing the shape of the breakthrough curve and the breakthrough time [8, 14]. Various sorption kinetic models, such as Thomas, Yoon-Nelson, Clark and Adam-Bohart, can be used to evaluate the performances for heavy metals removal [8, 15-17].

The aim of this study was to investigate the capacity of the Purolite S930Plus ion-exchange resin to remove copper from diluted aqueous solutions in a fixed-bed column. The influence of resin quantity (bed height) and resin regeneration on the removal process were considered. The obtained results were analyzed by linear regression using the most common sorption kinetic models: Yoon-Nelson, Adam-Bohart and Clark. The resin surface before and after sorption was examined by SEM and EDS.

RESULTS AND DISCUSSION

For industrial applications, the sorption experiments realized in a fixed-bed column are more suitable to be used than in batch mode. In order to evaluate the sorption abilities of the tested resin towards the Cu(II) ions removal from diluted solutions, several experiments were made using different amounts of adsorbent, at a fixed flow rate.

Effect of resin quantity

The breakthrough curves for copper sorption on Purolite S930Plus resin were recorded for various resin quantities ranged between 100 and 200 mg (various bed heights, from 3 to 6 cm), at a flow rate of 5 mL/min and an initial Cu(II) concentration (C_0) of 0.8 mM (pH = 4). The obtained results, based on the effluent concentration (C_t) at the sampling time (t), are

presented in Figure 1. It was observed that, in these conditions, copper sorption was very fast in the first minutes, afterwards, the sorption rate slowly decreased due to the resin saturation [18].

In the explored range of resin quantities, the breakthrough curves obtained did not follow the typical 'S-shape' curves. An incomplete 'S' breakthrough shape can be explained by the slow sorption kinetics of copper on the considered resin [18, 19].
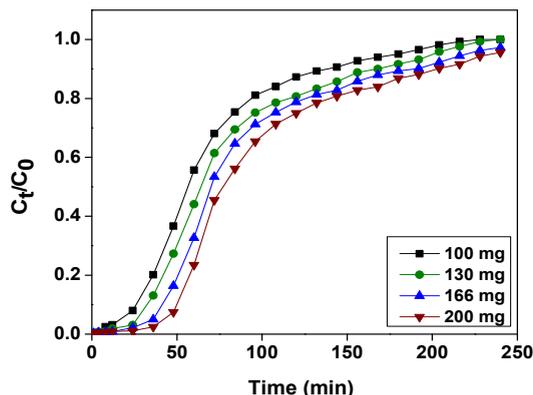
Figure 1. Breakthrough curves for Cu(II) sorption onto Purolite S930Plus ion exchange resin using different sorbent quantities (C_0 = 0.8 mM, T = 298 K, pH = 4).

The breakthrough time (t_b) increased by increasing the resin quantity (from 100 to 200 mg), which can be attributed to the increase of binding sites numbers, broadening the mass transfer zone [20]. The breakthrough time values were between 0.24 and 1 h when different resin quantities were used at an exhaustion time (t_s) of 5 hours. Also, it was noted that, increasing the resin quantity in the studied range, the values of sorption capacity (q_t) at t_s increased from 95 mg/g to 97 mg/g. The sorption capacity was calculated using the following equation:

$$q_t = \frac{C_0 - C_t}{M} \cdot \frac{V}{1000} + q_{t-1}$$
(1)

where q_{t-1} is the sorption capacity at time (t-1) (mg/g), V is the volume of copper solution (L) and, M is the mass of the resin (g) [18].

Regeneration studies

When the output effluent concentration passes the breakpoint values, the feed of the column is discontinued and the column should be regenerated [21]. The regeneration of Purolite S930Plus resin (100 mg) was made using a

3 N H$_2$SO$_4$ solution at a flow rate of 0.125 mL/min. The obtained results, presented in Figure 2, showed that the copper concentration in the effluent becomes very high in the first minutes, after that it decreased slowly until the resin was completely regenerated. A volume of 60 mL 3 N H$_2$SO$_4$ ensured the complete regeneration of the Purolite S930Plus resin, further desorption is negligible [22].
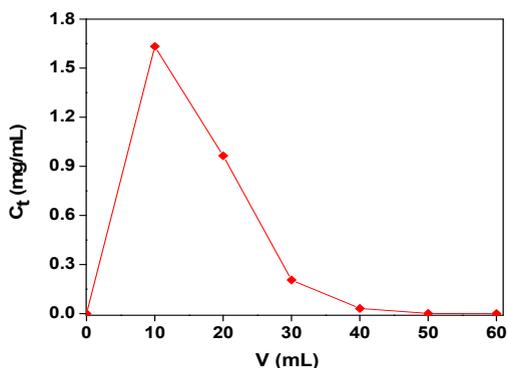
Figure 2. Copper concentration in effluent during the regeneration cycle.

SEM and EDS analysis

The morphology of Purolite S930Plus resin surface before and after Cu(II) adsorption were examined by SEM and the obtained images are presented in Figure 3. The smooth surface of resin turned thicker and coarser with granular flake material after adsorption of Cu(II), suggesting that the cooper was loaded on the surface of the resin [22]. Further, the presence of the adsorbed cooper on the resin surface was confirmed by the metal peaks that appear on the EDS spectra presented in Figure 4.
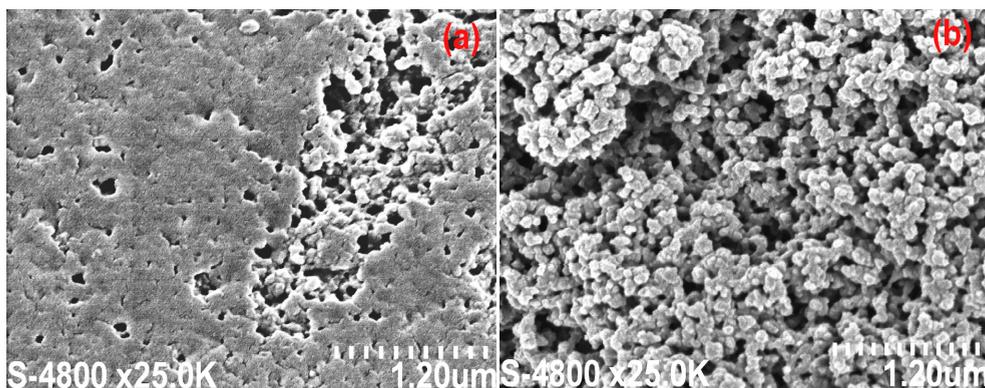
Figure 3. SEM images for Purolite S930Plus resin before (a) and after sorption (b)
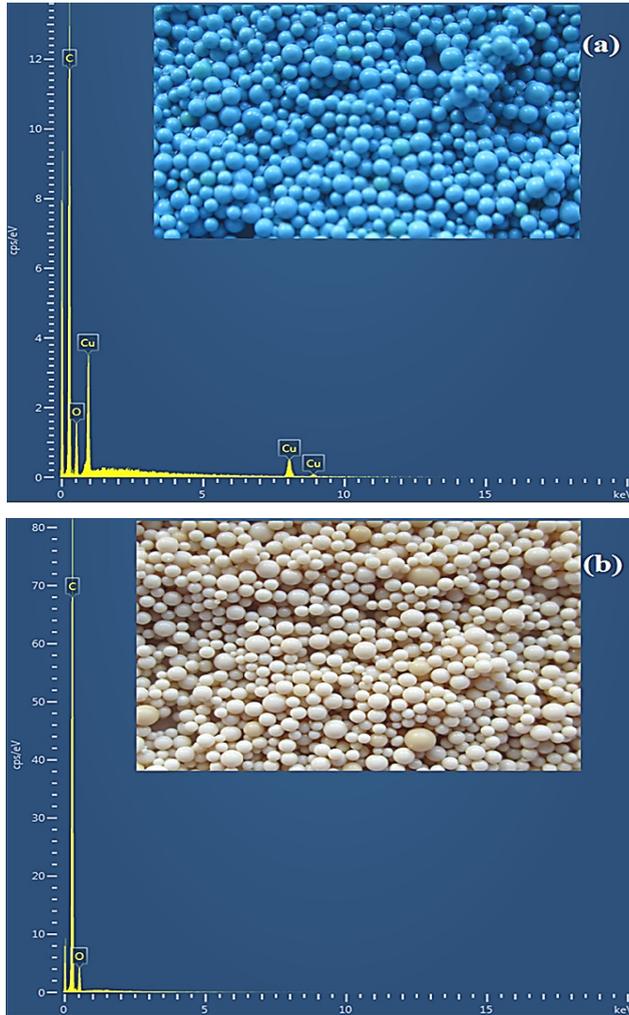
Figure 4. EDS spectra of Purolite S930Plus resin after Cu(II) sorption (a)
and after regeneration (b).

Reaction kinetic models

In order to study the kinetics of copper sorption, three kinetic models (Yoon-Nelson, Adams-Bohart and Clark) were considered [8, 17, 23].

Yoon-Nelson model is based on the assumption that the rate of decrease in the probability of adsorption of the adsorbate molecule is proportional to the probability of adsorbate adsorption and the probability of adsorbate breakthrough [23]. The Yoon-Nelson model for a single component system is expressed as:

167

$$\ln\left(\frac{C_t}{C_0 - C_t}\right) = t\,k_{YN} - \tau k_{YN} \qquad (2)$$

where, k_{YN} (1/min) is the Yoon-Nelson constant and τ (min) is the time required for 50% adsorbate breakthrough [23, 24].

The Yoon-Nelson kinetic parameters, k_{YN} and τ, were obtained from the slope and the intercept of the linear plot $\ln[C_t/(C_o-C_t)]$ against time (t), and presented in Table 1.

Table 1. Yoon-Nelson, Adams-Bohart and Clark parameters for the sorption of copper on Purolite S930Plus for different resin quantities

Sorbent quantity (mg)	Yoon-Nelson			Adams-Bohart			Clark		
	τ (min)	$k_{YN}\cdot10^{-2}$ (1/min)	R^2	$k_{AB}\,10^{-4}$ (L/mg·min)	N_0 (mg/L)	R^2	A	$r\cdot10^{-2}$ (min)	R^2
100	91.6	3.44	0.82	3.46	14.61	0.58	1.84	5.01	0.72
130	99.2	3.52	0.80	3.78	11.10	0.64	1.97	5.47	0.82
166	111.5	3.69	0.91	4.22	8.98	0.68	2.07	5.57	0.80
200	120.1	3.71	0.97	4.54	7.57	0.72	2.15	5.74	0.81

From Table 1, it can be seen that the values of k_{YN} increased as the resin quantity increased. Based on correlation coefficients values, the model presents a good applicability for copper removal using Purolite S930Plus resin at a sorbent quantity higher than 166 mg.

Adams-Bohart model is based on the assumption that the rate of adsorption is proportional with the concentration of the adsorbing species and the residual capacity of the adsorbent and is used for the description of the initial part of the breakthrough curve [17,18, 25].

The Adam-Bohart expression is given as:

$$\ln\frac{C_t}{C_0} = k_{AB}\,C_0 t - k_{AB}\,N_0\,\frac{Z}{U} \qquad (3)$$

where k_{AB} is the kinetic constant (L/mg·min), N_0 is the saturation concentration (mg/L), Z is the bed height of the column (cm) and U is the linear velocity of solution (cm/min).

The parameters describing the characteristic operations of the column (k_{AB} and N_0) were determined from the linear plot of $\ln(C_t/C_0)$ vs. time (t), using the slope and intercept values, respectively [17, 18, 25].

The calculated values of N_0, presented in Table 1, decreased with the increase of the bed height. Based on the obtained correlation coefficients, the Adams-Bohart model does not fit adequately the experimental data for the Purolite S930Plus resin, so its assumptions were not validated.

The Clark kinetic model is based on the use of a mass-transfer concept in combination with the Freundlich isotherm and has a precise analytical solution enabling determination of dynamic adsorption rate constants [17, 18]. In previous equilibrium studies, it was found that the Freundlich model was valid for the Cu(II) adsorption on Purolite S930Plus resin, which allows the use of the Freundlich constant (n = 1.97) [26] to calculate the parameters in the Clark model.

$$\ln\left[\left(\frac{C_0}{C_t}\right)^{n-1} - 1\right] = \ln A - rt \qquad (4)$$

where n is the Freundlich constant, A and r are the Clark constants [17].

The values of r and A, presented also in Table 1, were determined from the slope and the intercept of the linear plot of $\ln[(C_0/C_t)^{n-1}-1]$ vs. time (t). Based on the calculated correlation coefficients (Table 1), it was concluded that the Clark model does not fit adequately the experimental data.

CONCLUSIONS

In this study, the performance of an iminodiacetic acid chelating ion exchange resin (Purolite S930Plus) resin for copper removal was evaluated in a fixed-bed column. The obtained results revealed a classic behavior, showing that the increase of the used resin quantity and, implicitly, of the bead height induces the increase of the breakthrough time. The Purolite S930Plus resin was successfully regenerated using 3 N H_2SO_4. A volume of 60 mL ensured the complete regeneration (100 %) for 100 mg of resin. Based on the correlation coefficients values, the following series of kinetic models was depicted: Yoon-Nelson > Clark > Adam-Bohart. Also, the correlation coefficients values for Yoon-Nelson model indicate a better linearity at increased resin quantities, while, for the other models, lower correlation coefficients were obtained for copper removal using the Purolite S930Plus resin. According to the obtained results, it can be concluded that Purolite S930Plus resin is a good ionic exchanger for copper removal from diluted aqueous solutions, presenting also a good regeneration capability.

EXPERIMENTAL SECTION

The Purolite S930Plus resin, especially designed for heavy metals removal, was activated according to the supplier specifications [27]. Before usage, the dry resin was placed in double-distilled water for 24 h at a mass-volume ratio (M_{resin} : V_{water}) of 1:10.

Stock solution of 1000 ppm Cu(II) was prepared in double-distilled water using solid $CuSO_4 \cdot 5H_2O$ (from Merck, analytical grade). The initial pH of aqueous solutions was adjusted in the range 1.0 – 6.0 by adding small amounts of 0.1 M H_2SO_4 or 0.1M NaOH. In order to preserve the solution pH at the desired value, the resin was supplementary conditioned in a blank solution having similar acidity.

A plastic column, having an inner diameter of 0.45 cm and a total height of 7.0 cm, was used for the experiments. The column was equipped with two layers of nitrocellulose membranes (45 µm) to prevent the escape of the resin beads. The scheme of the experimental setup is presented in Figure 5.
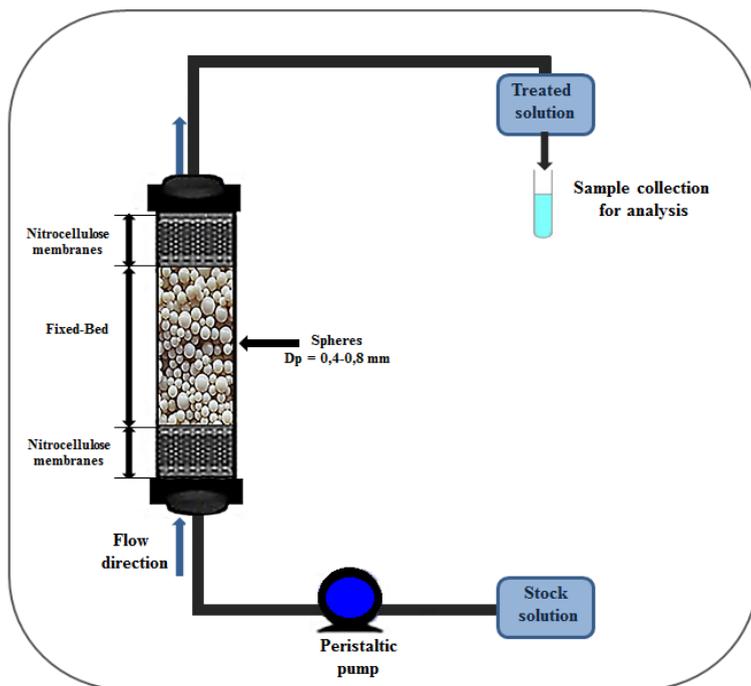
Figure 5. The experimental setup.

The synthetic solution, having an initial copper concentration of 0.8 mM, was allowed to pass through the column in continuous up-flow mode, at a 5 mL/min flow rate, using a peristaltic pump Reglo Digital (Ismatec, Switzerland). The treated solution was collected from the outlet of the column at different time intervals and analyzed by flame atomic absorption spectrometry using an Avanta PM spectrometer (GBC, Australia) exploited in the air-acetylene flame mode.

The surface morphology and the composition of the resin before and after copper sorption were analysed using a scanning electron microscope (SEM) combined with an energy-dispersive X-ray spectrometer (EDS) model Hitachi S-4500.

ACKNOWLEDGMENTS

<div align="center">

REFERENCES

</div>

1. R.R. Crichton, *Biological Inorganic Chemistry. An Introduction, Elsevier*, **2008**, 241.
2. M. Mihaly, A.F. Comanescu, E.A. Rogozea, A. Meghea, *Molecular Crystals and Liquid Crystals*, **2010**, *523*, 63.
3. N.N. Maximous, G.F. Nakhla, W.K. Wan, *Science, Engineering and Technology*, **2010**, *40*, 599.
4. R.W. Gaikwad, V.S. Sapkal, R.S. Sapkal, *Acta Montan. Slovaca*, **2010**, *15*, 298.
5. S.A. Dorneanu, B. Ferencz-László, P. Ilea, *Studia UBB Chemia*, **2008**, *1*, 97.
6. G. Tiravanti, D. Petruzelli, R. Passino, *Water Science and Technology*, **1997**, *36(2),* 197.
7. S. Rengaraj, K.H. Yeon, S.H. Moon, *Journal of Hazardous Materials*, **2001**, *87(1),* 273.
8. Q. Yang, Y. Zhong, X. Li, X. Li, K. Luo, X. Wu, H. Chen, Y. Liu, G. Zeng, **2015** in press, doi:10.1016/j.jiec.2015.01.022.
9. S. Kundu, A. Gupta, *Journal of Colloid and Interface Science*, **2005**, *290*, 52.
10. S. Mossa Hosseini, B. Ataie-Ashtiani, M. Kholghi, *Desalination*, **2011**, *276*, 214.
11. L. Monser, N. Adhoum, *Separation and Purification Technology*. **2002**, *26*, 137.
12. P. Suksabye, P. Thiravetyan, W. Nakbanpote, *Journal of Hazardous Materials*, **2008**, *160*, 56.

13. E.R. Monazam, J. Spenik, L.J. Shadle, *Chemical Engineering Journal*, **2013**, *223*, 795.
14. X. Sun, T. Imai, M. Sekine, T. Higuchi, K. Yamamoto, A. Kanno, S. Nakazono, *Journal of Industrial and Engineering Chemistry*, **2014**, *20*, 3623.
15. M.A. Acheampong, K. Pakshirajan, A.P. Annachhatre, P.N.L. Lens, *Journal of Industrial and Engineering Chemistry*, **2013**, *19*, 841.
16. H.P. Chao, C.C. Chang, A. Nieva, *Journal of Industrial and Engineering Chemistry*, **2014**, *20*, 3408.
17. O. Hamdaoui, *Journal of Hazardous Materials,* **2009**, *161*, 737.
18. E. Gîlcă, A. Măicăneanu, P. Ilea, *Water Science & Technology*, **2015**, *71(11)*, 1646.
19. Y.S. Al-Degs, M.A.M. Khraisheh, S.J. Allen, M.N. Ahmad, *Journal of Hazardous Materials*, **2009**, *165*, 944
20. B. Kiran, A. Kaushik, *Chemical Engineering Journal*, **2008**, *144*, 391.
21. M. Mureseanu, N. Cioatera, I. Trandafir, I. Georgescu, F. Fajula, A. Galarneau, *Microporous and Mesoporous Materials*, **2011**, *146*, 141.
22. C. Xiong, Y. Li, G. Wang, L. Fang, S. Zhou, C. Yao, Q. Chen, X. Zheng, D. Qi, Y. Fu, Y. Zhu, *Chemical Engineering Journal*, **2015**, *259*, 257.
23. B. Cheknane, M. Baudu, J. P. Basly, O. Bouras, F. Zermane, *Chemical Engineering Journal*, **2012**, *209*, 7.
24. M.M. Sekhula, J.O. Okonkwo, C.M. Zvinowanda, N.N. Agyei, A.J. Chaudhary, *Chemical Engineering and Processing*, **2012**, *3(2)*, 1.
25. A.A. Ahmad, B.H. Hameed, *Journal of Hazardous Materials*, **2010**, *175*, 298.
26. I. Bleotu, S.A. Dorneanu, M. Mureşeanu, E. Gîlcă, P. Ilea, *Revista de Chimie. (Bucharest)*, **2015**, *66(6)*, 797.
27. www.purolite.com/RelID/619508/isvars/default/purolite%C2%AE_s910.htm.

Dedicated to prof. dr. I. C. Popescu
on the occasion of his 70th anniversary

COLUMN AND BATCH REGENERATION STUDIES FOR ZINC REMOVAL ON DIFFERENT ANIONIC EXCHANGE RESINS

EMILIA GÎLCĂ, ANDRADA MĂICĂNEANU[a*], PETRU ILEA[a]

ABSTRACT. Five anion exchange resins were used to remove zinc chloride complexes from a synthetic acid pickling bath. The experiments were carried out for several cycles of adsorption-desorption in fixed bed column and batch mode. The results showed that the percent of zinc chloride sorption remained constant in the last three cycles (from six) in both cases. Comparing various resins, the following series was depicted based on the ionic exchange capacity: Purolite A600MB > Amberlite IRA410 > Purolite A103S > Purolite A400MBOH > Purolite NRW700. Also it was possible to concentrate the metal in smaller solution volume after regeneration, which will make its recovery much easier.

Keywords: regeneration, fixed bed, batch mode, zinc chloride

INTRODUCTION

The worldwide production and use of chemical compounds increased due to industrial proliferation and urbanization. The heavy metals are the most common pollutants found in effluents discharged from electroplating industries and cause serious environmental problems [1]. The most common method to treat these wastewaters is chemical precipitation followed by filtration or solid/liquid separation processes [2]. A method that could replace traditional solvent extraction systems can be the ion exchange process due to its ability to selectively and repeatedly adsorb and desorb metals [3].

In case of zinc, the principal sources of effluents are galvanizing processes. The main purpose of galvanizing is the protection of steel against corrosion, which can cause dangerous damage. During the pickling process

---

[a] *Department of Chemistry and Chemical Engineering, Babeş-Bolyai University, 11 Arany Janos st., RO-400028, Cluj-Napoca, Romania.*
[*] *Corresponding author andrada@chem.ubbcluj.ro*

the steel is dipped into a tank that contains acids. In the recent years, the sulfuric acid has been replaced by the hydrochloric acid due to its waste disposal cost which is smaller compared to sulfuric acid disposal [4]. The metals that contaminate the acid used in the pickling process are zinc and iron [5].

Selective separation of the chloride complexes of Zn^{2+} and Fe^{2+} is easy and based on their complexes stability since the iron does not form stable complexes at low acid concentrations [6].

The ionic state of zinc depends on concentration and acidity of the solutions. Thus the tetrachlorozincate $[ZnCl_4]^{-2}$ complex is formed in strong acid solution with HCl concentration in 1-6 mol/L range. With the decrease in acidity to 10^{-2} - 10^{-3} mol/L the amounts of aquacomplexes $[ZnCl_4(H_2O)_2]^{2-}$ and $[Zn(H_2O)_6]^{2+}$ increase. Therefore, anionic exchange resins can be used for $[ZnCl_4]^{-2}$ recovery [7]. In this context, the chloride complexes are retained in the resin bed by a reversible reaction. When the bed becomes saturated it must be regenerated. In this case, the volume of regenerate is much lower than the volume of the effluent and the metals are in a much higher concentration. Afterward, different methods such as precipitation, distillation or other recovery processes can be applied [5].

The main purpose of this study was to evaluate the ability of several anion exchangers to retain and desorb zinc chloride complexes in order to increase the zinc concentration in the regeneration step allowing its recovery by electrodeposition. Also in this study, the capacity of the Amberlite IRA410 resin was investigated for several cycles of sorption –desorption in fixed bed column and in batch mode.

RESULTS AND DISCUSSION

Fixed bed studies for resin usage

In our previous papers we concluded that besides other resin tested, Amberlite IRA410 resin was the best ionic exchanger for the removal of zinc ions as zinc chloride complexes [8]. The effect of different parameters were investigated in batch mode [8] and fixed bed column [9]. As sorption-desorption capacity for several cycles was not considered before, in this study, the results regarding this aspects were presented.

The experiments were carried out using a fixed bed containing 5 g of resin, 1.36 mL/min flow rate and 500 mg/L initial zinc concentration in a 24 mm diameter column. The synthetic solution (656 mL) was allowed to pass through the column in continuous down flow mode. The treated metal solution (20.5 mL) was collected at the outlet of the column every 15 min for 500 minutes and analysed [9]. The results obtained for zinc sorption by

Amberlite IRA410 for six cycles of sorption-desorption were presented in Figure 1. As it can be seen, the breakthrough curves did not follow the typical 'S-shape', which are regularly formed in ideal adsorption systems. The shape of the obtained breakthrough curves was due to the slow kinetics of zinc complex sorption on the resin, therefore an incomplete 'S' breakthrough shape was produced [9]. An increase of sorption-desorption cycles number does not lead to a substantial modification in ionic exchange capacity (Equation 2), values between 35.8 mg/g (first cycle) 35.5 mg/g (sixth cycle) were obtained. By comparing the six cycles curves it can be seen that the breakthrough behaviour remains unchanged with successive regeneration.
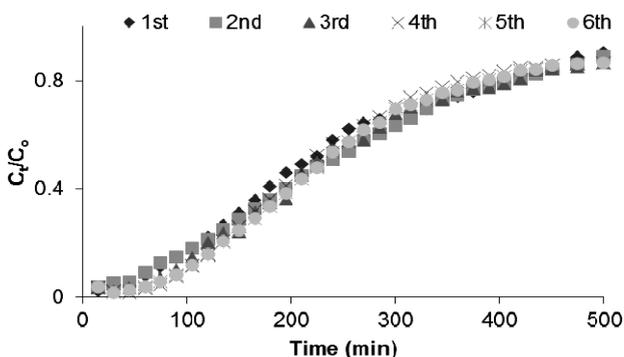
Figure 1. Breakthrough curves for Zn sorption during six sorption cycles in fixed bed column

Once the resin was saturated it is important to regenerate the resin in order to recover metal ions and also for the further use of the resin. The regeneration of the resin after the sorption cycles was made using double-distillate water.
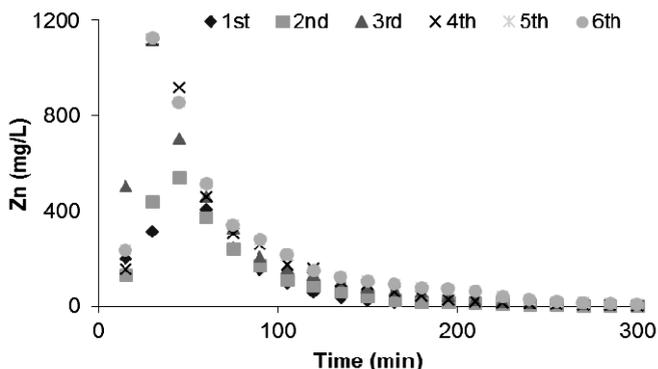
Figure 2. Zinc concentration during regeneration cycles in fixed bed column

The results obtained are presented in Figure 2. In the first minutes the concentration was very high, after that slowly decreased as the resin was regenerated.

Batch studies for resin usage
The batch studies were carried out for six sorption-desorption cycles using 100 mL solution (500 mg/L zinc initial concentration) contacted with 5 g of resin (Amberlite IRA410) for 300 minutes until the equilibrium was reached. The regeneration of the resin after the sorption cycles was made using double-distillate water.

The results (Figure 3) showed that the removal efficiency (Equation 3) decrease with the sorption-desorption cycles number and after the third cycle remained constant. The decline in efficiency was no more than 10% which showed that the resin had good potential to retain metal ions although it has been reused for several times [10].
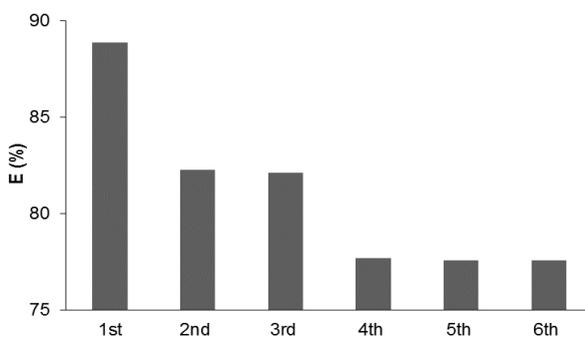
Figure 3. Removal efficiency after six sorption-desorption cycles in batch mode

Regeneration of different anionic exchange resins in batch mode
Regeneration of the resin is important in the economic development and implies the removal of metal loaded using an eluting agent without damaging the capacity of the adsorbent, making it reusable in several sorption-desorption cycles [11].

Five anion exchanger resins were tested in the same conditions for one sorption-desorption cycle using a higher volume of solution (400 mL) in this case in order to exhaust the resin. The results presented in Figure 4 showed that the maximum percent of sorption, about 48%, was obtained for Purolite A600MB and the minimum percent of sorption, about 42%, was obtained for Purolite A400NRW700. Comparing various resins, the following series was depicted based on their ionic exchange capacity: Purolite A600MB > Amberlite IRA410 > Purolite A103S > Purolite A400MBOH > Purolite NRW700.
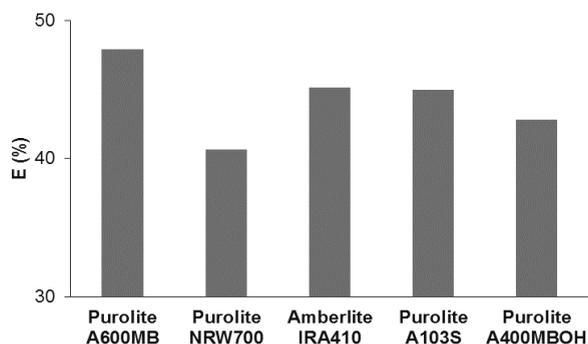
Figure 4. Removal efficiency for zinc sorption on different anionic exchange resins

The regeneration of the resins after the sorption cycle was made using double-distillate water and the obtained results are presented in Figure 5.
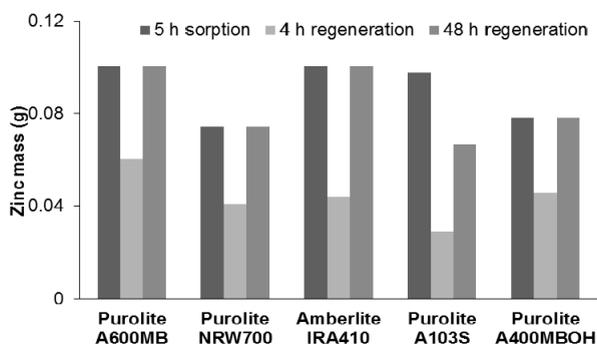
Figure 5. Zinc mass after sorption and regeneration studies

In order to identify if the resin was completely regenerated, zinc mass was calculated after sorption and regeneration. The zinc mass sorbed by the resin in 5 h was calculated taking into account the volume and the concentration of the solution used (400 mL, 500 mg/L), calculated by difference between the initial zinc concentration and the final zinc concentration. The zinc mass after regeneration was calculated, by taking into consideration the volume used for regeneration and the determined zinc concentration.

The maximum zinc mass desorbed after 4 h was obtained for Purolite A600MB and the minimum zinc mass for Purolite A103S. With a further increase in time, all the resins were completely regenerated with exception of Purolite A103S. Comparing various resins the following series was depicted based on recovered zinc mass after 4 h: Purolite A600MB > Purolite A400MBOH > Amberlite IRA410 > Purolite NRW700 > Purolite A103S.

Effect of the initial zinc and iron concentration

Taking into consideration that from the Purolite A600MB resin the highest quantity of zinc was recovered after 4 h regeneration and that usually iron is also presented in pickling baths, further sorption-desorption experiments with multicomponent solutions (zinc and iron) were also considered.

The experiments were carried out using 5 g of Purolite A600MB which was contacted with 400 mL solution containing zinc (500-900 mg/L) for 300 min at 500 rpm. In each case 1000 mg/L iron were also added. The obtained results are presented in Figure 6 (due to the fact that iron concentration remained unchanged, in order to preserve image clarity only one iron curve was presented).
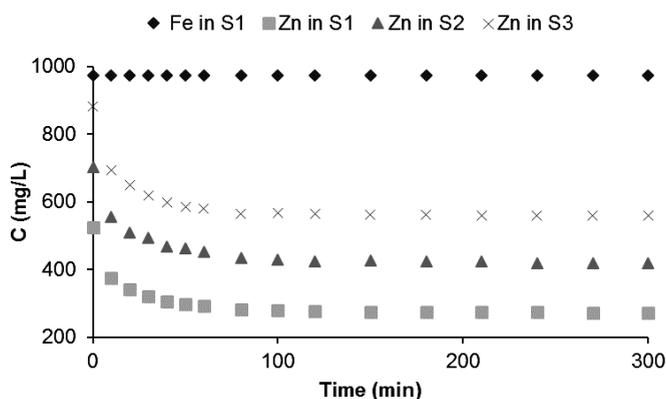
Figure 6. Effect of zinc initial concentration on zinc sorption by Purolite A600MB in presence of iron (S1=1000 mg/L Fe+500 mg/L Zn; S2=700 mg/L Zn +1000 mg/L Fe; S3=900 mg/L Zn+1000 mg/L Fe)

In this range of concentration, zinc sorption was rapid in the first 10 min, after that, the sorption rate slowly decreases as the process reaches equilibrium. The initial iron concentration remained constant during the experiments, due to the fact that in hydrochloric acid medium iron will not form complexes. The zinc ionic exchange capacity (Equation 1) at 500 mg/L was 5.02 mg/g (48% efficiency) and 6.48 mg/g (37% efficiency) at 900 mg/L.

The following experiments were made in order to determine the ability of this anionic exchange resin to be regenerated for further uses and to increase the zinc concentration in the regeneration step allowing its recovery by electrodeposition.

Desorption experiments for all the concentrations were carried out using different volumes of double-distilled water (20-80 mL). The obtained results were presented in Figure 7. The zinc mass increased with increasing the volume of the double-distillate water used. A volume of 80 mL double-distillate

water ensured the complete regeneration of the resin. The concentration of zinc in 80 mL was between 1.3-1.8 g/L in the studied range of concentration. Afterwards zinc electrodeposition could be applied in order to obtain pure zinc deposits.
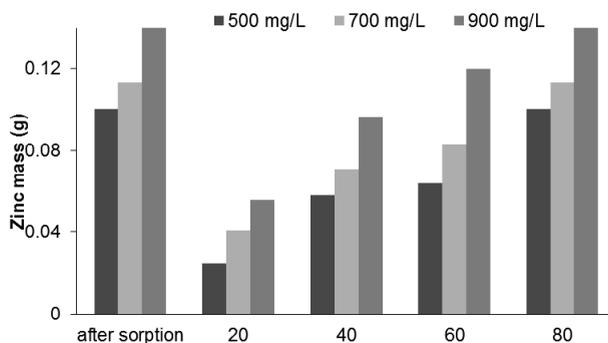
Figure 7. Desorption experiments using different volumes of water

CONCLUSIONS

Sorption-desorption experiments were carried out in fixed bed column and in batch mode for six cycles in order to investigate the capacity of the considered resins to retain zinc complexes. After several sorption-desorption cycles the decline in efficiency was maximum 10%, which indicated that the resins had good potential to remove zinc from a synthetic acid pickling bath. Purolite A600MB resin presents the best regeneration ability of those studied. Therefore it was possible to concentrate the metal in a smaller volume and afterwards zinc electrodeposition could be applied in order to obtain pure zinc deposits.

EXPERIMENTAL SECTION

Five strong base anionic exchange resins, Purolite A600MB Amberlite IRA410, Purolite A400MBOH, Purolite NRW700 and a weak base anionic exchange resin, Purolite A103S were considered in order to investigate their capacity to remove zinc chloride complexes. Before usage, the resins were soaked in double-distilled water for 24 hours.

Initial solutions were prepared by dissolving $ZnCl_2$ and $FeCl_2$ salt in hydrochloric acid 1 M.

The sorption experiments were realized in a fixed bed column where zinc solution of known concentration (500 mg/L) was allowed to pass through the column using a peristaltic pump for 500 min and in batch mode where 5 g of resin were contacted with 100 and 400 mL of zinc (500 mg/L) for 300 min under 500 rpm magnetic stirring. The treated solution collected at the outlet of the column and the samples of 1 mL taken from the solution at previously established time intervals (batch mode) were analyzed in order to determine the exact concentration of zinc using an atomic absorption spectrophotometer Avanta PM GBC (Australia).

The regeneration experiments were realized as follows: (a) in case of the fixed bed, the regeneration solution (distilled water) was allowed to pass through the column at 1.36 mL/min flow rate for 300 min; every 15 min, one sample was collected at the outlet of the column and analyzed; (b) in batch mode, by contacting the exhausted resin (5 g) with volumes between 20 and 80 mL double-distilled water for 48 hours without stirring; at the end of the experiment zinc concentration was determined.

Ionic exchange process and sorption-desorption cycles were followed using ionic exchange capacity (Equation 1, 2) and removal efficiency (Equation 3) [8, 9].

$$q_e = \frac{(C_0 - C_e)}{m} \cdot \frac{V}{1000} \text{ (batch) (1)} \quad q_t = \frac{(C_0 - C_e)}{m} \cdot \frac{V}{1000} + q_{t-1} \text{ (fixed bed)} \quad (2)$$

$$E(\%) = \frac{C_0 - C_e}{C_0} \cdot 100 \quad (3)$$

where, C_0, C_e are the initial and equilibrium zinc ion concentrations (mg/L); q_e is the ionic exchange capacity (mg/g) [8], q_t, q_{t-1} are the amount of zinc ions sorbed at times t and (t-1), respectively (mg/g); V is the volume of zinc ion solution (mL); m is the mass of resin (g) [9].

ACKNOWLEDGMENTS

REFERENCES

1. M. Revathi, M. Saravanan, A.B. Chiya, M. Velan, *Clean – Soil, Air, Water*, **2012**, *40(1),* 66.
2. I.H. Lee, Y.C. Kuan, J.M. Chern, *Journal of the Chinese Institute of Chemical Engineers,* **2007**, *38*, 71.
3. K. Northcott, H. Kokusen, Y. Komatsu, G. Stevens, *Separation Science and Technology*, **2006**, *41*, 1829.
4. N. Muthu, F. Abdul Aziz, R.B. Mohd Yusuff, *Global Journal of Researches in Engineering Civil and Structural Engineering,* **2013**, *13(6)*, 15.
5. E. Maraňón, Y. Fernández, F.J. Súarez, F.J. Alonso, H. Sastre*, Industrial & Engineering Chemistry Research*, **2000**, *39*, 3370.
6. M. Regel-Rosocka, *Journal of Hazardous Materials*, **2010**, *177*, 57.
7. O.N. Kononova, N.V. Mikhaylova, A.M. Melnikov, Y.S. Kononov, *Desalination,* **2011**, *274*, 150.
8. E. Gîlcă, A. Măicăneanu, P. Ilea, *Central European Journal of Chemistry*, **2014**, *12(8)* 821.
9. E. Gîlcă, A. Măicăneanu, P. Ilea, *Water Science & Technology*, **2015**, *71(11)*, 1646
10. Z. Zulfadhly, M.D. Mashitah, S. Bhatia, *Environmental Pollution*, **2001**, *112*, 463.
11. H. Kalavathy, B. Karthik, L.R. Miranda, *Colloids and Surfaces B: Biointerfaces,* **2010**, *78*, 291.

Dedicated to prof. dr. I. C. Popescu
on the occasion of his 70th anniversary

HYDRODYNAMIC CHARACTERIZATION OF THREE PHASE FLUIDIZED BED

SIMION DRAGAN[a*]

ABSTRACT. Hydrodynamics study plays an important role in the economical design and operation of three phase fluidized bed contactor. This paper presents the experimental investigation on the hydrodynamic behavior of a counter current gas-solid-liquid three phase fluidized bed. The results have shown that the pressure drop increases with the increase of gas velocity, spray liquid density and solid particle density. The expanded bed height increases with the increase of gas velocity and decreases with solid particles density.

Keywords: three phase fluidized bed contactor, pressure drop, expanded bed height

INTRODUCTION

Intensification of the mass transfer between a liquid and a gaseous phase needs as high contact area as possible between the two phases. So, is very important to construct such equipments which could generate as high interfacial area as possible. Fluidized beds offer very high interfacial area per unit volume of the active column. A specific equipment which uses relatively large size solid inert packing as the fluidizing media is the turbulent contact absorber [1].

Three phase fluidized bed column is mass transfer equipment in which the bed of low density packing is fluidized by the counter current flow of gas and liquid. The gas flows as a continuous phase and the liquid flows as a dispersed phase in absorber. The intensive mixing of the solid packing in the column determines high turbulence and therefore enhances the mass

---

[a] *"Babeş-Bolyai" University, Faculty of Chesmistry and Chemical Engineering, 11, Arany Janos St., RO-400028 Cluj-Napoca, Romania.*
[*] *Corresponding author: sdragan@chem.ubbcluj.ro*

transfer comparative to conventional fixed packed beds. This contact mode between phases determine low pressure drop in the column, very high interfacial contact area per unit volume of the column, and capability to process large volume of gases. These advantages make three phase fluidized bed absorbers technology favourable for pollution control.

There are two operating types for three phase fluidized bed [2]. In type I, the solid fluidization starts before flooding in the column, whereas in type II, fluidization starts after flooding in the column. Density of solid packing has a major contribution in deciding the mode of operation. For beds with relatively low-density particles ($\rho_s < 300$ kg/m^3), fluidization occurs at a gas velocity lower than the flooding point of the equivalent counter current fixed bed. For beds with relatively high-density particles ($\rho_s > 300$ kg/m^3), fluidization always occurs after the flooding point of the packed bed [2, 3].

Vunjak-Novakovic et al. [4] developed a chart for the demarcation of type I and type II modes of three phase fluidized bed operation, as shown in Figure 1.
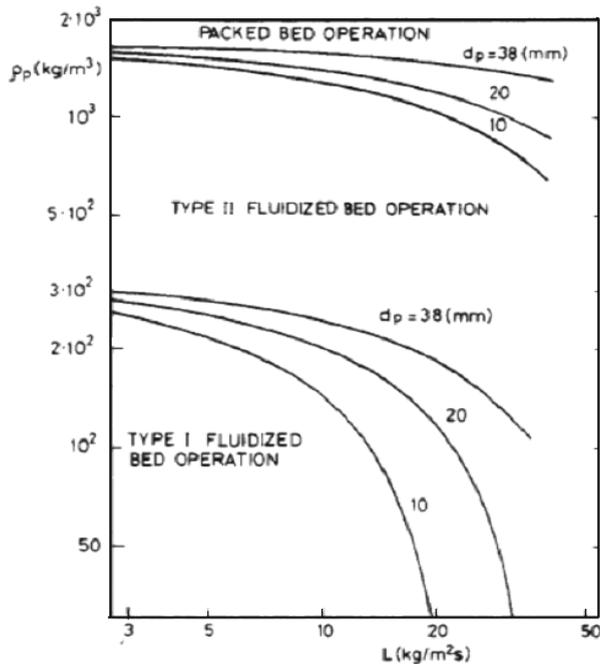
Figure. 1. Operating flooding zones in turbulent contact absorber [4].

Above classification of type I and type II regimes of turbulent contact absorber operation is very broad. The increase in liquid flow rate and decrease in solid packing diameter also shifts the regime from type I into type II.

Pressure drop, expanded bed height and liquid holdup are regarded as key hydrodynamic parameters of any mass transfer equipment The objectives of the present study were to determinate the pressure drop and fluidized bed expansion in gas-solid-liquid three phase fluidized bed column with low density solids.

RESULTS AND DISCUSSION

The hydrodynamic parameters important for mass transfer in fluidized equipments include: minimum fluidization velocity, pressure drop, expanded bed height and liquid holdup. For determination of these hydrodynamic characteristics were used experimental methods.

Pressure drop in any mass transfer device determines liquid holdup, interfacial contact area and its operating cost. In literature, the dependence of pressure drop on liquid and gas velocities, diameter and density of packing, static bed height and support grid free area have been studied. It is consensus in literature that pressure drop in fluidized bed contactor increases with increasing liquid flow rate at a fixed gas flow rate.

The momentum balances for gas and liquid phases in the bed under steady state condition can be expressed by next equations [5]:

$$\left(-\frac{dp}{dz}\right)^{bed} = \rho_g g + \left(-\frac{dp}{dz}\right)^{gas}_{friction}$$

$$\left(-\frac{dp}{dz}\right)^{bed} = \rho_l g + \left(-\frac{dp}{dz}\right)^{liquid}_{friction} \qquad (1)$$

Pressure drop due to friction in the gas phase is gas-liquid friction:

$$\left(-\frac{dp}{dz}\right)^{gas}_{friction} = \left(-\frac{dp}{dz}\right)^{g-l}_{f} \qquad (2)$$

and pressure drop due to friction in the liquid phase consists of two component, one is contributed by the solid phase and the other is contributed by the gas phase:

$$\left(-\frac{dp}{dz}\right)^{liquid}_{friction} = \left(-\frac{dp}{dz}\right)^{l-s}_{f} + \left(-\frac{dp}{dz}\right)^{l-g}_{f} \qquad (3)$$

Since the mutual forces at the interface are cancelled by each other, the equations become [5]:

$$\frac{\varepsilon_l}{1-\varepsilon_s}\left(-\frac{dp}{dz}\right)_f^{l-g}+\frac{\varepsilon_g}{1-\varepsilon_s}\left(-\frac{dp}{dz}\right)_f^{g-l}=0 \ \text{ or}$$

$$\left(-\frac{dp}{dz}\right)_f^{l-g}=-\frac{\varepsilon_g}{\varepsilon_l}\left(-\frac{dp}{dz}\right)_f^{g}$$

(4)

From equations (3) and (4) results:

$$\left(-\frac{dp}{dz}\right)^{bed}=\rho_l g+\left(-\frac{dp}{dz}\right)_f^{l-s}-\frac{\varepsilon_g}{\varepsilon_l}\left(-\frac{dp}{dz}\right)_f^{g}$$

(5)

where $\varepsilon_g+\varepsilon_l+\varepsilon_s=1$, are gas, liquid and solid holdup.

The measurements of the bed pressure drop in gas-solid-liquid three phase fluidized bed are presented in Figure 2 to Figure 4.
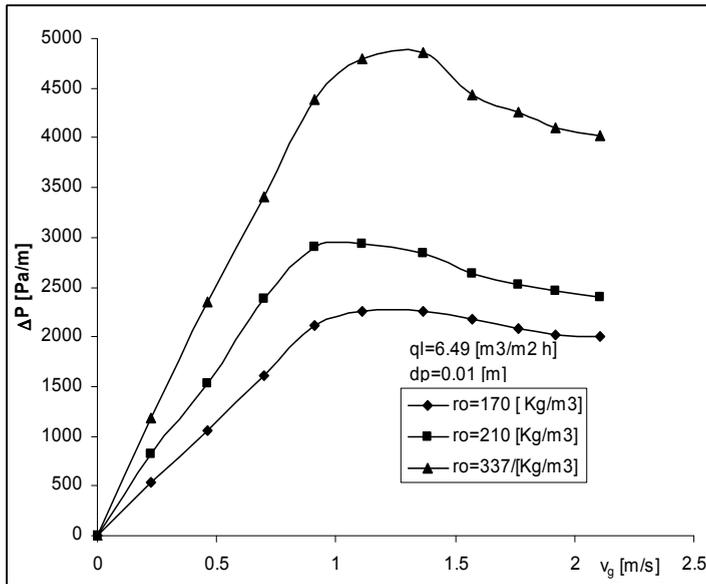
Figure 2. Influence of gas velocities and particle density on pressure drop at q_l = 6.49 m³/m²h.

Figures 2 and 3 show the increase of the pressure drop with the increase of gas velocities, solid particle density, spray liquid density and height solid packing.
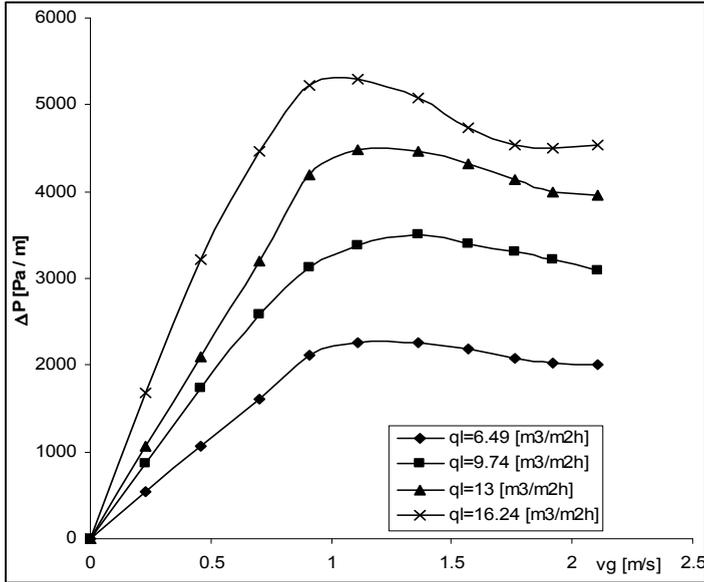
Figure 3. Influence of liquid spray density and gas velocities on pressure drop for packing with ρ = 170 kg/m^3.
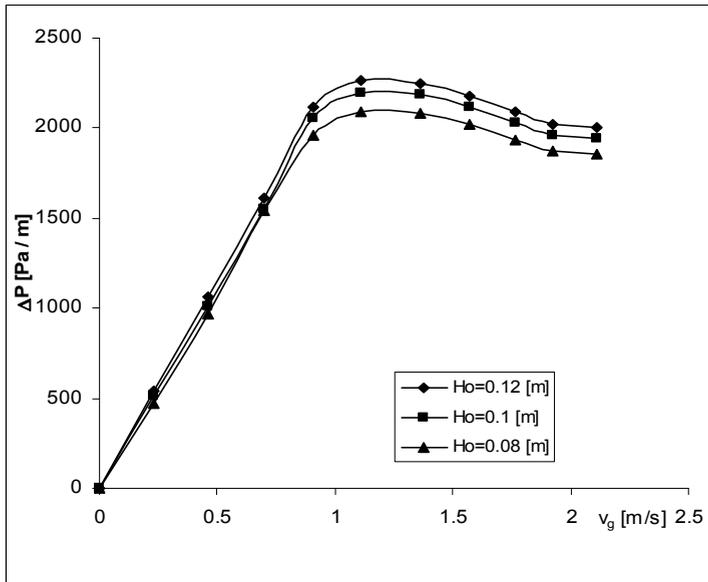
Figure 4. Effect of height of solid packing on pressure drop at q_l = 6.49 m^3/m^{2}h, for packing with ρ = 170 kg/m^3.

For a constant spray liquid density (q_l = ct.) and the increase gas velocity, the pressure drop increases until minimum fluidization velocity is attained. This zone of operation column is the static bed region. With further increase in gas velocity, the entire solid bed is in a fully fluidized state, thereafter it is a small change in pressure drop. This is the fluidized bed region. The column is preferably operated in the fully fluidized bed region, in which the turbulence of the bed increases with the increase of gas velocity and spray liquid density, until the true flooding point is reached.

The effect of increasing static bed height on pressure drop is given in Figure 4. There is a slight decreasing effect of static bed height on the reduced bed height for type I fluidization. This initial reduced pressure drop in bed height can be explained by considering that as the static bed height increases with the increase in weight of the bed, which is more than the force generated by the upward moving gas.

The static bed begins to expand once the superficial gas velocity reaches the minimum fluidization velocity. The expansion of the bed increases with the increase of gas velocity, due to the upward force of the gas which tends to lift the packing. During the experiments, it was observed that the bed expansion begins at lower gas velocities, when the spray liquid density is increasing, at the same density of the solid particles.

Variables which affect bed expansion are: gas flow rate, liquid flow rate, free area of the grid, density and diameter of the packing and static bed height. Expanded bed height was determined by visual observations. In the case of bed pulsation, maximum and minimum heights of the bed were noted and average height was selected.

Bed expansion data obtained in present study is represented in dimensionless form as ratio of the expanded bed height to the static bed height (H/H_0). The effect of liquid spray density and gas velocity on expanded bed height (H/H_0) is shown in Figures 5 and 6.

The static bed begins to expand once the superficial gas velocity reaches the minimum fluidization velocity. The expansion of the bed with the increase of gas velocity is due to the upward force of the gas which tends to lift the solid packing. During the experiments, it was observed that the bed expansion begins at lower gas velocities when the liquid spray density is increased. This means that the bed expands with the increase of gas velocity.

The solid packing with the same diameter but with higher density fluidizes to a smaller height, at the constant liquid spray density and constant gas velocity.
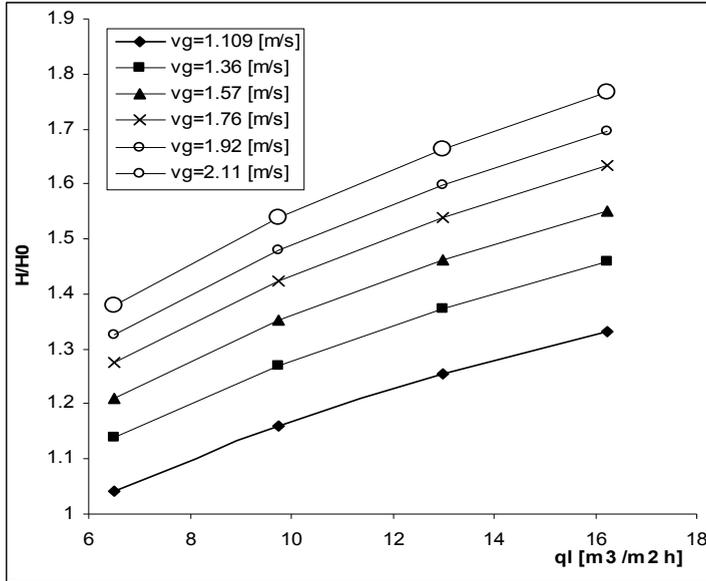
Figure 5. Influence of liquid spray density and gas velocities on expanded bed height, for packing with ρ = 170 kg/m^3.
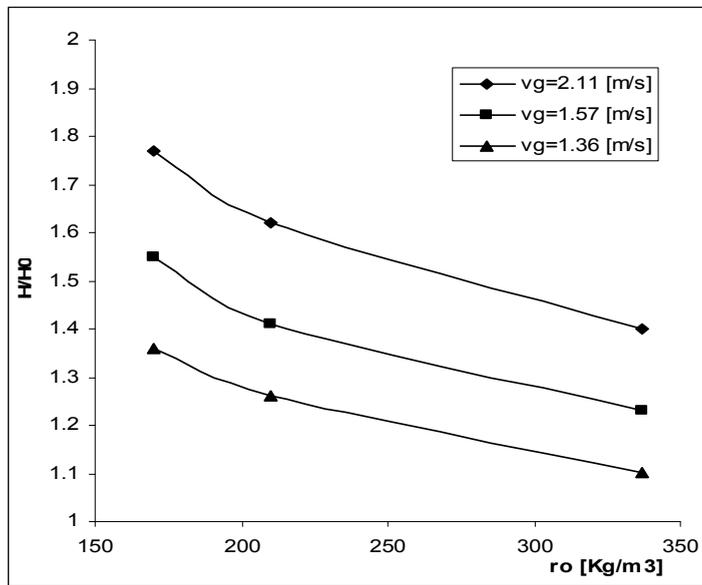
Figure 6. Influence of density of packing on bed expansion at q_l = 16.24 m^3/m^{2}h.

CONCLUSIONS

The pressure drop, expanded bed height and liquid holdup are regarded as the key hydrodynamic parameters of this mass transfer equipment.

Influence of gas velocities, solid density, liquid spray density and solid static bed height on pressure drop, expanded bed height for gas-solid-liquid three phase fluidized bed with low density solid was determined.

The pressure drop increases with the increase of gas velocities, solid particle density, spray liquid density and height solid packing. Pressure drop per unit bed height decreases lower when gas velocity increases over the minimum fluidization velocity.

The expansion of the bed with the increase of gas velocity is due to the upward force of the gas which tends to lift the solid packing.

EXPERIMENTAL

The schematic diagram of the experimental setup is shown in Figure 7.
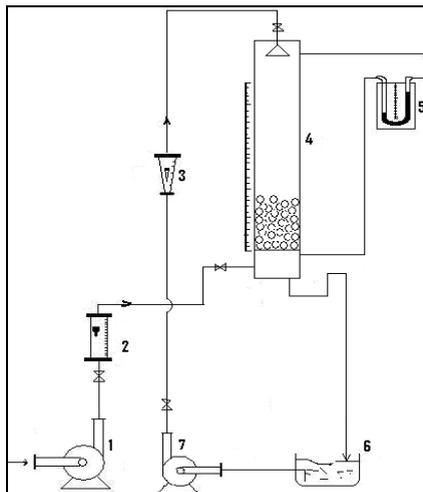
Figure 7. Schematic representation of experimental equipment.
Where: 1 - blower; 2 - air flow meter; 3 - water flow meter; 4 - fluidizing column;
5 - U-tube manometer; 6 - storage tank; 7 - centrifugal pump.

The column was made of glass, with 0.14 m diameter and 1.10 m height. The packing are hollow spheres of 0.01 m diameter and with the density of 170; 210 and 337 kg/m^3. The air as the continuous phase was fed at the bottom of the column and exit at the top. Water as dispersed

phase was sprayed from the liquid distributor over the column cross section. For measuring the fluidized bed height, a scale arrangement was made. The pressure drop across the bed was measured using manometer method and the height of the expanded fluidized bed was read on the scale and noted. Using these values, the minimum fluidization velocity, expanded bed height and liquid holdup can be determined. The experimental conditions are presented in Table1.

Table 1. Range of the experimental conditions

Variable	Range
Column diameter D_c, m	0.14
Diameter of solid particle d_p, m	0.01
Solid particle density, kg/m^3	170; 210; 337.
Static solid bed height H_0, m	0.12; 0.1; 0.08
Grid free area, %	78%
Liquid spray density q_l, m^3/m^2 h	6.49; 9.74; 13; 16.24
Gas velocity v_g, m/s	0 - 2.2

In literature it has been reported that the column diameter to packing diameter ratio should be higher than 10, in order to eliminate wall effects. The static bed height to column diameter ration should be lower than one to eliminate the pulsation and non-uniform fluidization. It has been reported in literature that the hydrodynamic and mass transfer effects of grid becomes negligible for grid free areas greater than 70 % [6]. All these conditions were fulfilled in the present study.

REFERENCES

1. A.E.R. Bruce, P.S.T. Sai, K. Krishnaiah, *Chemical Engineering Journal*, **2004**, *99*, 203.
2. A.S. Shabani, T. AsI, *International Journal of Chemical Engineering and Applications*, **2010***, 1*, 117.
3. B.K. O'Neill, D.J. Nicklin, N.J. Morgan, L.S. Leung, *Canadian Journal of Chemical Engineering*, **1972**, *50*, 595.
4. G.V. Vunjak-Novakovic, D.V. Vukovic, H. Littman, *Industrial and Engineering Chemistry Research*, **1987**, *26*, 958.
5. A.E.R. Bruce, R. Balasubramanian, P.S.T. Sai, K. Krishnaiah, *Chemical Engineering Science*, **2006**, *61*, 2089.
6. K. Soundarajan, K. Krishnaiah, *Indian Journal of Chemical Technology,* **1996**, *18*, 152.

Dedicated to prof. dr. I. C. Popescu
on the occasion of his 70th anniversary

SPECTRAL GRAPHITE AS ELECTRODE MATERIAL FOR THE ALL-VANADIUM REDOX FLOW BATERY

DANA-MARIA SABOU[a], SORIN-AUREL DORNEANU[a,*], PETRU ILEA[a]

ABSTRACT. The ability of unmodified or PbO_2 coated spectral graphite (SG), to act as positive electrode in an all vanadium redox flow battery was tested. Our results showed that the unmodified SG requires simple pretreatment and is efficient in terms of current due to a large active area, 4 time greater that the geometrical one. The PbO_2 deposits were grown on surfaces that previously received only basic treatment, but present a poor stability. In all experiments, large separations of anodic and cathodic peak potentials (between 118 and 1015 mV) were observed, proving the irreversibility of the V^V to V^{IV} redox couple on all studied materials.

Keywords: all vanadium battery, spectral graphite, cyclic voltammetry

INTRODUCTION

Electrochemical power sources are an important alternative tool for energy converting and storage. A special category is the Redox Flow Batteries (RFB) - secondary batteries that employ solvated redox couples. The marked interest for RFB displayed during recent years owes to the ever increasing necessity for storing the energy, especially that generated by the renewable, fluctuating sources as solar or wind power [1-4].

All vanadium redox flow battery (VRFB) is particularly attractive, because it avoids any irreversible cross-contamination, since the active redox couples in the two sides of the cell employ the same chemical element. The $V^{II/III}$ couple operates in the negative half-cell (eq. 1) and $V^{IV/V}$ in the positive half-cell (eq. 2).

---

[a] *Babeş-Bolyai University, Faculty of Chemistry and Chemical Engineering, 11 Arany Janos str., RO-400028, Cluj-Napoca, Romania,*
* *Corresponding author: dorneanu@chem.ubbcluj.ro*

$$V^{III} + e^- \leftrightarrow V^{II} \quad E^0 = -0.26V\,/\,EHN \quad\quad (1)$$
$$(V^{IV}O)^{2+} + H_2O \leftrightarrow (V^VO_2)^+ + 2H^+ + e^- \quad E^0 = +1.00V\,/\,EHN \quad (2)$$
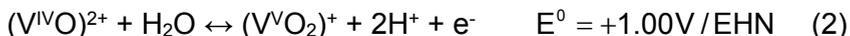
However, achieving high performances for VRFB strongly depends on the electrode material, which should ensure, simultaneously, as low as possible overpotentials for the reactions (1) and (2) and as high as possible overpotentials for the water decomposition reactions (3) and (4) that inherently occur in aqueous solutions:

$$H_2O \rightarrow \tfrac{1}{2}O_2 + 2H^+ + 2e^- \quad E^0 = +1.23V\,/\,EHN \quad\quad (3)$$
$$H_2O + e^- \rightarrow \tfrac{1}{2}H_2 + HO^- \quad E^0 = -0.83V\,/\,EHN \quad\quad (4)$$

Of outmost importance for the performance of all vanadium redox flow battery is the electrode material. A vast range of electrode materials was evaluated as both positive and negative electrodes for the VRFB. Many of the materials tested were carbon-based and graphite, in particular [5,6]. The properties that make graphite desirable are: good electronic conduction, good stability in highly acidic solutions and under a large window of potentials, marked porosity that ensures quite large reactive surface area by providing a multitude of redox reaction sites [7], low cost and easy manufacturing.

In general, the carbonaceous materials were found to perform well in the negative half of the cell [5,8]. Some deterioration was observed when they were used in the positive half-cell, attributed to the slow oxidation of the surface as a result of oxygen evolution during cell overcharge [9].

Some other electrode materials that were tried out include lead, gold, platinum, platinized titanium or other consecrated dimensionally stable anodes (DSAs), and gave mixed results [8]. Lead based electrodes received some special attention, being less costly and relatively stable in sulfuric acid systems. However, Pb becomes passivated in the potential range where the $V^{IV/V}$ redox couple reactions occur [5].

Nowadays, graphite is the typical choice for the VRFB electrodes. In addition to its above mentioned advantages, it provides satisfactorily large overpotentials towards the parasitic reactions (3) and (4). Of the various types tried out, such as rods, plates, cloths and felts, the latter are often preferred, based on their large specific surface. In order to achieve longer lifetime and superior energetic capacity (higher currents), there is a continuous focus on the improvement of the electrode material.

Several ways have been explored to this end, such as the use of additives [10], thermal treatment [5], or oxidative treatment [11] of the graphite surface. The electrode surface modification has been also tried out, in order

to enhance the electrochemical activity of the vanadium redox couples. Usually, it was done by electrodeposition of noble metals such as Pt, Au, Pd, or Ir [12-14] but Pb was also considered for the task.

Some recent work reports a doubling of the peak current density for the $V^{IV/V}$ system on a graphite felt electrode modified by coating with a layer of PbO_2 of approximately 2 μm, through pulse electrodeposition [15], but this improvement was only briefly explored. During our attempts to obtain cheap and improved electrodes for the positive half-cell, we decided to investigate the effect of spectral graphite (SG) modification with PbO_2. Over the graphite felt, SG presents better mechanical properties and enhanced purity; therefore, we considered it a promising choice as base material for PbO_2 deposition. In line with the low costs target, we also aimed to keep the pretreatment of the electrode surface at a minimal level. This paper reports on our results concerning the electrochemical behaviour of unmodified and modified SG electrodes towards the V^{IV}/V^V redox couple.

RESULTS AND DISCUSSION

As pointed out, the intended goal was to obtained and study PbO_2 modified electrodes, by using the spectral graphite (SG) as support. However, tests on the unmodified SG were required first.

Our studies were undertaken at 25 ºC in an aqueous solution containing 0.2 M total vanadium (0.1 M V^{IV} and 0.1 M V^V) in 2 M H_2SO_4, by using the cyclic voltammetry (CV). The voltammograms were recorded at 6 scan rates (v), between 5 and 100 mV/s, (always starting with the highest rate), over the 0.5 V to 1.5 V potential range (measured *vs.* an Ag/AgCl/KCl$_{sat}$ reference electrode). We did not to use lower potentials in order to avoid the reduction of V^{IV} to V^{III}.

Electrochemical behaviour of unmodified and pretreated SG electrodes

The first SG electrode (prepared as described in the experimental section) was used for measurements immediately after insertion in the solution, and exhibited an irreproducible behaviour.

Such outcome was hardly unexpected, since it is documented that the surface of graphite suffers changes in strongly acidic media [5] during the first potential scans. The changes consist on the formation of oxygen moieties which act as mediators for the electron transfer, by facilitating the adsorption of vanadium ions [11]. This process is regarded as an activation of the surface.

Repeated tests were made in order to establish the conditions in which the activation is completed (an equilibrium is reached at the surface), expressed as reproducible response of the electrode. This was accomplished if the freshly prepared electrode was first allowed to complete about 25 cycles over the 0.0 to 1.5 V range of potential at a scan rate of 50 mV/s, the first 15 of them performed in a solution of 2 M H_2SO_4 and the remaining 10 ones in the solution containing the vanadium species.

Figure 1 shows the cyclic voltammograms obtained on an SG electrode (SG I) pretreated as described above. At any scan rate, the second and third cycles overlapped very well, proving once more that the electrode surface has reached a stabilized state.

A second electrode (SG II), which was pretreated 15 cycles in H_2SO_4 followed by 20 cycles in the acidic V^{IV} - V^V solution, was tested with very similar results.

The pretreatment in the vanadium free H_2SO_4 solution proved to be essential, because other electrodes, treated for 35 cycles or more only in the vanadium containing solution, did not reach reproducible responses.

As illustrated in Figure 1, unusual high currents were registered for both the oxidation and the reduction peaks (1.8 to 8.1 mA for the anodic scan and 1.0 to 6.0 mA for the cathodic scan). Similar currents recorded on a graphite electrode are reported in literature when a 15 times more concentrated solution was used [10].
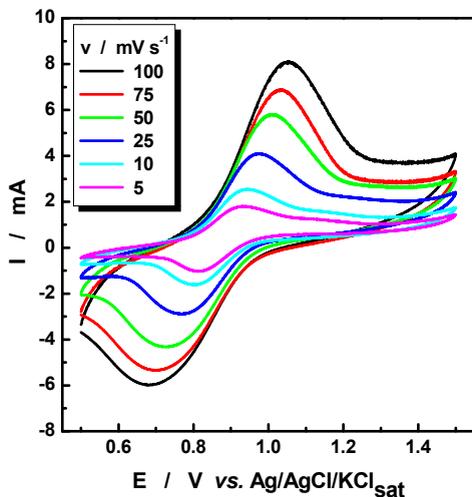
Figure 1. CV curves recorded in 0.1 M V^{IV} and 0.1 M V^V in aqueous 2 M H_2SO_4 on a spectral graphite electrode (SG I) at various scan rates, at T = 298 K

The cyclic voltammograms (Figure 1) also show some asymmetry and marked separation of the peaks. As known, for a totally irreversible process, the peak potential (E_p) is a function of the scan rate (v), shifting in a negative direction (for reduction) by an amount $1.15RT/nF$ (or $30/n$ mV at 25°C) for each tenfold increase in v [16]. Owing to the peak separation observed (ranging between 118 mV at v = 5 mV/s to 369 mV at v = 100 mV/s) the $V^{IV/V}$ redox process can be best characterized as irreversible.

Slightly higher peak separation (164 to 448 mV) and also marginally higher reduction peak currents (1.3 to 6.1 mA) were obtained with SG II. The oxidation peak currents stayed virtually the same (1.8 to 7.9 mA).

As shown in Figure 2, the dependences of the peak current on the square root of the scan rate for both electrodes proved to be linear, leading to the conclusion that the electrode process is diffusion controlled.

For an irreversible process, the equation describing the peak current takes the form [16]:

$$i_p = 0.4958 \left(\frac{n^3 F^3}{RT} \right)^{1/2} \alpha^{1/2} A C_0 D^{1/2} v^{1/2} \qquad (5)$$

where: i_p = peak current [A]; n = number of electrons transferred; F = Faraday constant [A s mol^{-1}]; R = Gas constant [J K^{-1} mol^{-1}]; T = temperature [K]; α = transfer coefficient (dimensionless); A = electrode area [cm^2]; C = concentration [mol cm^{-3}]; D = diffusion coefficient [cm^2 s^{-1}] and v = scan rate [V s^{-1}].
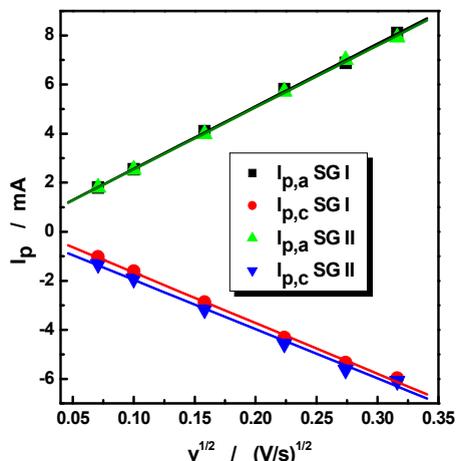
Figure 2. The oxidation (■▲) and reduction (●▼) peak current as a function of the square root of scan rate, for the two SG pretreated electrodes

The slopes of the plots in Figure 2 are dependent on the diffusion coefficient (D) and can be used to compute it. However, applying this treatment (with α = 0.5), D values of $7.28 \cdot 10^{-5}$ or $7.16 \cdot 10^{-5}$ cm^2 s^{-1} from the oxidation peaks and of $4.52 \cdot 10^{-5}$ or $4.78 \cdot 10^{-5}$ cm^2 s^{-1} from the reduction peaks were obtained with SG I and SG II, respectively. These values are in obvious disagreement with those reported in the literature [6,17], which are 20-50 times lower. However, these results were not surprising, considering the high current values recorded.

To shed more light on the matter, a platinum electrode disc with a surface of 0.0314 cm^2 was tested in our vanadium solution. The potential scan range was extended, from -0.1 V to 1.6 V, in order to allow a complete development of the peaks. For the platinum electrode, no activation was required. The second and third cycles of the voltammograms completely overlapped at all of the tested scan rates (between 25 and 200 mV/s). The CV curves obtained with this setup are presented in Figure 3. The irreversibility of the reaction is much more evident here (ΔE of 868 to 1015 mV), hence equation (5) was employed again to compute the diffusion coefficient D.
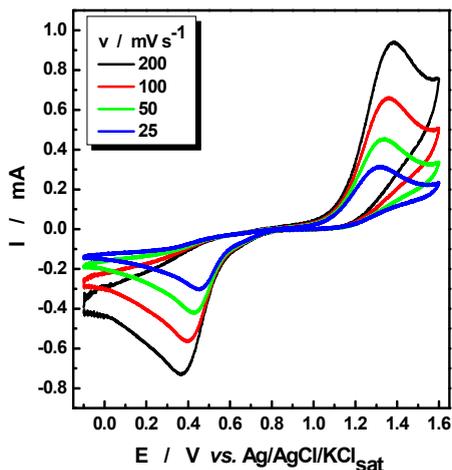
Figure 3. CV curves on a platinum disc (conditions like in Figure 1)

The values obtained were $2.68 \cdot 10^{-6}$ cm^2 s^{-1} from the anodic peaks and $1.22 \cdot 10^{-6}$ cm^2 s^{-1} from the cathodic ones. These values compare fairly well with those listed in literature, for instance $1.4 \cdot 10^{-6}$ cm^2 s^{-1} on glassy carbon, $2.4 \cdot 10^{-6}$ cm^2 s^{-1} on carbon paper and pyrolytic graphite, or $3.9 \cdot 10^{-6}$ cm^2 s^{-1} on plastic formed carbon [6, 17].

The difference between the two computed values may be a result of some interference of the water oxidation (eq. 3) in the anodic region. It is also conceivable that the difference in the volume of the two oxygenated vanadium oxoanions, and of the species that they form with H_2SO_4 in aqueous medium may result in slightly different diffusional properties.

The explanation for the high currents obtained on the SG electrodes must lay, therefore, in the value of the active surface, which should be higher. Indeed, some advancement of the solution in the pores of the material cannot be ruled out.

An estimation of the effective area of our electrode can be made assuming that the diffusion coefficients on the SG electrodes can be substituted by those obtained on platinum. Than, the ratio of the slopes obtained from the plots shown in Figure 2 is proportional to the ratio of the two active surfaces (eq. 6):

$$\frac{\text{slope}_{SG}}{\text{slope}_{Pt}} = \frac{A_{SG}}{A_{Pt}} \tag{6}$$

Keeping for each side of the reaction (oxidation and reduction) the diffusion coefficient as found, estimate values for the effective surface of SG were computed. The results obtained were 0.261 and 0.312 cm^2 with SG I and 0.259 and 0.303 cm^2 with SG II, averaging to 0.28 $\pm$ 0.03 cm^2. This is about 4 times higher than the geometrical surface (0.0707 cm^2).

Electrochemical behaviour of PbO_2 modified SG electrodes

Based on the Faraday law, we evaluated that a current of 1 mA applied for 60 s was required to deposit a layer of approximately 1 µm PbO_2 on the geometrical surface of our electrode. Two electrodes were prepared and tested, one coated with 1 µm (SG/Pb I) and the other with 2 µm of PbO_2 (SG/Pb II)

Prior to use, each PbO_2 coated electrode was pretreated for a number of 10 or 16 cycles respectively, over the 0.0 V to 1.5 V potential range, at 50 mV/s in the vanadium containing acidic solution. As the depositing of PbO_2 was carried out in acidic medium, and the surface was already coated, the H_2SO_4 pretreatment was not considered necessary. The CV tests were completed under the same conditions as those for the non coated electrodes.

The set of measurements made on SG/Pb I seemed to fall satisfactorily on the expected pattern. The CV curves obtained with SG/Pb I (Figure 4) show worse symmetry and slightly higher separation of the peaks (∆E between 188 and 567 mV) as compared to those of SG I (Figure 1) or SG II, arguing even stronger for the irreversibility of the redox process.

The measured currents for the anodic and cathodic peaks were still high, (1.63 to 6.09 and 1.66 to 7.25 respectively) but not higher than those obtained with the non coated electrodes. Further processing of the data led

to results similar to those for the unmodified SG electrodes. An effective area of the electrode of 0.26 ± 0.02 cm^2 resulted (0.235 and 0.277 cm^2 from oxidation and reduction peaks respectively).
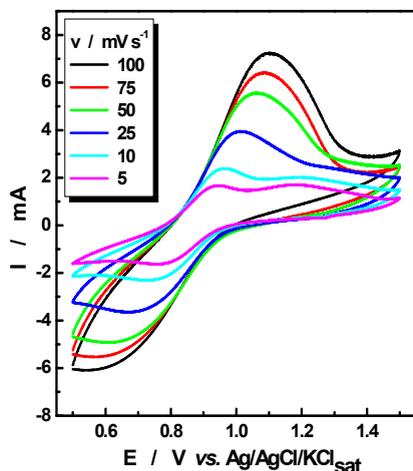
Figure 4. CV curves for a PbO$_2$ coated SG electrode (SG/Pb I)
(conditions like in Figure 1)

The electrode SG/Pb II exhibited irregular behaviour and, upon check, did not stand the test of reproducibility. This led us to suspect that the straightforward deposition without any pretreatment of the graphite surface does not result in a lasting coating and the PbO$_2$ layer is removed from the surface. Moreover, PbSO$_4$ may be formed, leading to partial blockage of the active centers of the surface.

Some microscopic images (Figure 5) seem to give further support to the instability hypotheses.

(A)   (B)   (C)
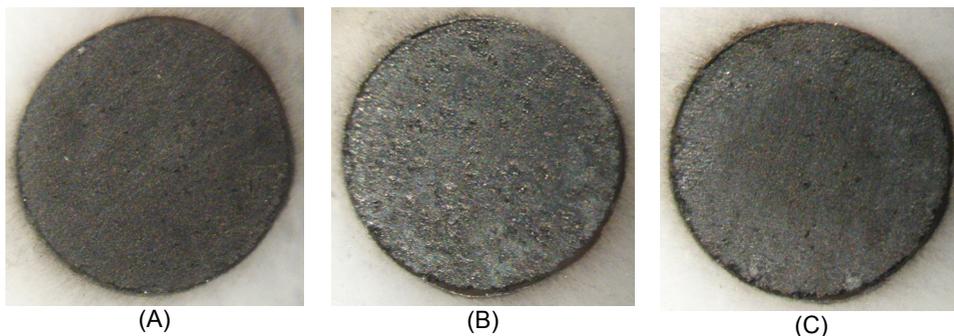
Figure 5. Microscopic images of SG/Pb II: the unmodified SG surface (A), after depositing a *approx.* 2 µm PbO$_2$ layer on the surface (B) and after the completion of the measurements in the 0.2 M vanadium in 2 M H$_2$SO$_4$ solution (C).

It appears that, after the completion of the set of measurements, either the graphite surface of the SG/Pb II is visible again or some different deposits were formed on top of the PbO_2 layer (Figure 5.C).

In light of this, it is probable that the thinner PbO_2 coating of SG/Pb I had been quickly removed during the 10 cycles in the $V^{IV} - V^V$ solution completed prior to measurements and the activation of the graphite surface was almost achieved. This explains the quite similar results to those obtained on non coated SG electrodes.

CONCLUSIONS

The spectral graphite is a promising electrode material, in terms of achieving high currents in VRFB in a simple way. Just like with felts, its active surface is higher than the geometrical one, owing to its porosity. Indeed, an effective surface 4 times higher than the geometrical one was found in our studies. Since reproducible behaviour could be obtained and with relatively little pretreatment, further efforts to study the properties of SG electrodes seem justified. Moreover, better mechanical properties may be envisioned, but studies of stability in time and further optimization of the activation procedure are required.

The attempts to modify the SG surface by electrodeposition of PbO_2 did not result in any improvement of the current. However, the PbO_2 layer was deposited on a surface that did not receive specific pretreatment and, under the circumstances, proved unstable. More efforts should be made in the direction of pretreatment of the surface prior to PbO_2 coating.

For the tested electrodes, large separations of anodic and cathodic peak potentials were observed, ranging between 118 and 567 mV for SG, 188 and 567 mV for SG/Pb, or 868 and 1015 mV for Pt, proving the irreversibility of the V^V to V^{IV} redox couple on all materials.

EXPERIMENTAL SECTION

The reagents used (solid $C_2H_2O_4$, $Pb(NO_3)_2$, NaF and 98 % H_2SO_4 and 0.1 M HNO_3 solutions) were all of analytical purity, and used as received (Merck, Aldrich).

A 0.2 M solution of VO_2^+ was prepared by dissolving the appropriate amount of V_2O_5, under constant stirring and heating, in a 2 M H_2SO_4 aqueous solution. A solution of 0.2 M VO^{2+} was prepared in a similar manner, with the difference that a stoichiometric amount of oxalic acid was added, to

achieve the reduction of V^V to V^{IV}. Equal volumes of the two solutions were mixed to obtain the final 0.1 M VO_2^+ and 0.1 M VO^{2+} in 2 M H_2SO_4 solution, which was employed in the experiments.

The electrochemical measurements were performed using a computer-controlled multipotentiostat, model DXC 238, (Datronix Computers, Romania). The application used for experiment control and data acquisition has been developed in our laboratory using the LabView 8.5 (National Instruments, USA) software. The stored data have been further processed using the Origin8 software (OriginLab, USA).

A three-electrode electrochemical glass cell (50 mL) was used for the cyclic voltammetry measurements. The working electrodes (WE) were made from spectral graphite (Ringsdorff-Werke GmbH, Germany) rods ($\varnothing$ = 3 mm, L = 25 mm) fixed in a Teflon holder, specially designed to allow for easy replacement of the electrode before each experiment. The surface of the each new graphite WE was first polished on a 1200 grit abrasive paper and abundantly washed with distilled water. The platinum disc electrode ($\varnothing$ = 2 mm) was also mirror polished with alumina paste (0.5 µm).

Spectral graphite rod ($\varnothing$ = 3 mm, L = 80 mm) was used as counterelectrode (CE), while an Ag/AgCl/KCl$_{sat}$ system was used as the reference electrode (RE) (E_{RE}=0.197 V $vs.$ ENH).

The PbO_2 coatings were obtained by galvanostatic electro-deposition, from an aqueous solution containing 0.23 M $Pb(NO_3)_2$, 0.03 M HNO_3 and 0.03 M NaF [15]. The cell used consisted of the electrode to be coated, a graphite plate with a high surface (6 cm^2) as CE and the Ag/AgCl/KCl$_{sat}$ system as RE, all dipped in the $Pb(NO_3)_2$ solution. Besides the polishing and washing, the electrode surface was dried under argon current prior to the PbO_2 electrodeposition.

Before each measurement at a new scan rate, the solution was stirred for 10 seconds (with a magnetic stirrer), in order to ensure the removal from the surface of the WE of any oxygen bubbles or redox products formed during previous scans.

REFERENCES

1. R. Schweiss, *Journal of Power Sources*, **2015**, *278,* 308.
2. B.S. Lee, D.E. Gushee, *Chemical Engineering Progress,* **2008**, *104,* S29.
3. C. Yao, H. Zhang, T. Liu, X.F. Li, Z.H. Liu, *Journal of Power Sources*, **2012**, *218*, 455.
4. M.S. Whittingham, *MRS Bulletin*, **2008**, *33*, 411.

5. A. Parasuramana, T.M. Lima, C. Menictasc, M. Skyllas-Kazacos, *Electrochimica Acta*, **2013**, *101*, 27.
6. M.H. Chakrabarti, N.P. Brandon, S.A. Hajimolana, F. Tariq, V. Yufit, M.A. Hashim, M.A. Hussain, C.T.J. Low, P.V. Aravind, *Journal of Power Sources*, **2014**, *253*, 150.
7. H. Kaneko, K. Nozaki, Y. Wada, T. Aoki, A. Negishi, M. Kamimoto, *Electrochimica Acta*, **1991**, *36*, 1191.
8. M. Rychcik, M. Skyllas-Kazacos, *Journal of Power Sources*, **1987**, *19*, 45.
9. H. Liu, Q. Xu, C. Yan, Y. Qiao, *Electrochimica Acta*, **2011**, *56*, 8783.
10. G. Wang, J. Chen, X. Wang, J. Tian, H. Kang, X. Zhu, Y. Zhang, X. Liu, R. Wang, *Journal of Energy Chemistry*, **2014**, *23*, 73.
11. W. Zhang, J. Xi, Z. Li, H. Zhou, L. Liu, Z. Wu, X. Qiu, *Electrochimica Acta*, **2013**, *89*, 429.
12. K.J. Kim, M.S. Park, J.H. Kim, U. Hwang, N.J. Lee, G. Jeong, Y.J. Kim, *Chemical Communications*, **2012**, *48*, 5455.
13. B. Sun, M. Skyllas-Kazakos, *Electrochimica Acta*, **1991**, *36*, 513.
14. W.H. Wang, X.D. Wang, *Electrochimica Acta*, **2007**, *52*, 6755.
15. X. Wu, H. Xu, L. Lu, H. Zhao, J. Fu, Y. Shen, P. Xu, Y. Dong, *Journal of Power Sources*, **2014**, *250*, 274.
16. A.J. Bard, L.M. Faulkner (Eds.), "Electrochemical Methods and Applications", Second Ed., Wiley, New York, **2001**, chapter 6, p 236.
17. C. Ding, H. Zhang, X. Li, T. Liu, F. Xing, *Journal of Physical Chemistry Letters*, **2013**, *4*, 1281.

*Dedicated to prof. dr. I. C. Popescu
on the occasion of his 70th anniversary*

DISSOLUTION OF BASE METALS FROM WPCBs USING Na$_2$S$_2$O$_8$ SOLUTION

SZABOLCS FOGARASI[a], FLORICA IMRE-LUCACI[b], PETRU ILEA[a], PAUL-ȘERBAN AGACHI[a], ÁRPÁD IMRE-LUCACI[a]**

ABSTRACT. The present work aimed to evaluate the performances of Cu, Zn and Ni dissolution from Waste printed circuit boards (WPCBs) obtained from mobile phones (MP) using different solid:liquid ratios (SLR) and oxidant concentration (C_{ox}). It was found that the increase of C_{ox} at constant SLR increases more the performances of Zn and Ni dissolution than it does for Cu. In contrast, the increase of SLR from 1:5 to 1:15 at constant C_{ox} diminished the dissolution efficiency of Ni by 79 %, of Zn with 55 % and in the case Cu by 22 %. The experimental results revealed that the most favorable conditions for the dissolution of Zn, Ni and Cu are provided at the SLR of 1:5 and 0.42 M Na$_2$S$_2$O$_8$.

Keywords: base metals, persulfate, WPCBs, leaching, solid:liquid ratio

INTRODUCTION

The current industrialization processes and continuous technological innovations led to accelerated and frequent replacement of electric and electronic equipments (EEE), especially computers and MP, leading to more rapid accumulation of waste electrical and electronic equipments (WEEE). Worldwide annual amount of WEEE is about 20-30 million tons and it is estimated that between 2010 and 2020 it will grow of 2 to 4 times. The EU produces around 8 million tons of WEEE every year, with an annual growth of 3-5 % [1]. Given that today MPs have become the most ubiquitous electronic

[a] *"Babeş-Bolyai" University, Faculty of Chemistry and Chemical Engineering, 11 Arany Janos Street, Cluj-Napoca, 400028, Romania*
[b] *"Babeş-Bolyai" University, Interdisciplinary Research Institute on Bio-Nano-Sciences, 42 Treboniu Laurian Street, Cluj-Napoca, 400271, Romania*
* *Corresponding author: aimre@chem.ubbcluj.ro*

product, they contribute significantly to the increased quantities of WEEE. In 2013, the number of MP subscriptions was approximately equal with the world population [2]. It is estimated that 100 million MP and 17 million computers are discarded annually considering that the lifespan of MP is 1-2 years and of computer 2-5 years [3, 4]. Since MP and computers include in their structure printed circuit boards the annual accumulation of WPCB reaches 1.5-2 million tons, which represents 3 % of the total WEEE [5, 6]. Most studies show that WPCBs include several major categories of materials: ferrous, non-ferrous metals, ceramics and plastics [7, 8]. Among them, in terms of quantity, with highest percentage is Cu, 17-40 %, and by value Au and Ag. Therefore, the recovery of metals from WPCBs found in MP is an ongoing concern as it contributes to the reduction of the negative impact on the environment and to the conservation of the natural metal resources [9, 10]. In the recent decades several research studies have been conducted for the development of processes able to recovery metals from MPs WPCB [5]. Thus, it have been used various procedures as: mechanical [11-13]; pyrometallurgical [14-16]; bio-leaching [17-19]; by using supercritical fluids [20, 21] and hydrometallurgical ones [1, 5, 22, 23]. Compared with the pyrometallurgical processes, the hydrometallurgical processes make possible the use of renewable leaching medium that can be reused in the process thereby reducing the amount of solution used and consequently the production costs [3].

On this basis, the current study focused on the dissolution of base metals from WPCBs removed from MP by using $Na_2S_2O_8$ which is an efficient and selective leaching agent. In this way, it was achieved the separation of base metals which are concentrated in the leaching solution from the precious metals (Au, Ag) that remain in the residue. For this purpose, the influence of C_{ox} and of the SLR on the performance of the leaching process of base metals from MPs' WPCBs was studied.

RESULTS AND DISCUSSION

The influence of SLR and $Na_2S_2O_8$ concentration on the dissolution degree of Cu, Zn and Ni

Preliminary tests showed that $Na_2S_2O_8$ is a strong oxidizing agent capable to selectively dissolve only Cu, Zn and Ni from WPBCs involving the following main chemical reactions:

$$Cu + Na_2S_2O_8 \rightarrow CuSO_4 + Na_2SO_4 \qquad (1)$$

$$Zn + Na_2S_2O_8 \rightarrow ZnSO_4 + Na_2SO_4 \qquad (2)$$

$$Ni + Na_2S_2O_8 \rightarrow NiSO_4 + Na_2SO_4 \qquad (3)$$
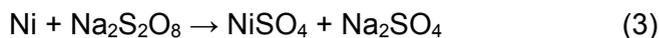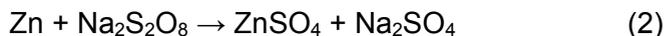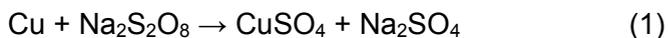
In order to determine the optimal conditions required to achieve advanced metal solubilization the dissolution degree of Cu, Zn and Ni was

evaluated at various C$_{ox}$ and SLR. Fig. 1 presents the results obtained for the dissolution of Cu at the SLR of 1:5, which reveals that the dissolution degree of Cu increases at constant value of SLR with the increase of C$_{ox}$. However, it seems like the dissolution rate reaches a maximum at 0.84 M Na$_2$S$_2$O$_8$ considering that is no significant differences between the performances obtained at 0.84 M and 1.26 M Na$_2$S$_2$O$_8$. This can be explained considering the fact that the dissolution process is controlled by diffusion. Thus, the accumulation of the reaction products will lead to the decrease of their diffusion from the reaction surface to the solution volume, significantly reducing the global rate of the process.
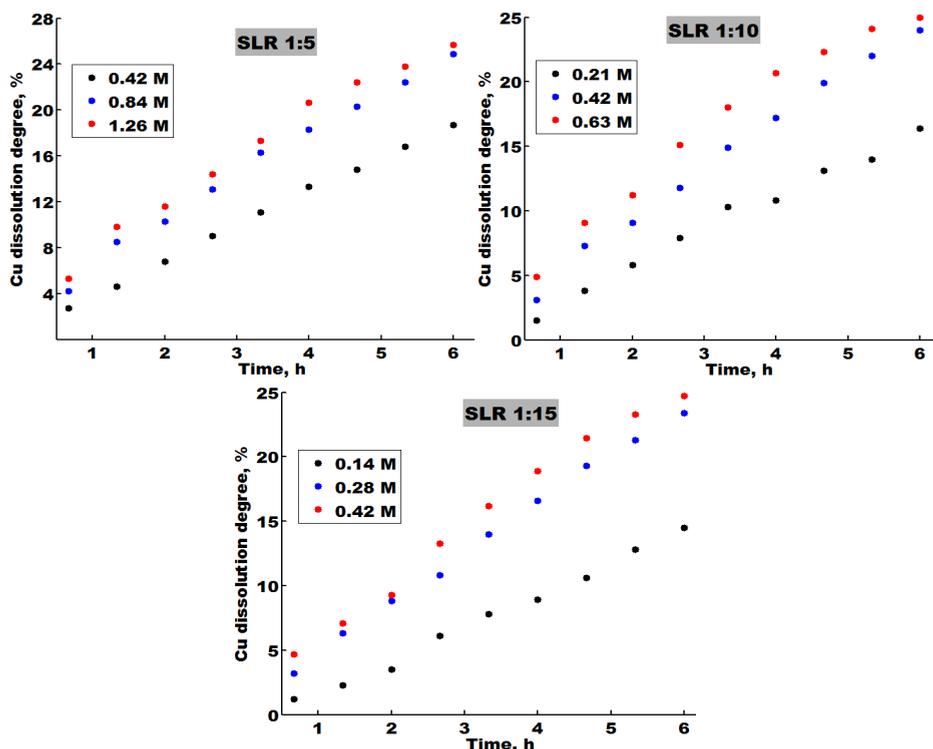
Figure 1. Cu dissolution degree vs. time at different Na$_2$S$_2$O$_8$ concentrations and SLR

Similar tendency can be observed from the results obtained for Cu at the SLR of 1:10. According to the data shown in Fig.1, the Cu dissolution degree values increased by 53 % between 0.63 M and 0.21 M Na$_2$S$_2$O$_8$, while between 0.63 M and 0.42 M Na$_2$S$_2$O$_8$ it was modified only with 4 %. In contrast, at the SLR of 1:5 the Cu dissolution degree values differed only by 36 % between the highest and lowest C$_{ox}$, which can be accounted to the lower volume of the leaching solution at SLR 1:5 than at SLR 1:10. As a result,

the accumulation of reaction products in the solution reduced the reaction rate more at SLR 1:5 than at SLR 1:10 even if the C_{ox} were higher at SLR 1:5.

The increase of the SLR to 1:15 increased even more the difference between the performances obtained at the lowest and highest C_{ox}. Fig. 1 shows that the Cu dissolution degree at 0.42 M $Na_2S_2O_8$ is almost twice compared to the one obtained at 0.14 M $Na_2S_2O_8$. It is important to note that the Cu dissolution degree dropped only with 4 % for the highest $Na_2S_2O_8$ concentrations with the increase of the SLR from 1:5 to 1:15 while for the lowest C_{ox} it changed with 29 %. Considering that the concentrations are decreasing with the increase of the SLR, it is evident that the diffusion rate of the oxidant from the bulk of the solution to the reaction surface will decrease as well. Moreover, since the duration of the experiments was the same, the increase of the SLR (volume) reduced significantly the amount of oxidant which could reach the reaction surface in time. This is the reason why significant difference were accoutered only at the lowest C_{ox} regardless the SLR.

In comparison to Cu, the dissolution of Zn is more strongly affected by SLR and C_{ox} variations considering the significant difference between the reactivity of the two metals. The dissolution of Zn (Table 1) occurs the most rapidly at the lowest SLR (1:5) reaching the highest dissolution degree of 94 % at 1.26 M $Na_2S_2O_8$. It is also obvious that regardless the SLR the dissolution degree of Zn differs more between the lowest and middle C_{ox} than between the middle and the highest C_{ox}. For instance, the dissolution degree of Zn increased with 106 % between 0.42 and 0.84 M $Na_2S_2O_8$ while between 0.84 and 1.26 M $Na_2S_2O_8$ with only 20 %. As a result, the dissolution degree of 38 % obtained in 6 h at 0.42 M $Na_2S_2O_8$ can be achieved in 100 min at 0.84 M $Na_2S_2O_8$ and in less than 1 h at 1.26 M $Na_2S_2O_8$. It can be noticed that (Table 1) the performances of the dissolution process of Zn were reduced significantly by the increase of SLR. Nevertheless, similarly to the dissolution of Cu, the dissolution degree values of Zn were diminished more at the lowest C_{ox} than at the highest. Therefore, the increase of the SLR from 1:5 to 1:15 lowered dissolution degree with 55 % for the lowest C_{ox} and with 26 % for the highest.

Table 1. Zn dissolution degree (%) vs. C_{ox} and SLR

SLR	Conc.	Time, min								
g:mL	M	40	80	120	160	200	240	280	320	360
	0.42	4.2	8.3	14	20	24	28	31	33	38
1:5	0.84	9.6	27.5	46	54	63	68	71	74	79
	1.26	14.1	45.6	67	79	84	88	91	93	94
	0.21	3.5	6.4	9	12	15	19	22	26	30
1:10	0.42	9.0	19.0	31	37	45	50	58	64	66
	0.63	8.2	19.3	33	48	63	71	78	81	84
	0.14	1.6	4.6	6	8	10	11	14	15	17
1:15	0.28	8.9	14.0	18	21	26	30	35	40	47
	0.42	9.0	16.8	27	33	45	54	59	65	69

The influence of SLR and Na$_2$S$_2$O$_8$ concentration on the dissolution process of Ni was also evaluated. It was found that Ni has higher dissolution rate at the SLR of 1:5 and 1.26 M Na$_2$S$_2$O$_8$ than Cu, achieving a dissolution degree of 44 % (Fig. 2). The results also revealed that the influence of the studied experimental conditions on the performances of Ni dissolution were more similar in their tendency with the ones obtained for Zn than the ones for Cu. However, at the SLR of 1:5 and 1:10 (Fig. 2) the dissolution degrees of Ni for the middle concentrations were closer to the ones obtained at the lowest concentrations. This means that Ni dissolution is more strongly affected by C_{ox} increase at the above mentioned SLRs than in the case of Zn, especially after 120 min of processing.
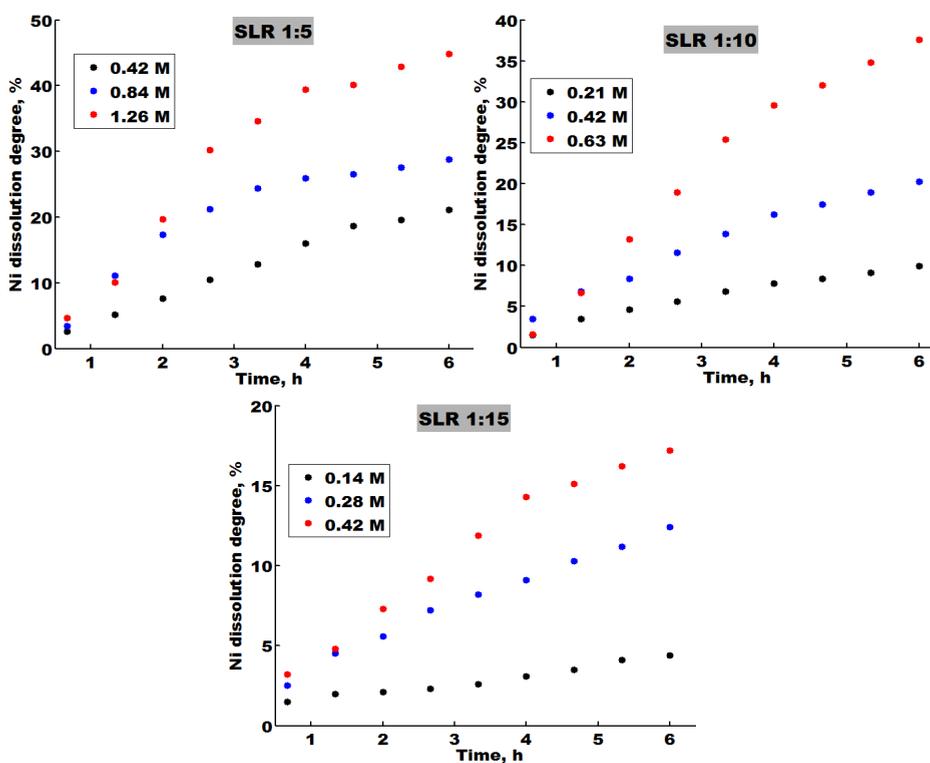
Figure 2. Ni dissolution degree vs. time at different Na$_2$S$_2$O$_8$ concentrations and SLR

On the other hand, at the SLR of 1:15 the dissolution degrees of Ni (Fig. 2) and Zn (Table 1) have similar tendency with the increase of C_{ox}. Still, it is remarkable that the dissolution rate of Ni drops more at the lowest concentration with the increase of SLR than for the other two metals. Hence, the increase of the SLR from 1:5 to 1:15 reduced the dissolution

degree with more than 80 % for the lowest C_{ox} and with 56 % for the highest one. It is also worth noting that among the metals, Ni has the lowest dissolution degrees at 0.14 M and 0.21 M $Na_2S_2O_8$ concentrations. For example at 0.14 M $Na_2S_2O_8$ the dissolution degrees of Cu and Zn are comparable while for Ni are 4 times smaller than for the other two metals, which means that it could be separated from Cu and Zn by selective leaching.

The influence of SLR and $Na_2S_2O_8$ concentration on the dissolution efficiency of Cu, Zn and Ni

The impact of secondary reactions Eq. (4) on the leaching of metals can be quantified by the dissolution efficiency (%/g) defined as the ratio between the dissolution degree of the metal (%) and the amount of $Na_2S_2O_8$ (g) used in the experiment.

$$2H_2O + 2Na_2S_2O_8 \rightarrow 2H_2SO_4 + 2Na_2SO_4 + O_2 \qquad (4)$$

Fig. 3 shows that for constant SLR the dissolution efficiency of Cu decreases with the increase of C_{ox} which means that the increase of the amount of oxidant in the same volume of leaching solution favors more the secondary reactions than the dissolution of Cu. In contrast, the increase of SLR at constant amount of $Na_2S_2O_8$ affects the same way the primary and secondary reactions since it gives the same performances for the middle and highest concentrations. Only at the lowest oxidant concentrations has the increase of SLR different impact on the dissolution of Cu and oxidant degradation.
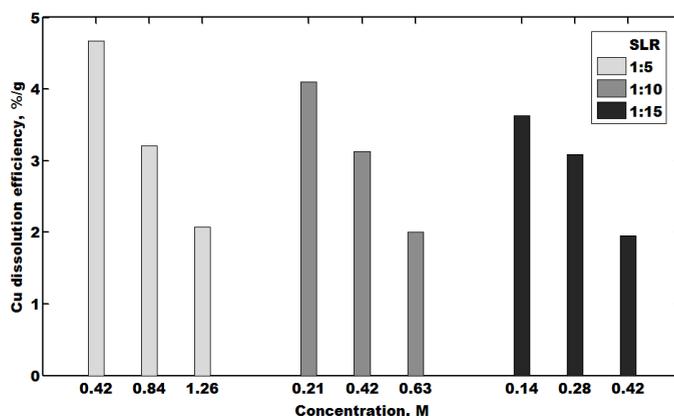
Figure 3. Cu dissolution efficiency vs. C_{ox} and SLRs after 6 h of leaching

Regardless the C_{ox}, the negative influence of SLR increase can be noticed in the case of Zn dissolution as well, (Fig. 4). It can be observed

that the middle concentration gives the best performance at each SLR, reaching the highest value of 9.82 %/g at 0.42 M $Na_2S_2O_8$ and SLR 1:5. This tendency can be explained considering that Zn can be dissolved by H_2SO_4 and $Na_2S_2O_8$ as well. As a result, the increase of the amount of oxidant will increase the dissolution rate of Zn, but at the highest concentrations (12 g $Na_2S_2O_8$) it will favor more the secondary reactions.
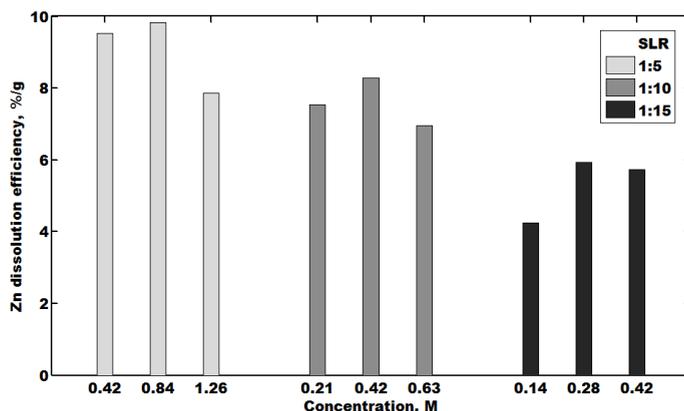
Figure 4. Zn dissolution efficiency vs. C_{ox} and SLRs after 6 h of leaching

Differently from Cu and Zn, in the case of Ni the dissolution efficiency is more strongly affected by the increase of SLR, dropping sharply between the SLRs of 1:5 and 1:15 by 4 times. Therefore, the highest value for the Ni dissolution efficiency (5.27 %/g) is obtained at the SLRs of 1:5 and 0.42 M $Na_2S_2O_8$ (Fig. 5).
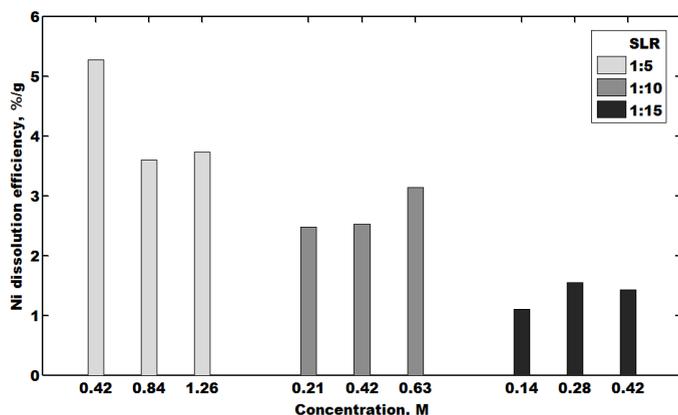
Figure 5. Ni dissolution efficiency vs. C_{ox} and SLRs after 6 h of leaching

On the other hand, the influence of C_{ox} depends on the value of the SLR probably due to the fact that Ni is more noble metal than Zn; being more hardly dissolved by H_2SO_4 resulted from the degradation of the oxidant.

CONCLUSIONS

The current paper proved that the dissolution of Cu, Zn and Ni from WPCBs obtained from MP can be performed with high efficiency and selectivity by using $Na_2S_2O_8$ solutions. The dissolution degree values obtained for various experimental conditions showed that Zn has the highest dissolution degree (max. 94.3 %) followed by Ni (max. 44.8 %) and Cu (max. 25.7 %), regardless the SLR or C_{ox}. It was also found that the dissolution rate of Zn and Ni are more strongly affected by the increase of SLR and concentration than Cu due to their higher reactivity. The results revealed that the increase of the SLR favors more the secondary reaction than the dissolution of metals. Moreover, there are significant differences between the performances obtained for Ni, Cu and Zn considering that the increase of SLR from 1:5 to 1:15 lowered the dissolution efficiency of Ni by 79 % while in the case of Zn 55 % and for Cu only 22 %. Based on the dissolution degree and dissolution efficiency values, the overall conclusion is that the most favorable conditions for the dissolution of Zn, Ni and Cu are provided at the SLR of 1:5 and 0.42 M $Na_2S_2O_8$.

EXPERIMENTAL SECTION

The leaching tests were carried out using 8 g of WPCB samples resulted from the mechanical processing of waste MP. Each WPCB was cut into about 18 pieces with an area of approx. 1 cm² and then mixed to obtain a relatively homogeneous material. The samples were subject to leaching tests (Table 2) with duration of 6 hours at room temperature using $Na_2S_2O_8$ solutions of different concentrations (0.14-1.26 M) and SLRs (1:5-1:15).

Table 2. Experimental conditions for the leaching tests

Mass of WPBC	Mass of $Na_2S_2O_8$	Solution volume	$Na_2S_2O_8$ conc.	S:L ratio
g		mL	M	g:mL
8	4	40	0.42	1:5
		80	0.21	1:10
		120	0.14	1:15
	8	40	0.84	1:5
		80	0.42	1:10
		120	0.28	1:15
	12	40	1.26	1:5
		80	0.63	1:10
		120	0.42	1:15

To determine the metal content a first dissolution was performed using aqua regia with duration of 24 hours. The undissolved material from the structure of WPCB was separated by filtration. The composition of the WPCB sample is shows in Table 3.

Table 3. Composition of the WPCB sample and of the metallic part

Material	Cu	Au	Ag	Zn	Ni	Pb	Sn	Fe	Non metals	Total
	wt.%									
WPCB sample	18.3	0.03	0.12	1.5	1.7	0.6	2.26	0.4	75.09	100

The solutions were sampled during the leaching test in order to determine the concentration of dissolved metals at different moments. The solid residue separated by leaching tests was further treated for 24 hours with aqua regia for complete dissolution of metals in order to determine the dissolution degree of each metal. The samples collected at different leaching stages and mineralized with aqua regia were analyzed for metal content with an atomic absorption spectrometer (AVANTA PM, GBC - Australia).

ACKNOWLEDGMENTS

REFERENCES

1. A. Tuncuk, V. Stazi, A. Akcil, E.Y. Yazici, H. Deveci, *Minerals Engineering*, **2012**, *25*, 28.
2. A.C. Kasper, G.B. Berselli, B.D. Freitas, J.A. Tenorio, A.M. Bernardes, H.M. Veit, *Waste Management*, **2011**, *31*, 2536.
3. L.H. Yamane, V.T. de Moraes, D.C. Espinosa, J.A. Tenorio, *Waste Management*, **2011**, *31*, 2553.
4. J. Cui, L. Zhang, *Journal of Hazardous Materials*, **2008**, *158*, 228.
5. S. Fogarasi, F. Imre-Lucaci, P. Ilea, Á. Imre-Lucaci, *Journal of Cleaner Production*, **2013**, *54*, 264.
6. Y. Zhong, D. Li, Z. Mao, W. Huang, P.A. Peng, P. Chen, J. Mei, *Journal of Hazardous Materials*, **2014**, *270*, 196.

7. F.O. Ongondo, I.D. Williams, T.J. Cherrett, *Waste Management*, **2011**, *31*, 714.
8. P. Kiddee, R. Naidu, M.H. Wong, *Waste Management*, **2013**, *33*, 1237.
9. M. Schluep, C. Hagelueken, R. Kuehr, F. Magalini, C. Maurer, C. Meskers, E. Mueller, F. Wang, "Recycling - from e-waste to resources", UNEP, **2009**.
10. R.S. Rubin, M.A.S.D. Castro, D. Brandão, V. Schalch, A.R. Ometto, *Journal of Cleaner Production*, **2014**, *64*, 297.
11. A. Das, A. Vidyadhar, S.P. Mehrotra, *Conservation and Recycling*, **2009**, *53*, 464.
12. J. Li, Z. Xu, Y. Zhou, *Journal of Electrostatics*, **2007**, *65*, 233.
13. J. Li, H. Lu, Z. Xu, Y. Zhou, *Journal of Hazardous Materials*, **2008**, *151*, 52.
14. G. Grause, M. Furusawa, A. Okuwaki, T. Yoshioka, *Chemosphere*, **2008**, *71*, 872.
15. H.-L. Chiang, K.-H. Lin, M.-H. Lai, T.-C. Chen, S.-Y. Ma, *Journal of Hazardous Materials*, **2007**, *149*, 151.
16. I. de Marco, B.M. Caballero, M.J. Chomón, M.F. Laresgoiti, A. Torres, G. Fernández, S. Arnaiz, *Journal of Analytical and Applied Pyrolysis*, **2008**, *82*, 179.
17. C. Guo, H. Wang, W. Liang, J. Fu, X. Yi, *Waste Management*, **2011**, *31*, 2161.
18. T.D. Chi, J.-C. Lee, B.D. Pandey, K. Yoo, J. Jeong, *Minerals Engineering*, **2011**, *24*, 1219.
19. N. Zhu, Y. Xiang, T. Zhang, P. Wu, Z. Dang, P. Li, J. Wu, *Journal of Hazardous Materials*, **2011**, *192*, 614.
20. F.R. Xiu, F.S. Zhang, *Journal of hazardous materials*, **2010**, *178*, 628.
21. J. Huang, M. Chen, H. Chen, S. Chen, Q. Sun, *Waste Management*, **2014**, *34*, 483.
22. E.Y. Kim, M.S. Kim, J.C. Lee, B.D. Pandey, *Journal of Hazardous Materials*, **2011**, *198*, 206.
23. I. Birloaga, I. de Michelis, F. Ferella, M. Buzatu, F. Veglio, *Waste Management*, **2013**, *33*, 935.

Dedicated to prof. dr. I. C. Popescu
on the occasion of his 70th anniversary

MELDOLA BLUE IMMOBILISED ON MESOPOROUS CARBON AEROGEL - NEW ELECTRODE MATERIAL FOR NADH ELECTROCATALYTIC OXIDATION

CARMEN IOANA FORŢ[a*], LIVIU COSMIN COTEŢ, GRAZIELLA LIANA TURDEAN, VIRGINIA DANCIU

ABSTRACT. The new modified electrodebased on Meldola Blue (MB) adsorbed onto carbon aerogel (CA) incorporated into chitosan matrix and deposited onto glassy carbon (GC) disc were used for NADH electrocatalytic oxidation. MB was immobilized by simple adsorption on mesoporous CA (MB-CA) and was immobilized on a GC disc using chitosan matrix. The morphological and structural characteristics of the new electrode material such as specific surface area, pore size distribution, pore volume, were obtained from N_2 adsorption - desorption isotherms and TEM measurements. The basic electrochemistry of adsorbed MB onto CA and its ability to catalyze NADH electrooxidation have been investigated by cyclic voltammetry and rotating disc electrode performed in different experimental conditions (potential scan rate, rotation speed, applied potential, NADH concentration, MB coverage). The electrocatalytic parameters of the investigated MB-CA/GC modified electrodes were estimated.

***Keywords**: electrocatalysis, NADH electrooxidation, carbon aerogel, mesoporous materials, redox dyes*

INTRODUCTION

The dehydrogenase subgroup, the majority of redox enzymes, required for operation the presence of $NAD(P)^+/NAD(P)H$ coenzyme. The key problem to solve for electrochemical applications (biosensors, biofuel cells, bioorganic synthesis) is the electrochemical regeneration of the soluble

[a] *"Babes-Bolyai" University, Faculty of Chemistry and Chemical Engineering, Department of Chemical Engineering, 11, Arany Janos St., 400028 Cluj-Napoca, Romania.*
[*] *Corresponding author: iladiu@chem.ubbcluj.ro*

redox cofactor. Many studies for cofactor electrochemical regeneration were focused on the NADH electrooxidation and it was concluded that in order to run this process on different conventional electrode materials relatively high overpotentials are required [1] or the presence of a suitable redox mediator is necessary [2].

Meldola Blue (MB), a phenoxazine compound involving two electrons/two protons in the redox process [3], is one of the best mediators for NADH catalytic oxidation for its high reaction rate [3]. Many electronically conducting materials (such as graphite [3], amorphous homemade zirconium phosphate (ZP) [2, 4] crystalline zirconium phosphate (α-ZP) [4 - 7] or crystalline titanium phosphate (α-TP) [5,6,8] were used in order to shift formal standard potential of MB (E°') towards more positive potentials, at a value allowing the operation of the modified electrode within the potential window essentially free of interfering reactions [9]. Also, an increase of this E°' value will indirectly induce an increase of the rate constant for NADH electrocatalytic oxidation [10].

Moreover, great efforts have been made to find materials onto or into which the mediators can be strongly bound to avoid their leaching under experimental conditions [2, 4-8], and in order to improve the sensors characteristics (*i.e.* stability, sensitivity and reproducibility).

Recently, porous carbon materials (aerogels and xerogels) were used as support material for the immobilization of different chemical species with catalytic properties [11, 12]. Carbon aerogels (CAs) have interesting properties, such as high specific surface area, porosity, and electrical conductivity, associated with a good chemical stability. Therefore, CAs are attractive materials for different applications such as electrode materials in supercapacitors and rechargeable batteries, catalyst supports, adsorbent materials and thermal insulators [11].

Thanks to its properties, which include excellent membrane-forming ability, high permeability toward water, good adhesion, biocompatibility, nontoxicity, and high mechanical strength, chitosan (Chi), is one of the most preferred materials used for immobilization of the active electrode materials [13].

In the present work, carbon aerogel (CA), a high mesoporous material, was used as support material for MB immobilization. The morphological and structural characteristics of the new electrode material such as specific surface area, pore size distribution, pore volume, were obtained from N_2 adsorption - desorption isotherms and TEM measurements. The resulted modified material MB-CA was deposited on the glassy carbon electrode (GCE) surface using chitosan matrix, and MB-CA/GCE was obtained. Aiming to evaluate the electrochemical behavior of the obtained modified electrodes, MB-CA/GCE, and their ability to catalyze the electrooxidation of

NADH cyclic voltammetry (CV) and rotating disc electrode (RDE) techniques were performed in different experimental conditions (potential scan rate, rotation speed, applied potential, NADH concentration, MB coverage). The obtained results (electrochemical and electrocatalytic parameters) allowed the estimation of the kinetic parameters of the new modified electrodes.

RESULTS AND DISCUSSIONS

Morphological and structural characterization of mesoporous CA

According to the IUPAC classification, the shape of the adsorption - desorption isotherm recorded for the mesoporous CA (Figure 1) corresponds to the type IV isotherm, which is typically associated with the "ink bottle" mesopores. Ordered mesoporous CA (median pore radius 5.15 nm) with high specific surface area (881 m^2g^{-1}) and high pore volume (1.518 cm^3g^{-1}) were obtained.
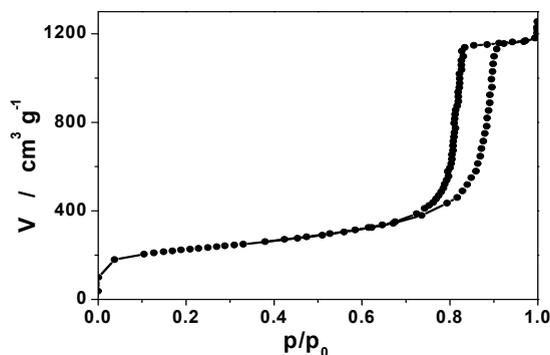
Figure 1. Adsorption-desorption isotherm for mesoporous CA
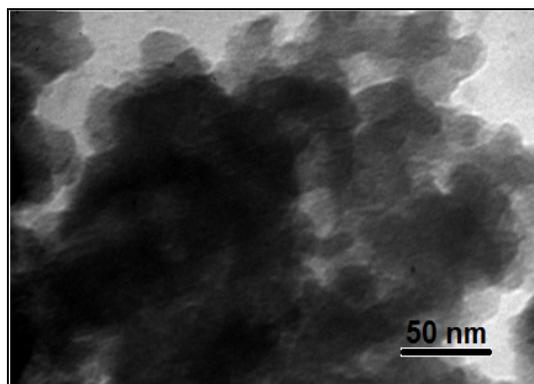
Figure 2. TEM image of mesoporous CA.

These properties cause special characteristics of carbon aerogel material, concerning both, the dispersion of the mediator on the carbon material surface (CA) and the easy access of the substrate to the mediator.

TEM image (Figure 2) confirms the porous three-dimensional structure of CA framework, build from interconnected nanoparticles, with an average diameter of about tens nm. The nanoparticles delimit mesopores with an average diameter of about few nm. The obtained results are in a good correlation with those obtained from BET analysis.

Electrochemical behavior of the MB-CA modified GC electrodes

A comparison between the cyclic voltammograms (CVs) recorded at MB-CA modified electrodes with similar measurements performed at bare GCE, show that MB-CA/GCE present one voltammetric peak pair, which is due to the oxido-reduction process involving the mediator redox couple (inset Figure 3).

The background current observed on the recorded CVs was higher for MB-CA modified electrode than that evidenced for the corresponding unmodified electrodes (GCE) (inset Figure 3). A plausible explanation of this fact should take into consideration that CA has high specific surface area, conferring a high electrochemical active surface to the modified electrodes [2].
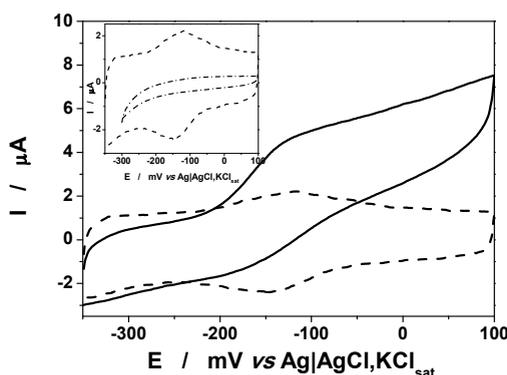
Figure 3. Electrocatalytic oxidation of NADH at MB-CA/GCE in the presence of 5 mM NADHand in its absence. Inset: Cyclic voltammogram recorded at MB-CA/GCE (---) and GCE (-·-··-). Experimental conditions: scan rate, 20 mV/s; supporting electrolyte, 0.1 M Tris buffer (pH 7); starting potential, -350 mV vs. Ag|AgCl,KCl$_{sat}$.

By continuous voltammetric cycling, within the potential window of practical interest, revealed that the peak current and the peak potential corresponding to the MB-CA redox wave are independent of the time evolution, proving a good short-term stability of MB-CA/GCE modified electrode. Thus, by using the relation: $((I_{pa})_{100th\ cycles}/(I_{pa})_{1st\ cycle}) *100\%$, it was found a current increase up to ~105 %(results not shown). These results

show an increase of the electrode activity due to its activation induced by the continuous potential cycling.

The peak separation value, ΔE_p = 40 mV ($\Delta E_p = E_{pa} - E_{pc}$, where E_{pa} and E_{pc} are the cathodic and anodic peak potentials), the width at half maximum current intensity ($W_{1/2\ anodic}$ = 110 mV and $W_{1/2catodic}$ = 100 mV), and the ratio between the intensity of the cathodic and anodic peaks (I_{pa}/I_{pc} = 1.1) point out a quasi-reversible redox process [2, 6, 7].

The values of the formal standard potential ($E^{\circ'}$) for MB-CA modified GCEs (evaluated as the average of the potentials for the oxidation and the reduction peaks) are in the optimal potential range for electroanalytical applications, and ensure an efficient production of enzyme active NAD^+ [9]. The value of $E^{\circ'}$ obtained for MB adsorbed onto CA presents a positive potential shift (-140 mV *vs*. Ag|AgCl,KCl$_{sat}$), compared to the $E^{\circ'}$ value observed for MB adsorbed directly onto graphite (–175 mV *vs*. SCE) [3].

Compared with the literature value of $E^{\circ'}$ obtained for MB adsorbed onto *α*-ZP [6, 7], and onto *α*-TP [6, 8] (-100 mV *vs*. Ag|AgCl,NaCl$_{3M}$, Tris buffer, pH 7), the $E^{\circ'}$ for MB-CA redox couple, presents a negative potential shift, which increases in comparison with the $E^{\circ'}$ for MB adsorbed onto amorphous ZP [2, 6] (+ 40 mV *vs*. Ag|AgCl,NaCl$_{3M}$, Tris buffer, pH 7). This behaviour can be assigned to the negative charge density of the compared support materials, moreover, the increase of negative charge density corresponds to the increase of $E^{\circ'}$ values [7].

$E^{\circ'}$ value, for MB-CA/GC electrodes, depends on the pH of the surrounding electrolyte, in the same manner as that reported for MB dissolved in aqueous solution [12], MB adsorbed on spectrographic graphite [3], on *α*-ZP [6,7] or on *α*-TP [6, 8]. In good agreement with previously published results [3], the $E^{\circ'}$ *vs.* pH dependence shows two linear regions: one with the slope of ~60 mV/pH (equivalent to a 2 e$^-$+ 2 H$^+$ redox process), and the second having the slope of ~30 mV/pH (equivalent to a 2 e$^-$+ 1 H$^+$ redox process) (Figure 4).
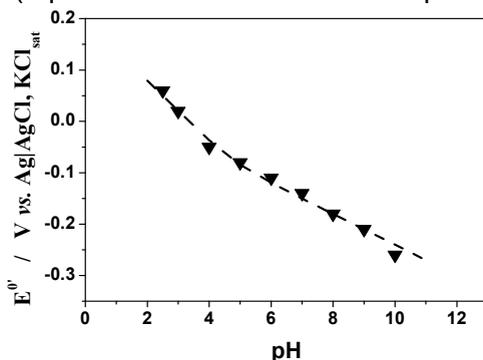
Figure 4. pH influence on the $E^{\circ'}$ value of MB-CA/GC electrode. Experimental conditions: see Figure 3.

This behavior indicates that, irrespective of the support material, the pK_a value for the adsorbed MB is around 4 [3]. Indeed, all experimental data were well fitted to the following nonlinear regression equation:

$$E = E^{0'} - 0.059 * pH + 0.029 * log(1 + 10^{pH - pK_a})$$

The calculated pK_a value for MB-CA/GCE is 4.7 ± 0.3 ($\chi^2 = 0.0001$, $R^2 = 0.9928$, N = 9), and is in good agreement with those reported for MB adsorbed on spectrographic graphite ($pK_a = 5$) [3].

The influence of a wide range of potential scan rates (0.001 – 1 V s^{-1}) at pH 7, on the electrochemical behavior of the immobilized redox mediator MB on the mesoporous CA was studied by recording the cyclic voltammograms. The dependence of the peak currents (I_{pa}) on the scan rate (v) is linear, with the slopes of log(I_{pa}) vs. log(v) dependencies of 0.9019 ± 0.0238 ($R^2 = 0.9945$, N = 19), close to the theoretical value (i.e., 1), confirming the immobilization of the redox mediator MB on the mesoporous CA (Figure 5).
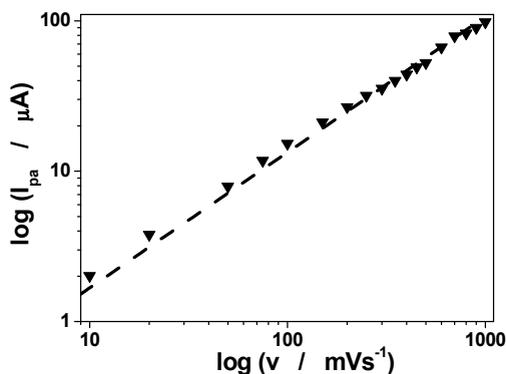
Figure 5. Influence of the potential scan rate on the anodic peak current recorded atMB-CA/GC electrode. Experimental conditions: supporting electrolyte, 0.1 M Tris buffer (pH 7).

Electrocatalytic NADH oxidation at MB-CA modified GC electrodes

MB-CA/GCE showed clear electrocatalytic activity for NADH oxidation. Thus, the cyclic voltammograms recorded at these electrodes in the presence of NADH (Figure 3, solid lines) present all the features of an electrocatalytic process: the oxidation peak is significantly increased, simultaneously with the disappearance of the reduction peak [2, 6 - 8].

The efficiency (E_{ff}) of the electrocatalytic oxidation of NADH at MB-CA / GCE was calculated according to the following relation:

$E_{ff} = (I_{cat} - I_0)/I_0$, where I_{cat} is the oxidation current intensity in presence of 5 mM NADH and I_0 is the oxidation current intensity observed

in its absence. The calculated electrocatalytic efficiency was 2.2, when the electrode was tested at 20 mV/s.

In order to establish the optimum surface coverage ensuring the highest electrocatalytic efficiency, the dependence of the catalytic current intensity on the surface coverage was investigated (Figure 6).
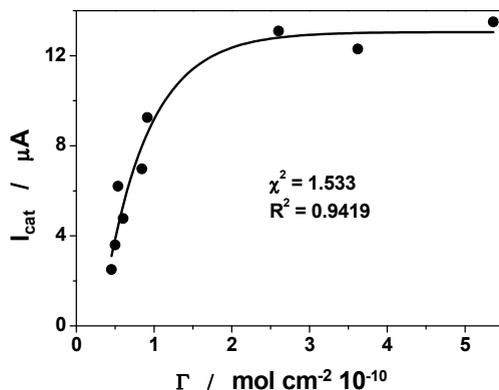
Figure 6. Dependence of NADH electrooxidation current on surface coverage of MB-CA/GCEs. Experimental conditions: scan rate, 2 mV/s; electrode rotation speed, 300 rpm; supporting electrolyte, 0.1 M Tris buffer (pH 7).

Therefore, the surface coverage (Γ) was estimated by using the equation: $\Gamma = Q/nFA$, where Q is the electric charge obtained by integrating the anodic peak, corrected for the background current; n, F and A are the number of electrons transferred in redox reaction, Faraday's constant and the electrode geometric area, respectively.

Above of a critical value (1.85×10^{-10} mol/cm^2), the catalytic response becomes practically independent on the surface coverage. Below this value the catalytic current depends almost linearly on the surface coverage. This suggests that besides the reaction rate and the mass transfer of NADH, additional kinetic restrictions may prevail. As consequence, all RDE experiments were performed in the range of surface coverage, where the catalytic current intensity is linearly dependent on the MB surface concentration [2, 7, 8].

RDE measurements allow the estimation of the apparent second order rate constants (k_{obs}) corresponding to different NADH concentrations, by using the Koutecky-Levich approach [2, 3, 8]. Table 1 summarizes the calculated parameters for MB-CA/GCE. Comparing the kinetic parameters values (*i.e.* K_M, k_{obs}, k_{+2}) obtained for MB-CA/GCE, with those obtained for MB adsorbed onto ZP [2], *α*-ZP [6, 7], or *α*-TP [6, 8] and incorporated in carbon paste electrodes, it can concluded that by using a very low amount of MB-CA immobilized onto GCE surface comparable values were obtained.

Table 1. Comparison of the kinetic and electrochemical parameters for NADH electrooxidation at different modified electrodes.

Electrode	$^b\Gamma$ mol·cm^{-2}	^aK_M mM	$^ak_{obs\,[NADH]=0}$ M^{-1}·s^{-1}	$^ak_{+2}$ s^{-1}	^{a}no. of electrons transfered	Ref. No.
MB-ZP-CPE	$6.2 \cdot 10^{-10}$	2	$8.5 \cdot 10^2$	1.7	1.94	[2]
MB-ZP-SG-CPE	$1.3 \cdot 10^{-9}$	2.5	$2.9 \cdot 10^2$	0.73	1.96	[2]
MB-ZP-SK-CPE	$5.6 \cdot 10^{-11}$	2.5	$7.2 \cdot 10^3$	18	1.6	[2]
MB-α-ZP-SK-CPE	$3.2 \cdot 10^{-11}$	1.2	$4.5 \cdot 10^3$	5.6	-	[7]
MB-α-TP-SK-CPE	$8 \cdot 10^{-12}$	1.7	$3.8 \cdot 10^3$	6.5	2.1	[8]
MB-CA/GCE	$1.8 \cdot 10^{-10}$	6.3	$1.27 \cdot 10^3$	8.06	1.3	This work

^{a} determinated from Koutecky-Levich treatment for RDE measurements.
^{b} determinated from CV measurements.

CONCLUSIONS

A simple and effective method has been successfully used for the preparation of the modified MB-CA/GCEs. The electrochemical parameter of the modified electrode (ΔE_p = 40 mV) points out the presence of the immobilized MB species on the electrode surface. The value of $E^{\circ'}_{MB-CA}$ is very close to the optimal potential range for the amperometric detection. The pH dependence of $E^{\circ'}_{MB-CA}$ was fitted by a nonlinear regression, allowing to estimate the pK_a of immobilized MB. The obtained kinetic parameters of the investigated electrode recommend it as a stable, sensitive and reproducible electrode for NADH electrooxidation.

ACKNOWLEDGMENTS

EXPERIMENTAL SECTION

CA synthesis. CA was prepared using a mixture of resorcinol (98% purity, Aldrich), formaldehyde (37% solution, Aldrich), Na$_2$CO$_3$ (99.9% purity, Aldrich), and deionized water, according to a previously reported sol-gel method [14].Thus, resorcinol (0.29 moles) was dissolved in bidistillated water (R/W = 0.2 g/ml). Formaldehyde solution was added to resorcinol solution (R/F = 0.5 molar ratio) under vigorous stirring. Na$_2$CO$_3$ 0.1 M aqueous solution was added drop by drop to the previous mixture (R/C = 500 molar ratio). Resulted solution was placed into tightly closed glass moulds and cured 1 day at

room temperature and 4 days at 70°C. After 15 days of aging at room temperature, the obtained wet gel was washed with acetone. Then, the wet gel was dried with CO_2 in supercritical condition (90 – 100 atm and 32°C) when the organic aerogel was obtained. This sample was pyrolysed in Ar atmosphere for 2 h at 850°C, when carbon aerogel was obtained.

Morpho-structural characterization of CA. Transmission electron microscopy (TEM) and nitrogen adsorption-desorption analysis were used for morpho-structural characterization of mesoporous CA.

TEM investigation of CA was performed with a Hitachi H-7000 microscope operating at 125 keV.

Nitrogen adsorption–desorption analysis were performed with Sorptomatic ADP (Thermo Electron Corp.) equipment after degassing around 100 mg of CA for 20 h at 106ºC in a vacuum (<1 mPa). From the carried out nitrogen adsorption analysis it was determined the specific surface areas by using the BET (Brunauer–Emmet–Teller) method and the pore size distribution and pore specific volume by the BJH (Barret–Joyner–Halenda) method.

Immobilisation of the organic dye (Meldola Blue) on the support material surface. The immobilization process was carried out using an aqueous solution of the organic dye (Meldola Blue, MB; Sigma, St. Louis, MO, USA) in a concentration of 0.001% (w/v). The procedure of immobilization was as follows: 50 mg of support material (CA) was added to 50 ml of dye solutionand the mixture was shaken for 1 h. The precipitate (MB-CA) was filtered, washed with de-ionized water anddried at room temperature.

Preparation of MB-CA/GCEs. The home-made glassy carbon disc electrodes were prepared by introducing glassy carbon rod into a Teflon holder, then was screwed onto a rotating disc electrode device (Radiometer Analytical, France) and was used as working electrode for cyclic voltammetry and rotating disc electrode measurements. The glassy carbon disc was thoroughly polished on alumina (1 µm Stuers, Copenhagen, Denmark), then rinsed with Milli-Q water. Chitosan solution was prepared by adding 10 mg chitosan (Sigma-Aldrich) to 10 mL of acetic acid (Sigma) 0.1 M. Then a suspension of 1 g/L MB-CA in chitosan solution was prepared. A volume of 5 µL from this suspension were placed onto clean GC electrode surface, and let to dry at room temperature. The geometrical area of the prepared modified electrodes was 0.049 cm^2.

Electrochemical measurements. The measurements were performed using a BAS 100 W Electrochemical Analyzer (Bioanalytical Systems, West Lafayette, IN, USA), which was connected to a PC microcomputer for potential control and data acquisition. The modified GCEs were used as working electrode, a platinum ring as the counter electrode, and Ag|AgCl,KCl$_{sat}$ as reference electrode. Cyclic voltammetry and rotating disc electrode

measurements were carried out in 0.1 M solution of Tris (Sigma). The pH of the electrolyte solutions was adjusted to the desired values by adding HCl or KOH (Merck).

All experiments were performed in deoxygenated electrolytes by bubbling argon for 20 min before each measurement. All reagents were used as received without further purification.

For each prepared modified glassy carbon, the surface coverage (Γ, mol cm^{-2}) was estimated through integration of the area of the wave registered by cyclic voltammetry.

NADH electrocatalytic oxidation study. The electrocatalytic oxidation of NADH using MB-CA/GCEs were investigated through addition of freshly prepared NADH (Sigma) solution of adequate concentration, by cyclic voltammetry and rotating disc electrode techniques.

REFERENCES

1. W.J. Blaedel, R.A. Jenkins, *Analytical Chemistry,* **1975**, *47*, 1337-1338.
2. C.I. Ladiu, I.C. Popescu, L. Gorton, *Journal of Solid State Electrochemistry,* **2005**, *9*, 296-303.
3. L. Gorton, A. Torstensson, A. Jaegfeldt, G. Johansson, *Journal of Electroanalytical Chemistry,* **1984**, *161*, 103-120.
4. C.I. Ladiu, R. Garcia, I.C. Popescu, L. Gorton, *Chemical Bulletin of "Politehnica" University of Timisoara,* **2004**, *49*, 51-55.
5. C.I. Ladiu, I.C. Popescu, R. Garcia, L. Gorton, *Romanian International Conference on Chemistry and Chemical Engineering*, **2005**, *2*, S10-11.
6. C.I. Forţ, I.C. Popescu, *Studia UBB Chemia*, **2011**, *4*, 255-264.
7. C.I. Ladiu, I.C. Popescu, R. Garcia, L. Gorton, *Revue Roumaine de Chimie,* **2007**, *52*, 67–74.
8. C.I. Ladiu, R. Garcia, I.C. Popescu, L. Gorton, *Revista de Chimie*, **2007**, *58*, 465-469.
9. L. Gorton, E. Csoregi, E. Dominguez, J. Emmeus, G. Jonsson-Pettersson, G. Marko-Varga, B. Persson, *Analytica Chimica Acta,* **1991**, *250*, 203-248.
10. L. Gorton, E. Dominguez, *Reviews in Molecular Biotechnology,* **2002**, *82*, 371-392.
11. C.I. Fort, L.C. Cotet, V. Danciu, G.L. Turdean, I.C. Popescu, *Materials Chemistry and Physics,* **2013**, *138*, 893-898.
12. L.T. Kubota, F. Munteanu, A. Roddick-Lanzilotta, A.J. McQuillan, L. Gorton, *Quimica Analitica,* **2000**, *19*, 15-27.
13. C.I. Fort, L.C. Cotet, A. Vulpoi, G.L. Turdean, V. Danciu, L. Baia, I.C. Popescu, *Sensors & Actuators: B. Chemical*, **2015**, *220*, 712-719.
14. L.C. Cotet, V. Danciu, V. Cosoveanu, I.C. Popescu, A. Roig, E. Molins, *Revue Roumaine de Chimie,* **2007**, *52*, 1077-1081.

Dedicated to prof. dr. I. C. Popescu
on the occasion of his 70th anniversary

PROTECTIVE TiO₂ COATINGS PREPARED BY SOL-GEL METHOD ON ZINC

GABRIELLA SZABÓ[a], EMŐKE ALBERT[b], ZOLTÁN HÓRVÖLGYI[b], LIANA MARIA MUREŞAN[a*]

ABSTRACT. The objective of this work was to develop new TiO₂ based coatings for producing an effective barrier as well as an appropriate support for inhibitors in corrosion protection of zinc. For this purpose, compact and mesoporous titania coatings on zinc substrates were prepared by sol-gel method (dip coating). For preparing mesoporous layers, cationic (cetyltrimethylammonium bromide, CTAB) or non-ionic (Pluronic PE 10300) surfactant templates were applied. The corrosion behaviour of the coatings was evaluated by open circuit potential measurements and Tafel interpretation of the polarization curves. The best corrosion resistance was noticed in the case of TiO₂ coated samples prepared in the presence of Pluronic surfactant.

Keywords: zinc; TiO₂, sol-gel method, dip- coating, corrosion

INTRODUCTION

The development of new effective anticorrosion pre-treatments for zinc substrates is an issue of great importance for corrosion technology due to the fact that hexavalent chromium conversion coatings are nowadays banished and efforts are made to replace them with other effective, but less toxic protective coatings [1].

[a] *Department of Chemical Engineering, "Babes-Bolyai" University, 11 Arany Janos St., RO-400028 Cluj-Napoca, Romania*
[b] *Budapest University of Technology and Economics, Department of Physical Chemistry and Materials Science, H-1521 Budapest, Budafoki út 6-8, Hungary*
[*] *Corresponding author: limur@chem.ubbcluj.ro*

Oxide coatings such as TiO_2 and SiO_2 act very efficiently as corrosion protectors of metals under different temperatures being environmentally - friendly and exhibiting excellent barrier properties as anticorrosive layers [2].

There are several techniques for the deposition of ceramic films and coatings on metal substrates, such as chemical / physical vapour deposition [3], plasma electrolytic oxidation [4], electrolytic deposition [5] and sol–gel process [1].

The sol-gel method is an environmentally friendly technique of surface protection resulting in high corrosion inhibition efficiency that can be used to prepare non-toxic conversion coatings on metals [6]. It involves conversion of small molecules (precursors) into a colloidal solution (sol) and then into an integrated network (gel) consisting of discrete particles and/or inorganic polymers [7].

TiO_2 can be prepared, for example, starting from precursor sols containing alkoxides (*e.g.*, tetrabutylorthotitanate) and diethanolamine dissolved in ethanol [8] and mixing them with water (with or without additives) in a certain ratio.

SiO_2 coatings can be prepared starting from a precursor solution consisting of tetraethylorthosilicate ($Si(OC_2H_5)_4$), H_2O, C_2H_5OH, and HCl, mixed at a certain molar ratio [9]. Different compounds (inhibitors, pigments, etc.) can be added in order to improve the physico-chemical properties of the coating.

Irrespective of the nature of the film, the two main techniques used to apply a sol-gel coating on the surface of a metallic substrate are dip-coating (the substrate is progressively dipped into and is extracted from the sol at a controlled rate) and spin-coating (an amount of sol is placed on the substrate that is rotated at high speed in order to spread the fluid by centrifugal force). In both cases, after the evaporation of the solvent, a thin, homogeneous film is formed on the metallic surface.

Continuing our previous researches in this field [10,11], the objective of this work was the development of new titania based coatings designed to produce an effective barrier as well as an appropriate support for inhibitors in corrosion protection of zinc. For this purpose, compact and mesoporous titania coatings on zinc samples were prepared by dip-coating. For preparing mesoporous layers, cationic (cetyltrimethylammonium bromide, CTAB) or non-ionic (Pluronic PE 10300) surfactant templates were applied. The corrosion behaviour of the coatings was evaluated by open circuit potential measurements and Tafel interpretation of the polarization curves and their performances were compared to those of previously reported SiO_2 coatings [11].

RESULTS AND DISCUSSION

The various types of TiO_2 layers on Zn substrates were obtained by dip-coating method from different precursor sols. The correlations of the coatings with their symbols are presented in Table 1.

Table 1. Summary of sample preparation, the used symbols (P: Pluronic PE 10300; CTAB: cetyltrimethylammonium bromide)

Symbol	Number of layers	Layer thickness* [nm]	Type of sample/ templating agent
TiO₂_K2	2	134 ±4	Compact TiO₂
TiO₂_K5	5	~330	
TiO₂_C1	1	104 ±4	Porous TiO₂/ CTAB
TiO₂_C4	4	~410	
TiO₂_P1	1	134 ±8	Porous TiO₂/ Pluronic
TiO₂_P3	3	~400	

• values estimated from UV-VIS spectra as shown below

Some mono- and multilayered coatings were also deposited on glass substrates for their optical characterization. Figure 1 shows the representative transmittance curves of the double-layered compact TiO_2 coating, the monolayered CTAB and Pluronic PE 10300 templated porous TiO_2 coatings, and their bare glass substrate.
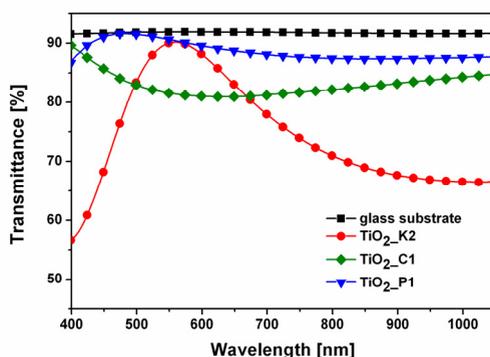
Figure 1. Transmittance spectra of the uncoated glass substrate, of the double-layered TiO₂ (TiO₂_K2), and monolayered CTAB (TiO₂_C1) and Pluronic (TiO₂_P1) templated porous TiO₂ coated samples.

All types of titania coated glass slides show lower transmittance values than their uncoated glass substrates (Figure 1). It can be observed that the Pluronic PE 10300 templated porous coating shows higher transparency then the titania coating prepared without using surfactant additive, in the whole studied wavelength range (Figure 1).

The obtained transmittance curves were analysed in terms of thin layer optical models. Transmittance spectra were fitted with a homogeneous layer model [12] supposing identical homogeneous coatings on both sides of the transparent substrate and perpendicular angle of incidence. The fitting procedures provided coating thickness and effective refractive index values. As the glass substrate had weak absorption, the transmittance spectra were corrected before fitting to eliminate this effect [12-13]. The fitting procedure used a Levenberg–Marquardt algorithm [14]. Porosity of coatings was estimated using the Lorentz-Lorenz formula [15-17]:

$$\frac{n_{eff}^2 - 1}{n_{eff}^2 + 2} = \alpha_1 \frac{n_1^2 - 1}{n_1^2 + 2} + (1 - \alpha_1) \frac{n_2^2 - 1}{n_2^2 + 2}$$

where the meaning of the used symbols are:

n_{eff}^2- effective refractive index of the layer

n_1-refractive index of anatase TiO_2 (estimated as 2.520, [18]

n_2-refractive index of the air (estimated as 1.00)

α_1-volume fraction of the TiO_2 component

The results of the fitting procedure and the calculated porosity values are presented in Table 2.

Table 2. Fitted effective refractive indices, layer thicknesses, and the calculated porosity values of the double-layered TiO_2 (TiO_2_K2), and monolayered CTAB (TiO_2_C1) and Pluronic (TiO_2_P1) templated porous TiO_2 coatings on glass estimated from UV-VIS spectra

Sample	Layer thickness [nm]	Effective refractive index	Porosity [%] (Lorentz-Lorenz)
TiO₂_K2	134 ± 5	1.945 ± 0.016	25±0.9
TiO₂_C1	104 ± 4	1.662 ± 0.009	42±0.6
TiO₂_P1	134 ± 8	1.590 ± 0.004	47±0.3

It can be observed that the thickness of monolayered porous coatings with Pluronic is about the same like that of the double-layered compact ones prepared on the same way, from a precursor sol without surfactant additive. On the other hand, Pluronic templated coatings porosity is slightly higher than that obtained with CTAB. It is worth mentioning that TiO_2 coatings prepared without surfactant additive (the so-called "compact" layers) show also a considerable porosity (25%) that was further increased by 17% and 22% by using surfactant in the case of CTAB and Pluronic templated porous TiO_2 coatings, respectively.

The titania coated silicon wafers were studied with Field Emission Scanning Electron Microscopy (FESEM) and cross-sectional images were

made in order to determine the thickness of the layers (Figure 2). For compact coatings the monolayer thickness was found to be 54 nm. The same parameter for the CTAB templated coating was found to be 94 nm and for the Pluronic templated one 144 nm. These thickness values are in good agreement with those calculated for the layers obtained on the microscope glass slides from UV-VIS spectra. According to our experience the structure of sol-gel coatings doesn't depend on the type of solid substrate (glass, silicon, zinc etc.).

Electrochemical investigations were started with the determination of the open circuit potential (OCP), and were continued with recording of polarization curves in an interval of ± 20 mV vs. OCP (linear polarization) in order to estimate the polarization resistance (R_p). These values are presented in Table 3.

From these values it can be concluded that porous multilayers have the best protection capabilities caused on the one hand by their greater thickness and on the other hand by the better wetting properties of precursor liquid of templating agents.

a

b

c

Figure 2. The FESEM images of the compact (a), CTAB templated (b) and Pluronic templated (c) TiO$_2$ layers on silicon substrate.

The OCP values of these samples were found to be slightly more positive compared to the reference Zn wafer (without coating) suggesting a possible better corrosion protection.

Table 3. The open circuit potential (OCP) and polarization resistance (R_p) for the TiO$_2$ layers deposited on Zn

Sample	R_p [Ωcm^2]	OCP [V vs. Ag/AgCl/KCl$_{sat}$]	R/N
Zn	98.5	-0.994	0.9991/ 28
TiO$_2$_K2	93.1	-1.013	0.9985/28
TiO$_2$_K5	208	-1.001	0.9980/38
TiO$_2$_C1	469	-0.948	0.9990/36
TiO$_2$_C4	352	-0.979	0.9940/74
TiO$_2$_P1	384	-0.974	0.9990/37
TiO$_2$_P3	448	-0.968	0.9990/40

Polarization curves were also recorded in the potential range ± 200 mV vs. OCP and are presented in Figure 3 for the compact coatings. The curves for the porous layers are presented in Figure 4.
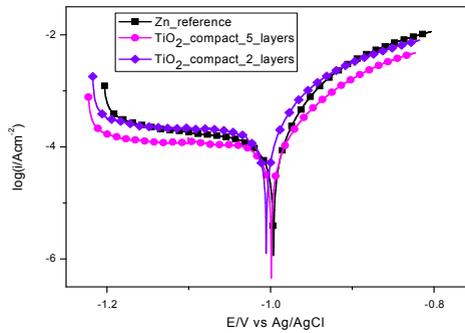
Figure 3. Polarization curves for the compact TiO$_2$ multilayered coatings on zinc
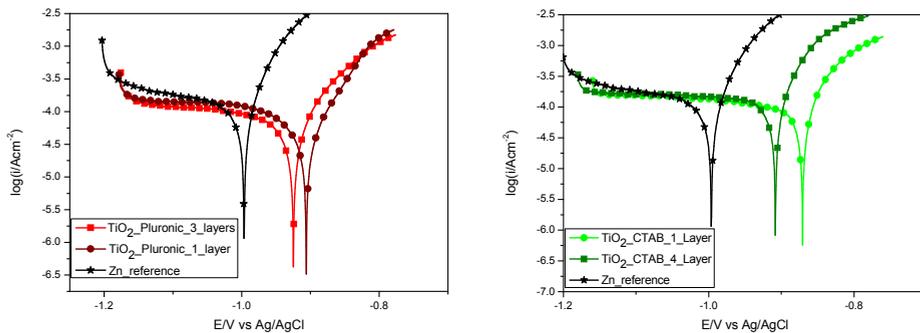
Figure 4. Polarization curves for the porous TiO$_2$ multilayered coatings on zinc templated with Pluronic (left) and CTAB (right).

The Tafel interpretation was used in order to extract the characteristic corrosion parameters (E_{corr}, i_{corr}, Tafel slopes b_a and b_c, presented in Table 4).

From the corrosion current densities one can conclude, that compact and CTAB templated coatings practically do not modify the corrosion behaviour of the Zn substrate, presumably due to the permeability of coatings. FESEM images revealed previously a granular structure of compact titania coatings [19, 20]. It was also observed that the CTAB template cannot modify the morphology of compact layers significantly [21]. Better results were obtained, however, for porous coatings templated with Pluronic (a triblock copolymer in which the central polypropylene glycol group is flanked by two polyethylene glycol groups); in this case the decrease of the corrosion current density was considerable, possibly due to the improved coating ability of precursor sols containing this surfactant and to the higher thickness of the layer. The lower permeability of Pluronic templated coatings may also be interpreted in terms of the irregular shaped pores in the coating. Using CTAB, the formation of cylindrical shaped pores is expected having a better permeability.

Table 4. The corrosion kinetics characteristic parameters for the TiO₂ coated Zn (E_{corr}-corrosion potential, i_{corr}-corrosion current density, b_c and b_a- cathodic and anodic Tafel slopes)

Sample	E_{corr} (V)	i_{corr} ($\mu A/cm^2$)	$-b_c$ (mV/dec)	b_a (mV/dec)
Zn	-0.996	12.15±3.9	36	20
TiO₂_K2	-1.005	16.36±2.3	23	37
TiO₂_K5	-0.999	12.62±0.6	14	11
TiO₂_C1	-0.870	13.63±1.0	16	10
TiO₂_C4	-0.860	15.45±1.2	12	11
TiO₂_P1	-0.906	8.08±0.47	10	8
TiO₂_P3	-0.925	7.87±0.41	12	11

All TiO₂ coatings were less protective than SiO₂ coatings prepared in similar conditions [11] revealing the higher permeability of titania coatings in comparison to the silica ones. For example, i_{corr} in the case of compact SiO₂ coating of 2 layers was almost ten times smaller (1.819 $\mu A/cm^2$) than in the case of compact TiO₂ coating of 2 layers (16.36 $\mu A/cm^2$). Almost the same finding is noticed in the case of Pluronic templated coatings: porous SiO₂ coating of 1 layer (3.832 $\mu A/cm^2$) comparing to porous TiO₂ coating of 1 layer (8.08 $\mu A/cm^2$). When CTAB was used the corrosion current density is 2.76 $\mu A/cm^2$ and 13.63 $\mu A/cm^2$) for porous SiO₂ coating of 1 layer and for porous TiO₂ coating of 1 layer, respectively.

CONCLUSIONS

Among the investigated titania coatings only the Pluronic templated ones showed slight corrosion protection of Zn presumable due to the less-permeable structure and better coating ability of their precursor sols.

As expected, multi-layered coatings were found to be more efficient than single ones. However, the results are inferior to those obtained with SiO_2 coatings on zinc prepared in similar way and reported elsewhere [11].

EXPERIMENTAL

Materials

Titanium (IV) butoxide (TBuOTi, for synthesis, ≥ 98%, Merck), ethanol (EtOH, a.r., > 99.7%, Reanal), nitric acid (HNO_3, special grade, 65%, Lach-Ner), cetyltrimethylammonium bromide (CTAB, cationic surfactant, 99+%, Acros Organics), Pluronic PE 10300 triblock copolymer (non-ionic surfactant, BASF, Ludwigshafen Germany) and distilled water (H_2O, 18.2 MΩ cm, purified with a Millipore Simplicity 185 filtration system) were used as starting materials for precursor sol synthesis.

Distilled water (18.2 MΩ·cm, purified with a Millipore Simplicity 185 filtration system), hydrochloric acid (HCl, purum, 37%, Fluka) and 2-propanol (2-PrOH, a. r., > 99.7%, Reanal) were used for cleaning the surface of the solid substrates.

Zinc wafers (Zn, 76x26x0.65 mm, Bronzker Bt, Hungary), silicon (Si) wafers and microscope glass slides (76×26×1 mm, Thermo Scientific, Menzel-Gläser) were used as solid substrates of the coatings.

In order to obtain the titania coatings three types of precursor sols were prepared. Titania precursor sol of compact coatings was prepared via the acid catalyzed controlled hydrolysis of titanium (IV) butoxide in ethanolic media [19]. Nitric acid was used as catalyst during the synthesis of precursor sol. The molar ratios for $TBuOTi:EtOH:HNO_3:H_2O$ were 1:27.95:0.49:0.82. For obtaining mesoporous titania coatings surfactant containing precursor sols were prepared by adding CTAB or Pluronic PE 10300 surfactant into the mixture of precursor sol. The molar ratios were 1:27.95:0.49:0.82:0.125 for $TBuOTi : EtOH : HNO_3 :H_2O :CTAB$, and 1 : 27.95 : 0.49 : 0.82 : 0.03 for $TBuOTi : EtOH : HNO_3 : H_2O : Pluronic$ PE 10300. The obtained mixtures were stirred for 2 hours at 60 ^{0}C.

For electrochemical investigation 0.2 g/L Na_2SO_4 (Riedel–de Haën, Germany) solution (pH=5) was used.

Apparatus and methods

In some cases titania coatings were deposited onto glass substrates and the optical properties were investigated by UV-Vis spectrometry. An

Analytic Jena Specord 200-0318 type spectrophotometer was used for taking the transmittance spectra of the bare glass substrates and of the samples at normal incidence. All transmittance spectra were recorded in the range of 400-1050 nm with 1 nm resolution and scanning speed of 5 nm/s.

For the electrochemical investigations a computer controlled potentiostat AUTOLAB, PGSTAT302N (Eco Chemie BV, Utrecht, Netherland) was used. Data registration/interpretation was carried out by a GPES programme. For measurements a classical three-electrode-cell was used, including the Zn wafers (coated and uncoated) as working electrodes, the reference Ag/AgCl/KCl saturated electrode and the Pt wire counter electrode.

Coatings prepared onto silicon wafers were studied with Field Emission Scanning Electron Microscopy (FESEM) as well. Top view and cross-sectional images were taken using a LEO 1540 XB Field Emission Scanning Electron Microscope applying 5.00 keV acceleration voltage. Cross-sectional images were used for the determination of layer thicknesses.

Preparation of TiO$_2$ coatings

The layers were deposited on microscope glass slides, Zn and Si wafers. Prior to the layer deposition the substrates were preliminarily prepared; Zn wafers were polished with emery paper (grade 1200) and subsequently treated with 0.1 M HCl solution, rinsed with 2-PrOH and Millipore distilled water. The microscope glass slide and Si wafer was cleaned with 2-PrOH impregnated cotton than rinsed with 2-PrOH and distilled water. All the substrates were dried at room temperature.

The sol-gel films were deposited on the above mentioned solid substrates by the dip-coating method. The substrates subsequently their preliminary preparation were immersed in the precursor sols and pulled out with a constant 12 cm/min withdrawal speed. All the deposited films were kept in a drying oven and annealed at 410ºC (coated Zn wafers) and at 450ºC (coated glass substrates).

Multilayer coatings were obtained by the repeated immersion of the wafers in one of the precursor sols. The heat treatment was applied only after the last withdrawal from the precursor sol.

Electrochemical characterization

For the electrochemical characterization in each case the open circuit potential was registered during one hour reaching stabilization.. Subsequently the polarization curves were recorded and Tafel interpretation was made in order to obtain corrosion current density, corrosion potential and Tafel slopes.

ACKNOWLEDGEMENTS

REFERENCES

1. D. Wang, G.P. Bierwagen, *Progress in Organic Coatings*, **2009**, *64*, 327.
2. S. Dalbin, G. Maurin, R.P. Nogueira, J. Persello, N. Pommier, *Surface and Coatings Technology* **2005**, *194*, 363.
3. D. Byun, Y. Jin, B. Kim, J. Kee Lee, D. Park, *Journal of Hazardous Materials*, **2000**, *73*, 199.
4. W. Simka, A. Krzakala, D.M. Korotin, Zhidkov I.S., Kurmaev E.Z., Cholakh S.O., Kuna K., Dercz G., Michalska J., Suchanek K., Gorewoda T., *Electrochim. Acta*, **2013**, *96,* 180.
5. P. Kern, P. Schwaller, J. Michler, *Thin Solid Films*, **2006**, *494*, 279.
6. L. Curkovic, H. Otmacic Curkovic, S. Salopekc, M. Majic Renjo, S. Šegota, *Corrosion Science*, **2013**, *77*, 176.
7. L.M. Muresan, Corrosion Protective Coatings for Ti and Ti Alloys Used for Biomedical Implants in "Intelligent Coatings for Corrosion Control", Eds. A. Tiwari, J. Rawlins, L.H. Hihara, Elsevier, ISBN 978-0-12-411467-8, **2014**, *Chapter 17*, 585
8. Tao FU, Xiao-Ming WU, Feng WU, Meng LUO, Bing-Hui DONG, Yuan JI, *Transactions of Nonferrous Metals Society of China*, **2012**, *22*, 1661.
9. Teng S, Liang W, Li Z, Ma X, *Journal of Alloys and Compounds*, **2008**, *464*, 452.
10. E. Albert, N. Cotolan, N. Nagy, G. Sáfrán, G. Szabó, L.M. Mureşan, Z. Hórvölgyi, *Microporous and Mesoporous Materials*, **2015**, *206*, 102.
11. E. Volentiru, M. Nyári, G. Szabó, Z. Hórvölgyi, L.M. Mureşan, *Periodica Polytechnica Chemical Engineering*, **2014**, *58*, 61.
12. E. Hild, A. Deák, L. Naszályi, Ö. Sepsi, N. Ábrahám, Z. Hórvölgyi, *Journal of Optics A: Pure and Applied Optics*, **2007**, *9*, 920.

13. D.S. Hinczewski, M. Hinczewski, F.Z. Tepehan, G.G. Tepehan, *Solar Energy Materials and Solar Cells*, **2005**, *87*, 181.
14. W.H. Press, B.P. Flannery, S.A. Teukolsky, W.T. Vetterling, *Numerical Recipes in C, The Art of Scientific Computing*, Cambridge Univ. Press, New York, **1988**.
15. L.V. Lorenz, *Ann. Phys. Chem.* **1880**, *11*, 70.
16. H.A. Lorentz, *Theory of Electrons*, Teubner, Leipzig, Germany, **1916**.
17. D. Grigoriev, D. Gorin, G.B. Sukhorukov, A. Yashchenok, E. Maltseva, H. Möhwald, *Langmuir*, **2007**, *23,* 12388.
18. A.F. Wells, *Structural Inorganic Chemistry*, Clarendon Press, Oxford, **1984**.
19. C. Trapalis, N. Todorova, M. Anastasescu, C. Anastasescu, M. Stoica, M. Gartner, M. Zaharescu, T. Stoica, *Thin Solid Films*, **2009**, *517*, 6243.
20. Á. Detrich, E. Hild, N. Nagy, E. Volentiru, Z. Hórvölgyi, *Thin Solid Films*, **2012**, *520*, 2537.
21. E. Albert, P.A. Albouy, A. Ayral, P. Basa, G. Csík, N. Nagy, S. Roualdès, V. Rouessac, G. Sáfrán, Á. Suhajda, Z. Zolnai, Z. Hórvölgyi, *RSC Advances*, **2015**, *5*, 59070.

Dedicated to prof. dr. I. C. Popescu
on the occasion of his 70th anniversary

CATALYTIC WET AIR OXIDATION OF PHENOL USING METAL MODIFIED ZEOLITIC VOLCANIC TUFFS

RALUCA PLEŞA CHICINAŞ[a], ZOLTÁN ZSEBE[a], HOREA BEDELEAN[b], MIRCEA DARABANTU[a], ANDRADA MĂICĂNEANU[a,*]

ABSTRACT. Zeolitic volcanic tuff modified with metals (Cu, Ce, Co, Ni, Zn, Mn and Fe) by ionic exchange was tested as catalyst in wet air oxidation process for phenol removal from aqueous solutions. The influence of temperature, air flow, catalyst quantity, phenol concentration, reaction time and catalyst grain size were considered. Also, the reaction was tested in two reactor types: batch and fixed bed. In the case of the batch reactor maximum value for the process efficiency, about 34%, was reached in the following conditions: 60°C, 60 L/h, 4 g catalyst, 1000 mg/L and 6 h reaction time. In case of the fixed bed reactor higher efficiencies were obtained, in the same reaction conditions.

Keywords: zeolite, phenol, catalytic wet air oxidation, chemical oxygen demand

INTRODUCTION

Zeolites are highly porous hydrated aluminosilicates with different cavity structures [1]. They are defined as crystalline substances with a structure characterized by a network of chained tetrahedrons [2]. The water from their structure can be easily removed by heating, without modification of the crystalline structure. After dehydration, zeolites become extremely receptive to receive other molecules in the blanks thus created [3]. Also, due to their negatively charged lattice balanced by mono and divalent

---

[a] *Babeş-Bolyai University, Faculty of Chemistry and Chemical Engineering, 11 Arany Janos st., RO-400028, Cluj-Napoca, Romania.*
[b] *Babeş-Bolyai University, Faculty of Biology and Geology, 44 George Bilascu st., RO-400015, Cluj-Napoca, Romania.*
* *Corresponding author: andrada@chem.ubbcluj.ro*

exchangeable cations, zeolites exhibit ion exchange property. Therefore, they can be used in a number of areas: waste water purification (urban, mining industry, radioactive, from the manufacture of detergents, the sugar factories), softening of industrial water etc. [3].

Zeolites consist of a wide variety of species, more than 40 natural species being known. The most abundant species is clinoptilolite, member of the heulandite group. Clinoptilolite is component of the zeolitic volcanic tuffs, which is a low cost material, widespread in many places of the world. Clinoptilolite has been shown to have high selectivity for certain pollutants with characteristics as high ion-exchange capacity, high specific surface area, rigid porous structures and low cheap prices. These characteristics make clinoptilolite a promising material for use in wastewater remediation [1, 4].

Catalytic wet air oxidation (CWAO) is an efficient technique designed to eliminate organic compounds from wastewaters when their concentration is small and other techniques are not feasible from the economic point of view [5]. Synthetic zeolite, ZSM-5, modified with metals (Fe, Cu) were previously tested in catalytic wet peroxide oxidation (CWPO) of phenol, reaching, in the case of Fe-ZSM, total organic carbon (TOC) efficiency of 45% (80°C and 7 h) [6,7], while mixt metal catalyst, Cu-Fe-ZSM, was used in oxidative degradation of Rhodamine 6G [8]. Previous tests realized on zeolitic volcanic tuff (Aluniş, Cluj County) modified with iron, Fe-ZVT, showed high phenol removal efficiencies in CWAO under mild conditions (atmospheric pressure, 60°C) [9].

Phenol, commonly chosen as "model" molecule for studies on catalytic oxidation of organic compounds in dilutes aqueous solutions, is considered as one of the most toxic pollutants, harmful to human health and to aquatic organisms [10]. According to the Romanian legislation [11], the maximum concentration of phenol in surface waters must be 1 $\mu g/dm^3$.

Hence, the aim of the present work was to study the possible use of metal (Cu, Ce, Co, Ni, Zn, Mn and Fe) modified zeolitic volcanic tuff (ZVT) as catalyst in the wet air oxidation of organic compounds. The influence of the reaction parameters (temperature, air flow, catalyst quantity, phenol concentration, reaction time), and of catalyst grain size (<0.2, 0.2-0.4 and 0.4-0.6 mm) were considered.

RESULTS AND DISCUSSION

A representative sample of zeolitic volcanic tuff (ZVT) collected from Măcicaş deposit (Cluj County, Transylvania, Romania) was used. Complete characterization of ZVT was included in a previous work [12]. The high quantity of secondary and hydrated material is indicated by the high value of loss of ignition (12%). The samples under investigation showed a

remarkable homogeneity in their mineralogical and chemical composition with a small variation in SiO_2 content. Also, the ZVT is low in Na and K content, but high in Ca. The main component of the ZVT is represented by volcanic glass (70-80%) as fragments with angular edges, pyrogenic materials also include K-feldspars, plagioclases, quartz, micas, amphiboles and opaque minerals. ZVT X-ray diffraction patterns obtained indicated the massive presence of clinoptilolite as the main zeolite species. The semi-quantitative estimation from XRD patterns indicated that the zeolite content reached values up to 80% from the crystallized fractions of the tuff. The ZVT contains abundant tabular clinoptilolite crystals that formed by the replacement of the vitric fragments. Finally, FTIR spectra of the ZVT samples indicated the presence of specific zeolite peaks [12].

Phenol CWAO results in batch reactor

The study of the temperature influence upon phenol oxidation process was conducted using 4 g Cu1-Z catalyst, 100 mL of phenol solution (1000 mg/L) and 20 L/h air flow at 40, 50 and 60°C, for 6 h. The results obtained in these conditions are presented in Figure 1. As expected, COD efficiency increased with the increase of temperature.
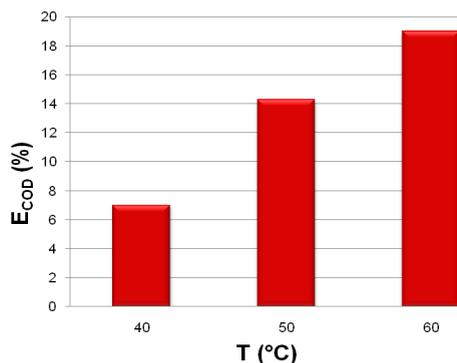
Figure 1. Temperature influence over the COD efficiency variation in the phenol CWAO process, for Cu1-Z catalyst (20 L/h, 4 g, 1000 mg/L, 6 h).

The influence of air flow upon the COD efficiency in the phenol oxidation process was studied at constant temperature 20°C, with the use of 100 mL (1000 mg/L) phenol solution, 4 g Cu1-Z catalyst at 20, 30, 40, 50, and 60 L/h air flow, for 6h. Maximum value of the COD efficiency, 33.73%, was calculated at 60 L/h. With an increase of the air flow, COD efficiency also increased, suggesting that oxygen diffusion process could be the rate determining step in the catalytic oxidation process. Maximum E_{COD} values thus obtained for all air flows are presented in Figure 2.
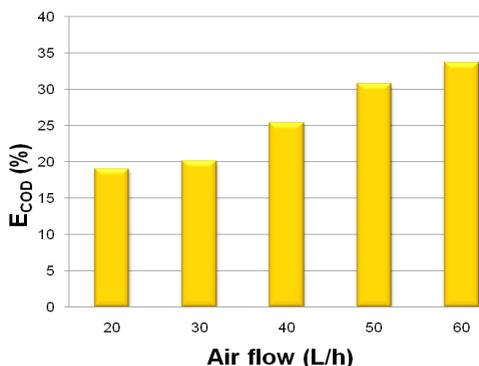
Figure 2. Variation of COD efficiency in the phenol CWAO process, at different air flows and constant temperature (60°C), for Cu1-Z catalyst (4 g, 1000 mg/L, 6 h).

The results obtained when various quantities of catalyst (2-5 g Cu1-Z) were used are presented in Figure 3.

Figure 3. Catalyst quantity influence over the COD efficiency variation in the phenol CWAO process, for Cu1-Z catalyst (20 L/h, 60°C, 1000 mg/L, 6 h).

Thus, an increase in catalyst quantity led to an increase of COD efficiency up to 4 g due to an increase in active centers number on the catalyst surface. Further increase of the catalyst quantity led to a decrease in COD efficiency, probably due to the agglomeration of the catalyst grains, which results in an increase of the diffusion limitation.

Phenol initial concentrations used were 250, 500, 750 and 1000 mg/L. As one can observed from Figure 4, an increase of phenol initial concentration led to an increase of the COD efficiency.
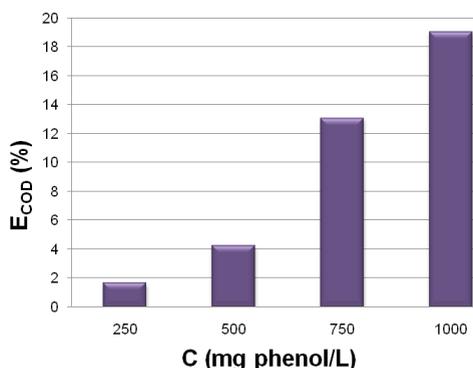
Figure 4. Variation of COD efficiency in the phenol CWAO process, at different phenol concentrations and constant temperature (60°C), for Cu1-Z catalyst (4 g, 20 L/h, 6 h).

The influence of the reaction time on the oxidation process of phenol was also investigated. Reaction conditions were chosen as: 20°C, 60 L/h air flow, 100 mL (1000 mg/L) phenol solution, using 4 g Cu1-Z catalyst and reaction time of 3, 4, 5 and 6 h. As expected, the acquired results, (Figure 5), showed that an increase of the reaction time led to an increase of COD efficiency.

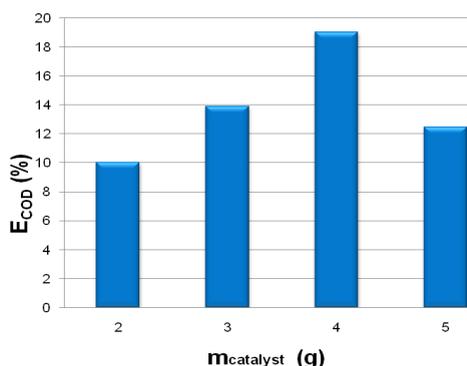
Figure 5. Time influence over the COD efficiency variation in the phenol CWAO process, for Cu1-Z catalyst (20 L/h, 60°C, 4 g, 1000 mg/L).

COD efficiency of the modified ZVT with various metals in the phenol CWAO process, in batch reactor, are presented in Figure 6. COD efficiencies reached for the considered catalysts have values in 19.76-33.72% range, with maximum value obtained for Cu1-Z.

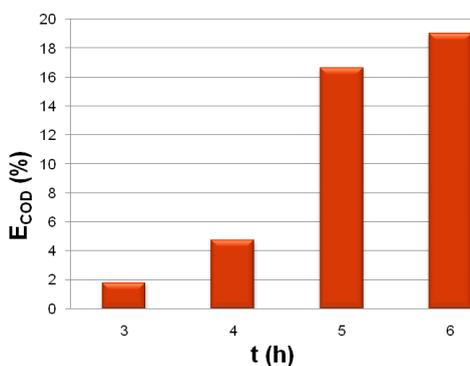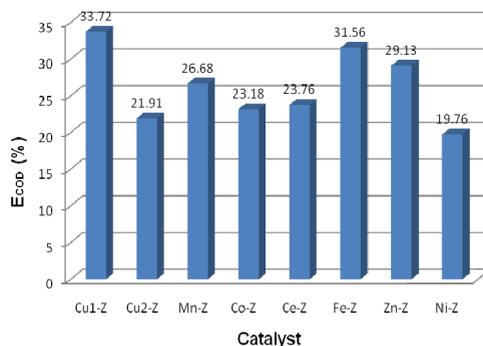**Figure 6.** COD efficiency in the phenol CWAO process, for various catalysts (60°C, 60 L/h, 4 g, 1000 mg/L, 6 h).

Phenol CWAO results in fixed bed reactor

The study of the CWAO process using the catalyst in fixed bed showed an improved COD efficiency, an increase of about 50% by comparison with batch conditions, was observed for the same reaction parameters (60°C, 20L/h, 1000 mg/L, 6 h, catalyst:solution = 1:25). When different grain sizes were used, a very small difference was observed, in favor of Cu4-Z (0.4-0.6 mm), Figure 7.
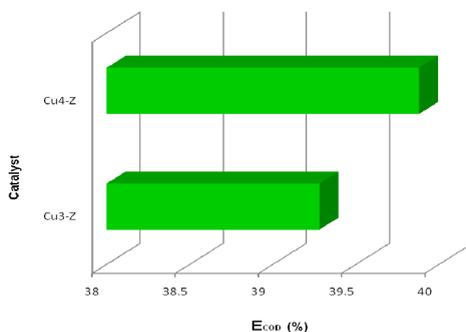
Figure 7. COD efficiency in phenol CWAO, in fixed bed reactor, for Cu3-Z and Cu4-Z catalyst (20 L/h, 60°C, 1 g, 1000 mg/L, 25 mL, 6 h).

CONCLUSIONS

The influences of temperature, air flow, phenol initial concentration catalyst quantity and time of reaction over the process efficiency were studied in the CWAO process using catalysts prepared by ionic exchange

on ZVT. An increase of the temperature, air flow, time, catalyst quantity, phenol concentration and time led to an increase of the process efficiency.

In the case of the batch reactor maximum value for the process efficiency, about 34%, was reached in the following conditions: 60°C, 60 L/h, 4 g catalyst, 1000 mg/L and 6 h reaction time. In case of the fixed bed reactor higher efficiencies were obtained, in the same reaction conditions.

Further studies will be performed in order to identify the optimum conditions for fixed bed reactor and oxidation pathways on this type of catalysts.

EXPERIMENTAL SECTION

Materials
In this work, a representative sample of ZVT collected from Măcicaş deposit (Cluj County, Transylvania, Romania) was used.

All reagents (organic and anorganic) were of analytical purity and used as received. Distilled water was used throughout this work.

Catalysts preparation
Ion exchange method used for catalysts preparation used by Măicăneanu *et al.* was applied with some modifications [9].

The stages involved in the preparation of the ZVT were as follows: crushing, grinding, size separation (< 0.2, 0.2-0.4 and 0.4-0.6 mm), washing with distilled water, drying at 105°C for 24 hours, treatment with NaCl 1 M under stirring (330 rpm) for 2 hours with a solid:solution weight ratio of 1:10, washing with distilled water (until chlorine ions were no longer detected with AgCl solution) and finally drying at 105°C for 24 hours. At the end of the above treatment, the ZVT-Na form was obtained. ZVT-Na form was used for further catalyst preparation taking into account that the ionic exchange process efficiency is improved by comparison with the raw ZVT sample [13, 14].

$$Z + NaCl \leftrightarrows Z\text{-}Na + Cl^- \qquad (1)$$

In order to obtain the chosen catalysts, ZVT-Na sample was further on subjected to an ionic exchange process upon treatment with a 0.5 N solution containing the desired metal ions, using a solid:solution weight ratio of 1:10. The ionic exchange reaction that takes place during this process is:

$$n(Z\text{-}Na) + M^{n+} \leftrightarrows (Z)_n M^{n+} + nNa^+ \qquad (2)$$
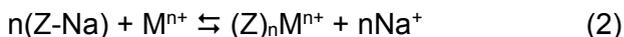
Depending on the ZVT-Na grain size and in order to avoid particle erosion, the ionic exchange procedure was conducted using magnetic stirring (500 rpm) in case of < 0.2 mm particle size and 3D stirring for 0.2-0.4 and 0.4-

0.6 mm particle size. The ionic exchange process was conducted for 24 h. After stirring, samples were separated from the precursor solution by centrifugation for 5 minutes at 5000 rpm (< 0.2 mm) and settling (0.2-0.4 and 0.4-0.6 mm). After separation, samples were washed several times with distilled water, dried at 105°C (24 h) and calcined 250°C (4 h, with a heating rate of 4°C/min). The obtained catalysts are listed in Table 1.

Table 1. Catalyst name, precursor and ZVT sample.

Catalyst label	Precursor	ZVT sample
Cu1-Z	$CuSO_4 \cdot 5H_2O$	ZVT-Na, <0.2 mm
Cu2-Z	$Cu(NO_3)_2 \cdot 3H_2O$	ZVT-Na, <0.2 mm
Cu3-Z	$CuSO_4 \cdot 5H_2O$	ZVT-Na, 0.2-0.4 mm
Cu4-Z	$CuSO_4 \cdot 5H_2O$	ZVT-Na, 0.4-0.6 mm
Ni-Z	$Ni(NO_3)_2 \cdot 6H_2O$	ZVT-Na, <0.2 mm
Zn-Z	$Zn(NO_3)_2 \cdot 6H_2O$	ZVT-Na, <0.2 mm
Co-Z	$Co(NO_3)_2 \cdot 6H_2O$	ZVT-Na, <0.2 mm
Mn-Z	$Mn(NO_3)_2 \cdot 4H_2O$	ZVT-Na, <0.2 mm
Ce-Z	$Ce(NO_3)_3 \cdot 6H_2O$	ZVT-Na, <0.2 mm
Fe-Z	$Fe(NO_3)_3 \cdot 9H_2O$	ZVT-Na, <0.2 mm

CWAO experiments

In case of the catalysts prepared using ZVT-Na < 0.2 mm, the CWAO process was carried out in a thermostated batch reactor, figure 8a, equipped with a magnetic stirrer (500 rpm) at atmospheric pressure. For a typical run, 100 mL of phenol solution (1000 mg/L) and 4 g catalyst were loaded into the reactor and the oxidation conditions were maintained for 6 h. Reaction temperature and air flow were 60°C and 20 L/h, respectively. For Cu1-Z catalyst, various reaction parameters were considered: temperature (40-60°C), catalyst quantity (2-5 g), phenol concentration (250-1000 mg/L), 20-60 L/h air flow and 3-6 h reaction time.

The catalysts prepared using 0.2-0.4 and 0.4-0.6 mm grain size (Table 1) were tested in a thermostated fixed bed reactor, figure 8b, placed on a 3D shaker (50 rpm), at atmospheric pressure. Typical conditions were: 25 mL phenol solution (1000 mg/L), 1 g catalyst, 60°C and 20 L/h air flow. The oxidation conditions were maintained for 6 h.

A blank sample (ZVT-Na), was also tested in the same reaction conditions. All the experiments were realized in triplicate, the presented values are averaged values.

The evolution of phenol oxidation process was followed by means of efficiency, calculated using $KMnO_4$ chemical oxygen demand (COD) values [9] obtained for the initial solution and at the end of CWAO reaction.

$$E_{COD}, \% = \frac{COD_i - COD_f}{COD_i} \cdot 100 \qquad (3)$$

where, COD_i is the initial value and COD_f is the final value at the end of CWAO reaction, in mg $KMnO_4$/L.

(a)   (b)
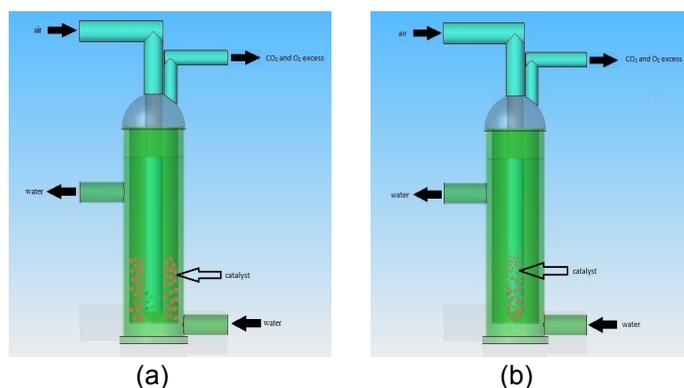
Figure 8. Reactors used in CWAO experiments: (a) thermostated batch reactor, (b) thermostated fixed bed reactor.

ACKNOWLEDGMENTS

REFERENCES

1. Md. Ahmaruzzaman, *Advances in Colloid and Interface Science,* **2008**, *143*, 48.
2. D.S. Coombs, A. Alberti, T. Armbruster, G. Artioli, C. Colella, E. Galli, J.D. Grice, F. Liebau, J.A. Mandarino, H. Minato, E.H. Nickel, E. Passaglia, D.R. Peacor, S. Quartieri, R. Rinaldi, M. Ross, R.A. Sheppard, E. Tillmanns, G. Vezzalini, *Canadian Mineralogist*, **1997**, *35*, 1571.
3. A. Măicăneanu, H. Bedelean, M. Stanca, "Zeoliţii naturali. Caracterizare şi aplicaţii în protecţia mediului", Cluj University Press, Cluj-Napoca, **2008**, chapter 1**.**
4. G. Cerri, A. Langella, M. Pansini, P. Cappelletti, *Clays and Clay Miner*als, **2002**, *50*, 127.

5. G. Busca, S. Berardinelli, C. Resini, L. Arrighi, *Journal of Hazardous Materials*, 2008, *160*, 265.
6. K. Maduna, A. Katovic, S. Zrncevic, *Journal of Hazardous Materials*, **2007**, *144*, 663.
7. Y. Yan, S. Jiang, H. Zhang, X. Zhang, *Chemical Engineering Journal*, **2015**, *259*, 243.
8. M. Dükkanci, G. Gündüz, S. Yilmaz, Y.C. Yaman, R.V. Prokhod˙ko, I.V. Stolyarova, *Applied Catalysis B: Environmental*, **2010**, *95*, 270.
9. A. Măicăneanu, M. Stanca, S. Burca, H. Bedelean, *Studia UBB Chemia*, **2008**, *53 (3)*, 7.
10. M.A. Barron, L. Haber, A. Maier, J. Zhao, M. Burron, 2002, EPA/635/R-02/006.
11. Ordin nr. 161 din 16/02/2006 pentru aprobarea Normativului privind clasificarea calităţii apelor de suprafaţăîn vederea stabilirii stării ecologice a corpurilor de apă.
12. A. Măicăneanu, H. Bedelean, S. Burcă, M. Stanca, *Separation Science and Technology,* **2011**, *46*, 1621.
13. K.D. Mondale, R.M. Carland, F.F. Aplan, *Mineral Engineering*, **1995**, *8*, 535.
14. M. Panayotova, B. Velikov, *Journal of Environmental Science and Health*, **2003**, *A38*, 545.

Dedicated to prof. dr. I. C. Popescu
on the occasion of his 70th anniversary

GROUNDWATER QUALITY IN SHALLOW WELLS FROM FELEACU VILLAGE, CLUJ COUNTY, ROMANIA

SILVIA BURCĂ[a], CERASELLA INDOLEAN[a], ANDRADA MĂICĂNEANU[a*]

ABSTRACT. This study includes monitoring of the most important physico-chemical parameters in ten shallow wells from Feleacu village, Cluj County, Romania, in order to establish if the water sources can be used as drinking water. dH_t, dH_T, COD, TDS, conductivity, pH, NO_2^-, NH_4^+, Mn^{2+} and Fe_{total} were determined using appropriate standard methods and compared with allowable values for drinking water, according to Romanian legislation. Based on the determined parameter values, most of the samples were characterized by high mineralization and some of them are contaminated with nitrite ions. Thus in order to ensure that the water consumed as drinking water will not create health problems to the population, periodically monitoring of physico-chemical parameters should be compulsory performed.

Keywords: groundwater, shallow wells, drinking water, quality parameters, monitoring

INTRODUCTION

On planet Earth, on large areas, drinking water supply is represented by the groundwater, particularly from wells, without the usage of electrical equipment [1]. According to statistics, in Romania, about 45% of the population lives in rural areas and more than 2500 villages benefit from centralized water supply system, the rest using their local water sources (wells, springs). Generally, wells in Romania are built at smaller depth, 20 meters, and there are not suitably covered [2, 3].

---

[a] Department of Chemical Engineering, Faculty of Chemistry and Chemical Engineering, Babeş-Bolyai University, 11 Arany Janos st., RO-400028, Cluj-Napoca, Romania.
* Corresponding author: andrada@chem.ubbcluj.ro

The groundwater quality parameters variation depend on the geological structure of the area, the activities that take place close to the points of sampling, the climatic conditions, the alternation of rainy and dry periods, etc. [4, 5].

Groundwater may contain natural impurities or contaminants, which can originate from watershed or soil. Water moving through underground rocks and soils may pick up magnesium, calcium, iron, manganese and chlorides. Some groundwater naturally contains dissolved elements such as selenium, boron, arsenic or radon – a gas formed by the natural breakdown of radioactive uranium in soil. These natural contaminants can produce various health problems depending on their amount [6, 8].

Also, groundwater is often polluted due to human activities, such as: fertilizers usage, animal manures, pesticides, improperly built and located septic systems for household wastewater, storm-water drains that discharge chemicals to groundwater, improper disposal or storage of wastes, chemical spills at local industrial sites [9-11].

Between groundwater pollutants, a special problem is generated by the presence of high nitrate/nitrite ions quantities. Naturally existent quantities are increased by various human activities (septic tanks, animal manures, fertilizers, etc.). Nitrogen compounds from soil are transformed and the nitrate ions are picked up by flowing water and transferred in groundwater. Therefore shallow wells drinking water in our country could reach many times higher levels that the allowable values according to Romanian legislation [12]. The actual toxicity is given by nitrite ions which are formed from nitrates ions in organisms or abiotic environment (water pipelines and storage tanks). The susceptibility to nitrite ions of new-born children and animals is due to the fetal hemoglobin, which has more affinity for oxygen, therefore forms methemoglobin quicker than in adults [12-18].

Water from wells can be consumed directly without previous treatments if groundwater is not in a contaminated area and if the well is properly built and maintained. Wells should be placed away from latrines or barns, and if possible, above or at the same level. Water quality must be regularly checked and periodically disinfected, while the well walls are cleaned and disinfected [18-20].

This paper includes a case study regarding groundwater quality in shallow wells from Feleacu village, Cluj County, Romania. The area was chosen taking into consideration the fact that this village is not connected to the centralized water supply even if is very close to Cluj-Napoca city.

RESULTS AND DISCUSSION

Based on water hardness, expressed in German degree, water can be classified as very soft (0-4 °d), soft (4-8 °dH), moderately hard (12-18 dH),

hard (18-30 °dH) and very hard (>30 °dH) [21]. Temporary hardness values determined in the collected water samples (W1-W10) are listed in Table 1, all values are above 5 °dH, value specified by the Romanian legislation. It can be seen that some values are quite high, as water collected in October 2013 from W4, W5, W7 wells. This indicates the presence of bicarbonates of calcium and magnesium, resulting from dissolution of minerals by meteoric waters. Small amounts of temporary hardness for W1, W3, W9 water samples are due to the fact that cleaning and disinfection was realized just a few days before sampling. Total hardness values, Table 1, showed that all water samples have high hardness and can be included in the category of very hard water (W1, W2, W4-W8, W10), hard (W9) and moderately hard (W3). Values showed in Table 1 and Figure 1 suggest that the total hardness is slightly higher for each well for samples collected in October and May, by comparison with those collected in March. This fact can be attributed to the higher temperatures registered in those months, when higher amounts of minerals are dissolved before they reach the groundwater level. Groundwater from these wells can be used as drinking water after preliminary boiling and cooling or storage in suitable containers for several hours when calcium and magnesium salts dissolved in water is deposited.

Table 1. Total and temporary hardness values of W1-W10 samples.

Well	October		March		May		Water type*
	dH_t	dH_T	dH_t	dH_T	dH_t	dH_T	
				(°dH)			
W1	16.24	37.52	10.92	32.20	16.24	33.04	Very hard
W2	16.80	40.32	13.44	42.28	14.00	39.20	Very hard
W3	13.44	16.24	8.40	21.28	11.76	22.96	Moderately hard
W4	20.44	44.52	13.44	39.76	16.24	33.04	Very hard
W5	21.00	38.36	12.32	35.00	15.68	32.48	Very hard
W6	17.92	47.88	15.12	43.12	16.80	47.60	Very hard
W7	23.52	45.92	14.00	30.52	16.24	35.28	Very hard
W8	17.36	31.36	10.08	29.96	14.56	34.72	Very hard
W9	5.60	33.60	3.92	25.48	3.36	24.08	Hard
W10	15.69	34.44	15.12	33.68	15.12	36.40	Very hard

* Based on dH_T values

Chemical oxygen demand (COD) values determined in the collected water samples are generally under the maximum allowable value (MAV) specified by the Romanian legislation (5 mg O_2/L or 12 mg $KMnO_4$/L) with exception of W1 and W3 samples collected in October and W7 collected in

March, which are close to MAV (Figure 2). Therefore, taking in account the diversity of factors that affect COD values, in the cases where high values were recorded, closer monitoring, identification of the exact cause and remediation of the identified problem are required.
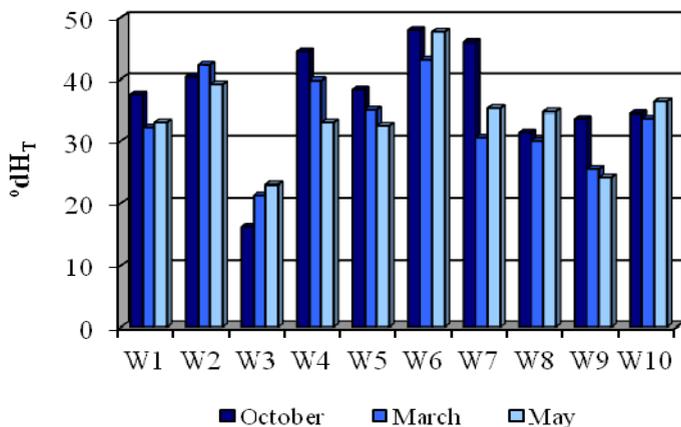
Figure 1. Evolution of total hardness values of W1-W10 samples over the monitoring time intervals.
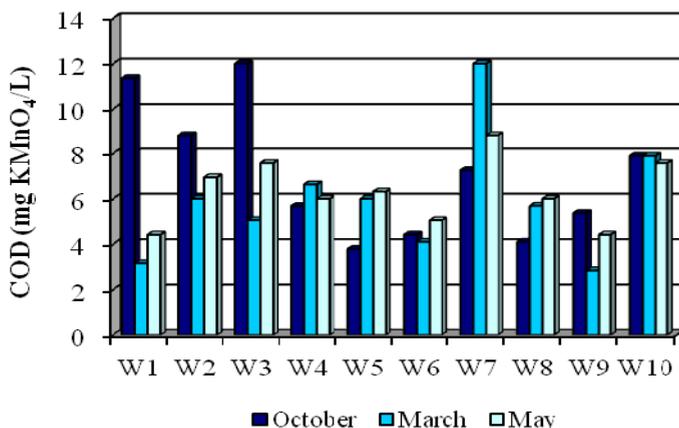
Figure 2. Chemical oxygen demand values of W1-W10 samples over the monitoring time intervals.

For total dissolved solids (TDS), in all water samples were registered values lower than the MAV specified by the Romanian legislation (1200 mg/L), Table 2. Also in case of most of the samples collected in March, TDS values are smaller than for those collected in October and

May. These values are correlated with COD and dH_T values for the same well. pH values determined for W1-W10 samples are all in the pH range specified by Romanian legislation (6.5-9.5), Table 2. Lower values were recorded for W9 (pH 6.50 – 6.80), while higher values were recorded for W1, W6, W7, Table 2.

Table 2. Solid residue and pH values of W1-W10 samples.

Well	TDS (mg/L)				pH			
	October 2013	March 2014	May 2014	MAV*	October 2013	March 2014	May 2014	MAV**
W1	560	240	680		7.54	8.43	7.65	
W2	800	680	920		6.98	7.86	7.81	
W3	720	200	360		6,78	7.80	8.06	
W4	640	160	600		7.03	8.33	7.91	
W5	880	560	400	1200	7.29	7.94	7.75	6.5-9.5
W6	840	760	480		7.30	8.20	7.52	
W7	1120	800	560		7.19	8.26	7.76	
W8	280	320	240		7.12	7.77	7.23	
W9	520	520	320		6.80	6.74	6.50	
W10	240	400	480		6.89	8.18	7.57	

* Acording to Romanian STAS 3638/76
** Acording to Romanian Laws 458/2002 and 311/2004

The electrical conductivity of water samples collected is relatively high, compared with water from Cluj-Napoca drinking water network (60-80 µS/cm), with values between 671 µS/cm for W3 in October 2013 and 1792 µS/cm for W7 in October 2013. All values are under the MAV value according to Romanian legislation (2500 µS/cm).

The concentration of nitrite ions in W1-W10 samples (Figure 3) have in general values under the MAV according to Romanian legislation (0.50 mg/L). In few cases, W1 and W10, were recorded very high values 1.094 and 1.606 mg/L, respectively. Relatively high values but below the maximum were recorded for samples W2, W7 and W9. These wells are located downstream of the house and household annexes, therefore groundwater can easily seep nitrogen. Taking in account the high toxicity of nitrite ions, this parameter has to be periodically checked and the consumption as drinking water stopped until treatment and removal of the pollution sources was realized.

Ammonium concentrations in all samples collected, as can be seen from Figure 4, have values below the MAV according to Romanian legislation (0.50 mg/L) the highest value recorded in a sample was 0.226 mg/L for W1 in March.

251
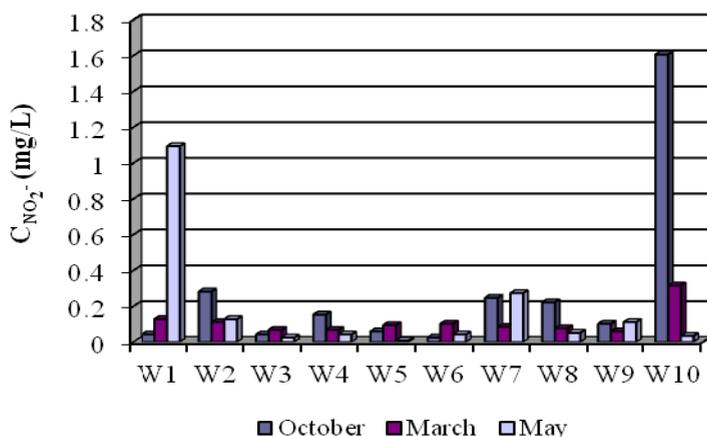
Figure 3. Nitrite ions concentration values in W1-W10 samples over the monitoring time intervals.
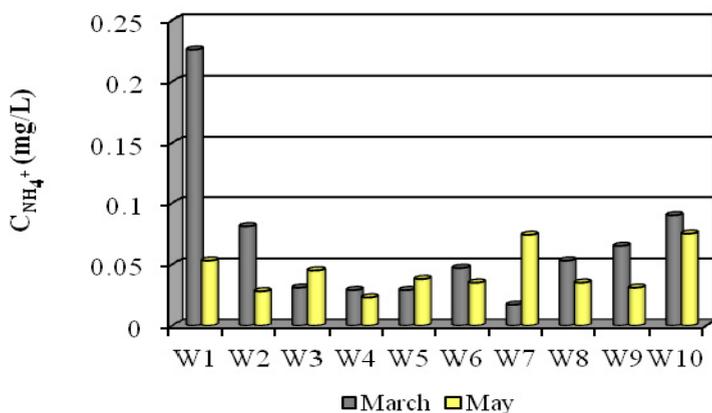
Figure 4. Ammonium concentration values in W1-W10 samples in March and May 2014*.*

Concentrations of manganese and iron ions are very small for all samples. Concentration values were below the MAV values imposed by the Romanian legislation, 50 µg Mn^{2+}/L and 200 µg Fe_{total}/L. In addition, iron ions are not toxic to the body, on the contrary, is considered a vital trace element, essential for the synthesis of heme from red blood cells and of myoglobin.

CONCLUSIONS

Based on the physico-chemical monitoring carried out (dH_t, dH_T, COD, TDS, conductivity, pH, NO_2^-, NH_4^+, Mn^{2+} and Fe_{total}) on 10 shallow well

waters from Feleacu village, Cluj County, Romania, it was found that in generally, groundwater is characterized by high mineralization (they are hard or very hard water) and often, due to human activity are contaminated with nitrite ions. Groundwater from these wells can be used as drinking water after preliminary boiling and cooling or storage in suitable containers for several hours, when calcium and magnesium salts dissolved in water are deposited. According with the results presented in this study, some of the considered wells present high concentrations of COD and NO_2^-, therefore closer monitoring, identification of the exact cause and remediation of the identified problems are required.

EXPERIMENTAL SECTION

Collection site and water sampling

Water samples were collected from 10 wells (W1-W10, Figure 5) located in Feleacu village, Cluj County, Romania, in October 2013, March and May 2014. This village is situated on Feleacu Massif, located on Someş River Plateau, Transylvania region. The Massif is oriented on the east-west direction over a length of 20 km, along which two other peaks are present, Peana (832 m), Măgura Sălicii (824 m) [20]. An important feature of this Massif is the presence of Sarmatians deposits, also known "Feleacu concretions". These deposits were created by gradual and long-time precipitation of $CaCO_3$ in the soil. $CaCO_3$ was initially trapped in the waters that soaked sandy layers, after that precipitation took place around limestone rock fragments or shells debris. Thus, these processes have led to the formation of concentric deposits of $CaCO_3$ around grains of sand [21, 22].

Climatic conditions in the area are moderate with not very cold winter and not excessively hot summers. The transition from winter to spring takes place usually in mid-March and from autumn to winter in November. Thus, average annual temperatures are between 8-9°C, and mean annual precipitation ranges from 600 to 700 mm [22].

In terms of hydrography, Feleacu village area has no running water or lake, however, geological substrate in this region has allowed the emergence and development of aquifer, which is the main water source for villagers in discussion. Sarmatian deposits allow accumulation of water with the formation of aquifers, fed directly by water infiltration. These accumulations have thus the character of an aquifer with fresh water [22-24]. Due to the special bedrock, these waters are characterized by a high degree of mineralization.

Water samples were collected in plastic containers, previously rinsed 2-3 times with the water sample, completely filled, and then closed

so that no air bubbles remain inside the bottle. On wells equipped with pumps, water sample was collected after a minimum of 10 minutes run, while from wells with extraction bucket collection was made introducing the bucket at 10-30 cm below the water mirror. After collection, bottles were placed in dark boxes. Until the analyses were run, water samples were kept at temperatures below 5°C and processed within 6 h from collection.

Water samples analysis

Wells water samples were characterized using the physico-chemical methods according to Romanian legislation (Laws 458/2002, 311/2004). The following water quality parameters were determined: temporary hardness (dH_t) and total hardness (dH_t) in degrees German (°dH), pH, chemical oxygen demand (COD-Mn) in mg $KMnO_4$ mg/L, solid residue (mg/L), electrical conductivity (µS/cm), Mn, Fe_{total}, NO_2^-, NH_4^+ (mg/L). pH and electrical conductivity were determined using a Consort C863 pH meter (SR ISO 10523/96, SR ISO 7887/97). Total dissolved solids (TDS) were determined using gravimetric method (Romanian STAS 3638/76). Temporary and total hardness and chemical oxygen demand were determined by volumetric method (Romanian STAS 7313-82, STAS 3326-76, STAS 3002-85). Concentration of Mn^{2+}, Fe_{total}, NO_2^- and NH_4^+ were determined using molecular absorption (SR 8662-1, 2/96, SR 13315/96, STAS 3048/2-96, STAS 6328/85) using an UV VIS Spectrometer Jenway 6305. Each sample was measured three times, the averaged values were presented.
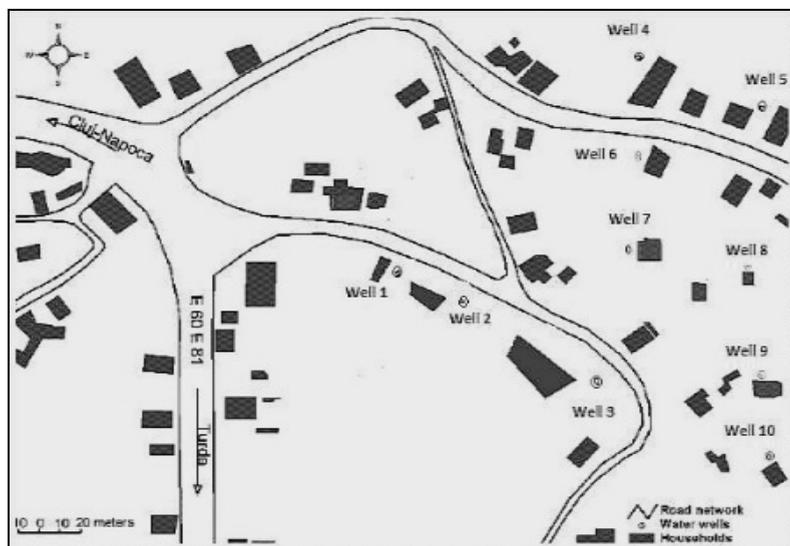
Figure 5. Location of the water wells, Feleacu village, Cluj County.

REFERENCES

1. M. Chiba, A. Sinohara, M. Sekine, *Journal of Radioanalytical and Nuclear Chemistry*, **2006**, *269*, 526.
2. M. Mănescu, "Poluarea apelor subterane: studii de caz", Editura Orizonturi Universitare, Timişoara, **2002**, 240.
3. A. Cineti, "Resursele de ape subterane ale României", Editura Tehnică, Bucureşti, **1999**, 296.
4. Y. Ranran, C. Baoshan, *Procedia Environmental* Sciences, **2010**, *2*, 1745.
5. M.A. Barron, L. Haber, A. Maier, J. Zhao, M.Burron, "Toxicological review of phenol" EPA/635/R-02/006, **2002**.
6. Ordin nr. 161 din 16/02/**2006** pentru aprobarea Normativului privind clasificarea calităţii apelor de suprafaţă în vederea stabilirii stării ecologice a corpurilor de apă.
7. M. Sabio, F. Zamora, J. Gañan, C.M. González-García, J.F. González, *Water Research*, **2006**, *40*, 3053.
8. Y.S. Li, Archives of *Environmental Contamination* and *Toxicology*, **1996**, *31*, 562.
9. S. Cater, M. Stefan, J. Bolton, A. Safarzadeh-Amiri, *Environmental Science* & *Technology*, **2000**, *34*, 659.
10. J. Anotai, M-CH. Lu, P. Chewpreecha, *Water Research*, **2006**, *40*, 1841.
11. L. Bissey, J. Smith, R. Watts, *Water Research*, **2006**, *40*, 2463.
12. World Health Report **2007**, "A safer future: global public health security in the 21st century", World Health Organization, 1211 Geneva 27, Switzerland.
13. M Tokumura, A. Ohta, H. Znad, Y. Kawase, *Water Research*, **2006**, *40*, 3775.
14. J. Casado, J. Fornaguera, M.I. Galán, *Water Research*, **2006**, *40*, 2511.
15. Z. Guojun, J. Shulan, X. Beidou, *Desalination,* **2006**, *196,* 32.
16. Z. Kassam, L. Yerushalmi, S. Guiota, *Water, Air & Soil Pollution*, **2003**, *143*, 179.
17. M. Sanchez-Polo, J. Rivera-Utrilla, U. Gunten, *Water Research*, **2006**, *40*, 3375.
18. J. Rivera-Utrilla, J. Méndez-Díaz, M. Sánchez-Polo, M.A. Ferro-García, I. Bautista-Toledo, *Water Research*, **2006**, *40*, 1717.
19. M. Stanca, A. Măicăneanu, C. Indolean, "Caracterizarea, valorificarea şi regenerarea principalelor materii prime din industria chimică şi petrochimică", Editura Presa Universitară Clujeană, Cluj-Napoca, **2007**, 22.
20. M. Ielenicz, "Dealurile şi podişurile României", Editura Fundaţiei „România de mâine", Bucureşti, **1999**, 244.
21. C. Baciu, "Hidrogeologie. Elemente teoretice şi aplicaţii practice", Editura Cărţii de Ştiinţă, Cluj-Napoca, **2004**, 151.
22. N. Mészáros, O. Clichici, "Pe poteci cu bănuţei de piatră: ghid geologic al zonei Cluj", Editura Tipored, Bucureşti, **1967**, 60.
23. C. Nertan, C. Roşu, *Environment & Progress*, **2010**, *12*, 293.
24. R. Dzhamalov, *Geology and Ecosystems*, **2009**, 183.

Dedicated to prof. dr. I. C. Popescu
on the occasion of his 70th anniversary

POROUS COLLAGEN SCAFFOLDS FOR BONE REGENERATION

ROXANA-DIANA PASCA[a,b], GHEORGHE TOMOAIA[b], AURORA MOCANU[a], IOAN PETEAN[a], ALEXANDRA-GERTRUD PALTINEAN[a], OLGA SORITAU[c], MARIA TOMOAIA-COTISEL[a,*]

ABSTRACT. This work presents an innovative procedure to fabricate collagen (COLL) structures with controlled porosity using Langmuir technique of building the self-assembled collagen structures, alone or in the presence of the cross linker APTES [(3-aminopropyl) triethoxy silane], at the interface between air and aqueous saline subphase. Then, at selected surface pressures, the COLL structures were transferred from the interface on solid substrate (glass or mica) by Langmuir-Blodgett (LB) technique, finally obtaining porous COLL scaffolds. The morphology and porosity of COLL scaffolds were characterized by atomic force microscopy (AFM). The porous COLL structures are densified progressively at higher silane concentrations and/or at higher surface pressures. Collagen scaffolds have high potential for use in bone regeneration and tissue engineering.

Keywords: Collagen type I, APTES, Langmuir-Blodgett technique, porous scaffolds, atomic force microscopy

INTRODUCTION

The cells interaction with scaffolds is deeply dependent on the surface characteristics, like topography, porosity and composition of scaffolds.

[a] *Babeş-Bolyai University of Cluj-Napoca, Faculty of Chemistry and Chemical Engineering, 11 Arany Janos str., RO-400028, Cluj-Napoca, Romania.*
[b] *Iuliu Hatieganu University of Medicine and Pharmacy, Orthopedic Department,47 Traian Mosoiu str., RO-400132, Cluj-Napoca, Romania.*
[c] *The Oncology Institute "Prof. Dr. Ion Chiricuta", 34-36 Republicii str.,RO-400015, Cluj-Napoca, Romania*
[*] *Corresponding author: mcotisel@chem,ubbcluj.ro, mcotisel@gmail.com*

To mimic the biological environment [1-4], we have chosen the type I collagen (COLL) for fabrication of scaffolds. Undoubtedly, COLL scaffolds possess strong advantages for use in regenerative medicine. However, the relatively reduced mechanical properties of COLL scaffolds appear to limit their utility in orthopedic medicine. This situation can be overcome through addition of a second phase [5-13], like hydroxyapatite (HAP), leading to composite scaffolds, or by using crosslinking approach applied to collagen fibers [14, 15]. However, the fibrous collagen scaffolds, fabricated at controlled surface pressures in the presence of APTES, are not yet reported. Therefore, to better control the pores architecture of scaffolds, in this work, we develop an innovative procedure to fabricate porous collagen scaffolds by self-assembling of collagen molecules, in the absence and the presence of APTES, which is recognized as a cross linker for collagen fibers [14, 15].

First, collagen molecules are self-assembled as a layer at the interface between air and aqueous solution of 2M NaCl, both in the absence and the presence of APTES, and characterized by compression isotherms, in terms of surface pressure versus mean molecular area of collagen [16-19]. Secondly, the collagen interfacial film is then transferred at a controlled surface pressure on the solid surface (like glass or mica) by Langmuir-Blodgett technique [20-22]. Further, the collagen transferred layers are analysed by AFM [23-29], to determine the role of APTES on the structure, morphology and porosity of resulted collagen scaffolds.

RESULTS AND DISCUSSION

The collagen (molecular) aqueous solution of pH 3 is very stable [30, 31]. This COLL acidic solution is spread on the aqueous subphase of 2M NaCl of pH 5.5. By spreading at the interface, the collagen molecules are coming into contact with the aqueous subphase of higher pH, causing them to self-assemble, rather than going into this subphase.

Fig. 1 shows compression isotherms of COLL layers, in the absence (Fig. 1A) and in the presence of APTES (Fig. 1B), spread on 2M NaCl solution. In the inset of Fig. 1B, the compression isotherm is given for APTES solely spread at the same interface air/aqueous solution. These isotherms demonstrate the interfacial behaviour of COLL (Fig. 1A), COLL-APTES (Fig. 1B) and APTES layers (inset of Fig. 1B) on the same saline subphase. Results show that self-assembled layers are highly stable and surface pressures are constant for many hours. Therefore, these layers are appropriate for transfer from the interface to solid substrate at selected surface pressures, generating porous COLL scaffolds.
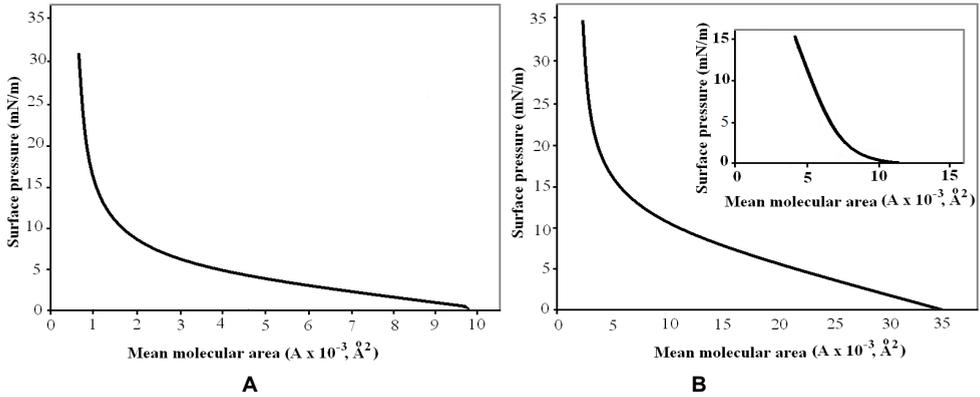
Figure 1. Compression isotherms for self-assembled layers: collagen (Fig. 1A), collagen cross-linked by APTES (Fig. 1B, for volume ratio, 1: 1, COLL-APTES) in aqueous solution used for layer spreading, and APTES (inset in Fig. 1B); each layer was spread at the interface between air and aqueous solution of 2M NaCl, at room temperature.

The compression isotherm (Fig. 1B) for the COLL-APTES layer is highly expanded than that for COLL layer (Fig. 1A). This effect can be related to the interaction of COLL and APTS in interfacial film, either by crosslinking COLL fibrils into COLL fibers or by forming COLL and APTES complexes at the interface. The stability of COLL-APTES layers is higher, as exemplified by the highest surface pressure, like 35 mN/m, which is easily obtained. Additionally, the stable COLL-APTES layers can be also formed directly on water, suggesting that the salting out effect of saline subphase is not important in this case.
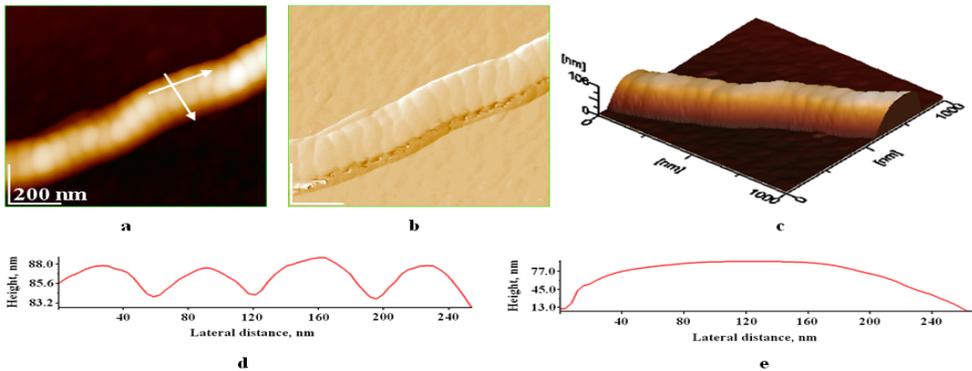
Figure 2. Collagen fiber transferred on glass substrate from the air/aqueous phase of 2M NaCl, at 30 mN/m. 2D topography (a), amplitude (b), 3D-topography (c), cross section profiles along the arrows in image (a), parallel with long axis of COL fiber (d) and perpendicular on COLL fiber (e). Scanned area 1 μm × 1 μm. Surface roughness (RMS) 32.3 nm, on scanned area (a).

The presence of 2 M NaCl in aqueous subphase (pH 5.5) is crucial for high stability of pure collagen self-assembled layers, due to the strong reduction in the COLL solubility in water. Thus, the collagen molecules are kept at the interface and accordingly, they are allowed to self-assemble in COLL fibers, as demonstrated in AFM images (Fig. 2).

The structure of COLL fibers, which are transferred at 30 mN/m from air/water interface is similar to the native banding structure of collagen fibers [24, 28, 29], obtained in different aqueous dispersions. Specifically, COLL molecules form long interfacial fibers (Fig. 2a-c) with strong periodicity of 65 nm along the long axis of COLL fibers (Fig. 2d), in substantial agreement with reported data for native banding in the COLL fibers [24, 28]. Increasing the transfer surface pressures, collagen fibers are better packed at the air/water interface, and consequently in the obtained fibrous COLL scaffolds. The increased surface pressures seem to enhance the native banding in the COLL fibers, rather than to affect the width of the COLL fibers (Fig. 2e).
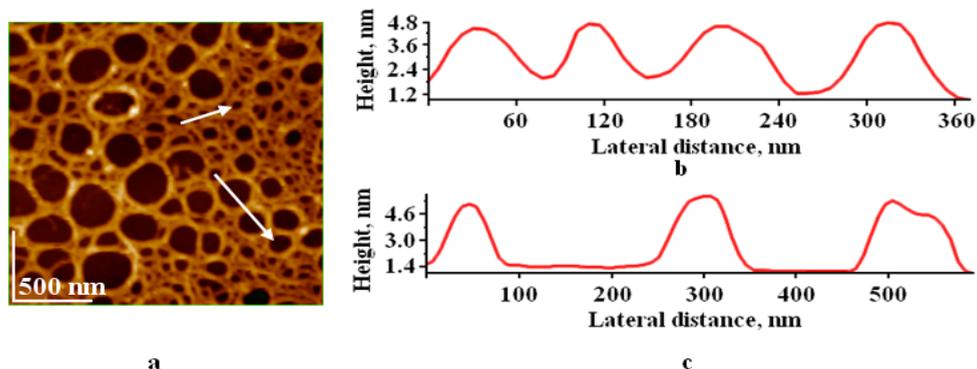
Figure 3A. 2D-topography image (a) on LB layer of collagen-APTES self- assembled patterns for volume ratio, 1:1, used as spreading solution (Fig. 1B), transferred on glass from aqueous phase of 2M NaCl, at 15 mN/m. 2D-topography (a); two cross section profiles (b and c), along the 2 arrows given in image (a); Scanned area 2 μm × 2 μm; RMS 1.7 nm on scanned area (a). Average pore diameters (b and c), from about 90 nm to 150 nm.

In the presence of APTES, collagen molecules formed a complex tight network of strongly interwoven strands, as observed by AFM imaging (Figs. 3-5). The size and the density of pores are strongly dependent on the APTES concentrations in the spreading aqueous solution of collagen, at the air/water interface, and on the surface pressures (Figs 3-5) used to transfer the COLL-APTES self-assembled layers on solid substrates (e.g., glass or mica). The generated interfacial COLL-APTES structures are porous and transferred on solid substrate lead to the COLL-APTES porous scaffolds, which are completely different than those formed from COLL fibers (Fig. 2).
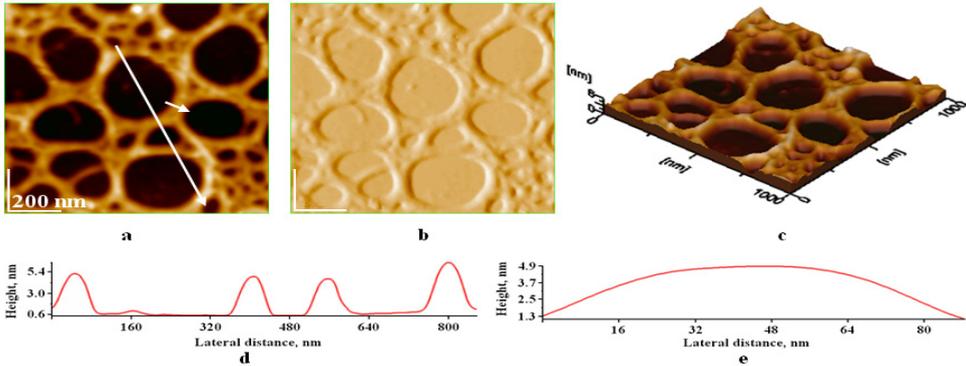
Figure 3B. COLL-APTES self-assembled patterns. 2D- topography (a), amplitude (b), 3D topography (c); two cross section profiles (d and e), along the 2 arrows given in image (a); Scanned area 1μm × 1μm; RMS 1.9 nm on scanned area (a). Details as in Fig. 3A. Porous layer analysis: average pore diameters (d), from about 40 nm, 150 nm to 240 nm. COLL fiber thickness is almost constant of about 70 ± 6 nm (an example is given in (e) cross section profile.
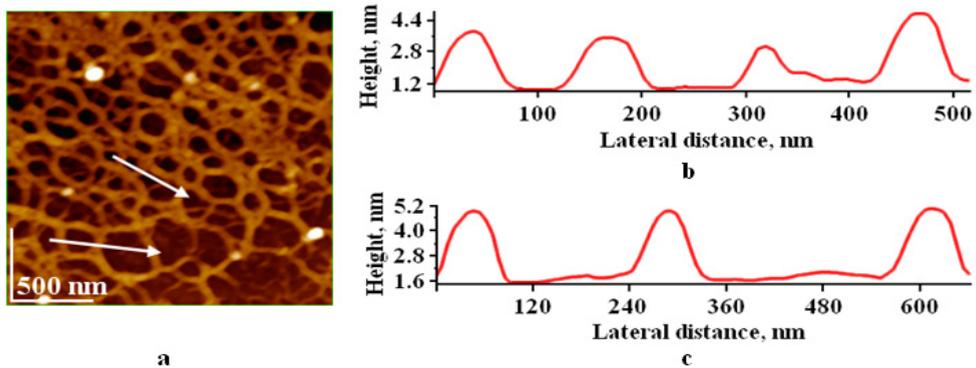
Figure 4. Collagen-APTES self-assembled patterns, for volume ratio of 1:2, used in spreading solution, at the air/water interface. AFM images on LB layer transferred on glass, at 25 mN/m: 2D-topography (a); two cross section profiles (b and c), along the 2 arrows given in image (a). Scanned area 2 μm × 2 μm. RMS 1.5 nm. Average pore diameters (b and c), from about 30 nm, 160 nm to 210 nm. COLL fiber thickness is almost constant of about 70 ± 8 nm.

Another important characteristic of porous COLL scaffolds obtained in presence of APTES is related to their very low surface roughness, as given by the root mean square, RMS, measured by AFM of about 1 or 2 nm, for the outmost layer of scaffold. These porous COLL-APTES scaffolds are rather smooth in comparison with the fibrous COLL scaffolds, where

RMS was much higher (Fig. 2). Thus, by using LB technique it is possible to monitor the morphology, porosity and surface roughness of different types of porous collagen scaffolds.
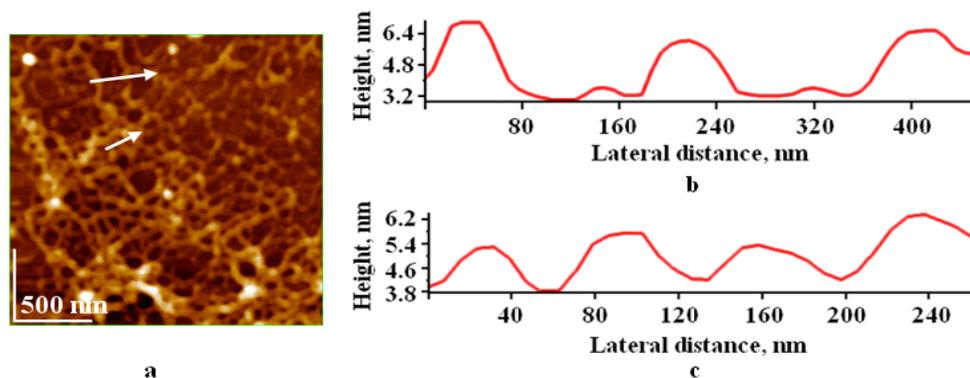
Figure 5. Collagen- APTES self-assembled patterns, for volume ratio of 1:3, used in spreading solution. AFM images on LB layer transferred on glass from air/water interface, at 35 mN/m. 2D-topography (a); two cross section profiles (b and c), along the 2 arrows given in image (a); Scanned area 2 μm × 2 μm; RMS 1.7 nm. Average pore diameters (b and c), from about 20 nm, 80 nm to 140 nm. COLL fiber thickness is almost constant of about 70 ± 10 nm.

CONCLUSIONS

This methodology used to obtain collagen scaffolds of controlled porosity represents an experimental premier in nanotechnology of mimetic scaffolds. The potential of porous collagen scaffolds for use as bone scaffolds will be further assessed in human osteoblasts culture in terms of cell adhesion, proliferation and differentiation. Preliminary results clearly indicate that these scaffolds mimic the extracellular matrix and show a higher cell adhesion, proliferation and differentiation than scaffolds with hydroxyapatite alone. These findings also suggest that the porous combined scaffolds made of nanostructured collagen fibers mineralized with hydroxyapatite and silanized with APTES could have high promises for use in the bone regeneration, hard tissue engineering and orthopedic applications.

EXPERIMENTAL SECTION

Collagen type I, from bovine Achilles tendon (MW 300 kD) and 3-aminopropyl triethoxysilane (APTES), each of the highest purity, were purchased from Sigma-Aldrich (Steinheim, Germany) and used as received. Acetic acid and sodium chloride pro analysis were purchased from Merck

(Darmstadt, Germany). Ultra pure deionized water with a resistivity greater than 18 MΩ·cm at 25°C was obtained from an Elga apparatus and used in all experiments [16-19]. Its pH was 5.5 and its surface tension was higher than 71.8 mN/m at 25°C. Optically polished glass (hydrophilic) and mica (freshly cleaved) were used as solid supports in the Langmuir-Blodgett transfer process, as shown elsewhere [20-22].

Collagen was dissolved in about 0.2 M acetic acid (at pH 3) to a concentration range from 0.5 mg/ml to 1 mg/ml. The collagen aqueous solution was spread drop-wise at the air/aqueous saline solution (e.g., 2M NaCl) interface, directly in Langmuir trough [16-19]. The layer was generally allowed to equilibrate for 10 min up to 1 hour after spreading. Then, the collagen layer at the air/water interface was compressed at constant speed of 10 mm/min, and the compression isotherm was recorded by using the balance KSV 5000 [20-22]. The accuracy of the measurements is ± 0.1 mN/m. At a constant surface pressure, in the range from 15 mN/m to 35 mN/m, the collagen layer was transferred from air/water interface on hydrophilic glass or mica by Langmuir-Blodgett technique [20-22]. Further, the collagen scaffolds comprising glass or mica substrates covered by the self-assembled layer of collagen, in the absence or the presence of APTES, were dried in air and imaged by AFM [23-29].

ACKNOWLEDGMENTS

REFERENCES

1. G.M. Cunniffe, F.J. O'Brien, *Journal of Metals (JOM)*, **2011**, *63*, 66.
2. K. Anselme, *Biomaterials*, **2000**, *21*, 667.
3. J. Dobkowski, R. Kolos, J. Kaminski, H.M. Kowalczynska, *Journal of Biomedical Materials Research*, **1999**, *47*, 234.
4. A.E. Sorkio, E.P. Vuorimaa-Laukkanen, H.M. Hakola, H. Liang, T.A. Ujula, J.J. Valle-Delgado, M. Österberg, M.L. Yliperttula, H. Skottman, *Biomaterials*, **2015**, *51*, 257.
5. J. Ni, M. Wang, *Materials Science and Engineering C*, **2002**, *20*, 101.
6. Y. Liu, M. Wang, *Current Applied Physics*, **2007**, *7*, 547.
7. I. Sopyan, M. Mel, S. Ramesh, K.A. Khalid, *Science and Technology of Advanced Materials,* **2007**, *8*, 116.
8. G. Tomoaia, A. Mocanu, I. Vida-Simiti, N. Jumate, L.-D. Bobos, O. Soritau, M. Tomoaia-Cotisel, *Materials Science and Engineering* C, **2014**, *37*, 37.

9. A. Mocanu, G. Furtos, S. Rapuntean, O. Horovitz, C. Flore, C. Garbo, A. Danisteanu, Gh. Rapuntean, C. Prejmerean, M. Tomoaia-Cotisel, *Applied Surface Science*, **2014**, *298*, 225.
10. G. Tomoaia, O. Soritau, M. Tomoaia-Cotisel, L.-B. Pop, A. Pop, A. Mocanu, O. Horovitz, L.-D. Bobos, *Powder Technology,* **2013**, *238*, 99.
11. G. Tomoaia, L.-B. Pop, I. Petean, M. Tomoaia-Cotisel, *Materiale Plastice,* **2012**, *49*, 48.
12. G. Tomoaia, M. Tomoaia-Cotisel, L.-B. Pop, A. Pop, O. Horovitz, A. Mocanu, N. Jumate, L.-D. Bobos, *Revue Roumaine de Chimie,* **2011***, 56*, 1039.
13. J. Brandt, S. Henning, G. Michler, W. Hein, A. Bernstein, M. Schulz, *Journal of Materials Science: Materials in Medicine,* **2010**, *21*, 283.
14. R.N. Raghavan, T. Muthukumar, N. Somanathan, T.P. Sastry, *Materials Science and Engineering C,* **2013**, *33*, 1983.
15. J.-Y. Baek, Z.-C. Xing, G. Kwak, K.-B. Yoon, S.-Y. Park, L. S. Park, I.-K. Kang, *Journal of Nanomaterials,* **2012**, *2012,* 171804.
16. M. Tomoaia-Cotisel, A. Sen, P.J. Quinn, *Journal of Colloid and Interface Science,* **1983***, 94*, 390.
17. J. Zsako, M. Tomoaia-Cotisel, E. Chifu, *Journal of Colloid and Interface Science,* **1984***, 102*, 186.
18. A. Mocanu, R.-D. Pasca, O. Horovitz, M. Tomoaia-Cotisel, *Studia UBB Chemia*, **2010**, *55*, 303.
19. M. Tomoaia-Cotisel, R.-D. Pasca, O. Horovitz, A. Mocanu, *Revue Roumaine de Chimie,* **2011**, *56,* 1047.
20. M. Tomoaia-Cotisel, A. Mocanu, *Revista de Chimie (Bucharest),* **2008**, *59*, 1230.
21. M. Tomoaia-Cotisel, G. Tomoaia, V.-D. Pop, A. Mocanu, O. Cozar, N. Apetroaei, Gh. Popa, *Studia UBB Physica*, **2004**, *49*, 141.
22. L.J. Noe, M. Tomoaia-Cotisel, M. Casstevens, P.N. Prasad, *Thin Solid Films*, **1992**, *208*, 274.
23. O. Horovitz, G. Tomoaia, A. Mocanu, T. Yupsanis, M. Tomoaia-Cotisel, *Gold Bulletin*, **2007**, *40*, 295.
24. S. Strasser, A. Zink, M. Janko, W.M. Heckl, S. Thalhammer, *Biochemical and Biophysical Research Communications,* **2007**, *354,* 27.
25. S.E. Woodcock, W.C. Johnson, Z. Chen, *Journal of Colloid and Interface Science*, **2005**, *292,* 99.
26. Y.F. Dufrene, T.G. Marchal, P.G. Rouxhet, *Langmuir,* **1999**, *15,* 2871.
27. L. Pastorino, E. Dellacasa, S. Scaglione, M. Giulianelli, F. Sbrana, M. Vassalli, C. Ruggiero, *Colloids and Surfaces B: Biointerfaces,* **2014***, 114*, 372.
28. G. Tomoaia, M. Tomoaia-Cotisel, A. Mocanu, O. Horovitz, L.-D. Bobos, M. Crisan, I. Petean, *Journal of Optoelectronics and Advanced Materials,* **2008**, *10*, 961.
29. L.-D. Bobos, G. Tomoaia, Cs. Racz, A. Mocanu, O. Horovitz, I. Petean, M. Tomoaia-Cotisel, *Studia UBB Chemia*, **2008**, *53*, 99.
30. A.J.J. Goffin, J. Rajadas, G.G. Fuller, *Langmuir,* **2010**, *26*, 3514.
31. F. Jiang, H. Horber, J. Howard, D.J. Muller, *Journal of Structural Biology*, **2004**, *148*, 268.

Dedicated to prof. dr. I. C. Popescu
on the occasion of his 70th anniversary

BIOCOMPOSITES FOR ORTHOPEDIC APPLICATIONS

GHEORGHE TOMOAIA[a], AURORA MOCANU[b], LIVIU-DOREL BOBOS[b], LACRIMIOARA-BIANCA POP[b], OSSI HOROVITZ[b], MARIA TOMOAIA-COTISEL[b,*]

ABSTRACT. A complex nano-hydroxyapatite (HAP) with.0.6 wt% Mg, 0.2 wt% Zn and 0.2 wt% Si was synthesized by the precipitation method. Composites of HAP with collagen (HAP-COL), HAP with chitosan (HAP-CHI) and HAP-COL-CHI were also prepared. The obtained biomaterials were characterized by X-ray diffraction (XRD), FTIR and FT-Raman spectroscopy, and by transmission electron microscopy (TEM) imaging. These biocomposites are potentially useful for hard tissue repairs and orthopedic applications.

Keywords: nano-hydroxypatite, collagen, chitosan, composites.

INTRODUCTION

Bones are formed mainly from hydroxyapatite, $Ca_{10}(PO_4)_6(OH)_2$ (HAP) and collagen, mostly type I collagen (COL). Therefore, HAP-COL composites are able to mimic skeletal bones and consequently, they are suitable to be used as bone substitutes [1]. The properties of such biocomposites depend on the manufacturing conditions and crosslinking agents [2]. Chitosan (CHI), a polysaccharide containing N-acetyl glucosamine and glucosamine units can also be used in bone tissue engineering, due to its biodegradability, biocompatibility, capacity to form structures suitable for cell ingrowth and osteoconduction [3]. Moreover, it is shown that COL and CHI as well as multi-substituted HAP significantly inhibit the growth of bacterial pathogens, which is the major cause of prosthesis related infections [4].

[a] *Iuliu Hatieganu University of Medicine and Pharmacy, Orthopedic Department, 47 Traian Mosoiu str., RO-400132, Cluj-Napoca, Romania*
[b] *Babeş-Bolyai University, Faculty of Chemistry and Chemical Engineering, 11 Arany Janos str., RO-400028, Cluj-Napoca, Romania*
* *Corresponding author: mcotisel@chem,ubbcluj.ro mcotisel@gmail.com*

Consequently, this work is focused on the development of novel biocomposites for orthopaedic applications, with ability to promote specific cellular response at molecular level with minimally invasive surgery. In the following, we present an improved method to build homogeneous biocomposites made of HAP and COL (HAP-COL), HAP and chitosan (HAP-CHI) and HAP-COL-CHI, for different weight ratios. The used hydroxyapatite is a substituted nano-hydroxyapatite (HAP), with.0.6 wt% Mg, 0.2 wt% Zn and 0.2 wt% Si, which possesses an improved bioactivity, leading to a better osteointegration [5-10].

RESULTS AND DISCUSSION

The *X-ray diffraction patterns* of HAP powder calcined at 650° C for 6 hours (Fig. 1a) show the high crystallinity degree of this powder while both COL and CHI present an amorphous structure (Fig. 1b). All the composites HAP-CHI, HAP-COL and HAP-CHI-COL showed diffraction patterns (Fig. 1c) and crystallinity similar to the HAP powder.

a.   b.

c.
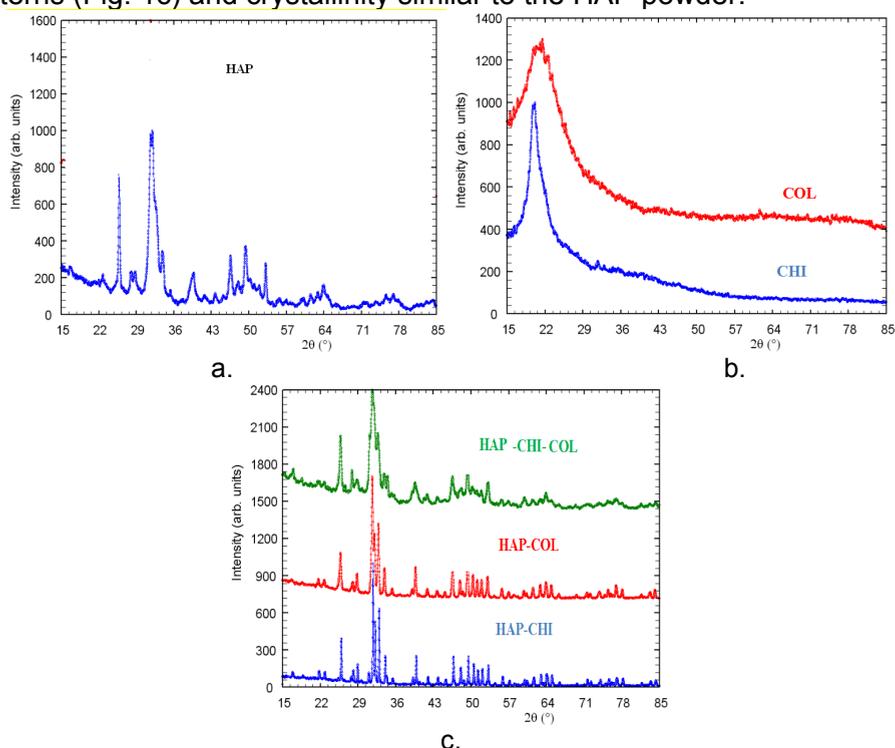
Figure 1. X- Ray powder diffraction patterns of HAP (calcined at 650 ºC) (a), COL and CHI samples (b), and HAP-CHI (93:7), HAP-COL (70:30) and HAP-CHI-COL (68.5 :5.5 :26) powders (c).

FTIR spectra are compared in Fig. 2. The spectrum of the *hydroxyapatite* with 0.2% Si, 0.6% Mg and 0.2% Zn presents the usual phosphate bands; the most intense is the P-O stretching vibration band, v_3 [11] (maxima at 1033 and 1094 cm^{-1}). The P-O bend vibration band, v_4 [12] shows maxima at 564 and 603 cm^{-1}, while the maximum at 633 cm^{-1} is assigned to the structural OH (libration vibration). In the 4000-3000 cm^{-1} region, we find absorption bands originating from H-O vibrations: the broad band (maximum at 3434 cm^{-1}) due to absorbed water with hydrogen bonding O-H…O [13], overlapped with the band of structural OH (from hydroxyapatite) at 3570 cm^{-1} [14]. The band with the maximum at 1636 cm^{-1} is also due to absorbed water [14].
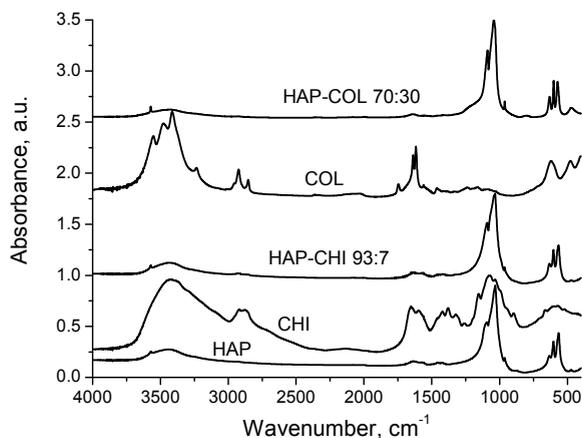
Figure 2. FTIR spectra of HAP, CHI, HAP-CHI, COL, and HAP-COL

Chitosan has a backbone similar to cellulose, but containing NH$_2$ groups which partially substitute the OH groups. It can also contain N-acetyl groups, -NH-CO-CH$_3$, if the deacylation of chitin was not complete. The large band at 3000-3500 cm^{-1} is due to hydrogen bonded O-H and N-H stretching vibrations (maximum at 3425 cm^{-1}). The peaks at 2917 and 2877 cm^{-1} are characteristic of the C-H vibration [15]. The peaks at 1648 and 1597 cm^{-1} correspond to the amide I (C=O stretching) and amide II (N-H bending) bands respectively [16] from the residual -NH-CO-CH$_3$ groups. The amide III band, assigned to C-N stretching and C-N-H bending, appears at 1324 cm^{-1} [17]. The peak at 1377 cm^{-1} is the characteristic band of CH$_3$ symmetrical deformation mode. The broad band with peaks at 1073 and 1154 appears from the C-O-C stretching vibration characteristic for polysaccharide structure of chitosan [18-20].

The *HAP-CHI composite* sample presents absorption bands arising from HAP and CHI, while the peaks due to CHI are rather small, since the proportion of CHI in the composite is low. For instance, the phosphate peak is shifted from 1094 to 1092 cm^{-1} due the superposition of the C-O-C peak of chitosan (1073 cm^{-1}). Since TEOS was used as crosslinking agent for chitosan/collagen and hydroxyapatite, the small absorption peak at 769 cm^{-1} could be related to the formation of hydrogen bonds between silanol (Si-OH) groups of the silica network and amide- and oxy-groups of chitosan. Other small peaks in the region of 1223 cm^{-1} show characteristic absorption for the Si–O–Si band [15].

Collagen, a protein composed mainly from the amino acids glycine, proline, and hydroxyproline, also presents the large band at 3300-3600 cm^{-1} for hydrogen bonded O-H and N-H vibrations (the highest peak at 3414 cm^{-1}). The C-H stretching vibrations in CH_3 and CH_3 groups are responsible for the peaks at 2924 and 2853 cm^{-1} [16, 21]. Amide I band appears at 1638, amide II at 1569 and CH_2 wagging and deformation at 1617 cm^{-1} [22, 23]. The absorption at 1084 cm^{-1} arises from C-OH stretching vibrations [22].

As in the case of HAP-CHI, the *HAP-COL composite* presents a FTIR spectrum similar to that of HAP, with slight shifts in the maxima, due to the interactions with COL. The new band appeared at 800 cm^{-1} indicates the presence of Si-OH groups in the hybrid system HAP-COL. The FTIR spectrum of HAP-COL-CHI composite (not presented) is similar to the spectra of the HAP-COL and HAP-CHI composites.

The *FT Raman spectra* (Fig. 3) complete the information furnished by FTIR spectroscopy, since some vibrational modes inactive or weakly manifested in FTIR spectra are more visible in Raman spectra. For *HAP*, the most intense band is that corresponding to the symmetric stretching mode (v_1) of the PO_4 group, which was inactive in FTIR; it is situated at 969 cm^{-1}. The v_3 mode, dominant in the FTIR spectra, is here represented by two weak peaks at 1015 and 1087 cm^{-1}. Other vibration modes of the PO_4 group are present: v_4 with three distinct peaks in the domain 546-610 cm^{-1}, and v_2 at 405 and 438 cm^{-1}.

The Raman spectrum of *chitosan* presents a low-intensity doublet at 1589 and 1601 cm^{-1}, assigned to the scissoring vibration of NH_2 groups. The main peak, at 2885 cm^{-1} is attributed to the stretching vibrations of CH groups [24], while that at 3301 cm^{-1} represents the vibrations of N-H bonds. The band with the peak at 1375 cm^{-1} corresponds to the CH_3 symmetrical deformation mode.

In the HAP-CHI composite, the intense phosphate band of apatite, with maximum at 961 nm, is present, while the bands of chitosan are barely visible, due to its small proportion. A new broad high-intensity band appears (maximum at 769 cm^{-1}, with a shoulder at about 700 cm^{-1}).
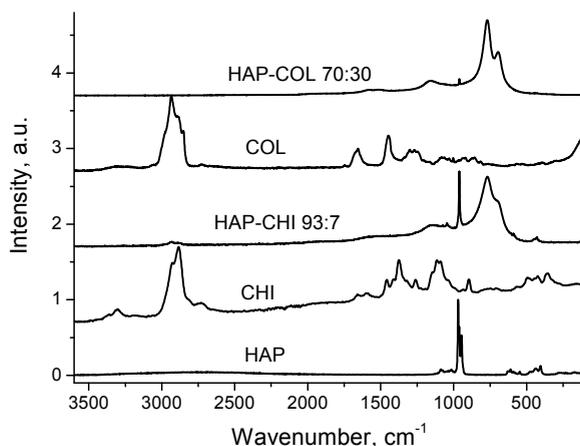
Figure 3. FT-Raman spectra of HAP, CHI, HAP-CHI, COL, and HAP-COL

For *collagen,* in the Raman spectrum, the most important band, at 2935 cm^{-1} is associated with CH_3 and CH_2 deformations, and so is the 1448 cm^{-1} band [25]. N-H stretching contributes to the 3290 cm^{-1} peak. The amide I band appears at 1655, and the amide III band at 1269 cm^{-1} [26].

In the Raman spectrum of the HAP-COL composite, the bands of HAP are considerably attenuated (e.g. the phosphate band at 961 cm^{-1}). and so are the COL bands. As for the HAP-CHI composite, a new intense band appears, with maxima at 770 and 695 cm^{-1}. These bands are probably due to the cross linking generated by TEOS.

Observations from *TEM micrographs* (Fig. 4) reveal that HAP and its composites with COL and CHI, present similar rod like structures (acicular particles*),* with average width 11 nm, and average length 37 nm.

CONCLUSIONS

A multi substituted nano-hydroxyapatite with Mg, Zn and Si was prepared and presents a characteristic acicular structure. Its binary and ternary composites with collagen and/or chitosan were obtained using TEOS as a binding agent. The acicular aspect of HAP nano-particles was preserved in obtained biocomposites (HAP-COL, HAP-CHI and HAP-CHI-COL), as judged by TEM images. The interactions among the components are revealed by FTIR and FT-Raman spectroscopy. Mechanical and biological tests on scaffolds made from these biomaterials are now under investigation in order to further develop biocomposites to be used as new bone substitutes with improved biocompatibility. In vitro cell culture studies are the centre of our future research to continue the biocomposites development, for dental and orthopaedic applications.

a   b

c   d
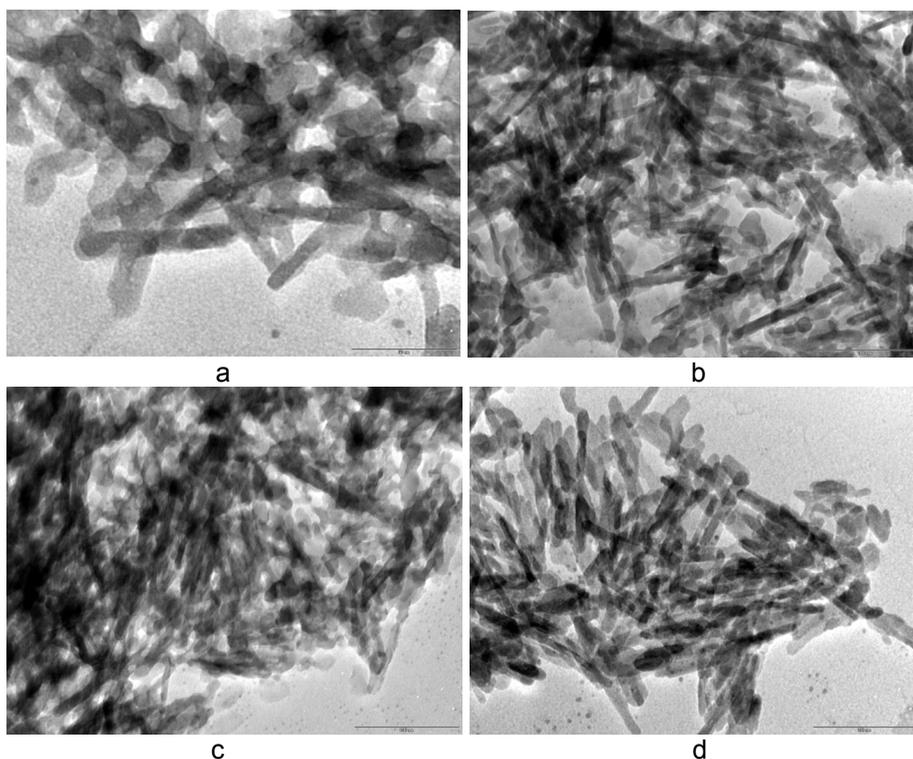
Figure 4. Representative TEM images of HAP powder after thermal treatment at 650°C (a); HAP-CHI (b); HAP-COL (c) and HAP-CHI-COL (d).

EXPERIMENTAL SECTION

Materials. Calcium nitrate hydrated, $Ca(NO_3)_2 \cdot 4H_2O$, diammonium hydrogen phosphate, $(NH_4)_2HPO_4$, magnesium nitrate hexahydrate, $Mg(NO_3)_2 \cdot 6H_2O$, all p.a. products, tetraethyl orthosilicate **(**TEOS*, 98 wt%***)***, ethanol, nonylphenol, 4-(2,6-dimethylheptan-4-yl)phenol, and acetic acid were purchased from Merck; zinc nitrate hexahydrate, $Zn(NO_3)_2 \cdot 6H_2O$, purum 99%, sodium silicate (molar $Na_2O:SiO_2$ ratio of 1:3.2), and ammonia solution (25%), collagen type I (COL) and chitosan (medium molecular weight), were obtained from Sigma-Aldrich.

Syntheses: Nano-hydroxyapatite modified with silicon, magnesium and zinc (HAP) was prepared by co-precipitation method. A solution containing calcium nitrate, nonylphenol (as surfactant), magnesium and zinc nitrates (for a final 0.6 wt% Mg, and 0.2 wt% Zn content in the HAP powder) was prepared (pH 6.3). Another solution contained $(NH_4)_2HPO_4$, nonylphenol, sodium silicate ($Na_2O:SiO_2$ molar ratio 1:3.2) for a final 0.2 wt% Si content in HAP; the pH was adjusted to 11.5 by adding 25% ammonia solution. The two solutions with a

Ca/P molar ratio 5/3, corresponding to that in stoichiometric hydroxyapatite, were mixed (2-3 sec) at 60°C under vigorous stirring (800 rpm). The reaction mixture was stirred for 24 h at 70°C for maturation, allowing the calcium phosphates, precursors to HAP, to nucleate and grow, the process being controlled by the presence of nonylphenol. The precipitate was separated by filtration, washed with distilled water until no NO_3^- ions were detected, and dried by lyophilization (Alpha 1-2 LDplus Freeze Dryer) to avoid particles agglomeration and then calcined at 650 °C for 6 h.

HAP-COL composite was prepared from a 2% wt. collagen solution in 1% acetic acid (pH 2.5 – 3), with a TEOS solution in ethyl alcohol, mixed with calcined HAP powder under intense stirring for 24 h (pH 7, adjusted with 10% sodium hydroxide solution). The HAP/COL ratio was 70:30. The precipitate obtained was kept under continuous stirring at room temperature for 24 h and then it was dried by lyophilization. *HAP-CHI composite* was obtained by the same procedure from a 2% wt. chitosan solution in 1% acetic acid (pH 3.5), with TEOS solution and HAP powder (pH 7 adjusted with 10% NaOH solution). The HAP/ CHI ratio was 93:7. The *HAP-CHI-COL biocomposite* was obtained analogously by coprecipitation from a 2% collagen solution (pH 3-3.5), a 2% chitosan solution (pH 3.5) and HAP powder, with TEOS solution and HAP powder (pH 7 adjusted with 10% NaOH solution). The composite contained 68.5% HAP, 26% COL and 5.5% CHI.

Nanopowders characterization. X-ray diffraction measurements were carried out on a DRON 3 type diffractometer, in Bragg-Brentano geometry and applying CuK$_\alpha$ radiation at 25 kV and 20 mA. *FT-IR spectra* were obtained with a JASCO 6100 FTIR spectrophotometer in the 4000-400cm^{-1} spectral domain with a resolution of 4 cm^{-1} by using KBr pellet technique. *FT Raman spectra* were obtained with a the FRA 106/S FT-Raman Module attached to Bruker EQUINOX 55; an Nd:YAG laser was used (wavelength 1064 nm) and a liquid nitrogen cooled germanium detector (D418-T). The spectra were recorded for wave numbers below 3600 cm^{-1} with resolution 2 cm^{-1}. *Transmission electron microscopy* (TEM: JEOL-JEM 1010, Japan) images have been recorded with JEOL standard software.

ACKNOWLEDGMENTS

REFERENCES

1. D.A. Wahl, J.T. Czernuszka, *European Cells and Materials*, **2006**, *11*, 43.
2. P. Angele, J. Abke, R. Kujat, H. Faltermeier, D. Schumann, M. Nehrlich, B. Kinner, C. Englert, Z. Ruszczak, R. Mehrl, R. Mueller, *Biomaterials*, **2004**, *25*, 2831.

3. J. Venkatesan, S.K. Kim, *Marine Drugs,* **2010**, *8*, 2252.
4. G.A. Carlson, J.L. Dragoo, B. Samimi, D.A. Bruckner, G.W. Bernard, M. Hedrick, P. Benhaim, *Biochemical and Biophysical Research Communications*, **2004**, *321*, 472.
5. S.L. Seet, *Science Asia*, **2009**, *35*, 255.
6. G. Tomoaia, A. Mocanu, I. Vida-Simiti, N. Jumate, L.D. Bobos, O. Soritau, M. Tomoaia-Cotisel, *Materials Science and Engineering C*, **2014**, *37*, 37.
7. S.J. Kalita, H.A. Bhatt, *Materials Science and Engineering*: C, **2007**, *27*, 837.
8. G. Tomoaia, M. Tomoaia-Cotisel, L.B. Pop, A. Pop, O. Horovitz, A. Mocanu, N. Jumate, L.-D. Bobos, *Revue Roumaine de Chimie*, **2011**, *56*, 1039.
9. G. Tomoaia, O. Soritau, M. Tomoaia-Cotisel, L.-B. Pop, A. Pop, A. Mocanu, O. Horovitz, L.-D. Bobos, *Powder Technology*, **2013**, *238*, 99.
10. A. Mocanu, G. Furtos, S. Rapuntean, O. Horovitz, C. Flore, C. Garbo, A. Danisteanu, G. Rapuntean, C. Prejmerean, M. Tomoaia-Cotisel, *Applied Surface Science*, **2014**, *298*, 225.
11. V.M. Bhatnagar, *Experientia*, **1967,** *23*, 10.
12. C.B. Baddiel, E.E. Berry, *Spectrochimica Acta*, **1966**, *22*, 1407.
13. A. Sionkowska, J. Kozłowska, *International Journal of Biological Macromolecules*, **2010**, *47*, 483.
14. A.Y.P. Mateus, C.C. Barrias, C. Ribeiro, M.P. Ferraz, F.J. Monteiro, *Journal of Biomedical Materials Research Part A*, **2008**, *86A*, 483.
15. F. Al-Sagheer, S. Muslim, *Journal of Nanomaterials*, **2010**, Article ID 490679, 7 pages, doi:10.1155/2010/490679.
16. A. Sionkowska, M. Wisniewski, J. Skopinska, D. Mantovani, *International Journal of Photoenergy*, **2006**, Article ID 29196, p. 1-6.
17. M. Miya, R. Iwamoto, S. Yoshikawa, S. Mima, *International Journal of Biological Macromolecules*,**1980**, *2*, 323.
18. E. de Souza Costa-Júnior, M.M. Pereira, H.S. Mansur, *Journal of Materials* Science*: Materials in Medicine*, **2009**, *20*, 553.
19. K.S.V. Krishna Rao, B.V. Kumar Naidu, M.C.S Subha, M. Sairam, T.M. Aminabhavi, *Carbohydrate Polymers*, **2006**, *66*, 333.
20. C. Radhakumary, G. Divya, P.D. Nair, S. Mathew, C.P. Reghunadhan Nair, *Journal of Macromolecular Science Part A- Pure and Applied Chemistry*, **2003**, *40*, 715.
21. A. Sionkowska, M. Wisniewski, J. Skopinska, C.J. Kennedy, T.J. Wess. *Journal of Photochemistry and Photobiology A: Chemistry*, **2004**, *162*, 545.
22. C. Petibois, G. Gouspillou, K, Wehbe, J.P. Delage, G. Déléris, *Analytical and Bioanalytical Chemistry*, **2006**, *386*, 1961.
23. G. Socrates, "Infrared and Raman Characteristic Group Frequencies. Tables and Charts", J. Wiley and Sons Ltd., UK, **2004**.
24. K. Zhang, J. Helm, D. Peschel, M. Gruner, T. Groth, S. Fischer, *Polymer*, **2010**, *51*, 4698.
25. C. Gullekson, L. Lucas, K. Hewitt, L. Kreplak, *Biophysical Journal*, **2011**, *100*, 1837.
26. B.G. Frushour, J.L. Koenig, *Biopolymers*, **1975**, *14*, 379.

Dedicated to prof. dr. I. C. Popescu
on the occasion of his 70th anniversary

COMMONLY USED RAW FRUIT AND VEGETABLE JUICES OVERALL ANTIOXIDANT ACTIVITY DETERMINATION BY MEANS OF BRIGGS-RAUSCHER REACTION

NORBERT MUNTEAN[a], GABRIELLA SZABÓ[a,*]

ABSTRACT. The antioxidant capacity of commonly used raw fruit and vegetable juices was determined by means of the Briggs-Rauscher oscillating system in batch conditions. Though it is very important to know the composition of a juice mixture sometimes it is not enough to predict the behavior, because of the interaction of the different components. Antioxidant mixtures can present discrepancy in their activity compared to the individual values of the different components. Inhibition times at different concentrations were determined for a number of juices; they presented a linear dependence *vs.* their concentration. The relative antioxidant activity of a mixture of juices was measured and compared to that of the individual juices and a synergistic effect was found.

Keywords: *Briggs-Rauscher oscillating reaction, inhibitory effect, analytical method, raw fruit juice antioxidant capacity*

INTRODUCTION

The Briggs-Rauscher (BR) oscillating reaction was described for the first time four decades ago [1] and represents the iodination and oxidation of malonic acid by iodate and hydrogen peroxide, catalyzed by manganous ion in acidic media. Several papers reported on the investigations regarding the mechanism of it [2-5]. According to their proposed skeleton mechanism the global reaction is the sum of a radical and a non-radical path.

---

[a] *Department of Chemistry and Chemical Engineering of Hungarian Line, "Babeş-Bolyai" University, Cluj-Napoca, 11 Arany Janos Str, Romania, RO-400028.*
* *Corresponding author: gszabo@chem.ubbcluj.ro.*

The existence of free radicals in the BR system was observed by Franz [6] and was evidenced by Cervellati and Furrow [7] through the interaction of them with soy antioxidants. They reported that the inhibitory effect caused by the addition of aqueous extracts of soy flour to an active BR mixture, consisted in the immediate cessation of oscillation. After the consumption of antioxidants contained in the extract, the oscillatory regime was regenerated.

It was developed a new method for monitoring the relative antioxidant activity [8] based on the inhibition time, namely the time elapsed between the cessation and the regeneration of the oscillatory regime. Cervellati et al. determined the relative antioxidant activity for several vegetable and fruit extracts [9], some natural polyphenols [10, 11] the effect of ascorbic acid [12] of hydroalcoholic solutions of antioxidants [13] and of the German red wine [14]. The influence on the active BR mixture of some other species, like lipoic acid [15], tea infusions [16] and some medicinal plants [17], e.g. Balanites aegyptiaca [18], Leontopodium alpinum [19], Cynara scolymus [20], was also studied. Pasteurized and sterilized commercial red orange juices [21] antioxidant activity was also determined with this method. The antioxidant components of tart cherries [22], sweet grapefruit and white grapefruit [23] were characterized. Temperature dependence of the overall antioxidant activity of red wine [24] was investigated.

The BR reaction under flow conditions is very sensitive to small perturbations caused by the analyte addition to the system resulting in the modifications of the oscillation parameters, such as amplitude or period. The determination of the resorcinol antioxidant activity was reported in continuous stirred tank reactor (CSTR) [25].

Kinetically important intermediates of the BR system are I^-, I_3^-, oxyiodine species like HOI, HIO_2, HOO• and iodomalonic acid (IMA); their concentration oscillates between a maximum and minimum value. The free radicals play a key role in the oscillating behavior, and their interaction with antioxidants changes the dynamics of the BR reaction. Recently CO_2 and CO evolution was observed in the BR system [26] and it was reported that this is also the consequence of a radical path [27]. The inhibitory effect was accounted for the fast reaction between the antioxidants and the main intermediates of the BR system, e.g. the hydroperoxyl radicals [9, 11].

Antioxidants are defined as molecules that, in low concentrations compared to those of a substrate, significantly delay or prevent the oxidation of that substrate. In plants they act as chemical self-protective agents against pathogens, also providing defense against various forms of environmental stress such as the harmful UV-B radiation and the reactive oxygen species. Phytochemical investigation of several plant extracts

demonstrated that free radical scavenger components are mainly the anthocyanins, flavonols, flavanols, folates and carotenoids. Plant phenolics are characterized as aromatic compounds that possess one or more phenolic hydroxyl groups.

Dietary antioxidants may affect human health, possibly by acting as antioxidants, are scavengers of reactive oxygen species (ROS), anticarcinogens and cardio protective agents. The plant based antioxidants are believed to have a better biological effect than the synthetic ones [28]. The fruits like dark-purple berries, raspberries, red currant and pomegranate have a high level of hydrolysable tannins, quercetin, gallic acid, anthocyanins, and cyanidins [29]. Apples are a significant source of flavonoids. It was noticed that the apple peels contain more antioxidant compounds, especially quercetin, than the apple flesh [30]. The citrus species are source of phytochemicals such as flavanones, hesperidin and naringenin, vitamin C and carotenoids [31-32]. The beetroot is one of the few vegetables that contain a group of highly bioactive pigment known as betanins, which have high antioxidant and anti-inflammatory capabilities [33].

Recently, it was reported [34] that antioxidant mixtures presented some discrepancy in their antioxidant capacity in comparison with the individual values. In some cases synergetic effects were observed, while in others antagonistic ones were seen.

In the past decades, several analytical methods were developed to determine the antioxidant activity [35]. All the methods are based on the generation of free radicals and their detection. The chemical reaction between these species is monitored usually spectrophotometrically (TEAC assay, DPPH assay, B-carotene bleaching assay) or by measuring chemo luminescence (PCL assay) or electron spin resonance (ESR assay).

The testing system of these assays differs in the pH value (3.3–10.5) of the medium and in the nature of the radicals. Some assays are suitable only for hydrophilic antioxidants, others for hydrophobic and lipophilic ones. The antioxidant activity of the most substances depends on pH so it's difficult to make a comparison of the obtained values. The activity of the examined antioxidants gives different ranking orders from assay to assay.

In our study the used method was that based on the BR reaction. It works for water soluble antioxidants in acidic medium at a low pH value. Some of the free radicals of the BR reactions are present in the human body too so the conclusions regarding the antioxidant activity of the juices can be useful for a healthy diet.
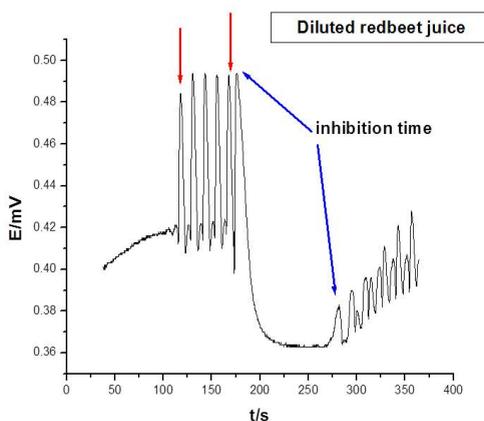
In this paper, the antioxidant activity of several raw fruit and vegetable juice was studied by the BR method. Selected for testing were the most commonly used fruit juices, like orange, apple, and pomegranate.

Also two vegetable juices were examined (beetroot and carrot), because they are the most recommended by medical staff as a dietary supplement. (It is daily practice that for patients who are under chemotherapy is recommended the red beet consumption). The behavior of the apple, orange, beetroot and carrot mixture against BR free radicals was studied. The inhibition time obtained for the mixture was compared with that of the individual values of the mixture components. Four berries: blackberry, raspberry, blueberry and red currant were also studied. It was reported that berries are considered "super fruits" because of their rich nutrition values. It is to be mentioned, that so far none of these berries were studied by the BR method.

RESULTS AND DISCUSSION

The antioxidant activity of fruit juices

Perturbation of the oscillatory BR system with a diluted fruit juice causes the immediate cessation of the oscillations; the time elapsed between the cessation and the return of the oscillations is the so called inhibition time (Figure 1). The first arrow indicates the addition of the hydrogen-peroxide to the BR system and the start of the oscillatory regime. The second arrow marks the addition of the antioxidant that causes the quenching of the oscillations.

Figure 1. The effect of the red beet juice on the active BR mixture.

The antioxidant activity of the different fruit juices was obtained for several dilutions and the calibration curves were drawn for each of them by linear fitting. Variation of the inhibition time with respect to antioxidant concentration was found to be linear (Figure 2).

The following equations can be obtained after applying the linear fitting.

$t_{inh} = -201.0(\pm 80.7) + 1.69 \cdot 10^5 (\pm 781.9) \cdot [blueberry]$

$t_{inh} = -270.2(\pm 11.9) + 1.35 \cdot 10^5 (\pm 562.2) \cdot [raspberry]$

$t_{inh} = -87.4(66.0) + 0.91 \cdot 10^5 (\pm 639.8) \cdot [red\ currant]$

$t_{inh} = -191.9(\pm 75.5) + 1.67 \cdot 10^5 (\pm 731.0) \cdot [blackberry]$

These equations evidenced that the blueberry and the blackberry have almost the same activity.

Beside of the berries, the antioxidant activity of orange, apple (peeled and unpeeled) and pomegranate was studied. The results are presented in the Figure 3. The calibration curve of the unpeeled apple juice has a steeper slope than the peeled one. Evidently, the antioxidant activity varies in the same way.
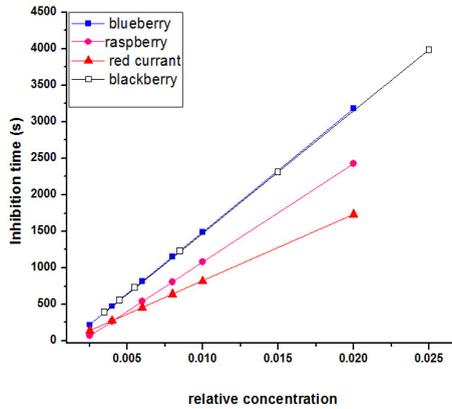
Figure 2. The calibration curves of the berries: a) blueberry(■), b) raspberry(●); c) red currant(▲); d) blackberry(□)
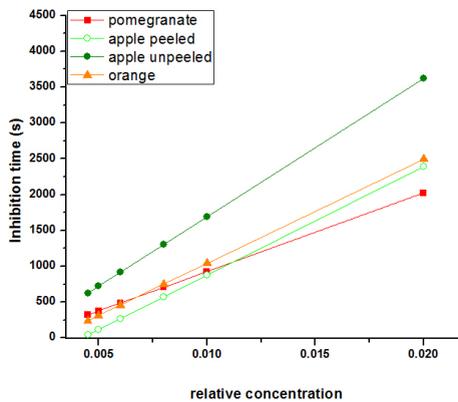
Figure 3. The calibration curves of the a) apple unpeeled (●), b) apple peeled (○); c) orange (▲); d) pomegranate (■)

The obtained equations of the calibration curves are given below.

t_{inh}=-243.3($\pm$53.2)+1.93*10^5 ($\pm$657.8) * [apple, unpeeled]

t_{inh}=-644.2 ($\pm$23.9)+1.51*10^5 ($\pm$172.2) * [apple, peeled]

t_{inh}=-414.6 ($\pm$66.0)+1.45*10^5($\pm$567.8) * [orange]

t_{inh}=-170.7($\pm$19.2)+1.10*10^5($\pm$748.4) *[pomegranate]

The effect of the mixture

The antioxidant activity of an unpeeled apple, beetroot, orange and carrot juice mixture was investigated and compared with the individual activities. The inhibition effect of this mixture on the BR reaction was measured and plotted.

In the Figure 4, the calibration curves for the individual juices and the mixture are plotted.
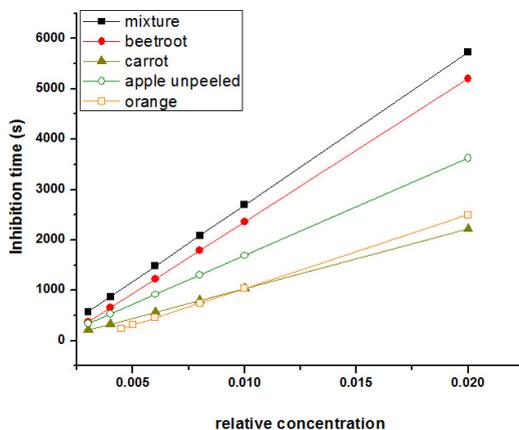
Figure 4. The calibration curves of the: a) mixture (■); b) beetroot (●); c) apple, unpeeled (○); d) orange (□); e) carrot (▲).

The calibration curves were obtained by linear fitting:

t_{inh}=-338.5($\pm$32.4)+3.03*10^5($\pm$6346.0) * [mixture]

t_{inh}=-479.1($\pm$17.1)+2.84*10^5($\pm$351.3.0) * [beetroot]

t_{inh}=-139.9($\pm$27.4)+1.18*10^5($\pm$961.5) * [carrot]

The inhibition time (at a certain concentration) of the mixture is higher than as expected considering the individual inhibition times of the components.

There are three different ways for calculating the relative antioxidant activities, with respect to concentration, to inhibition time and to the calibration curve slope [8].

First of all in order to determine a relative activity there must be chosen a standard. In our case this is the beetroot. From the calibration curve equation of the substance chosen as standard was determined the concentration that should give the same inhibition time as the sample. The ratio between this value and the concentration of the sample gives the relative activity, *i.e.*

$$R.A.C. = [standard]/[sample]$$

The concentration of the standard that gives a certain inhibition time can be calculated from its calibration curve.
Relative activity with respect to slopes (R.A.S.): is the ratio between the slope of the calibration curve of the sample and that of the standard; *i.e.*

$$R.A.S. = slope_{(sample)}/slope_{(standard)}.$$

Relative activity with respect to inhibition times (R.A.T.): is the ratio between the inhibition time of the sample and that of the standard at the same concentration:

$$R.A.T. = t_{inhib(sample)}/t_{inhib(standard)}.$$

The chosen concentration must be specified together with the R.A.T. values. These relative antioxidant activities were determined for the studied juices. The obtained results are presented in table 1.

Table 1. Values R.A.C and R.A.S and R.A.T. for investigated fruits

	R.A.C $(c_{standard}=0.01)$	R.A.S	R.A.T $(c_r=0.01, t_{inh}=2368$ s$)$
Mixture	1.12	1.07	1.14
Beetroot	1	1	1
Apple unpeeled	0.76	0.68	0.71
Apple peeled	0.48	0.53	0.37
Blackberry	0.68	0.58	0.62
Blueberry	0.69	0.59	0.63
Raspberry	0.54	0.47	0.46
Carrot	0.53	0.41	0.44
Orange	0.53	0.51	0.44
Pomegranate	0.49	0.39	0.39
Red currant	0.48	0.32	0.34

The R.A.T. values reveal which of the juices with the same concentration provide longer inhibition time. The R.A.S. values explain the development of the antioxidant activity related to the concentration of the juice. The R.A.C values compare the sample's concentration with that of the chosen standard for a certain inhibition time.

The best antioxidant activity was obtained for beetroot and it was chosen as the standard. The anthocyanin rich blueberry and blackberry obtained the highest rank, not only among the berries, but also among the other most commonly consumed fruit juices. Despite of the fact that pomegranate is called "super fruit" its antioxidant activity is relatively poor compared to those of the above mentioned berries. The raspberry and the pomegranate obtained a lower position in this rank.

CONCLUSIONS AND OUTLOOK

The active BR system was used as an analytical method to determine the antioxidant activity of some raw juices. The analytical signal was the inhibition time which shows linear dependence vs. the relative concentration. In order to compare the antioxidant activity, the R.A.C., R.A.T. and R.A.S. values were calculated. According to the R.A.C orders of antioxidant activity rank is:

Beetroot > unpeeled apple > blueberry > blackberry > raspberry > carrot = orange > pomegranate > red currant = peeled apple

The unpeeled apple, beetroot, orange and carrot mixture presented synergetic effect.

The BR analytical method is an excellent tool to measure the antioxidant activity of water soluble antioxidants because it is inexpensive and quick.

EXPERIMENTAL SECTION

The measurements were performed in a 20 mL double-walled glass batch reactor, connected to a FALC FA 90 thermostat (accuracy ± 0.1°C) in order to maintain the constant 20°C temperature. Continuous stirring was provided by a FALC 60 magnetic stirrer at a constant stirring rate. Oscillations were monitored with a double-junction saturated calomel electrode (SCE) as a reference electrode and a Pt electrode. They were connected to a computer through a PCI 6036 E data-acquisition interface. The oscillations were recorded through the LabView data-acquisition program and were processed by means of Microcall Origin 6.0 program.

For the preparation of the BR active mixture malonic acid (MA) (Fluka, puriss.), KIO_3 (Fluka, puriss. p.a.; $\geq$99.5%), KI (Riedel-deHaën, puriss. p.a.), H_2SO_4 (97%, Merck, p.a.), $MnSO_4*H_2O$ (Reanal) were used as received and the H_2O_2 (Fluka, puriss. p.a. ACS; $\geq$30%) was standardised by manganometric analysis. The stock solutions were obtained from doubly distilled water and they had the following concentrations: $[KIO_3]_0$=0.134 M,

$[H_2SO_4]_0$=0.358 M $[MA]_0$=0.2 M, $[MnSO_4]_0$=0.02 M, $[H_2O_2]_0$=2.6 M. They were kept in the thermostat at a constant temperature (20ºC). The BR systems were obtained by mixing the appropriate amounts of stock solutions (2 mL of each component) in such a way that finally resulted the initial   composition $[KIO_3]_i$=0.0268 M, $[H_2SO_4]$=0.0716 M $[MA]$=0.04 M, $[MnSO_4]$=0.004 M, $[H_2O_2]$=0.52 M. The order of mixing was: malonic acid, $MnSO_4$, H_2SO_4, KIO_3, and H_2O_2. Oscillations start after the addition of the H_2O_2. After the fifth oscillation 0.5 mL diluted raw juice was added to the reactor using a micropipette.

The following fruits and vegetables were selected for inclusion in the study: pomegranate, orange, apple, blackberry, raspberry, blueberry, red currant, carrot and red beet (beetroot). Except the orange and pomegranate, all the fruits and vegetables were cultivated in the region of Cluj. Orange, pomegranate, beetroot, apple and carrot was peeled to remove the outer skin, chopped into small pieces and passed through a juice extractor to produce the fresh, raw fruit or vegetable juice. For comparison was made an unpeeled apple juice too which presented a different behavior compared with the peeled apple juice. Several stock solutions of the fresh raw juices were made by the dilution of 5 mL of each sample to 10 mL with distilled water. Further and consecutive dilutions were made.

During the experiment, the appropriate dilutions of each juice were taken to give inhibition times which were of a reasonable length of time. Juices which were perceived as being low in antioxidant activity from the initial testing were examined at a lower dilution than juices with a higher antioxidant activity.

A sample which combined apple, orange, carrot and red beet (beetroot) was prepared by pouring equal quantities of these juices and was also tested at different dilutions.

ACKNOWLEDGMENTS

REFERENCES

1. T.S. Briggs, W.C. Rauscher, *J. Chem. Edu.*, **1973**, *50*, 496.
2. D.O. Cooke, *J. Chem. Soc., Chem. Commun.* **1984**, *9*, 589.
3. S.D. Furrow, R.M. Noyes, *J Am. Chem. Soc.* **1982**, *104*, 38, 42.
4. P. De Kepper, I.R. Epstein, *J Am. Chem. Soc.* **1982**, *104*, 49.
5. J. Happel, P.H. Sellers, *J. Phys. Chem*, **1991**, *95*, 7740.
6. D.A. Franz, *J. Chem. Edu.*, **1991**, *68*, 57.

7. R. Cervellati, N. Crespi-Perellino, S. Furrow, A. Minghetti, *Helv. Chim. Acta*, **2000**, *83*, 3179.
8. R. Cervellati, K. Höner, S. Furrow, C. Neddens, S. Costa, *Helv. Chim. Acta*, **2001**, *84*, 3533.
9. K. Höner, R. Cervellati, *Eur. Food Res. Technol*., **2002**, *215,* 437.
10. R. Cervellati, C. Renzulli, M.C. Guerra, E. Speroni, *J. Agric. Food. Chem*., **2002**, *50*, 7504.
11. S. Dall'Acqua, R. Cervellati, M.C. Loi, G. Innocenti, *Food Chemistry*, **2008**, *106*, 745.
12. K. Höner, S. Furrow, R. Cervellati, *Helv. Chim. Acta*, **2004**, *87*, 735.
13. R. Cervellati, K. Höner, S. Furrow, F. Mazzanti, *Helv. Chim. Acta*, **2002**, *85*, 2523.
14. K. Höner, R. Cervellati, C. Neddens, *Eur. Food Res. Technol.,* **2002**, *214,* 356.
15. G. Szabo, Cs. Bolla, L. Janos, Cs. Racz, *Studia UBB Chemia*, **2003**, *48*, 181.
16. N. Muntean, G. Szabo, *Studia UBB Chemia*, **2013**, *58*, 175.
17. J. Barillari, R. Cervallati, S. Costa, R. Iori, *J. Agric. Food Chem.,* **2006**, *54,* 9773.
18. R. Cervellati, G. Innocenti, S. Costa, M.C. Guerra, S. Dall' Acqua, P. Govoni, E. Speroni, *J. Ethnopharm.,* **2005**, *98,* 117.
19. S. Schwaiger, R. Cervellati, C. Seger, E.P. Ellmerer, H. Stuppner, *Tetrahedron,* **2005**, *61,* 4621.
20. E. Speroni, R. Cervellati, P. Govoni, *J. Ethnopharm,* **2003**, *86,* 203.
21. A. Fiore, L. La Fauci, R. Cervellati, N.C. Guerra, E. Speroni, S. Costa, *Mol. Nutr. Food Res.,* **2005**, *49,* 1129.
22. H. Wang, M.G. Nair, M. Gale, S. Yu-Chen Chang, A.M. Booren, J. Ian Gray, D.L. DeWit: *J. Nat. Prod.* **1999**, *62,* 294.
23. S. Gorinstein, M. Cvikrová, I. Machackova, R. Haruenkit, Y-S. Park, K. Yamamoto, A.L. Martinez Ayala, E. Katrich, S. Trakhtenberg, *J. Food Chem.* **2004**, *84,* 503.
24. E. Prenesti, S. Toso, S. Berto, *J Agric Food Chem.,* **2005**, *53,* 4220.
25. N. Muntean, I. Baldea, G. Szabo, Z. Noszticzius, *Studia UBB Chemia*, **2010**, *55*, 121.
26. G. Szabó, A. Csavdari, L. Onel, G. Bourceanu, Z. Noszticzius, M. Wittmann, *J. Phys. Chem. A.* **2007**, *111*, 601.
27. N. Muntean, G. Szabó, M. Wittmann, T. Lawson, Z. Noszticzius, J. Fülöp, L. Onel, *J. Phys. Chem. A.* **2009**, *113*, 9102.
28. S. Sen, R. Chakraborty, *The Role of Antioxidants in Human Health,* ACS Symposium Series, **2011**, *1083,* 1.
29. E. Sariburun, S. Sahin, C. Demir, C. Türkben, V. Uylaşer, *J Food Sci*., **2010**, *75(4),* 328.
30. C. Alasalvar, J.M. Grigor, D. Zhang, P.C. Quantick, F. Shahidi, *J Agric. Food Chem*., **2001**, *49,* 1410.
31. A. Gil-Izquierdo, M.I. Gil, F. Ferreres, *J. Agric. Food Chem*., **2002**, *50 (18)*, 5107
32. A. Zarfeshany, S. Asgary, S.H. Javanmard*., Adv. Biomed. Res*., **2014**, *25*, 100.
33. J.J. Vulic, T.N. Cebovic, J.M. Canadanovic-Brunet, G.S. Cetkovic, V.M. Canadanovic, S.M. Djilas, V.T. Tumbas Saponjac, *J. Funct. Foods*., **2014**, *6*, 168.
34. M. Mladen, M. Dika, *Food Chem*., **2012**, *131*, 296.
35. B.L. Halvorsen, K. Holte, M.C.W. Myhrstad, I. Barikmo *The Jour. of Nutr.,* **2002**, *132 (3),* 461.

Dedicated to prof. dr. I. C. Popescu
on the occasion of his 70th anniversary

ANTIMICROBIAL ACTIVITY SCREENING OF BENZOTHIAZOLYL-PHENOTHIAZINE DERIVATIVES

ADRIANA GROZAV[a*], VALENTIN ZAHARIA[a], CASTELIA CRISTEA[b], NICODIM IOSIF FIT[c]

ABSTRACT. The antimicrobial activity of a series of benzothiazolyl-10*H*-phenothiazine derivatives against Gram positive Bacteria (*Staphylococcus aureus* and *Bacillus cereus*), Gram negative Bacteria (*Escherichia coli*, *Salmonella enteritidis*, *Pseudomonas aeruginosa*) and fungus *Candida albicans* respectively, was screened using diffusion method and minimal inhibitory concentrations (MIC) were assessed by broth serial dilution procedure. *Candida albicans*, *Bacillus cereus* and *Pseudomonas aeruginosa* were proved to be susceptible to the benzothiazolyl-10*H*-phenothiazine derivatives (MIC 0.02-1.3 µg/mL)

Key words: *phenothiazine, benzothiazole, antibacterial, diffusion, broth dilution, minimal inhibitory concentration*

INTRODUCTION

Phenothiazine and benzothiazole are heterocyclic aromatic structures largely employed as pharmacophoric units. A careful selection of the substitution pattern of the phenothiazine unit enabled a large spectrum of biological activities such as neuroleptic, antimicrobial, anthelmintic, etc. [1,2], while benzothiazole derivatives were also screened as antimicrobial [3], anticancer [4], antihelmintic [5], and antidiabetic [6] agents.

[a] *Faculty of Pharmacy, "Iuliu Haţieganu" University of Medicine and Pharmacy, RO-400012, Victor Babes 41, Cluj-Napoca, Romania.*
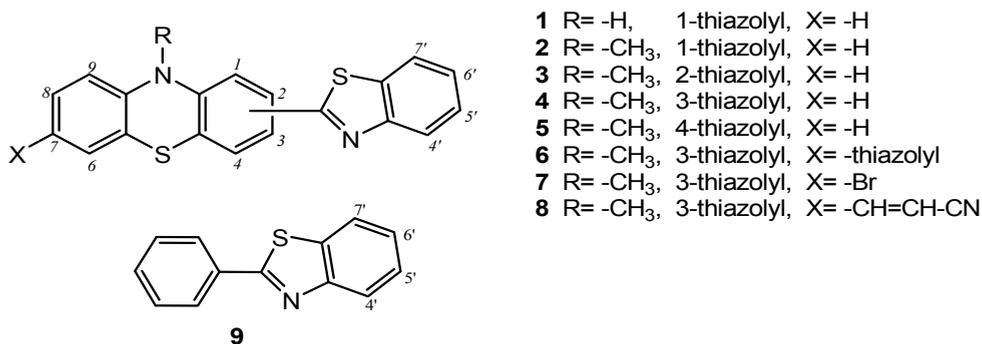[*] *Corresponding author: adriana.ignat@umfcluj.ro*
[b] *Babes-Bolyai" University, Faculty of Chemistry and Chemical Engineering, RO-400028, Cluj-Napoca, Romania.*
[c] *Agricultural Sciences and Veterinary Medicine Cluj-Napoca, Faculty of Veterinary Medicine, Microbiology Department, Cluj Napoca, RO-400337, Romania.*

Continuing our research in the biological activity evaluation of new synthetic compounds containing phenothiazine and thiazole units assembled in the same molecular structure [7-10], we report here the antimicrobial screening of a series of new derivatives containing joint phenothiazine and thiazole units [11].

RESULTS AND DISCUSSIONS

The series of benzothiazolyl-phenothiazine derivatives selected for the evaluation of antimicrobial activity contain different substitution patterns at the phenothiazine unit as shown in Figure 1. C-substituted regioisomer series cover derivatives with benzothiazol-2-yl unit attached in positions 1-4 of the phenothiazine moiety and the heterocyclic nitrogen atom in an NH (**1**), or N-methyl group (**2-5**). Symmetrical 3,7-disubstituted phenothiazine derivatives contain two benzothiazolyl groups (**6**), while unsymmetrical derivatives include a halogene (**7**), or a 2-cyano-vinyl group (**8**) apart the benzothiazole substituent. 2-Phenyl-benzothiazole (**9**) was also included in the tested series for a relative examination of the properties induced by the benzothiazole unit.

1 R= -H,   1-thiazolyl, X= -H
2 R= -CH$_3$, 1-thiazolyl, X= -H
3 R= -CH$_3$, 2-thiazolyl, X= -H
4 R= -CH$_3$, 3-thiazolyl, X= -H
5 R= -CH$_3$, 4-thiazolyl, X= -H
6 R= -CH$_3$, 3-thiazolyl, X= -thiazolyl
7 R= -CH$_3$, 3-thiazolyl, X= -Br
8 R= -CH$_3$, 3-thiazolyl, X= -CH=CH-CN

Figure 1. Structure of synthetic derivatives subjected to the antimicrobial activity screening

The *in vitro* antimicrobial susceptibility of Gram positive bacteria: *Staphylococcus aureus* and *Bacillus cereus*, Gram negative bacteria: *Escherichia coli*, *Salmonella enteritidis*, *Pseudomonas aeruginosa* and *Candida albicans* fungus respectively, was screened using diffusion method; minimuml inhibitory concentration (MIC) of compounds **1-9** were determined using broth serial dilution procedure.

The examination of the inhibition zones resulted by diffusion procedure pointed out an intermediate response of *S. aureus, B. cereus*, *P.*

aeruginosa (Table 1) to the tested compounds **1-9**, while the rest of the tested bacterial strains seemed resistant. Based on this method, 3-(benzothiazol-2-yl)-10-methy-10*H*-phenothiazine **4** was observed to be the most efficient of the series, even more efficient than amoxicillin against *B. cereus* and with an antifungal activity slightly better than miconazole against *C. albicans.*

Table 1. Inhibition zone diameter (mm) obtained by diffusion procedure using compounds **1-9** in solution 63 mM in DMSO[a].

Compound (25 μl/disc)	*S. aureus*	*B. cereus*	*P. aeruginosa*	*C. albicans*
1	6	6	0	0
2	6	0	0	0
3	6	6	0	6
4	12	18	10	25
5	6	6	0	6
6	6	7	6	6
7	6	7	7	8
8	9	8	6	0
9	7	7	12	7
Amoxicillin[b]	40	9	0	-
Miconazole[c]				21

[a]DMSO produced no inhibition zone; [b]25μg/disc; [c]10 μg/disc.

The minimum inhibitory concentration (MIC) determined by broth dilution using ten concentrations derived from serial twofold dilution indicate antifungal and antibacterial activity for each compound in the series with MIC between 0.02-1.3 μg/ml. As it may be seen from figure 2, in the mono-benzothiazolyl-phenothiazine series characterized by enhanced antimicrobial activity, 1-, 2- and 3-substituted phenothiazine derivatives (**1, 2, 3** and **4**) were the most effectives against *C. albicans* (with MIC around 0.02-0.04 μg/ml), while *B. cereus* was effectively inhibited by 1- and 3-benzothiazolyl-phenothiazines (**1, 2** and **4**). When the benzothiazolyl substituent was situated in position 4 of the phenothiazine unit (**5**) the observed activity against *B. cereus* appeared largely diminished (MIC ≈1.3 μg/mL).

A lower susceptibility of Gram negative bacteria to benzothiazolyl-phenothiazine derivatives **1-8** may be observed in figure 3. The best results were achieved in the inhibition of *P. aeruginosa. E. coli* and *S. enteritidis* were susceptible to the unsymmetrical 3,7-disubstituted benzothiazolyl-phenothiazine derivatives containing bromine **7**, or 2-cyano-vinyl group **8** (MIC 0.8 and 0.4 μg/ml respectively).

The antimicrobial activity of 2-phenyl-benzothiazole **9** was observed to be less effective as compared to benzothiazolyl-phenothiazine derivatives **1-8** in each case.
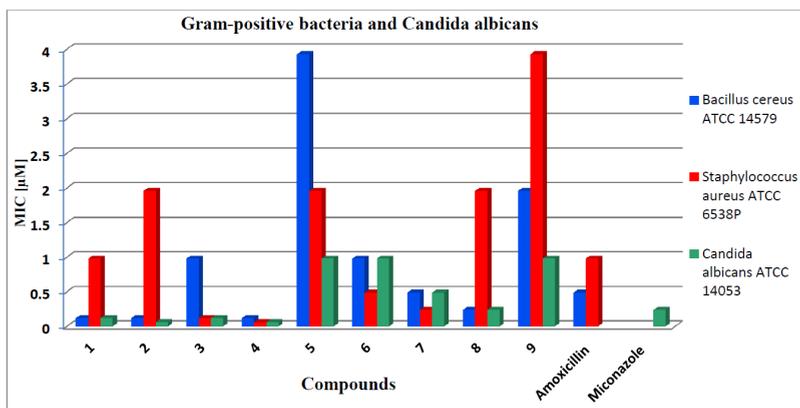
Fig. 2. Antimicrobial activity of benzothiazolyl-phenothiazine derivatives evaluated using broth dilutions method (tested serial concentrations: 0.06, 0.12, 0.24, 0.49, 0.98, 1.96, 3.93, 7.85, 15.75 and 31.5 µM).
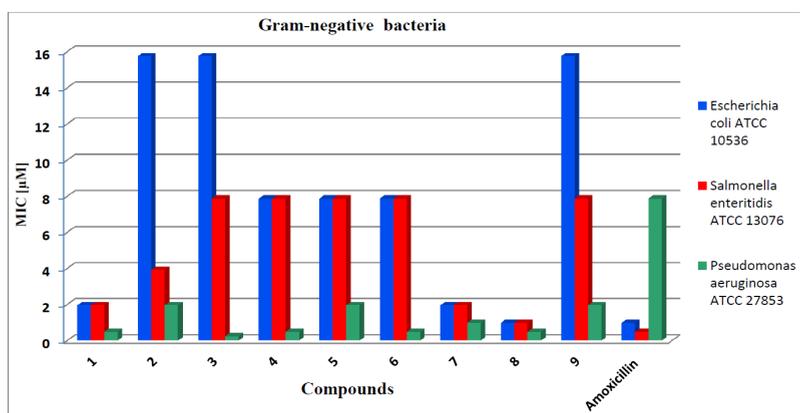
Fig 3. Antibacterial activity of benzothiazolyl-phenothiazine derivatives evaluated using broth dilutions method (tested serial concentrations: 0.06, 0.12, 0.24, 0.49, 0.98, 1.96, 3.93, 7.85, 15.75 and 31.5 µM).

CONCLUSIONS

Based on the described *in vitro* antimicrobial susceptibility test, the synthetic benzothiazolyl-phenothiazine derivatives developed a better antimicrobial activity as compared to 2-phenyl-benzothiazole.

Mono 1-, 2- and 3-benzothiazolyl-phenothiazine derivatives were effective against *C. albicans*, *B. cereus* and *P. aeruginosa.* Connecting the benzothiazolyl substituent in position 4 of the phenothiazine unit diminishes this antimicrobial activity.

Symmetrical 3,7-disubstituted phenothiazine derivatives containing two benzothiazolyl groups were less efficient than mono 3-substituted derivative.

S. aureus, *E. coli*, and *S. enteritidis* were less susceptible to the antibacterial benzothiazolyl-phenothiazine derivatives.

EXPERIMENTAL

Materials:
Gram positive bacterial strains: *Staphylococcus aureus* ATCC 6538P and *Bacillus cereus* ATCC 14579.

Gram negative bacterial strains: *Escherichia coli* ATCC 10536, *Salmonella enteritidis* ATCC 13076 and *Pseudomonas aeruginosa* ATCC 27853

Fungus: *Candida albicans* ATCC 14053
Mueller Hinton Agar (Merck, Germany)
Sabouraud dextrose agar (Merck, Germany)

Antimicrobial tests:
a) The Diffusion method was carried out according to standard methods described by CLSI-M02-A10 [12] and Markey and co. [13]. A bacteria culture which has been adjusted to 0.5 McFarland standard, 10^6UFC/ml in physiological solution was used to inoculate Muller Hinton agar plates, followed by incubation at 37 ± 2^0C for 24 hours. For the susceptibility tests, on each test plate were made wells (5 mm diameter) in radial disposition and 25 µl from 63 mM solution of synthetic compounds in DMSO were disposed. Seven compounds were tested on a plate. The standard commercial antibiotic amoxicillin (25µg**)** was used for positive control and DMSO solvent for negative control. After incubation at 37 ± 2^0C for 24 hours the plates were examined for inhibition zone, which was measured and recorded in mm.

The fungus was cultivated and tested on Sabouraud dextrose agar with incubation at 37 ± 2^0C for 48h in aerobic conditions. The tests were repeated three times to ensure reliability.

b) Broth dilution procedure was carried out according to the protocols previously described [12,13] with minor modifications according to the properties of tested compounds. MIC was determined using microdilution trays with 96 wells. In each well were introduced 50µl Mueller Hinton broth and 50 µl of diluted antimicrobial agents. Serial two fold dilutions were prepared starting with a stock solution 63 mM in DMSO and distilled water. 5 µl suspension of bacteria in physiological solution standardized to 0.5 McFarland was added in each well and the plates were incubated at 37 ± 2^0C for 24 h under aerobic conditions. Each tray included a growth control well and a sterility (uninoculated) well.

For the fungus Sabouraud dextrose broth was used and incubation was performed at 37 ± 2^0C for 48h in aerobic conditions.

The amount of growth in the wells containing the antimicrobial agent was compared with the amount of growth in the growth-control well.

ACKNOWLEDGMENTS

REFERENCES

1. K. Pluta, B. Morak-Młodawska, M. Jeleń, *Eur. J. Med. Chem.,* **2011**, *8*, 3179.
2. K.V. Tandon, H.K. Maurya, A. Tripathi, G.B. ShivaKeshava, P.K. Shukla, P. Srivastava, D. Panda, *Eur J. Med. Chem.*, **2009**, 1086.
3. S. Gupta, N. Ajmera, N. Gautam, R. Sharma, D. Gauatam, *Ind. J. Chem.,* **2009**, *48B*, 853. b) R.M. Kumbhare, V.N. Ingle, *Ind. J. Chem.*, **2009**, *48B*, 996. c) Y. Murthi, D. Pathak, *J. Pharm. Res*., **2008**, *7*(3), 153.
4. H.L.K. Stanton, R. Gambari, H.C. Chung, C.O.T. Johny, C. Filly, S.C.C. Albert, *Bioorg. Med. Chem*., **2008**, *16*, 3626. b) I. Hutchinson, M.S. Chua, H.L. Browne, V. Trapani, T.D. Bradshaw, A.D. Westwell, *J. Med. Chem.,* **2001**, *44*, 1446.
5. M. Sreenivasa, E. Jaychand, B. Shivakumar, K. Jayrajkumar, J. Vijaykumar, *Arch. Pharm. Sci. Res*., **2009**, *1*(2), 150.
6. S. Pattan, C. Suresh, V. Pujar, V. Reddy, V. Rasal, B. Koti, *Ind. J. Chem*., **2005**; *44B*, 2404-2408.
7. A. Ignat, T. Lovasz, M. Vasilescu, E. Fischer-Fodor, C.B. Tatomir, C. Cristea, L. Silaghi-Dumitrescu, V. Zaharia, *Arch. Pharm. Chem. Life Sci.,* **2012**, *345*, 574.
8. V. Zaharia, A. Ignat, N. Palibroda, B.Ngameni, V. Kuete, C.N. Fokunang, M.L. Moungang, B.T. Ngadjui, *Eur. J. Med. Chem.*, **2010**, *45*, 5080.
9. A. Ignat, V. Zaharia, C. Mogosan, N. Palibroda, C. Cristea, L. Silaghi-Dumitrescu, *Farmacia,* **2010**, *58*, 290.
10. A. Grozav, L.I. Găină, V. Pileczki, O. Crisan, L.Silaghi-Dumitrescu, B. Therrien, V. Zaharia, I. Berindan-Neagoe, *Int. J. Mol. Sci.,* **2014**, *15*, 22059.
11. B. Brem, E. Gal, C. Cristea, L. Găină, A. Grozav, V. Zaharia, L. Silaghi-Dumitrescu, *Studia UBB Chemia*, **2015**, *60* (2), 371.
12. CLSI. Methods for Dilution Antimicrobial Susceptibility Tests f or Bacteria That Grow Aerobically; Approved Standard–Ninth Edition. CLSI document M07-A9. Wayne, PA: Clinical and Laboratory Standards Institute, **2012**.
13. B.K. Markey, F.C. Leonard, M. Archambault, A. Cullinane, D. Maguire. Clinical Veterinary Microbiology. Elsevier, Edinburgh, London, New York, Oxford, Philadelphia, St Louis, Sydney, Toronto, **2013**.